Dissertation zur Erlangung des naturwissenschaftlichen Doktorgrades
der Graduate School of Science and Technology,
Julius-Maximilians-Universität Würzburg

Femtosecond spectroscopy of photolysis reactions in the liquid phase

Femtosekundenspektroskopie von Photolysereaktionen in der flüssigen Phase

vorgelegt von
Johannes Walter Knorr

aus
Wiesentheid

Würzburg, 2015

Eingereicht am: . . . .
Stempel des GSST Büro

Mitglieder des Promotionskomitees:

Vorsitzende/r: . . . .

1. Betreuer: Prof. Dr. Patrick Nürnberger (Ruhr-Universität Bochum)

2. Betreuer: Prof. Dr. Tobias Brixner

3. Betreuer: Prof. Dr. Volker Engel

Tag des Promotionskolloquiums: . . . .

Doktorurkunden ausgehändigt am: . . . .

Kurzfassung

Im Rahmen dieser Dissertation wurden Methoden der ultraschnellen optischen Spektroskopie angewandt, um Photolysereaktionen in der flüssigen Phase zu untersuchen. Neben molekularen Studien, welche sich mit der stark spin-abhängigen Reaktivität von Diphenylcarben (DPC) in binären Lösungsmittelgemischen und den Ligandendissoziationsreaktionen von sogenannten CO-freisetzenden Molekülen (CORMs, engl.: CO-releasing molecules) befassten, war ein wesentlicher Bestandteil dieser Arbeit die Implementierung und Charakterisierung von Methoden zur Verbesserung und Erweiterung der Signaldetektion in Aufbauten zur zeitaufgelösten Anrege-Abfrage-Spektroskopie.

Die generelle Annahme, dass es sich bei DPC um ein archetypisches Triplett-Grundzustands-Arylcarben handelt, wurde kürzlich durch Matrixisolationsstudien in Frage gestellt. In jenen Untersuchungen offenbarte DPC, eingebettet in Argon-Matrizen, durch die Modifizierung der Carbenumgebung mit geringen Mengen an Methanol-Dotiermolekülen, eine bislang unbekannte Reaktivität. Komplementär dazu wurden im Rahmen dieser Arbeit Messungen in der flüssigen Phase bei Raumtemperatur durchgeführt. Femtosekundenzeitaufgelöste Anrege-Abfrage-Spektroskopie mit Abfragepulsen aus dem sichtbaren und ultravioletten Spektralbereich diente dabei zur Aufklärung der primären Reaktionsprozesse von DPC in Lösungsmittelgemischen. Es zeigte sich, unterstützt durch quantenchemische Simulationen unserer Kollaborateure, dass konkurrierende Reaktionspfade auftreten, welche nicht nur von den Lösungsmittelmolekülen in der unmittelbaren Umgebung abhängen, sondern auch von deren Wechselwirkung mit anderen Lösungsmittelmolekülen. Eine ausführliche Analyse, sowohl der Solvatationsdynamiken als auch der Menge an aufkommenden Intermediaten, bekräftigte die Bedeutung eines Komplexes der durch Wasserstoffbrückenbindung mit einem protischen Lösungmittelmolekül entsteht — in auffallender Ähnlichkeit zu Komplexen die bei kryogenen Temperaturen gefunden wurden.

Das Abfragen der transienten Absorption eines Moleküls im mittleren Infrarot wird durch die hohe chemische Spezifität von molekularen Schwingungssignaturen begünstigt. Um dieses spektrale Fenster zu untersuchen, bietet die CPU-Methode (engl.: chirped-pulse upconversion) eine vielversprechende Alternative zur konventionellen direkten Mehrkanal MCT-Detektion. Daher widmet sich ein Kapitel dieser Arbeit einem direkten Vergleich der beiden Detektionsmethoden. Im Rahmen eines exemplarischen Anrege-Abfrage-Experiments zeigte sich, dass die zusätzliche nichtlineare Wechselwirkung zu einem erhöhten Rauschniveau bei der Verwendung der CPU-Technik führt. Dennoch konnte eine Korrekturprozedur erfolgreich getestet werden, die es ermöglicht, jene zusätzlichen Rauschbeiträge, die durch Fluktuationen der fundamentalen Laserstrahlung hervorgerufen werden, zu entfernen. Am wichtigsten für eine Vielzahl spektroskopischer Anwendungen ist jedoch, dass die CPU-Technik auf Grund der hohen Pixel-Anzahl moderner CCD-Kameras mit einer signifikant erhöhten Detektionsbandbreite punkten kann.

Für biologische Anwendungen besteht steigendes Interesse an Molekülen zur kontrollierten Verabreichung von Gasotransmittern wie Kohlenstoffmonoxid (CO) oder Stickstoffmonoxid (NO). Vielversprechend sind hierbei Übergangsmetallkomplexe, welche in

der Lage sind, jene kleinen Signalmoleküle nach Photoanregung freizusetzen. Dennoch ist nur sehr wenig über die charakteristischen Zeitskalen der Ligandendissoziation in dieser Molekülklasse bekannt. Daher wurden im Rahmen dieser Arbeit zwei Komplexe mit Femtosekundenzeitauflösung untersucht: $[\text{Mn(CO)}_3(\text{tpm})]\text{Cl}$ mit tpm = tris(2-pyrazolyl)methane, ein Mangankomplex mit drei Carbonylliganden, desses selektive und zytotoxische Wirkung gegenüber Krebszellen nachgewiesen ist, und $[\text{Mo(CO)}_2(\text{NO})(i\text{Pr}_3\text{tacn})]\text{PF}_6$ mit $i\text{Pr}_3\text{tacn} = 1,4,7\text{-triisopropyl-}1,4,7\text{-triazacyclononane}$, ein Molybdänkomplex, der sowohl CO- als auch NO-Liganden enthält. Mit Hilfe von Anrege-Abfrage-Spektroskopie in verschiedenen spektralen Bereichen, unterstützt durch quantenchemische Berechnungen und lineare Absorptionsspektroskopie, konnte gezeigt werden, dass beide Komplexe jeweils einen CO-Liganden innerhalb der ersten Pikosekunden nach UV-Anregung abspalten können. Die Ergebnisse ergänzen bestehende Studien, welche die Ligandenfreisetzungseigenschaften der Moleküle unter Langzeitbelichtung untersuchten. Die zusätzliche Information – gewonnen auf der ultraschnellen Zeitskala – ermöglicht ein umfassendes Verständnis der einzelnen Reaktionsschritte, welche mit der Ligandendissoziation in dieser Molekülklasse verbunden sind. Daher könnten die Studien neue Anreize zur Entwicklung modifizierter Moleküle schaffen, welche für spezifische Anwendungen geeignet sind.

Abstract

Within the framework of this thesis, photolysis reactions in the liquid phase were investigated by means of ultrafast optical spectroscopy. Apart from molecular studies dealing with the highly spin-dependent reactivity of diphenylcarbene (DPC) in binary solvent mixtures and ligand dissociation reactions of so-called *CO-releasing molecules* (CORMs), special emphasis was put on the implementation and characterization of methods improving and extending the signal detection in conventional pump–probe transient absorption setups.

The assumption of DPC being an archetypal triplet-ground-state arylcarbene was recently questioned by matrix-isolation studies at low temperatures. DPC embedded in argon matrices revealed a hitherto unknown reactivity when the carbene environment was modified by small amounts of methanol dopant molecules. To complement these findings with liquid-phase experiments at room temperature, femtosecond pump–probe transient absorption spectroscopy with probing in the visible and ultraviolet regime was employed to unravel primary reaction processes of DPC in solvent mixtures. Supported by quantum chemical simulations conducted by our collaborators, it was shown that a competition between the reaction pathways occurs that not only depends on the solvent molecule near-by but also on its interaction with other solvent molecules. In-depth analysis of the solvation dynamics and the amount of nascent intermediates corroborates the importance of a hydrogen-bonded complex with a protic solvent molecule, in striking analogy to complexes found at cryogenic temperatures.

Probing the transient absorption of molecules in the mid-infrared spectral range benefits from the high chemical specificity of molecules' vibrational signatures. The technique of *chirped-pulse upconversion* (CPU) constitutes a promising alternative to standard direct multichannel MCT detection when accessing this spectral detection window. Hence, one chapter of this thesis is dedicated to a direct comparison between both detection methods. By conducting an exemplary pump–probe transient absorption experiment, it became evident, that the additional nonlinear interaction step is responsible for increased noise levels when using CPU. However, a correction procedure capable of removing these additional noise contributions—stemming from the fundamental laser radiation used for upconversion—was successfully tested. Perhaps most importantly for various spectroscopic applications, CPU scored with a significantly extended detection bandwidth owing to the high pixel numbers of modern CCD cameras.

Transition-metal complexes capable of releasing small molecular messengers upon photoactivation are promising sources of gasotransmitters such as carbon monoxide (CO) or nitric oxide (NO) in biological applications. However, only little is known about the characteristic time scales of ligand dissociation in this class of molecules. For this purpose, two complexes were investigated with femtosecond time resolution: $[\text{Mn(CO)}_3(\text{tpm})]\text{Cl}$ with tpm = tris(2-pyrazolyl)methane, a manganese tricarbonyl complex which has proven to be selective and cytotoxic to cancer cells, and $[\text{Mo(CO)}_2(\text{NO})(i\text{Pr}_3\text{tacn})]\text{PF}_6$ with $i\text{Pr}_3\text{tacn}$ = 1,4,7-triisopropyl-1,4,7-triazacyclononane, a molybdenum complex containing both carbonyl and nitrosyl ligands. By conducting pump–probe transient absorption measurements in different spectral probing windows supported by quantum chemical calculations and linear absorption spectroscopy, it was shown that both complexes are able

to release one CO ligand within the first few picoseconds after UV excitation. The results complement existing studies which focused on the molecules' ligand-releasing properties upon long-term exposure. The additional information gained on an ultrafast time scale provides a comprehensive understanding of individual reaction steps connected with ligand release in this class of molecules. Hence, the studies might create new incentives to develop modified molecules for specific applications.

List of Publications

Reference [1]:

J. Knorr, P. Sokkar, S. Schott, P. Costa, W. Thiel, W. Sander, E. Sánchez-García and P. Nuernberger,
Tracing Primary Processes of Diphenylcarbene in Solvent Mixtures: A Solvent Rivalry,
manuscript in preparation (2015).

Reference [2]:

J. Knorr, S. Schott, J. Riefer, C. Nagel, U. Schatzschneider, and P. Nuernberger,
Ultrafast photochemistry of a carbonyl-nitrosyl molybdenum complex,
manuscript in preparation (2015).

Reference [3]:

J. Knorr, P. Rudolf, and P. Nuernberger,
A comparative study on chirped-pulse upconversion and direct multichannel MCT detection,
Optics Express **21**, 30693-30706 (2013).

Reference [4]:

P. Rudolf, F. Kanal, J. Knorr, C. Nagel, J. Niesel, T. Brixner, U. Schatzschneider, and P. Nuernberger,
Ultrafast Photochemistry of a Manganese-Tricarbonyl CO-Releasing Molecule (CORM) in Aqueous Solution,
J. Phys. Chem. Lett. **4**, 596-602 (2013).

Further publications which are not related to this thesis:

Reference [5]:

H. Thierschmann, M. Henke, J. Knorr, L. Maier, C. Heyn, W. Hansen, H. Buhmann, and L. W. Molenkamp,
Diffusion thermopower of a serial double quantum dot,
New J. Phys. **15**, 123010 (2013).

Articles mentioned in the List of Publications have partly been used in this dissertation. The following table itemizes to what extent the different sections of the publications have been reused at which position in this work. The permissions for reproducing the original articles was granted by the respective publishing company holding the copyright. For the corresponding documents, see pp. LXXIII–LXXIV. Additionally, the sources of adapted figures are indicated at the end of the corresponding figure captions.

publication	usage	dissertation
Ref. [1]	text, figures, and schemes will (partly) be used and modified in the publication currently in preparation	pp. 61–79 pp. XXIII–XXXI
Ref. [2]	text, figures, and schemes will (partly) be used and modified in the publication currently in preparation	pp. 100–106 pp. XXXV–XXXVI
Ref. [3][1] p. 1 p. 3 p. 3 pp. 4–5 pp. 5–14	mainly reproduced with minor modifications reproduced, modified, and extended reproduced, modified, and extended reproduced, modified, and extended mainly reproduced with minor modifications	p. 81 pp. 33–34 p. 82 pp. 53–59 pp. 82–92
Ref. [4][2] pp. 1–7 Fig. 2 Fig. 3	modified reproduced data reproduced	pp. 94–100 p. XXXIII p. XXXIV

[1]Reproduced and adapted with permission from Optics Express, 2013, 21, pp. 30693–30706. © (2013) Optical Society of America.

[2]Reproduced and adapted with permission from Journal of Physical Chemistry Letters, 2013, 4, pp. 596–602. © (2013) American Chemical Society.

Contents

Introduction

The absorption of a photon, i.e., one quantum of light, prepares a molecular system in an excited state and initiates (a manifold of) subsequent photophysical or photochemical processes which either take place in a concerted or stepwise manner. Prominent examples are ranging from isomerizations via reactions affecting a molecule's spin-state to processes that involve the cleavage and formation of chemical bonds. Whereas the process of photon absorption can be considered to happen instantaneously, subsequent dynamics typically happen on a femtosecond (fs) to nanosecond (ns) time scale, still several orders of magnitude faster than everyday phenomena evident at a macroscopic level. Only the development of ultrafast spectrocopic techniques based on modern femtosecond laser sources made it possible to access the microscopic scale and study molecular dynamics on the time scales on which they actually occur. The field of *femtochemistry*, pioneered by Ahmed Zewail who was awarded with the Nobel Prize in Chemistry in 1999, therefore not only opened up the possibility to determine the characteristic time scale on which a chemical reaction takes place but also enabled one to identify chemical intermediates and analyze their temporal behavior [6–8].

The liquid phase offers, in contrast to the gas phase, several channels for energy relaxation to a molecular system in an excited state [9]. This thesis, however, deals with photo-initiated reaction mechanisms in the liquid phase in which the absorption of a ultraviolet (UV) or visible (VIS) photon leads to the photolysis of particular ligands or atoms preparing a molecule in a metastable state which *ipso facto* constitutes the starting point for subsequent reaction steps. But how to follow such photoinduced dynamics? In a pump–probe experiment in the UV to VIS spectral regime, ultrashort pulses are exploited to first excite and secondly probe an electronically excited state of a molecular system via the observation of changes in characteristic absorption signatures [10, 11]. This approach allows for a direct observation of processes happening on excited-state potential energy surfaces (PES) such as photoinduced electron transfer or trans-cis isomerization reactions. Due to the liquid environment, however, typical spectral features in the UV to VIS spectral region are very broad and almost featureless. Ultrafast investigations in this spectral region based on sophisticated two-dimensional (2D) [12, 13] or even multidimensional spectrocopic approaches [14, 15] mainly dealt with photophysical phenomena and provided, with the exception of few specialized photosynthetic chromophore complexes, only limited information about structural changes as well as intra- and intermolecular interactions. Nevertheless, first steps have been made to apply these concepts also for the study of photochemical phenomena [16, 17]. To easily gain structural information, e.g., to determine a molecule's conformation or to assess the presence of particular substituents, nuclear magnetic resonance (NMR) experiments are one alternative. However, due to experimental constraints, it is not feasible to directly use NMR for real-time ob-

servation of chemical dynamics. The gap between ultrafast time resolution and structural sensitivity was bridged by the development of ultrafast infrared (IR) light sources and corresponding spectroscopic techniques [18]. Especially the mid-infrared (MIR) spectral region, often termed as fingerprint region due to its exquisite sensitivity for conformation, structure, and environment, is a popular spectroscopic playground to investigate dynamical processes which are manifested in changes in the molecule's vibrational signatures. Therefore, often a UV or VIS pump pulse is used to trigger a photoreaction by accessing an electronically excited state, whereas subsequent probing in the MIR spectral region reveals structural changes owing to the relatively sharp vibrational absorption lines. In doing so, one has to accept slight losses regarding the time resolution due to the inherently different wavelengths involved and typical vibrational linewidths which set the ultimate limit. However, most dynamical processes are easily accessible with nowadays experimental possibilities independent of the wavelength of the employed laser pulses [19]. Within this thesis, probing in the UV to VIS or MIR region is used complementary with respect to particular interrogations regarding the molecular system under investigation. The work's structure is given as follows.

In Chapter 2, the theoretical concepts are summarized which are necessary for the understanding and interpretation of the experimental findings presented in this thesis. This starts with a mathematical description of ultrashort laser pulses and their role in nonlinear frequency conversion processes. Furthermore, the concept of pump–probe spectroscopy is introduced, complemented by a brief theoretical treatment of molecules' electronic and vibrational structure. Prior to the presentation of results from ultrafast studies, a detailed description of the employed experimental techniques is given in Chapter 3.

Via broadband probing in the UV to VIS spectral regime [20], Chapter 4 sheds new light on the primary reaction pathways of singlet diphenylcarbene (DPC) in the presence of a solvent. In combination with quantum chemical simulations performed by the group of Dr. Elsa Sánchez-García at the Max-Planck-Institut für Kohlenforschung in Mülheim an der Ruhr, it is shown that the efficiency of different reaction channels can be controlled in a non-trivial way by employing solvent mixtures. Our observations at room temperature in the liquid phase are in line with results from recent matrix-isolation studies at cold temperatures conducted by our collaborators who also provided the sample (group of Prof. W. Sander, Organic Chemistry 2, Ruhr University Bochum) [21, 22]. Shifting the probing window towards longer wavelengths, Chapter 5 deals with methods to detect MIR pulses. In particular, the newly established technique of chirped-pulse upconversion (CPU) [23, 24] is directly compared to conventional direct multichannel MCT detection with respect to their applicability in ultrafast infrared vibrational spectroscopy. Weighing up the benefits and disadvantages of each technique, the results highlight the great potential of CPU as a versatile and easy-to-handle alternative to standard detection schemes. Both techniques are employed in Chapter 6 to study ligand dissociation reactions from transition-metal complexes capable of releasing small molecular messengers such as carbon monoxide (CO) or nitric oxide (NO) upon photoactivation. Despite the steadily growing interest in CO-releasing molecules (CORMs) due to their huge potential as therapeutic agent in biological applications [25, 26], only little is known about the primary processes of ligand dissociation from this class of molecules. Hence, the experiments pre-

sented in this thesis for the first time illustrate ultrafast CO-release from a manganese tricarbonyl complex in aqueous solution. This finding is complemented by measurements on a molybdenum complex which contains two CO and one NO ligand. Corresponding quantum-chemical calculations supplementing the experimental findings were mainly performed by our collaborators who also carried out the synthesis of the molecules (group of Prof. U. Schatzschneider, Inorganic Chemistry, University of Würzburg).

Chapter 7 finally summarizes the experimental findings and provides a discussion on future experiments which may extend the scope of this work. Beyond transient absorption spectrosocopy, Appendix A discusses a developed extension which turns an existing UV-pump/MIR-probe spectrometer into a fluorescence detection scheme that might be utilized in future quantum control experiments.

Theoretical background

This chapter provides the theoretical framework for the experiments presented in this thesis. The work's goal is to elucidate primary reaction dynamics after photolysis in selected molecular systems. Ultrashort laser pulses thereby are not only used to induce the breaking of a chemical bond and start a reaction sequence, but also to monitor the progression of the latter. To evaluate and interpret the experiment's outcome, it is therefore vital to not only have detailed knowledge about the properties of the ultrashort light fields involved, but also to understand how the latter affect several nonlinear processes which are necessary to conduct transient absorption (TA) measurements suited to gain meaningful information about a molecular system. Therefore, Sec. 2.1 provides a mathematical description of ultrashort laser pulses in time- and frequency-domain and treats the spatial propagation of Gaussian laser beams. The section also discusses the effect of dispersion which can affect the light fields—sometimes intentionally, often unwanted. Nonlinear frequency conversion processes are introduced in Sec. 2.2 as a tool to generate and characterize light fields in different spectral regimes. After a description of light-induced processes in the context of molecules' electronic and vibrational structure including a brief introduction into quantum chemical calculations in Sec. 2.3, the scope of TA spectroscopy in different spectral domains is treated theoretically (Sec. 2.4). Finally, Sec. 2.5 is devoted to the technique of chirped-pulse upconversion (CPU) which allows for the detection of MIR light fields after upconversion to the VIS regime.

2.1 Mathematical formalism of ultrashort laser pulses

The mathematical description of propagating ultrashort light fields in spatially uniform and nonmagnetic media is based on the inhomogeneous wave equation which can be derived from Maxwell's equations [27, 28]:

$$-\nabla \times \left(\nabla \times \mathbf{E}(t,\mathbf{r})\right) - \frac{1}{c^2}\frac{\partial^2}{\partial t^2}\mathbf{E}(t,\mathbf{r}) = \mu_0 \frac{\partial^2}{\partial t^2}\mathbf{P}(t,\mathbf{r}) \,, \qquad (2.1.1)$$

where $c = \sqrt{\epsilon_0 \mu_0}$ is the speed of light in vacuum, and ε_0 and μ_0 the permittivity[1] and permeability[2] of free space, respectively. The equation illustrates the relation including possible coupled dependencies between the electromagnetic field $\mathbf{E}(t,\mathbf{r})$ and the dielectric

---

[1] $\varepsilon_0 = 8.854187817... \times 10^{-12}$ F/m [29]
[2] $\mu_0 = 4\pi \times 10^{-7}$ N/A^2 = 12.566370614... $\times 10^{-7}$ N/A^2 [29]

polarization $\mathbf{P}(t, \mathbf{r})$ both in space and time. The source term on the right side of Eq. (2.1.1) accounts for a medium's response on an external electric field but likewise accounts for a medium's influence on the electric field. For the description of light fields used in this thesis, propagation is assumed to happen exclusively along the z-axis. Moreover, it is assumed that $\mathbf{E}(t, \mathbf{r})$ can be separated in a function $\mathbf{E}^+(t, z)$, which describes the beam's temporal structure, its propagation along the z-axis, and its polarization state, as well as a function $u^+(\mathbf{r})$ that describes the spatial beam profile:

$$\mathbf{E}(t, \mathbf{r}) \propto u^+(\mathbf{r}) \, \mathbf{E}^+(t, z) \; + \; \text{c.c.} \; , \tag{2.1.2}$$

where the conjugate-complex form of the preceding terms is denoted as c.c.. Before the interplay between $\mathbf{E}(t, \mathbf{r})$ and $\mathbf{P}(t, \mathbf{r})$ will be discussed, both functions on the right side of Eq. (2.1.2) will be described separately.

2.1.1 Ultrafast laser pulses—a Fourier pair

Via Fourier transformation, ultrafast laser pulses can be described both in temporal and spectral domain [30]. Each description carries the same information, whereby practical reasons typically suggest the selection of a particular description. To emphasize this duality, in the following, both bijective descriptions are used in parallel (note the arguments of the respective functions). Furthermore, the discussion will be limited to a fixed point in space (no z-dependence) and the vectorial character of the electric field will be neglected. The Fourier transform (denoted by $\mathcal{F}$), as defined by

$$\mathcal{F}\Big\{E(t)\Big\} = E(\omega) = \frac{1}{\sqrt{2\pi}} \int_{-\infty}^{\infty} E(t) \, e^{-i\omega t} \mathrm{d}t \; , \tag{2.1.3}$$

allows one to switch from a time- to a frequency-domain representation of the electric field. Likewise, switching back to a time-domain representation of the electric field is possible via an inverse Fourier transform (denoted by $\mathcal{F}^{-1}$):

$$\mathcal{F}^{-1}\Big\{E(\omega)\Big\} = E(t) = \frac{1}{\sqrt{2\pi}} \int_{-\infty}^{\infty} E(\omega) \, e^{i\omega t} \mathrm{d}\omega \; . \tag{2.1.4}$$

The assumptions for the electric field made above give rise to a real-valued scalar function, which describes the time-domain electric field via a real-valued temporal amplitude $A(t)$, which is equivalent to the temporal envelope of the electric field, and a temporal phase function $\Phi(t)$:

$$
\begin{aligned}
E(t) &= 2A(t)\cos(\Phi(t)) = A(t) \, e^{i\,\Phi(t)} + \text{c.c.} \\
&= E^+(t) + E^-(t) \; .
\end{aligned}
\tag{2.1.5}
$$

Skipping the second summand on the right side of Eq. (2.1.5) gives rise to a complex-valued function which is in line with Eq. (2.1.2) and allows for a convenient mathematical treatment:

$$E^+(t) = A(t)\, e^{i\,\Phi(t)} \;. \tag{2.1.6}$$

Describing its oscillatory behavior, the properties of the electric field are decisively determined by $\Phi(t)$. It is straightforward to separate nonlinear contributions from the (main) contribution assigned to the carrier frequency ω_0:

$$\varphi(t) = \Phi(t) - \omega_0 t \;. \tag{2.1.7}$$

Combining Eqs. (2.1.6) and (2.1.7), the electric field can thus be rewritten as a product of a complex envelope and an oscillatory term accounting for ω_0:

$$
\begin{aligned}
E^+(t) &= A(t)e^{i\,\varphi(t)} \times e^{i\omega_0 t} \\
&= \hat{A}(t)\, e^{i\omega_0 t} \;.
\end{aligned} \tag{2.1.8}
$$

The so-called *slowly varying envelope approximation* (SVEA) assumes that $\hat{A}(t)$ does not vary significantly within one optical cycle [28]:

$$\left|\frac{d}{dt}\hat{A}(t)\right| \ll \omega_0|\hat{A}(t)| \;. \tag{2.1.9}$$

Since pulses used in this thesis do not range in the few-cycle regime [31], it is justified to factor out the linear modulation and describe electric fields via Eq. (2.1.8).

A Fourier transform of the real-valued electric field reveals the spectral-domain relation

$$E(\omega) = E^*(-\omega) \;, \tag{2.1.10}$$

where the asterik indicates the conjugate-complex form [32]. For a unambiguous description of the electric field, however, it is sufficient to account for positive frequencies only:

$$
E^+(\omega) =
\begin{cases}
E(\omega) & \forall \; \omega \geq 0 \;, \\
0 & \forall \; \omega < 0 \;.
\end{cases} \tag{2.1.11}
$$

In analogy to Eqs. (2.1.3) and (2.1.4), $E^+(\omega)$ and $E^+(t)$ can be transformed into each other [confer Eq. (2.1.8)]:

$$\mathcal{F}\Big\{E^+(t)\Big\} = E^+(\omega) = A(\omega)\, e^{-i\Phi(\omega)} \;, \tag{2.1.12}$$

$$\mathcal{F}^{-1}\Big\{E^+(\omega)\Big\} = E^+(t) = \hat{A}(t)\, e^{i\omega_0 t} \;, \tag{2.1.13}$$

whereby Eq. (2.1.12) contains a real-valued amplitude (or envelope) function $A(\omega)$ and an exponential term which includes the spectral phase function $\Phi(\omega)$.

2.1.2 Ultrafast laser pulses—the role of different Fourier coefficients

For the description of various pulse properties, it is helpful to expand the phase function of an ultrafast laser pulse into a Taylor series. For the description in time domain, the phase function reads

$$\Phi(t) = \sum_{j=0}^{\infty} \frac{a_j}{j!} t^j \ , \ \text{with} \ a_j = \frac{\mathrm{d}^j \Phi(t)}{\mathrm{d}t^j}\bigg|_{t=0} \ , \tag{2.1.14}$$

where, for simplicity and without any restriction regarding the generality of the description, it is assumed that the electric field is centered around $t = 0$. The absolute phase (or carrier envelope phase, CEP) is given by the zeroth-order coefficient a_0 and determines the position of the oscillation peaks with respect to the pulse envelope. Without sophisticated stabilization methods vital for experiments with few-cycle pulses [33–35], the CEP of pulses stemming from conventional femtosecond laser systems fluctuates from pulse to pulse. For pulse durations used within this thesis, however, the CEP can be neglected. The first-order coefficient a_1 is identical to the carrier frequency ω_0, whereby variations from ω_0 arise from higher-order terms. In general, the momentary frequency, i.e., an electric field's oscillation frequency in a certain moment in time, is given by the first derivative of $\Phi(t)$ with respect to time:

$$\omega_m(t) = \frac{\mathrm{d}\Phi(t)}{\mathrm{d}t} = \omega_0 + \frac{\mathrm{d}\varphi(t)}{\mathrm{d}t} \ . \tag{2.1.15}$$

Hence, within the SVEA, $\varphi(t)$ describes deviations of the light field's oscillations from the carrier frequency ω_0. Pulses exhibiting a constant $w_m(t)$ are called unchirped, which is given when $a_j = 0$ for all $j \geq 2$. For the case that $w_m(t)$ is increasing with time, i.e., when $\mathrm{d}\omega_m(t)/\mathrm{d}t > 0$, pulses are called upchirped. In the opposite case, i.e., when $\mathrm{d}\omega_m(t)/\mathrm{d}t < 0$, pulses are called downchirped. Linearly chirped pulses, i.e., pulses whose momentary frequency changes linearly in time, given for the case when $a_j = 0$ for all $j \geq 3$, are treated separately in Sec. 2.1.4.

For the description in frequency domain, the phase function reads

$$\Phi(\omega) = \sum_{j=0}^{\infty} \frac{b_j}{j!} (\omega - \omega_0)^j \ , \ \text{with} \ b_j = \frac{\mathrm{d}^j \Phi(\omega)}{\mathrm{d}\omega^j}\bigg|_{\omega=\omega_0} \ , \tag{2.1.16}$$

where it is considered, that the spectral amplitude is typically centered around ω_0. In this frequency domain representation, b_0 determines the pulse's CEP, while a variation in b_1 is reflected in a temporal translation of the laser pulse (confer Fourier transform shift

theorem [36]). Importantly, b_1 does not affect the shape of a pulse's temporal envelope $A(t)$. However, applying higher-order spectral phase coefficients does affect both the temporal envelope and the temporal phase. Already the case of a linearly chirped pulse, as will be further detailed in Sec. 2.1.4, shows that identical spectral intensities can correspond to laser pulses with different durations.

2.1.3 Ultrafast laser pulses—estimates and macroscopic properties

For a rough assessment of a pulse's properties, it can be helpful to describe the pulse duration Δt and the spectral width $\Delta\omega$ via the full width at half maximum (FWHM) of the corresponding intensity profiles:

$$\Delta t \ = \ FWHM\{I(t)\} \ , \tag{2.1.17}$$

$$\Delta\omega \ = \ FWHM\{I(\omega)\} \ . \tag{2.1.18}$$

Owing to the interdependent description in time or frequency domain, both parameters can only be varied within the so-called *time-bandwidth product*

$$\Delta\omega\Delta t \geq 2\pi c_B \ , \tag{2.1.19}$$

whereby the constant c_B depends on the actual pulse shape and the definition of $\Delta\omega$ and Δt. Assuming a Gaussian-shaped spectrum and defining the latter two quantities according to Eqs. (2.1.17) and (2.1.18), c_B is equal to $4\ln(2)/(2\pi) = 0.441$. For a treatment of different $I(\omega)$ profiles, see Refs. [28, 37]. It should further be emphasized, that the definitions given in Eqs. (2.1.17) and (2.1.18) are only meaningful in the case of simple pulse shapes as those used within this thesis. For concepts that provide valuable estimates, i.e., not the complete electric field function, in the case of complicated pulse shapes, see Refs. [28, 38, 39]. With respect to Eq. (2.1.19), it is important to note, that pulses which satisfy the criterion

$$\Delta\omega\Delta t = 2\pi c_B \tag{2.1.20}$$

are called Fourier-limited, transform-limited, or bandwidth-limited. When describing the electric field properties in the frequency domain, this scenario is realized for any given spectrum if all spectral phase coefficients b_j are equal to zero for $j \geq 2$ [confer Taylor expansion in Eq. (2.1.16)] [40]. In the time domain, this situation is analogously realized if all temporal phase coefficients a_j are equal to zero for $j \geq 2$ [confer Taylor expansion in Eq. (2.1.14)]. It is important to mention that symmetry properties of the Fourier transform determine that $\Phi(\omega)$ and $\varphi(t)$ generally do not resemble each other and have to be calculated via Eqs. (2.1.12) and (2.1.13). As will be discussed and graphically illustrated in Sec. 2.1.4, one exception can be the case of a purely quadratic spectral or temporal phase dependence.

Apart from the microscopic oscillatory behavior of the electric field, its overall intensity is defined as the average of $E^2(t)$ over one optical cycle. This quantity is given in the SVEA-regime by:

$$I(t) = c_o \varepsilon_0 n \frac{1}{T} \int_{t-\frac{T}{2}}^{t+\frac{T}{2}} E^2(t') \mathrm{d}t' = 2c\varepsilon_0 n A(t)^2 \ , \qquad (2.1.21)$$

where n is the index of refraction of the medium in which the intensity is calculated. The corresponding spectral-domain description reads [41]

$$I(\omega) = 2c\varepsilon_0 n A(\omega)^2 \ . \qquad (2.1.22)$$

With regard to experiments, it shall be mentioned that $I(\omega)$ can directly be measured with a spectrometer. Since the latter works in the linear regime, spectra measurements are not sensitive to phase modulations and thus, more elaborate techniques have to be utilized to characterize ultrashort laser pulses as will be discussed later.

Another valuable quantity is the energy fluence, which calculates the electric field's amount of energy per unit area. Based on the equality of the description in both domains, this quantity is given by (Parseval's theorem) [42, 43]:

$$F = \int_{-\infty}^{\infty} I(t) \mathrm{d}t = \int_{-\infty}^{\infty} I(\omega) \mathrm{d}\omega \ . \qquad (2.1.23)$$

However, the total pulse energy W, which can be measured on the macroscopic level by simple means, requires integration over the spatial coordinates [confer Eq. (2.1.2)].

2.1.4 Linearly chirped laser pulses

Especially with regard to the technique of chirped-pulse upconversion, the following section is devoted to the description of linearly chirped laser pulses [44]. Linearity in this context means, that for pulses with Gaussian spectra the application of a second-order spectral phase results in a linear modulation of the pulse's momentary frequency $\omega_m(t)$. If b_2 is the only contribution to the spectral phase function $\Phi(\omega)$ and if one considers a Gaussian spectrum with a spectral width $\Delta\omega$ [defined according to Eq. (2.1.18)], the pulse's electric field is given in the temporal domain via

$$E^+(t) = c_t \exp\left(-\frac{2\ln(2)\Delta\omega^2 \, t^2}{[4\ln(2)]^2 + b_2^2 \Delta\omega^4}\right) \exp\left(i\omega_0 t + i\frac{b_2 \, t^2}{2[4\ln(2)]^2/\Delta\omega^4 + 2b_2^2}\right) \ , \quad (2.1.24)$$

with the constant quantity c_t. For a bandwidth-limited Gaussian pulse with duration $\Delta t_0 = 4\ln(2)/\Delta\omega$ [confer Eq. (2.1.20)], the amplitude function $A(t)$ in Eq. (2.1.24) can be expressed by

$$A(t) = \exp\left(-\frac{2\ln(2)\Delta t_0^2 \, t^2}{\Delta t_0^4 + [4\ln(2)]^2 b_2^2}\right) \qquad (2.1.25)$$

and represents a Gaussian envelope of $E^+(t)$. Hence, $I(t)$ also has a Gaussian shape, whereby the parameter b_2 determines how strong its temporal FWHM deviates from the minimal temporal width Δt_0:

$$\Delta t(b_2) = \sqrt{\Delta t_0^2 + b_2^2 \Delta \omega^2} \; . \tag{2.1.26}$$

Thus, any nonzero value of b_2 leads to a temporal enlongation of the pulse accompanied by a linear modulation of its momentary frequency [confer Eq. (2.1.15)]

$$\omega_m(t) = \frac{d\Phi(t)}{dt} = a(b_2)t \; , \tag{2.1.27}$$

whereby the sign and value of the prefactor

$$a(b_2) = \frac{b_2}{[4\ln(2)]^2/\Delta\omega^4 + b_2^2} \tag{2.1.28}$$

describes the extent of upchirp ($b_2 > 0$, lower frequencies precede higher ones) or downchirp ($b_2 < 0$, higher frequencies precede lower ones). For large values of b_2, i.e., $|b_2| \gg \Delta t^2$, Eq. (2.1.28) can be approximated as $a(b_2) \approx 1/b_2$.

The effect of b_2 on several pulse parameters is visualized in Fig. 2.1. In particular, the electric field [(a) and (e), confer Eq. (2.1.24)], the spectral intensity together with the corresponding phase function $\Phi(\omega)$ [(b) and (f), confer Eq. (2.1.16)], the temporal intensity together with the corresponding phase function $\varphi(t)$ [(c) and (g), confer Eq. (2.1.7)], and the momentary frequency $\omega_m(t)$ [(d) and (h), confer Eq. (2.1.15)] are juxtaposed for a bandwidth-limited [$\Phi(\omega) = 0$] and a linearly downchirped [$\Phi(\omega) = -1/2 \times 100 \text{ fs}^2(\omega - \omega_0)^2$] Gaussian laser pulse ($\omega_0 = 2.35$ rad/fs, $\Delta\omega = 0.30$ rad/fs). This comparison illustrates two exceptional cases as only for Gaussian-shaped spectra a constant or quadratic phase dependence in the spectral domain is resembled in the time domain and vice versa. The effect of b_2, i.e., the downchirped character, is manifested in an increasing oscillation period with time accompanied by an overall temporal elongation [see Fig. 2.1(e)]. For the exemplary chosen parameters, the pulse is stretched from a FWHM of 9.2 fs (bandwidth limit) to a FWHM of 31.4 fs [confer Eqs. (2.1.17) and (2.1.26)]. Since both pulses exhibit the same energy fluence [confer Eq. (2.1.23)] determined by identical spectral intensity profiles $I(\omega)$, the temporal elongation is furthermore accompanied by a smaller maximum value of $I(t)$. While the bandwidth-limited pulse exhibits a constant momentary frequency $\omega_m(t) = \omega_0$, the negative quadratic spectral phase translates into a negative quadratic temporal phase and therewith leads to a linearly decreasing momentary frequency with time [confer Eq. (2.1.15)].
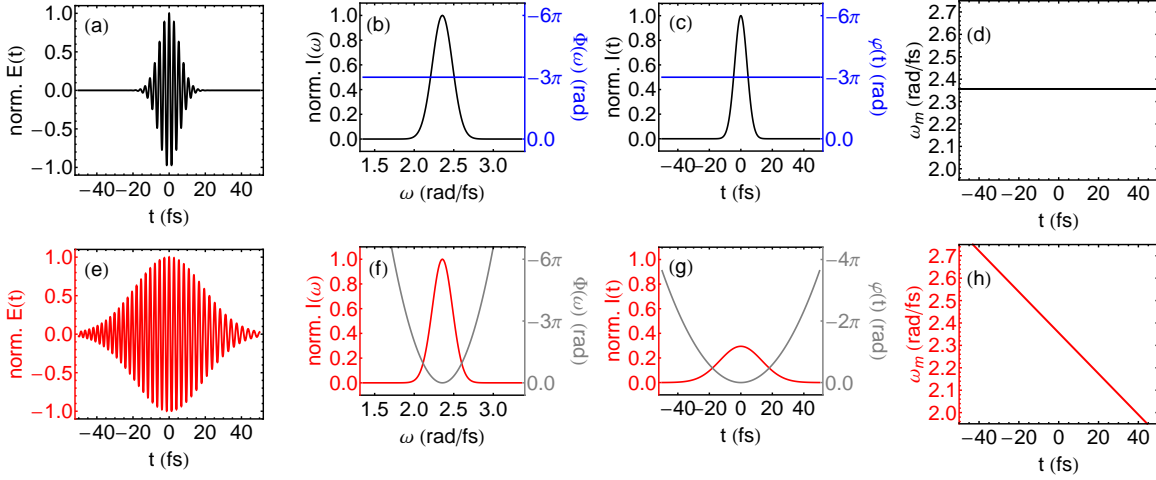
Figure 2.1: Linearly-chirped versus bandwidth-limited laser pulses. For the case of identical Gaussian-shaped spectra centered around $\omega_0 = 2.35$ rad/fs ($\lambda_0 = 800$ nm) with a FHWM of $\Delta\omega = 0.30$ rad/fs ($\Delta\lambda = 102$ nm), characteristic pulse properties are illustrated for a bandwidth-limited pulse [top row, (a)-(d), $\Phi(\omega) = 0$] and a downchirped pulse [bottom row, (e)-(h), $\Phi(\omega) = -1/2 \times 100$ fs$^2(\omega - \omega_0)^2$]: (a) and (e) depict the normalized electric fields; (b) and (f) provide a combined depiction of the spectral intensity and phase; (c) and (g) provide a combined depiction of the temporal intensity and phase; the area under the intensity profiles is normalized to account for an equal energy fluence of both pulse shapes; (d) and (h) visualize the pulses' momentary frequency.

2.1.5 Beam propagation and effects of dispersion

The preceding section dealt with snapshots of laser pulses at a given point in space. This section addresses that light fields progating through media are subject to dispersion. How this may affect the pulses' properties is described in this section. Contrary to Sec. 2.2 which will focus on nonlinear processes, this section deals with processes in which the polarization—according to classical electrodynamics—exhibits a linear response to the electric field scaled by the dielectric susceptibility tensor, which in this case is treated as a scalar quantity:

$$P(\omega, z) = \varepsilon_0 \chi(\omega) E(\omega, z) \ . \tag{2.1.29}$$

Once more, the wave equation [Eq. (2.1.1)] is the starting point for a mathematical treatment. When assuming plane waves, i.e., when neglecting the spatial beam profile $u^+(\mathbf{r})$, Eq. (2.1.1) after Fourier transformation can be reduced to

$$\left(\frac{\partial^2}{\partial z^2} + \frac{\omega^2}{c^2}[1 + \chi(\omega)]\right) E(\omega, z) = 0 \ . \tag{2.1.30}$$

One solution of Eq. (2.1.30) are the traveling waves

$$
\begin{aligned}
E(\omega, z) &= E^+(\omega, 0)\, e^{-i\,k(\omega)\,z} + \text{c.c.} \\
&= E^+(\omega, z) + E^-(\omega, z) \ ,
\end{aligned}
\tag{2.1.31}
$$

whereby $E^+(\omega, 0)$ is equivalent to $E^+(\omega)$ [confer Eq. (2.1.12)] and where the wavevector

$$
k(\omega) = \frac{\omega\, \tilde{n}(\omega)}{c}
\tag{2.1.32}
$$

is pointing into the z-direction. The complex index of refraction

$$
\begin{aligned}
\tilde{n}(\omega) &= \sqrt{1 + \chi(\omega)} \\
&= n(\omega) - i\kappa(\omega)
\end{aligned}
\tag{2.1.33}
$$

thereby accounts for refraction and dispersion via the real part $n(\omega)$ and for processes like absorption or gain in a medium via the imaginary part[3] $\kappa(\omega)$.

For the propagation along the z-direction, two independent polarization directions in the xy-plane do exist for the electric field vector. Hence, birefringent materials play a special role as they can be oriented in such a way, that the index of refraction differs between these two polarization directions. Consequently, both components propagate through the medium with different phase velocities

$$
v_p(\omega) = \frac{c}{n(\omega)} \ .
\tag{2.1.34}
$$

Birefringent materials exhibit at least one axis of anisotropy, the so-called *optical axis*. Typically one speaks of a ordinary (extraordinary) wave for the field's polarization component perpendicular (parallel) to this axis. In general, a complex function of the relative orientation of the optical axis as well as the direction of the incoming laser beam and its polarization determines the propagation of light in birefringent materials. The special case that ordinary and extraordinary wave propagate collinearly, i.e., both waves have identical directions of $\mathbf{k}$, can be realized when the optical axis is oriented perpendicular to the wavevector.

A circumstance which is often found in experiments is the propagation of laser pulses through optical elements leading to changes in both the pulses' temporal and spectral properties. In the SVEA-regime, propagation through a dispersive material of length L

---

[3]$\kappa(\omega)$ is also known as *extinction coefficient*.

with an index of refraction $n(\omega)$ leads to an additional phase contribution:

$$
\begin{aligned}
\Phi(\omega, L) &= \Phi(\omega, 0) + k\, L \\
&= \Phi(\omega, 0) + \frac{\omega\, n(\omega)\, L}{c} \ .
\end{aligned}
\tag{2.1.35}
$$

Regarding the spectral phase function [confer Eq. (2.1.16)], the additional phase contribution has to be accounted for in the corresponding Taylor coefficients:

$$
b_j = \left. \frac{\mathrm{d}^j \Phi(\omega, L)}{\mathrm{d}\omega^j} \right|_{\omega = \omega_0} \ .
\tag{2.1.36}
$$

For propagation in vacuum, i.e., when $n(\omega) = 1$ for all frequencies, this would only lead to changes in b_0 and b_1. In particular, the propagation from $z = 0$ to $z = L$ is accounted for in a constant phase $k_0 L$ imprinted in b_0 and a temporal shift L/c of the pulse's maximum imprinted in b_1. In a dispersive medium, the first-order coefficient becomes

$$
b_1 = \left. \frac{\mathrm{d}\Phi(\omega, 0)}{\mathrm{d}\omega} \right|_{\omega = \omega_0} + \frac{L}{c} \left. \left(n + \omega \frac{\mathrm{d}n(\omega)}{\mathrm{d}\omega} \right) \right|_{\omega = \omega_0} \ .
\tag{2.1.37}
$$

With the *group velocity*

$$
v_g(\omega_0) = \left(\left. \frac{dk}{d\omega} \right|_{\omega = \omega_0} \right)^{-1}
\tag{2.1.38}
$$

describing the actual velocity of the pulse envelope in the dispersive material, and the *group delay*

$$
\tau_g(\omega_0) = \frac{L}{v_g(\omega_0)}
\tag{2.1.39}
$$

determining the pulse's propagation time within the medium, b_1 can thus be rewritten as

$$
b_1 = \left. \frac{\mathrm{d}\Phi(\omega, 0)}{\mathrm{d}\omega} \right|_{\omega = \omega_0} + \frac{L}{v_g(\omega_0)} \ .
\tag{2.1.40}
$$

The so-called *group-delay dispersion* (GDD)

$$
\left. \frac{\mathrm{d}\tau_g(\omega)}{\mathrm{d}\omega} \right|_{\omega = \omega_0} = \frac{L}{c} \left. \left(2 \frac{\partial n(\omega)}{\partial \omega} + \omega \frac{\partial^2 n(\omega)}{\partial \omega^2} \right) \right|_{\omega = \omega_0}
\tag{2.1.41}
$$

accounts for changes in the second-order coefficient, and therefore accounts for changes in the temporal shape of laser pulses [confer Secs. 2.1.1 and 2.1.4]. Moreover, the so-called *group-velocity dispersion* (GVD) parameter—a material-specific quantity—can be derived from Eq. (2.1.41) by dividing out the linear distance dependence [28]:

$$\frac{\mathrm{d}\left(\frac{1}{v_g(\omega)}\right)}{\mathrm{d}\omega}\bigg|_{\omega=\omega_0} = \frac{1}{c}\left(2\frac{\partial n(\omega)}{\partial \omega} + \omega\frac{\partial^2 n(\omega)}{\partial \omega^2}\right)\bigg|_{\omega=\omega_0} . \tag{2.1.42}$$

Since a coefficient $b_2 \neq 0$ leads to linearly chirped laser pulses (confer Sec. 2.1.4), the GVD parameter reflects the amount of linear chirp introduced per unit distance in the medium. It is noteworthy that the propagation through a dispersive medium also has an influence on higher-order spectral phase coefficients that in turn affect the pulse's temporal profile. Hence, for the design of an experiment—especially when employing short pulses with short wavelengths—it is crucial to consider the dispersive effect of every optical component in the beam paths [45]. If necessary, e.g., when bandwidth-limited pulses are desired, countermeasures need to be taken to remove unwanted phase contributions. One way is to use sophisticated pulse shaping techniques to modify the pulses' phase function. However, sometimes it can already be sufficient to simply add additional (well-defined) dispersive material to compensate for phase distortions.

2.1.6 Spatial properties of a Gaussian laser beam

So far, the mathematical description of the electric field neglected $u^+(\mathbf{r})$, i.e., the beam's transverse properties including its profile and phase variations [confer wave equation in Eq. (2.1.1) and its solution in Eq. (2.1.2)]. To model these properties, solutions of the paraxial wave equation (see Ref. [28]), which can be derived from Eq. (2.1.1) after separating the time-dependent part and assuming vacuum conditions [$\mathbf{P}(t, \mathbf{r}) = 0$], need to be found. Most femtosecond light sources operate in the fundamental transversal electromagnetic mode TEM$_{00}$. This solution of the paraxial wave equation can be written in Cartesian coordinates as

$$u^+(\mathbf{r}) = u_0 \frac{1}{\sqrt{1 + z^2/z_0^2}} e^{-i\psi(z)} e^{ik(x^2+y^2)/2R(z)} e^{-(x^2+y^2)/w^2(z)} . \tag{2.1.43}$$

For the case of a beam waist of radius w_0 at $z = 0$, Eq. (2.1.43) is graphically illustrated in Fig. 2.2. The TEM$_{00}$ Gaussian mode is characterized by the following quantities:

- The so-called *Rayleigh range*

$$z_0 = \frac{\pi w_0^2}{\lambda} \tag{2.1.44}$$
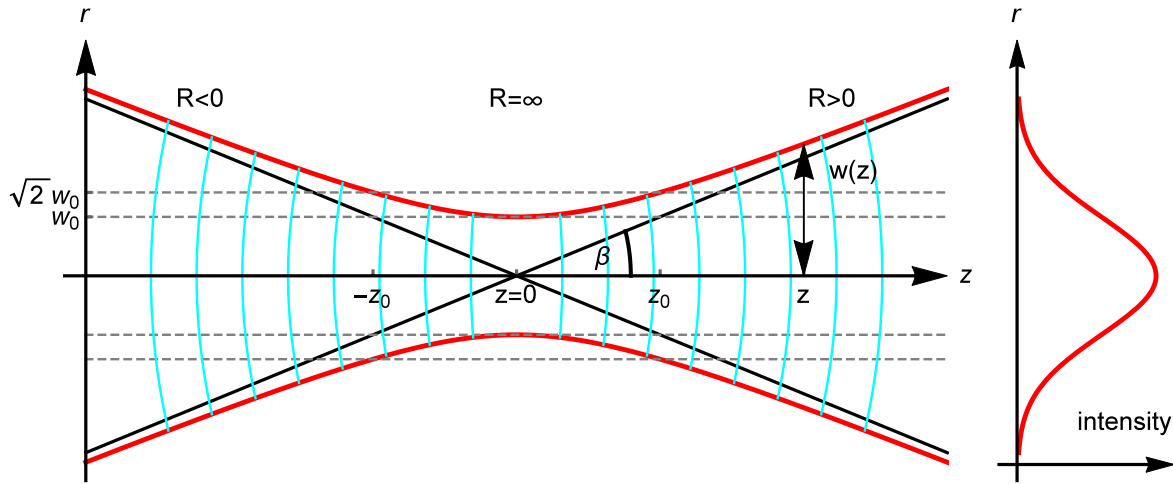
Figure 2.2: Propagation of a fundamental Gaussian laser beam. Left: Exhibiting a beam waist at $z = 0$, the hyperbolic lines (red) illustrate the spot size $w(z)$ being the distance from the z-axis (represented by the transverse distance r) where the electric field amplitude is equal to $1/e$ of the on-axis amplitude. The cyan colored lines visualize the beam's wavefront and its corresponding radius of curvature $R(z)$. Starting from the maximum focus w_0 at $z = 0$, $w(z)$ reaches a value of $\sqrt{2}w_0$ at the Rayleigh length z_0, and eventually evolves in a linear fashion for longer propagation distances (black lines). In the latter regime—the so-called *far-field limit*—$R(z)$ becomes equal to z and the beam's divergence is given by β. Right: Intensity distribution of the TEM_{00} Gaussian mode versus the distance from the z-axis. Figure adapted from Ref. [46, 47].

describes the extent of the waist region and is defined as the distance (along the z-direction) after which

- the *spot size*

$$w(z) = w_0 \left(1 + \frac{z^2}{z_0^2} \right)^{1/2} \tag{2.1.45}$$

has increased by a factor of $\sqrt{2}$ with respect to the beam waist at $z = 0$. Within the Rayleigh range the beam is called collimated and its diameter does not vary significantly. The definition of the Rayleigh range [Eq. (2.1.44)] illustrates an important property of Gaussian beams: a tight focus is always connected with a short Rayleigh range.

- The *radius of curvature*

$$R(z) = z + \frac{z_0^2}{z} \tag{2.1.46}$$

is represented by the second phase term in Eq. (2.1.43). For large distances from

the beam waist, i.e., within the far-field limit, the curvature is equivalent to the curvature of a spherical wave originating from the spot $z = 0$ and hence, Eq. (2.1.46) becomes $R(z) \approx z$. As indicated in Fig. 2.2,

- the *divergence angle in the far-field limit* β becomes

$$\beta \approx \frac{w(z)}{z} \qquad (2.1.47)$$

- and the *spot size in the far-field limit* is given by

$$w(z) \approx \frac{z\lambda}{\pi w_0} \ . \qquad (2.1.48)$$

In experiments, lenses or focusing mirrors are used to adjust beam diameters to the desired size, which is particularly important if different pulses need to be overlapped to perform a nonlinear interaction process. Hence, it is often helpful to estimate the beam waist in the focus by replacing $w(z)$ in Eq. (2.1.48) with the spot size of a collimated beam entering a focusing optic with focal length f.

2.2 Nonlinear processes

In general, it is not sufficient to directly use the output of ultrafast laser sources—which typically deliver pulsed near-infrared (NIR) laser light at a central wavelength of about 800 nm—for spectroscopic applications. Instead, it is common practice to employ processes which are based on the nonlinear response of a medium's polarization on an electric field. These nonlinear processes, as discussed in the following, allow for the generation of (tunable) UV, VIS, or MIR pulses, and thus enable one to access spectral regions of interest. While being treated individually within the scope of this section, an overview of nonlinear processes relevant for this thesis is given in Fig. 2.3.

2.2.1 Higher-order susceptibility

In Sec. 2.1.5, the polarization has been treated as a linear response to the electric field. This assumption is no longer valid for the case of highly intense ultrashort laser pulses propagating through a medium. Instead, higher orders of $E(\omega)$ need to be accounted for:

$$P(\omega) = \varepsilon_0 \sum_{j=1}^{\infty} \chi^{(j)} E(\omega)^j = P^{(1)}(\omega) + P^{(2)}(\omega) + P^{(3)}(\omega) + \ ... \ , \qquad (2.2.1)$$
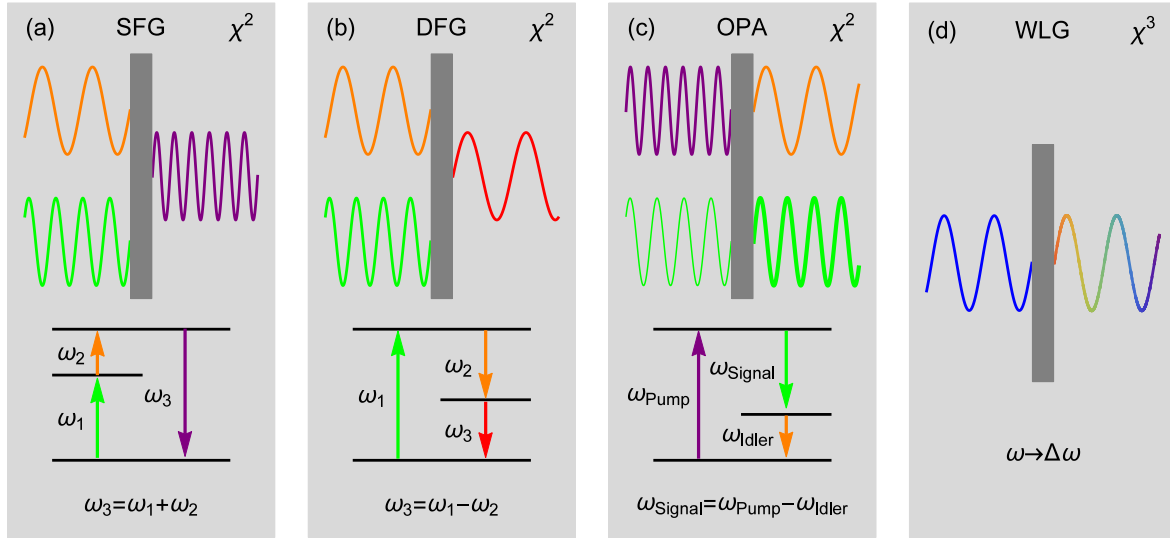
Figure 2.3: Nonlinear frequency conversion processes and corresponding energy levels involved. (a) Sum-frequency generation (SFG) describes the process of mixing two incident photons with different frequencies creating a photon having a frequency equal to the sum of both incident frequencies. For the special case that both incident photons share the same frequency, one speaks of second-harmonic generation (SHG). (b) Via difference-frequency generation (DFG), a photon is created having a frequency equal to the difference between the two incident frequencies. (c) Optical parametric amplification (OPA) describes the amplification of a weak signal beam (the so-called *seed beam*) using pump photons of another frequency. Besides the amplified signal field, a weak idler beam is created. (d) The $\chi^{(3)}$-process of white-light generation (WLG) facilitates the broadening of spectra by focusing laser fields into nonlinear media.

with the susceptibilities $\chi^{(j)}$. The vectorial character of the polarization and the electric field implies that each susceptibility $\chi^{(j)}$ of jth order is a tensor of rank $j+1$. Hence the second-order polarization component pointing in the y-direction can be calculated via

$$P_y^{(2)}(\omega_q) = \varepsilon_0 \sum_{jk} \sum_{(nm)} \chi_{yjk}^{(2)}(-\omega_q; \omega_n, \omega_m) E_{1,j}(\omega_n) E_{2,k}(\omega_m) , \qquad (2.2.2)$$

where the summation is carried out over all $j, k = x, y, z$ and over all frequencies ω_n and ω_m with the condition $\omega_q = \omega_n + \omega_m$. Hence, a new radiation field at a frequency ω_q is generated via the interaction of two (different) light fields.

The symmetry properties of a material are reflected in the components of the susceptibility tensors $\chi^{(j)}$ (see Refs. [41, 48] for further information). For a material with inversion symmetry, i.e, a medium with a centrosymmetric structure, inverting the direction of the electric fields, i.e., replacing $E(\omega)$ with $-E(\omega)$ [confer Eq. (2.2.2)], has to change the polarization's sign. This criterion can be fulfilled since centrosymmetric media do not exhibit susceptibility contributions of even order. Thus, only media without inversion symmetry or where it is locally broken can give rise to contributions from even-

order susceptibilities to the nonlinear polarization. While the latter situation is rather an exception (see Sec. 2.2.2 for $\chi^{(2)}$ processes in birefringent crystals), most media exhibit a non-vanishing third-order susceptibility tensor (see Sec. 2.2.3 for the $\chi^{(3)}$ process of self-phase modulation).

2.2.2 $\chi^{(2)}$ frequency conversion processes

Owing to their lack of inversion symmetry, birefringent crystals are commonly used to conduct $\chi^{(2)}$ frequency conversion processes. Famous examples are among others β-barium borate (BBO), lithium triborate (LBO), or lithium niobate (LNB)—serving for applications from the UV to the MIR spectral region [49]. For efficient energy transfer in a $\chi^{(2)}$ process, the conservation of momentum for parallely propagating beams implies, that the wavevectors corresponding to the initial frequencies ω_n and ω_m, and the new frequency ω_q need to obey the relation

$$k_n + k_m = k_q \ . \tag{2.2.3}$$

Deviations from Eq. (2.2.3) can be described via the so-called *phase mismatch*

$$\Delta k = k_q - k_n - k_m \ . \tag{2.2.4}$$

A non-vanishing Δk leads to a periodically oscillating energy transfer in the crystal caused by destructive interference between light fields of frequency ω_q created at different positions in the crystal. Nevertheless, as will be discussed in the following, solutions of Eq. (2.1.1) can be found. For the case that the intensity of the nascent light field is small compared to the initial light fields, the generated intensity after propagating through a nonlinear crystal (NC) of thickness L is given by

$$I(\omega_q, L) \propto \frac{\omega_q^2 L^2}{n(\omega_q)} \left| P^{(2)}(\omega_q) \right|^2 \mathrm{sinc}^2\left(\frac{\Delta k L}{2} \right) \ . \tag{2.2.5}$$

The periodically oscillating energy transfer mentioned above is reflected in the oscillatory behavior of Eq. (2.2.5). If the crystal's thickness represents an integer multiple of the coherence length $L_c = 2\pi/\Delta k$, $I(\omega_q, L)$ exhibits a maximum for ω_q and goes to zero in between. Besides the conservation of momentum, the involved light fields need to obey the energy conservation law

$$\omega_n + \omega_m = \omega_q \ . \tag{2.2.6}$$

Together with Eq. (2.1.32), and for the case that absorption can be neglected, Eq. (2.2.6) can be rewritten as

$$\frac{k_n}{n(\omega_n)} + \frac{k_m}{n(\omega_m)} = \frac{k_q}{n(\omega_q)} \ . \tag{2.2.7}$$

In general, owing to material dispersion, it holds that $n(\omega_q) \neq n(\omega_n) \neq n(\omega_m)$. However, phase matching, i.e., the case of $\Delta k = 0$, can be achieved for instance by employing uniaxial birefringent crystals. As explained in Sec. 2.1.5, such crystals exhibit—for a given wavelength—different refractive indices for ordinary and extraordinary waves. Thus, phase matching for one frequency combination can be achieved by choosing the right crystal orientation with appropriate polarization directions of the incident light fields.

Provided that two of the three electric fields in Eq. (2.2.2) are linearly polarized and oriented perpendicular to the optical axis, i.e., in the case of two ordinary waves, one speaks of type-I phase-matching. The tensorial properties of $\chi^{(2)}$ imply the existence of non-vanishing contributions to the polarization [confer Eq. (2.2.2)] if not all electric fields have the same polarization directions. While the ordinary index of refraction $n_o(\omega)$ is independent of the crystal orientation, changing the angle θ between the propagation direction of the light fields and the crystal's optical axis allows one to tune the extraordinary index of refraction

$$n_e(\omega, \theta) = n_o(\omega) \, n_e(\omega) \left[n_o(\omega)^2 \sin^2 \theta + n_e(\omega)^2 \cos^2 \theta \right]^{-1/2} \tag{2.2.8}$$

between the two extreme values $n_e(\omega, 0°) = n_o(\omega)$ and $n_e(\omega, 90°) = n_e(\omega)$, whereby a distinction is made between negative $[n_o(\omega) > n_e(\omega)]$ and positive $[n_o(\omega) < n_e(\omega)]$ uniaxial crystals.

Sum- and difference frequency generation

In general, the two frequencies ω_n and ω_m, which give rise to a second-order polarization, do not have to be equal [confer Eq. (2.2.2)]. Hence, two different laser beams can be mixed to create a new light field with frequency $\omega_q = \omega_n + \omega_m$ via *sum-frequency generation* (SFG) [see Fig. 2.3(a)], a process exploited for instance in the technique of chirped-pulse upconversion as will be discussed in Sec. 2.5. For a type-I SFG arrangement, the optimal phase-matching angle can be calculated by combining Eqs. (2.2.3), (2.2.6), and (2.2.8) [50]:

$$\theta = \arcsin \left[\frac{n_o(\omega_q)^2 n_e(\omega_q)^2}{n_o(\omega_q)^2 - n_e(\omega_q)^2} \left(\frac{[\omega_n + \omega_m]^2}{[n_o(\omega_n)\omega_n + n_o(\omega_m)\omega_m]^2} - n_o(\omega_q)^{-2} \right) \right]^{1/2} \ . \tag{2.2.9}$$

When a laser beam (frequency ω_0) is mixed with itself, a special case of SFG, namely the process of *second-harmonic generation* (SHG), enables the generation of light at a central frequency of $2\omega_0$. Moreover, a SFG crystal setting simultaneously allows for the process

of *difference-frequency generation* (DFG) [see Fig. 2.3(b)], i.e., the creation of light at a central frequency of $\omega_m = \omega_q - \omega_n$ or $\omega_n = \omega_q - \omega_m$. For a mathematical treatment of phase-matching conditions in biaxial crystals, the interested reader is referred to the literature [48]. In general, 2^3 different types of phase-matching can be realized by mixing any possible combination of three ordinary or extraordinary waves in Eq. (2.2.2). For the case of SFG via type-I phase matching, Eq. (2.2.2) can be reduced to

$$P_y^{(2)}(\omega_q) = \varepsilon_0 \sum_{(nm)} \chi_{yxx}^{(2)}(-\omega_q; \omega_n, \omega_m) E_{1,x}(\omega_n) E_{2,x}(\omega_m) \ , \qquad (2.2.10)$$

where the highest frequency is the y-polarized extraordinary wave and the other light fields are ordinary waves.

When phase matching of broad spectra is desired, one has to consider the so-called *acceptance bandwidth* of a NC. The latter accounts for the fact that most frequencies suffer from an inevitable phase mismatch which is determined by variations of the sinc-function over the spectral region of interest [confer Eq. (2.2.5)]. As can be seen from Eq. (2.2.5), the use of thin crystals reduces the phase mismatch Δk at the expense of a reduced conversion efficiency. For sufficiently thin crystals and pulses in the SVEA-regime, it can be approximated that the sinc^2-term as well as the prefactors in Eq. (2.2.5) are constant values. In the case that the susceptibilities can be assumed to be independent of frequency [51] and under the assumption of efficient broadband phase-matching, the electric field in the time domain can be derived via Fourier transform:

$$E_q^{(2)}(t) = \varepsilon_0 \chi^{(2)} E_1(t) E_2(t) \ . \qquad (2.2.11)$$

The electric fields' polarization directions, which are neglected in Eq. (2.2.11) to underline the equation's generality, determine whether the process of SFG or DFG is phase-matched. As the electric field is a real-valued quantity given by the sum of $E^+(t) + E^-(t)$ [confer Eq. (2.1.5)], the nascent field $E_q(t)$ generally comprises both the type-I SFG contribution $E_{q,y}^{\mathrm{SFG}}(t) = \varepsilon_0 \chi^{(2)}(E_{1,x}^+(t) E_{2,x}^+(t) + \mathrm{c.c.})$ as well as the type-I DFG contribution $E_{q,x}^{\mathrm{DFG}}(t) = \varepsilon_0 \chi^{(2)}(E_{1,y}^+(t) E_{2,x}^-(t) + \mathrm{c.c.})$. However, typically only one process actually takes place in a specific combination of NC and incoming laser fields. The overall signal of the nascent fields generated via SFG or DFG is proportional to the product of the initial intensities:

$$S^{\mathrm{SFG/DFG}} \quad \propto \int_{-\infty}^{\infty} |E_q^{\mathrm{SFG/DFG}}(t)|^2 \mathrm{d}t \quad \propto \int_{-\infty}^{\infty} I_1(t) I_2(t) \mathrm{d}t \ . \qquad (2.2.12)$$

In the case of SHG, i.e., when the relation $E_1(t) = E_2(t)$ holds, the overall signal S^{SHG} exhibits a quadratic dependence on the intensity of the fundamental light field. As the highest overall SHG yield is achieved by transform-limited pulses, recording S^{SHG}—for instance with a photodiode—can provide a valuable estimate of pulse durations by simple means.

Optical parametric amplification

A process which is strongly related to DFG is the so-called *optical parametric amplification* (OPA) [see Fig. 2.3(c)]. At this, a weak seed wave at frequency ω_{signal} (the *signal* beam) is overlapped with an intense beam at frequency ω_{pump} (the *pump* beam) in a NC. The OPA process gives rise to a field at $\omega_{\text{idler}} = \omega_{\text{pump}} - \omega_{\text{signal}}$ (the *idler* beam) via DFG accompanied by an amplified signal field. The energy transfer from the pump beam to the signal beam is possible since additional photons at frequency ω_{signal} can be stimulated by the existence of photons at the latter frequency [41]. In this thesis, the OPA process is exploited to generate tunable laser pulses in the UV [see Section 3.2.2] and MIR spectral region [see Section 3.4.1] by amplifying weak seed beams generated via white-light generation—a process which will be discussed in the following section.

2.2.3 $\chi^{(3)}$ frequency conversion processes

First observed by Alfano and Shapiro in the 1970s [52, 53], the $\chi^{(3)}$ process of white-light generation (WLG) [see Fig. 2.3(d)], i.e., the generation of broad spectra by focusing intense laser pulses into transparent media, is exploited in a variety of spectroscopic applications [54, 55]. Despite its importance, the interplay of different processes contributing to WLG has not completely been deciphered so far. Self-phase modulation (SPM) seems to be the most important process in WLG, while also other effect such as self-steepening, self-focusing, and Raman-like processes may contribute [28, 56, 57]. While the role of WLG—sometimes also called supercontinuum generation [54]—for experiments presented in this thesis will be detailed in Chap. 3, this section provides a brief mathematical description of SPM.

In Sec. 2.2.2, frequency conversion processes have been introduced on the basis of NCs which exhibit a non-vanishing second-order susceptibility $\chi^{(2)} \neq 0$ due to the lack of inversion symmetry. As opposed to this, the process of SPM is based on the third-order susceptibility $\chi^{(3)}$ which is found in most media. The third-order polarization [confer Eq. (2.2.11) for the corresponding second-order process] of the medium gives rise to the electric field contribution

$$E_q^{(3)}(t) = \varepsilon_0 \chi^{(3)} E_1(t) E_2(t) E_3(t) \ . \tag{2.2.13}$$

For the case of identical fields, i.e., when $E_1(t) = E_2(t) = E_3(t)$, by including the intensity definition from Eq. (2.1.21), and by neglecting the process of third-harmonic generation [28], the total polarization of the medium can be expressed as

$$P(t) = \varepsilon_0 \chi^{(1)} E^+(t) + \frac{3\chi^{(3)}}{2c\varepsilon_0 n} I(t) E^+(t) + \text{c.c.} \ . \tag{2.2.14}$$

Obviously, $P(t)$ depends linearly on $E^+(t)$, while the effective susceptibility is dependent

on $I(t)$. Using Eq. (2.1.33) and defining the linear index of refraction as $n_0 = \sqrt{1 + \chi^{(1)}}$, the complete index of refraction reads[4]

$$n(t) = n_0 \sqrt{1 + \frac{3\chi^{(3)}}{2c\varepsilon_0 n_0^3} I(t)} \quad \approx n_0 + \frac{3\chi^{(3)}}{4c\varepsilon_0 n_0^2} I(t) \quad := n_0 + n_2 I(t) \ . \tag{2.2.15}$$

Hence, owing to the intensity dependence of $n(t)$, a pulse propagating in a medium with sufficiently large $\chi^{(3)}$ will experience a temporal phase modulation. Using the wavevector definition from Eq. (2.1.32), the complete temporal phase at a fixed point z_0 in space [58] can be written as

$$\begin{aligned} \Phi(t, z_0) &= \varphi(t, 0) + \omega_0 t - \frac{n\,\omega_0}{c} z_0 \\ &= \varphi(t, 0) + \omega_0 t - \frac{\omega_0 \, z_0}{c}[n_0 + n_2 I(t)] \ . \end{aligned} \tag{2.2.16}$$

Thus, the pulse's momentary frequency [confer Eq. (2.1.15)] becomes

$$\omega_m(t, z_0) = \frac{\mathrm{d}\varphi(t, 0)}{\mathrm{d}t} + \omega_0 - \frac{\omega_0 \, n_2 \, z_0}{c} \frac{\mathrm{d}I(t)}{\mathrm{d}t} \ . \tag{2.2.17}$$

Via Fourier transform [confer Eq. (2.1.3)] it can be shown that changes in the temporal phase also affect the spectral amplitude. SPM in particular leads to upchirped laser pulses since red-shifted frequencies are generated at the leading edge ($\mathrm{d}I/\mathrm{d}t > 0$) and blue-shifted frequencies are generated at the trailing edge ($\mathrm{d}I/\mathrm{d}t < 0$). Under proper experimental conditions, pulses can be created whose spectral widths significantly exceed the initial spectrum.

Pulses generated via WLG do not have a constant momentary frequency anymore and hence the pulses' different spectral components arrive at different times at a given point in space. If necessary for a specific spectroscopic application, pulse compression techniques can be applied that compensate for changes in the temporal phase imposed in the process of WLG [59, 60]. With respect to this thesis, however, the additional chirp can be accounted for in the data analysis. With regard to the experimental usage, it is furthermore important to note that the spectral coverage of pulses generated via WLG depends on the medium and the wavelength of the generating beam, whereby the latter also predetermines the polarization of the supercontinuum. Further effects based on higher-order susceptibility are discussed with regard to their relevance in TA measurements in Sec. 2.4.

---

[4]In Eq. (2.2.15) it has been assumed that $n_0 \ll n_2 I(t)$, with n_2 describing the coupling strength between the index of refraction and the electric field [28].

2.3 Molecules and light

Light can initiate transitions between molecular states, whereby, depending on the wavelength of the absorbed photon, either rotational, vibrational, or electronic excitations can occur [61]. Hence, light can be utilized to gain insight into a molecular system by assessing its energetic levels. To better understand the related physical and chemical processes occurring after photoexcitation, this section provides an introduction into the quantum-mechanical framework of molecular states and corresponding transitions whose characteristic time scales can be analyzed by ultrafast TA spectroscopy—a method which will be introduced in Sec. 2.4.

2.3.1 Born-Oppenheimer approximation

A molecular system—consisting of at least two atoms—is fully described via its Hamiltonian [43, 62]

$$\mathcal{H}(\mathbf{r}, \mathbf{R}) = \mathcal{T}_{\mathrm{N}} + \mathcal{T}_{\mathrm{e}} + \mathcal{V}_{\mathrm{eN}} + \mathcal{V}_{\mathrm{e}} + \mathcal{V}_{\mathrm{N}} \ , \tag{2.3.1}$$

which contains the kinetic energies $\mathcal{T}$ of the nuclei (index N) and the electrons (index e) as well as the Coulomb potentials $\mathcal{V}$ between electrons and nuclei and among themselves. Molecular states—represented by their molecular wave functions $|\Psi_{\mathrm{mol}}(\mathbf{r}, \mathbf{R})\rangle$—and their corresponding energy levels E are determined by the time-independent Schrödinger equation

$$\mathcal{H}(\mathbf{r}, \mathbf{R})|\Psi_{\mathrm{mol}}(\mathbf{r}, \mathbf{R})\rangle = \mathrm{E}|\Psi_{\mathrm{mol}}(\mathbf{r}, \mathbf{R})\rangle \ , \tag{2.3.2}$$

where the coordinates $\mathbf{r}$ and $\mathbf{R}$ correspond to the electrons and nuclei, respectively. In what follows, contributions owing to spin and rotational motion are neglected. While an exact solution even for small molecules is not feasible, Eq. (2.3.2) can be solved by introducing the *Born-Oppenheimer approximation*. The latter assumes, based on the huge mass difference of three or more orders of magnitude between electrons and nuclei [61], that electrons can almost instantaneously follow the movement of nuclei. This in turn suggests that the motion of electrons and nuclei can be separated from each other, i.e., the electron-nuclear correlation can be neglected [43, 63]. In analogy to thermodynamic approximations where dynamic changes happening under equilibrium conditions need to be described [64], the Born-Oppenheimer approximation is also known as *adiabatic* approximation. Importantly, the latter fails for instance in the presence of conical intersections [65]—a scenario which shall not be discussed here. The Born-Oppenheimer approximation gives rise to define the total vibronic (i.e., simultaneously electronic and vibrational) molecular wave function $|\Psi_{\mathrm{mol}}(\mathbf{r}, \mathbf{R})\rangle$ as a product of the electronic wave

function $|\Psi_e(\mathbf{r}, \mathbf{R})$ and the nuclear wave function $|\Psi_N(\mathbf{R})\rangle$:

$$|\Psi_{mol}(\mathbf{r}, \mathbf{R})\rangle = |\Psi_e(\mathbf{r}, \mathbf{R})\rangle\, |\Psi_N(\mathbf{R})\rangle \; . \tag{2.3.3}$$

As the electron motion can thus be treated for a fixed internuclear geometry, the nuclear position vector $\mathbf{R}$ takes the role of a parameter in the electronic wave function $|\Psi_e(\mathbf{r}, \mathbf{R})\rangle$ and the energy eigenvalues E. Overall, electronic eigenvalues E($\mathbf{R}$), so-called *potential energy curves*, have to be calculated by solving Eq. (2.3.2) for every value of $\mathbf{R}$. The nuclear motion is determined by an effective potential which is given by the sum of E($\mathbf{R}$) and $\mathcal{V}_N$. Thus, for the nuclei Eq. (2.3.2) can be written as

$$\mathcal{H}(\mathbf{r}, \mathbf{R})|\Psi_N(\mathbf{R})\rangle = [\mathcal{T}_N + E(R) + \mathcal{V}_N(\mathbf{R})]|\Psi_N(\mathbf{R})\rangle = E|\Psi_N(\mathbf{R})\rangle \; . \tag{2.3.4}$$

Hence, the overall electronic and vibrational structure of a molecular system, which is determined by its full Hamiltonian [confer Eq. (2.3.1)], consists of vibrational levels on top of potential energy curves E($\mathbf{R}$) that reflect electronic states. In general, as several coordinates need to be introduced to describe the overall nuclear motion, multi-dimensional potential energy surfaces (PESs) are necessary to describe the electronic structure of polyatomic molecules [61].

2.3.2 Vibrational structure of molecules

For polyatomic molecules consisting of N atoms, $3N$ coordinates are necessary to describe the overall motion. Three out of these $3N$ degrees of freedom can be assigned to translation and three (or two for the case of a linear molecule) degrees of freedom are assigned to rotational movement. Thus, $3N - 6$ (or $3N - 5$ for the case of a linear molecule) degrees of freedom remain for the description of molecules' vibrational structure. For vibrations around the equilibrium position $Q = 0$, the potential energy can be expanded in the Taylor series

$$V(Q) = V_0 + \sum_i \left(\frac{\partial V}{\partial Q_i}\right)Q_i + \frac{1}{2}\sum_{i,j}\left(\frac{\partial^2 V}{\partial Q_i \partial Q_j}\right)Q_i Q_j + ... \; , \tag{2.3.5}$$

where Q describes the vibrational amplitude and where the partial derivatives determine the force constants. The so-called *harmonic approximation* only accounts for zeroth-, first-, and second-order contributions in Eq. (2.3.5). After coordinate transformation, the $3N$ differential equations that describe the molecule's motion can be disentangled to yield $3N - 6$ uncoupled normal mode equations. For the (unusual) case that all atoms oscillate with the same frequency and have a fixed phase, a superposition of these normal modes of vibration is sufficient to describe any molecular motion. The overall vibrational energy of the molecular system is then given by the sum over all *Eigenenergien* that correspond

to independent normal modes in the harmonic approximation:

$$E = \sum_i \hbar\omega_i(v_i + 1/2) \ , \tag{2.3.6}$$

where $\hbar$ refers to Planck's reduced constant[5]. In general, the harmonic approximation fails and higher-order force constants are necessary to describe the potential energy of a molecular system properly [confer Eq. (2.3.5)]. Hence, Eq. (2.3.6) has to be modified with anharmonic correction terms that involve the vibrational quantum numbers of several dependent normal modes. In general, this modification leads to an unequal spacing between different vibrational energy levels [66]. One typical case of anharmonicity is the so-called *diagonal frequency shift* of excited vibrational modes, which, as illustrated in Fig. 2.4(a), leads to decreasing energy differences for higher quantum numbers.

2.3.3 Molecular transitions and energy diagrams

One common way to visualize a molecule's energetic spectrum is the so-called *Jablonski diagram* [61], which is depicted for a fictitious molecular system in Fig. 2.4(a). At this, rotational levels have been excluded for clarity. Starting from the electronic ground state S_0, the absorption of a photon (with adequate energy) leads to an electronic excitation that also involves the excitation of higher vibrational states. Typically in solution, this vibrational excess energy is quickly lost via *vibrational cooling* (VC) and transferred to the solvent [a process known as intermolecular *vibrational energy transfer* (VET)] or distributed over the entire molecule [a process known as *intramolecular vibrational relaxation* (IVR)] [9, 68]. With respect to what follows, it is noteworthy that owing to a typically anharmonic energetic spacing between vibrational states [confer Sec. 2.3.2 and Fig. 2.4(b)], VC is reflected in spectral shifts which are detectable in TA measurements (see Sec. 2.4). For instance, after excitation a large amount of internal vibrational energy may be present in the ground state of the reactant or the product (so-called *hot molecules*) causing initially red-shifted absorption bands. Eventually, as the system dissipates the excess energy, these bands blue-shift reflecting the molecule's relaxation towards the vibrational ground state. Returning to the situation depicted in Fig. 2.4(b), electronic relaxation processes occurring after VC comprise non-radiative (nr) and radiative (r) transitions which are either spin-conserving [nr: internal conversion (IC); r: fluorescence] or involve a change in the spin multiplicity [nr: intersystem crossing (ISC); r: phosphorescence]. As will be further detailed in Sec. 2.4, stimulated emission (SE) and excited-state absorption (ESA) are further light-induced transitions which can occur when excited molecules interact with another photon—contrary to an initial excitation from the molecular ground state as discussed above [61].

In the Jabloski diagram, a simplification has been made as energy levels were represented by horizontal lines thereby neglecting the dependence on the nuclear coordinates **R**. While it is typically not feasible to visualize to entire multi-dimensional PES of a

---

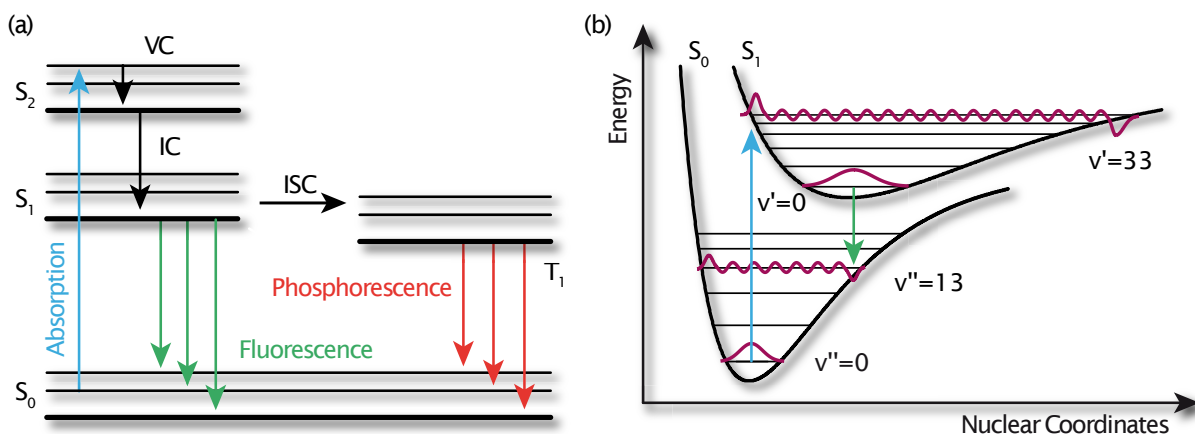[5] $\hbar = 1.054571800(13) \times 10^{-34}$ Js [29]

Figure 2.4: Diagrams representing energetic states and possible transitions of molecular systems. (a) The Jablonski diagram illustrates possible molecular relaxation processes occurring after the absorption of a photon which induces an initial vibronic transition from the electronic ground state S_0 to the second excited state S_2 (blue arrow). Electronic eigenstates (thick black lines) and corresponding vibrational eigenstates (thin black lines) are organized vertically by energy and grouped horizontally by spin multiplicity. Subsequent relaxation processes may comprise several non-radiative (black arrows) and radiative (colored arrows) transitions between molecular states. While internal conversion (IC) and fluorescence are spin-conserving processes, phosphorescence and intersystem crossings (ISCs) change a molecule's spin multiplicity. Moreover, purely vibrational (non-radiative) transitions known as vibrational relaxation or vibrational cooling (VC) may occur. (b) Section of an one-dimensional cut through a multidimensional potential energy surface along one nuclear coordinate. The schematic depicts the potential wells of the electronic S_0 and S_1 state with corresponding vibrational levels. The exemplary vibronic transitions of absorption (blue) and fluorescence (green) occur—according to the Franck-Condon principle—most likely between vibrational states whose respective wave functions (purple curves) exhibit the greatest overlap. Figure adapted from Ref. [67].

molecule, often it is already helpful to plot cuts through a PES along one nuclear coordinate. Furthermore, this way of presenting a molecule's energetic levels allows one to visualize the so-called *Franck-Condon principle* which explains why an electronic transition is typically connected with a vibrational excitation: as shown for the processes of absorption and fluorescence, vertical vibronic transitions are more likely due to shifted minima positions of the electronic potential curves (corresponding to the S_0 and S_1 state) accompanied by the solutions of Eq. (2.3.2) which reveal that wave functions of higher-lying vibrational states exhibit an increasing probability density at the border of the corresponding potential wells [43, 63]. Hence, the Franck-Condon principle treats transitions between different electronic states to happen quasi instantaneously on a molecule's vibrational time scale and without changes in the nuclear positions. The corresponding transition probability is proportional to the absolute square of the dipole matrix element

$$M_{\mathrm{if}} = \left[-e \sum_j \langle \Psi_{\mathrm{f}}^{\mathrm{e}} | \mathbf{r}_j | \Psi_{\mathrm{i}}^{\mathrm{e}} \rangle \right] \times \langle \Psi_{\mathrm{f}}^{\mathrm{n}} | \Psi_{\mathrm{i}}^{\mathrm{n}} \rangle \, , \qquad (2.3.7)$$

where e refers to the elementary charge[6], and where i denotes the initial and f the final electronic or vibrational state, respectively. While the first factor is the so-called *electric dipole transition moment* which accounts for the redistribution of the electrons, the second factor is the so-called *Franck-Condon factor* that describes the wave function overlap of the involved vibrational states [63].

2.3.4 Quantum chemical calculations

Especially in the case of complex molecular structures, experimentally acquired spectroscopic data is only of limited information value without the help of theoretical calculations. In Chap. 4, advanced femtosecond pump–probe spectroscopy is complemented by hybrid Quantum Mechanics/Molecular Mechanics (QM/MM) calculations when pursuing primary processes of diphenylcarbene (DPC) in binary solvent mixtures. The calculations, performed by Dr. Pandian Sokkar and Dr. Elsa Sánchez-García (Max-Planck-Institut für Kohlenforschung, Mülheim an der Ruhr), enable to capture solvent effects and specific interactions governing the stability of DPC. In the QM/MM approach, an appropriate level of quantum chemistry theory is chosen to selectively address chemical processes occurring in certain regions of a molecular system, while the surrounding part is treated by a MM force field [69–71]. In Chap. 6, light-induced ligand dissociation reactions of transition-metal complexes are studied. Thereby, the release of small molecular messengers such as carbon monoxide (CO) or nitric oxide (NO) gives rise to the appearance of MIR absorption bands which are associated with groups in the reactant and product molecules. Molecular ground state calculations based on *density functional theory* (DFT) are in this respect a versatile tool allowing for an assignment of nascent spectral features to putative molecular configurations [72, 73]. In a nutshell, DFT allows for the computation of numerical solutions of Eq. (2.3.2) even for the case of large molecules containing many interacting electrons. The experimental findings presented in Chap. 6 are furthermore supported by calculations based on *time-dependent density functional theory* (TD-DFT) [74–77]. Therewith, excited molecular states can be studied theoretically which in turn allows for a deeper understanding of molecular processing happening after photoexcitation, e.g., structural changes caused by the spatial redistribution of the electronic probability density. The results from DFT calculations (performed mainly by the group of Prof. U. Schatzschneider, Inorganic Chemistry, University of Würzburg) on the investigated transition-metal complexes can be found in Appendix C. Further details on the employed theoretical methods can be found in the references mentioned above.

---

[6]$e = 1.6021766208(98) \times 10^{-19}$ C [29]

2.4 Transient absorption spectroscopy

Ultrafast optical *transient absorption* (TA) spectroscopy is a commonly used subtype of pump–probe spectroscopy. Thereby, a laser pulse (the so-called *pump* pulse) is employed to excite an initially relaxed molecular system via a molecular transition to a non-equilibrium state which in turn can be the starting point for several photophysical or photochemical processes which finally once more end in a relaxed molecular state. The reaction sequence is monitored in real time by observing changes in the molecule's absorption characteristics seen by the interaction with another time-delayed pulse (the so-called *probe* pulse) with the *pumped* and *unpumped* sample volume. The latter distinction can be made as typically every second pump pulse is blocked by a mechanical chopper. In particular, pump-induced changes in the sample lead to changes in the transmitted probe spectrum which is detected spectrally resolved (see Fig. 2.5). Depending on the probe pulse's spectral coverage, the molecule is probed either via its electronic or vibrational transitions. By varying the time delay τ between the pump and probe pulse, the sample's temporal evolution after photoexcitation can thus be reconstructed by following changes in its time-resolved (*transient*) absorption. Owing to experimental limitations, the temporal probing window is usually limited to several nanoseconds [20]. While early *flash photolysis* experiments pioneered by Norrish and Porter offered a milli- to microsecond precision by employing two short light flashes as pump and probe, respectively [78, 79], only the development of ultrashort light sources allowed for experiments with a sub 100 fs time resolution, thus enabling researchers to enter the characteristic time scale of intra- and intermolecular processes [7, 80]. This section comprises a brief introduction into the theory behind pump–probe TA spectroscopy and discusses possible signal contributions (Sec. 2.4.1), complemented by general remarks on probing in different spectral regimes (Sec. 2.4.2).

2.4.1 Signal contributions and their origin

Given the intensity $I_0(\lambda)$ of the probe beam at wavelength λ before passing a sample of thickness d, the *Lambert-Beer law*

$$I(\lambda, \tau) = I_0(\lambda)\, e^{-\sigma(\lambda)N(\tau)d} \tag{2.4.1}$$

describes the probe beam's intensity at wavelength λ after passing the sample, where $\sigma(\lambda)$ is the wavelength-dependent cross section and $N(\tau)$ is the number of molecules which absorb at wavelength λ. Reusing Eq. (2.4.1), one typically speaks of a sample's absorbance or *optical density* (OD)

$$OD(\lambda, \tau) \;=\; -\log_{10}\left[\frac{I(\lambda, \tau)}{I_0(\lambda)}\right] \;=\; \frac{1}{\ln(10)}\, \sigma(\lambda)N(\tau)d\;. \tag{2.4.2}$$

Figure 2.5: Schematic of a transient absorption experiment. Pump pulses are spatially overlapped with probe pulses in a sample flow cell, whereas the time delay τ between the pulses is controlled by a linear translation stage. The intensity of the probe pulses after passing the sample is detected frequency-resolved with a spectrometer. For shot-to-shot detection of light-triggered changes in a molecule's absorption characteristics, a mechanical chopper is used to block every second pump pulse. By continuously scanning τ, a data set can be derived which maps the temporal evolution of the excited subensemble via changes in the absorption signatures in the spectral regime which is covered by the probe spectrum.
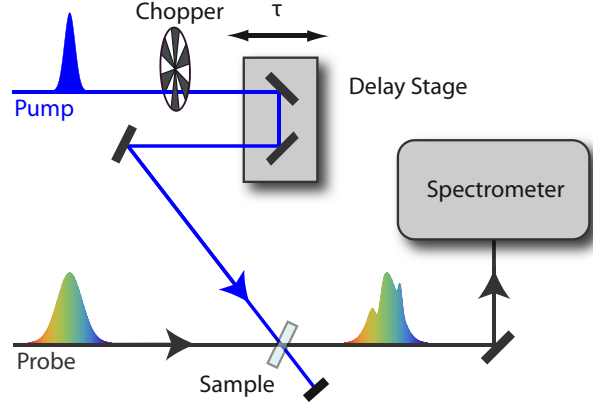
For the case that the probe beam propagates through the *unpumped* sample, the detector records a time-independent reference value $I_{\text{ref}}(\lambda) = I_0(\lambda)\,exp[-\sigma(\lambda)N_0 d]$ [confer Eq. (2.4.1)]. To quantify pump-induced changes in the sample's absorbance at a certain wavelength and time delay, one typically calculates the differential optical density

$$\Delta OD(\lambda,\tau) \;=\; -\log_{10}\left[\frac{I(\lambda,\tau)}{I_{\text{ref}}(\lambda)}\right] \;=\; \frac{1}{\ln(10)}\,\sigma(\lambda)\Big[N(\tau) - N_0\Big]d\;, \qquad (2.4.3)$$

determined by probe spectra recorded after passing through the *pumped* and *unpumped* sample volume, respectively.

For a deeper understanding of possible signal contributions in TA measurements, it is important to consider that pump–probe spectroscopy is a third-order nonlinear spectroscopic technique. Note that this is furthermore the lowest possible order of a nonlinear interaction in centrosymmetric systems including the samples investigated in this thesis (confer Sec. 2.2.1). The third-order polarization $P^{(3)}$ generated in the sample originates from two interactions with the pump and one interaction with the probe field. This polarization constitutes a source term and hence, the wave equation [confer Eq. (2.1.1)] can be written as

$$\frac{\partial E(t)}{\partial z} = \frac{i\omega_{\text{PR}}}{\epsilon_0 c}\,P^{(3)}(t)\;, \qquad (2.4.4)$$

whereby in the SVEA-regime and within the small signal limit the corresponding solution is given by

$$E_{\text{PR,total}}(t) = E_{\text{PR}}(t) + E_{\text{S}}(t),\; E_{\text{S}}(t) = \frac{i\omega_{\text{PR}}L}{\epsilon_0 c}\,P^{(3)}(t)\;, \qquad (2.4.5)$$

where L is the sample's optical path length. Hence, depending on the phase relation between the original probe field $E_{PR}(t)$ and the field emitted by the sample $E_S(t)$, transient gain or absorption will be observed. Since the detector's response is too slow to follow the electric field directly, one always detects a temporally integrated signal

$$\int_{-\infty}^{\infty} dt \ |E_{PR,total}(t)|^2 = \int_{-\infty}^{\infty} dt \ \left[|E_{PR}(t)|^2 + |E_S(t)|^2 + 2\text{Re} E_{PR}(t) E_S(t) \right]. \qquad (2.4.6)$$

The first term on the right side of Eq. (2.4.6) is constant and merely reflects the signal that would be measured without any pump interaction. This contribution does not contain any information about the sample's temporal evolution and is automatically subtracted when calculating TA signals according to Eq. (2.4.3). While the second term can be neglected in the small signal limit, the last term carries the desired information about pump-induced molecular dynamics which are manifested in positive or negative signal modulations [81]. Overall, four types of signal contributions may appear in TA measurements (independent of the spectral probing window). All TA signals are related to relaxation processes which can cause changes in a molecule's absorption characteristics (confer Sec. 2.3.3). In particular, one observes positive or negative TA signals depending on whether the probe pulse connects the molecular state of the excited subensemble to a higher- or lower-lying target state, respectively.

- **Ground-state bleach** (GSB): The excitation of a molecular system to a higher-lying state by the pump pulse removes population from its ground state. Hence, the ground state transition is bleached, i.e., less molecules are absorbing, leading to a negative ΔOD signal at the corresponding spectral position. The GSB signal may exhibit a full or a partial recovery after a certain time reflecting the amount of excited population which has relaxed back to the ground state. Hence, the residual GSB signal can be utilized to evaluate the fraction of excited population which takes an irreversible reaction pathway, i.e., it indicates a reaction's quantum yield.

- **Excited-state absorption** (ESA): As long as a molecular system is in an excited state, the absorption of another photon can induce a transition to an even higher-lying state. Hence, a positive ΔOD signal can appear which corresponds to a transition between excited molecular states.

- **Product absorption** (PA): Besides ESA, positive ΔOD signals can furthermore originate from the appearance of absorption bands which belong to photoproducts. For instance, one might observe a short-lived radical, a triplet state, or the final photoproduct of a photolysis reaction. Often, PA signals can be related to a residual GSB signal.

- **Stimulated emission** (SE): The pump interaction may populate an emissive state that shows fluorescence. Photon emission can then be stimulated by another photon of the probe pulse. Hence, owing to the increase of probe light, a negative ΔOD signal will be detected. In the case of an initial electronic or vibronic excitation,

due to VC and a higher Franck-Condon factor for a transition to higher vibrational levels in the electronic ground state, SE typically appears red-shifted with respect to the GSB signal (confer Kasha's rule [82]).

Data acquired in TA measurements is typically visualized in a so-called *transient map*, where color-coded ΔOD signals are plotted against wavenumber and time delay. This multi-dimensional data set may reflect several molecular processes occurring simultaneously but on different time scales. Hence, a global analysis which fits the data set to a theoretical model and helps to unravel the underlying processes may become desirable [83]. However, often it is already instructive to evaluate cuts along the wavenumber axis (so-called *difference spectra*) or along the time delay axis (so-called *transients*).

2.4.2 Characteristics of different measurement configurations

The appearance of various features which do not reflect real dynamics of an investigated molecular system need to be considered when analyzing the result of a TA measurement. The most important ones, which can be more or less pronounced depending on the combination of pump beam, probe beam, and sample, are briefly outlined in the following.

Coherent artifact

The *coherent artifact* [84, 85], which is an unwanted feature appearing in TA measurements in the liquid phase that potentially masks early molecular dynamics, is predominantly caused by so-called *cross-phase modulations* (XPMs). This nonlinear interaction between the (intense) pump pulse and the flow cell with its containing solvent leads to a modulation of the real part of the optical medium's refractive index [86, 87]

$$n(t) = n_0 + n_2 |E(t)|^2 \ , \tag{2.4.7}$$

where $|E(t)|^2$ describes the pump pulse's temporal envelope, which in turn affects the probe pulse's spectrum and phase. For the case of spectrally-resolved TA spectroscopy, this results in an undesired short-living signal around time zero, i.e., when pump and probe pulse overlap temporally. Depending on experimental parameters such as the flow cell material or the pump pulse's intensity and duration, the effect can be more or less pronounced. Especially in cases in which the coherent artifact overlaps with contributions from the so-called *perturbed free induction decay*—an effect discussed in the following paragraph—it can be challenging to apply correction procedures to distinguish between early molecular dynamics and artifacts [87, 88]. It is noteworthy, that analyzing the coherent artifact in pure solvents is one way to determine the experimental setup's temporal resolution providing similar values for instance compared to a SFG cross-correlation measurement between the pump and probe pulse [20, 89].

Perturbed free induction decay

TA measurements in the MIR spectral region may also be influenced by an effect called *perturbed free induction decay* (PFID). The latter appears when dephasing times of vibrational coherences (up to 1 ps) exceed the time resolution of the experimental apparatus [81, 90, 91]. The resonant excitation of a vibrational transition gives rise to a coherent polarization which radiates the so-called *free induction decay* (FID). For negative time delay ($\tau < 0$), i.e., when the probe pulse reaches the sample first, the decaying FID gets perturbed and disappears upon electronic excitation by the pump pulse. This process possibly modifies the strength and position of the absorption line. For the case of spectrally-resolved UV-pump/MIR-probe TA spectroscopy, PFID leads to an additional TA signal which decays from time zero towards negative time delay with the transition's dephasing time and which is also present at frequencies close to the line center. For the case of finite time resolution, PFID contributions can also appear shortly after time zero, i.e., within the cross-correlation time of the pump and probe pulse, hence constituting another complication in the observation of ultrafast molecular dynamics. Mind that typical dephasing times of electronic transitions of molecules in solution are well below 100 fs making the effect of PFID negligible for probing in the UV to VIS spectral region. With regard to studies in the MIR spectral region, however, it is noteworthy that signal contributions originating from PFID can be suppressed by Fourier filtering if necessary [92].

Influence of probe chirp

When ultrashort MIR pulses are employed to probe vibrational dynamics of molecular systems (confer Sec. 3.4), different colors of the probe pulse arrive at the sample (almost) simultaneously. However, when probing in the UV to VIS spectral region with broadband pulses generated via WLG (confer Secs. 2.2.3 and 3.3), the pulses' positive chirp has to be considered which may additionally be influenced by dispersive material in the beam path. Both effects result in a wavelength-dependent time zero, i.e., the time delay when pump and probe pulse overlap, with typical variations on the order of several hundreds of femtoseconds. The probe chirp can easily be characterized by analyzing the coherent artifact (see above) ideally in pure solvent. Its wavelength-dependent temporal appearance can thereby be exploited to define time zero for each transient individually. To analyze difference spectra in general, the entire transient map needs to be corrected globally by fitting the temporal center of the coherent artifact to a lower-order polynomial and appropriately shifting each transient [20].

2.5 Chirped-pulse upconversion

Revealing the vibrational dynamics of molecules by mapping their TA in the MIR spectral range is commonly used to gain insight into chemical processes on a microscopic scale [18]. Over the last decades the development of commercially available amplified

femtosecond laser systems, accompanied by the establishment of optical parametric amplifiers capable of generating stable ultrashort MIR pulses [55, 93, 94], gave rise to a vast variety of time-resolved investigations on diverse systems in different environments. In the liquid phase for instance, studies are ranging from small molecules via organometallic compounds to large proteins [4, 95–113]. Thus, probing in the MIR spectral range has proven to be an unprecedentedly sensitive method to follow the structural evolution of a molecular system in real time. However, detecting MIR signals simultaneously with high spectral bandwidth and high spectral resolution still constitutes a challenging task. This is addressed by chirped-pulse upconversion (CPU), a technique which has the potential to replace conventional detection methods.

2.5.1 Introduction and motivation

Standard direct multichannel MIR detection uses liquid nitrogen cooled photodiode arrays based on compound semiconductors as InAs, InSb, or HgCdTe (MCT). Commercially available IR spectrometers are limited to a maximum of 128 pixels, so that combining detector arrays is one way to increase the number of detection channels [113, 114]. Nevertheless, often a compromise between spectral resolution and spectral bandwidth has to be found. Different techniques have been reported, circumventing this issue by transferring the MIR signals to the VIS regime [95, 96, 115, 116]. The technique of CPU in particular uses a strongly chirped near-infrared pulse (CP) to upconvert MIR signals via sum-frequency mixing in a NC [23]. Simply put, upconversion is done by adding a constant local frequency of the CP to the MIR field (see Fig. 2.6 for graphical illustration). As a result, mature silicon CCD technology can be used to detect the upconverted radiation. However, for narrow spectral features which correspond to long features in the time domain, the signal field is mixed with a range of wavelengths of the CP. This is equivalent to mixing with nonlinear phase variations which lead to phase modulations in the upconverted field that in turn cause spectral broadening. This section comprises a mathematical treatment of CPU including a description on how to remove phase distortions in order to improve the spectral resolution of CPU [24].

Considering a field $E_{\mathrm{MIR}}(t)$ being mixed with a field $E_{\mathrm{CP}}(t) = A(t)\exp[-i\omega_0 t + i\varphi(t)]$ (central frequency ω_0) in a SFG arrangement (confer Sec. 2.2.2) at $t = 0$ under conditions of perfect phase matching, a CPU field is created that is proportional to the time-domain product

$$E_{\mathrm{CPU}}(t) = \eta E_{\mathrm{MIR}}(t) E_{\mathrm{CP}}(t) = \eta E_{\mathrm{MIR}}(t) e^{-i\omega_0 t} A(t) e^{i\varphi(t)} \ , \qquad (2.5.1)$$

with the coefficient η describing among other terms the second-order nonlinear coefficient of the crystal and the $\pi/2$ phase shift between the polarization and the radiated field [24]. The envelope of the CP is accounted for in a real-valued envelope function $A(t)$, which reaches its maximum value when the pulses are overlapped [$A(0) = 1$]. In the case of large linear chirp, i.e., for large values of b_2 (confer Sec. 2.1.4), the parabolic CP time-domain phase function is given by $\varphi(t) = t^2/2b_2$ [for sign convention, confer Eq. (2.1.24)] [117, 118]. The first CP term in Eq. (2.5.1), i.e., $e^{-i\omega_0 t}$, describes the desired process of upconversion
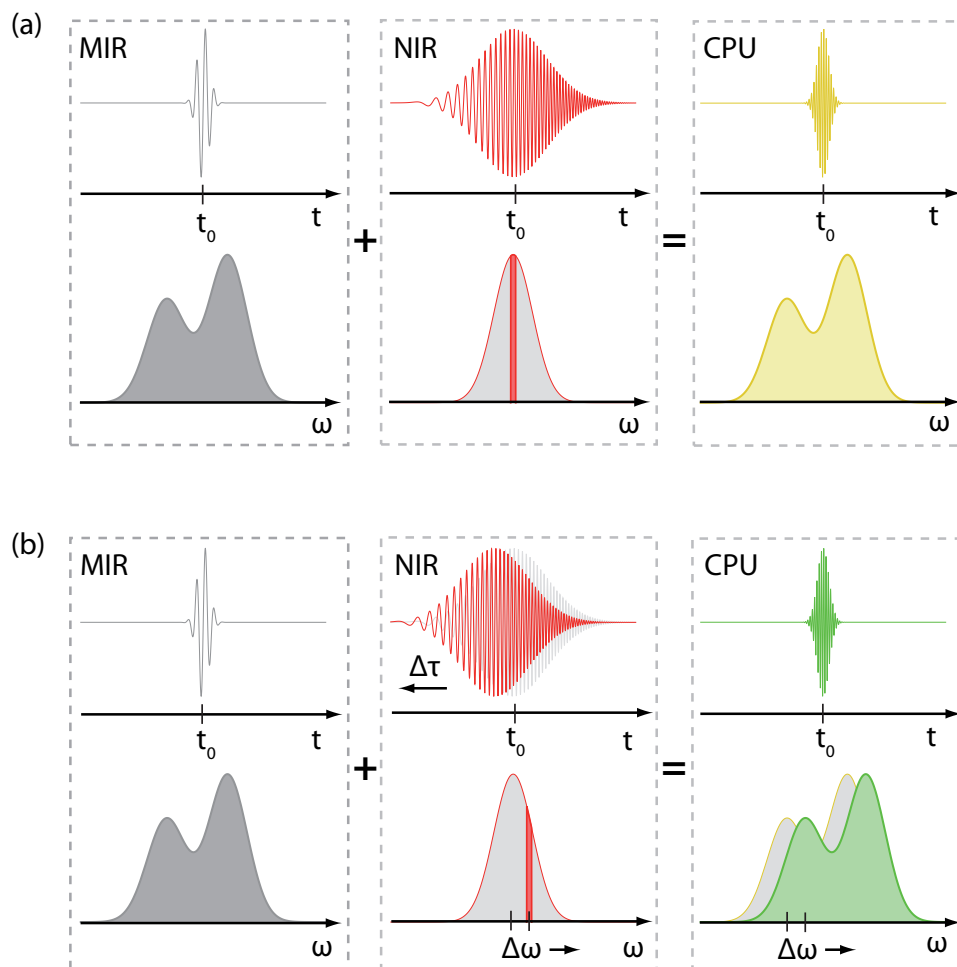
Figure 2.6: Joint representation of chirped-pulse upconversion in time and frequency domain. (a) An ultrashort MIR laser pulse is mixed in a SFG process with a strongly positively chirped NIR pulse (CP) to generate an ultrashort VIS pulse. Since the frequency of the CP can be considered as constant within the window of temporal overlap, the MIR pulse is mixed with a quasi monochromatic NIR pulse, leading to a translation of the MIR spectrum to the VIS regime without changes in the spectral shape. (b) The MIR pulse is mixed with a quasi monochromatic component of the CP. Thus, for the case of a CP which is positively chirped, a temporal delay $\Delta\tau$ of the CP translates into a frequency shift $\Delta\omega$ of the upconverted field towards higher frequencies [in (a) the CP's central frequency is used for upconversion]. If narrow features are present in MIR spectra, cross-phase modulations need to be removed from upconverted spectra. See text for further explanations.

via addition of a *monochromatic* frequency ω_0. Multiplying the MIR field with the second term, i.e., $A(t)$, results in a convolution in the frequency domain. However, effects on the spectral resolution can be excluded for CP stretching factors employed within this thesis. By contrast, it is vital to account for the third term, i.e., $e^{i\varphi(t)}$, which causes phase modulations in time that in turn can distort CPU spectra in the presence of narrow spectral features.

2.5.2 Removing cross-phase modulations

While the correction procedure can also be applied in multidimensional spectroscopy, i.e., in the case that the CPU field in general is fully characterized [24], the following discussion is devoted to the case of absorption spectroscopy, and thus holds in the linear transmission regime and for pump–probe absorption spectroscopy where the causality principle can be exploited. Given a short probe field $E_{\mathrm{PR}}(t)$ (centered at $t = 0$) and a field $E_{\mathrm{S}}(t)$ being radiated by the sample, for the case of small absorption the spectral intensity profile of the MIR spectrum is given by

$$I(\omega) = |E_{\mathrm{PR}}(\omega) + E_{\mathrm{S}}(\omega)|^2 \approx |E_{\mathrm{PR}}(\omega)|^2 + E_{\mathrm{PR}}^*(\omega)E_{\mathrm{S}}(\omega) + E_{\mathrm{PR}}(\omega)E_{\mathrm{S}}^*(\omega) \; , \qquad (2.5.2)$$

where a contribution from $|E_{\mathrm{S}}(\omega)|^2$ has been assumed to be negligible. Importantly, the field $E_{\mathrm{S}}(t)$ is zero before $E_{\mathrm{PR}}(t)$ interacts with the sample. However, depending on sample dephasing times, the signal can be arbitrarily long for positive times. Likewise, this interference between $E_{\mathrm{PR}(t)}$ and $E_{\mathrm{S}(t)}$ is reflected in the CPU spectrum

$$I_{\mathrm{CPU}}(\omega) \approx |E_{\mathrm{PR,CPU}}(\omega)|^2 + E_{\mathrm{PR,CPU}}^*(\omega)E_{\mathrm{S,CPU}}(\omega) + E_{\mathrm{PR,CPU}}(\omega)E_{\mathrm{S,CPU}}^*(\omega) \; . \qquad (2.5.3)$$

How phase modulations [manifested in $E_{\mathrm{S,CPU}}(t)$] distort CPU spectra and how they can be corrected is visualized in Fig. 2.7 for the case of upconverting a Gaussian-shaped MIR spectrum transmitted through a narrow Lorentzian absorption line [Fig. 2.7(a)]. Note that exemplary parameters are chosen which resemble those used within this thesis (confer Sec. 3.4.2 and Chap. 5). While the main envelope of the corresponding CPU spectrum matches the shape of the MIR spectrum, a strong oscillatory behavior, which appears red-shifted with respect to the absorption line, is caused by cross-phase modulations. As it can be seen from Fig. 2.7(b), the latter severely distort the narrow absorption feature. After Fourier transformation, Eq. (2.5.3) reads

$$
\begin{aligned}
\mathcal{F}\Big\{ I_{\mathrm{CPU}}(\omega) \Big\}(t) \;\; &\approx \;\; E_{\mathrm{PR,CPU}}(-t) \otimes E_{\mathrm{PR,CPU}}(t) \\
&+ \;\; E_{\mathrm{PR,CPU}}^*(-t) \otimes E_{\mathrm{S,CPU}}(t) + E_{\mathrm{PR,CPU}}(t) \otimes E_{\mathrm{S,CPU}}^*(-t) \; , (2.5.4)
\end{aligned}
$$

where $\otimes$ denotes the convolution product. The three terms on the right side of Eq. (2.5.4) are overlapping, and hence can not be addressed individually. However, overlap is only
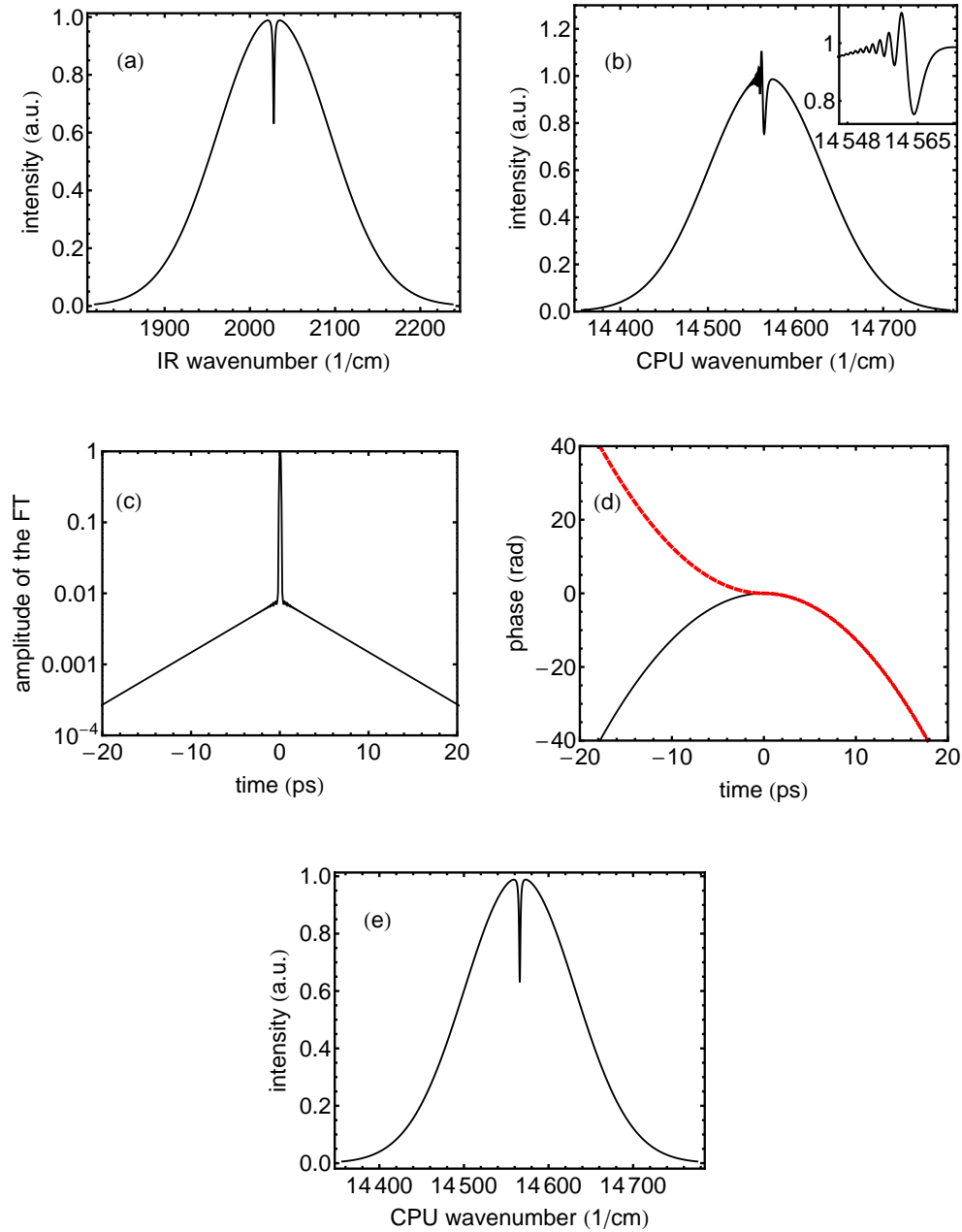
Figure 2.7: Removing cross-phase modulations from CPU spectra. (a) Simulated spectrum of a Gaussian laser pulse centered at $\tilde{\nu}_{\mathrm{MIR},0} = 2028$ cm^{-1} [$\Delta\tilde{\nu}_{\mathrm{MIR}} = 154$ cm^{-1} (FWHM)] after transmission through a Lorentzian absorption line centered at $\tilde{\nu}_{\mathrm{Abs}} = 2028$ cm^{-1} [0.2 OD, $\Delta\tilde{\nu}_{\mathrm{Abs}} = 1.8$ cm^{-1} (FWHM)]. (b) Spectrum shown in (a) after upconversion with a chirped NIR pulse [$\tilde{\nu}_{\mathrm{NIR},0} = 12538$ cm^{-1}, $\Delta\tilde{\nu}_{\mathrm{NIR}} = 143$ cm^{-1} (FWHM), $b_2 = -3.97$ ps^2]; the inset highlights spectral distortions caused by cross-phase modulations. (c) Amplitude of the Fourier transform of the spectral intensity shown in (b), i.e., $|\mathcal{F}\{I_{\mathrm{CPU}}(\omega)\}(t)|$. (d) Time-dependent phase $\varphi(t)$ of the CP (black line) and time-dependent phase $\varphi_{\mathrm{corr}}(t)$ used for spectra correction (red dashed line). (e) CPU spectrum shown in (b) after removal of cross-phase modulations. Correction procedure performed according to Ref. [24].

given around $t = 0$, which is also the region where cross-phase modulations can be neglected. The latter circumstance makes possible to apply a correction procedure which makes use of causality: for $t > 0$, only the second term on the right side of Eq. (2.5.4) will contribute, which necessitates the subtraction of $\varphi(t)$ from the correlation product; for $t < 0$, only the third term on the right side of Eq. (2.5.4) will contribute, which necessitates the subtraction of $-\varphi(-t)$ from the correlation product. Taken together, cross-phase modulations can be removed by subtracting the phase function

$$\varphi_{\mathrm{corr}}(t) = \varphi(|t|)sign(t) \tag{2.5.5}$$

from the time-domain CPU spectrum, whereby $sign(t)$ is the sign function. Eventually, the corrected CPU spectrum can be obtained by an inverse Fourier transformation [see Fig. 2.7(e)]. Further details on the correction procedure can be found in Ref. [24].

Meanwhile, CPU has become a well-established technique in the field of ultrafast MIR spectroscopy [105, 110, 119–123] and pulse characterization [23, 124]. Furthermore, CPU has been applied in the lower energetic regime of 1000-1800 cm^{-1} by using a AgGaGeS$_4$ crystal instead of the commonly used MgO:LiNbO$_3$ crystal [125] or to detect ultrabroad MIR continua [126]. Alternatively, CPU was used for upconversion of a MIR supercontinuum spanning from 200 to 5500 cm^{-1} by replacing the upconversion crystal by gas media; apart from a reduced upconversion efficiency, an almost unlimited upconversion bandwidth has been reported [127]. Considering these achievements, it is of broad interest to assess the individual strengths and weaknesses of CPU and direct multichannel MCT detection. For this purpose, Chap. 5 juxtaposes both techniques in a TA experiment with MIR probe pulses. The corresponding experimental setup is detailed in Sec. 3.4.2.

Experimental techniques

The previous chapter outlined the theoretical description of frequency conversion processes and their connection to pump–probe investigations in the context of the principles of light-matter interaction. How such investigations are realized in the laboratory is described in this chapter. After a brief description of the femtosecond light source, the employed frequency conversion techniques and their application in different pump–probe configurations are described. Besides the UV-pump/VIS-probe detection scheme, being the method of choice when scrutinizing primary processes of diphenylcarbene in solvent mixtures in Chap. 4, special emphasis is put on a detailed description of the UV-pump/MIR-probe detection scheme, allowing for simultaneous detection via direct multichannel MCT detection or via chirped-pulse upconversion to the VIS regime, which is characterized in Chap. 5 and employed in Chap. 6 to reveal vibrational dynamics of transition metal complexes. To complement this, the characterization of UV pulses is described. Finally, a detection scheme that allows for combining transient absorption and fluorescence spectroscopy, as utilized in Appendix A, is presented.
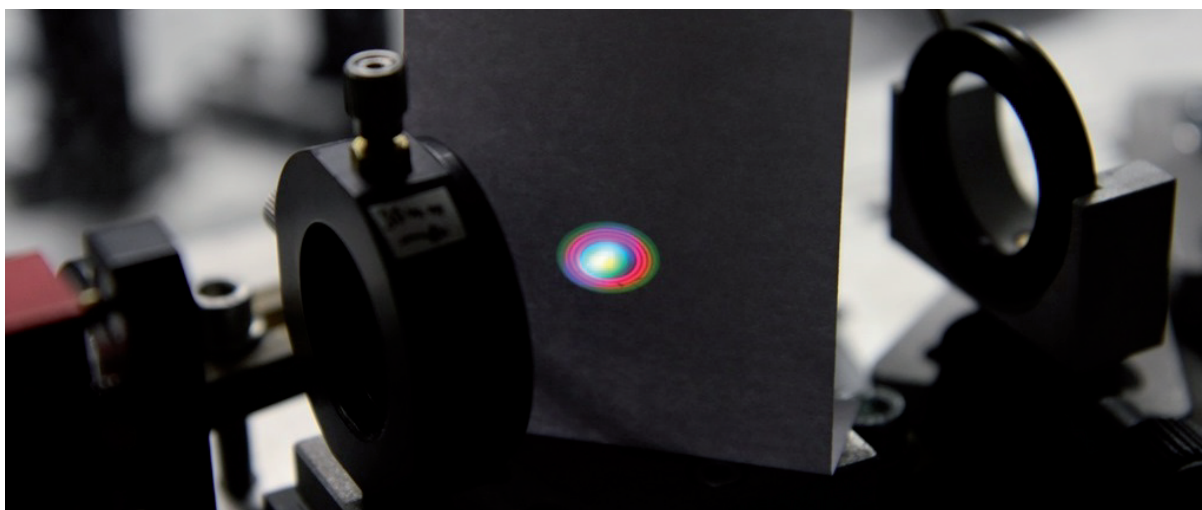
Picture illustrates the generation of white light in sapphire for the case of supersaturation.
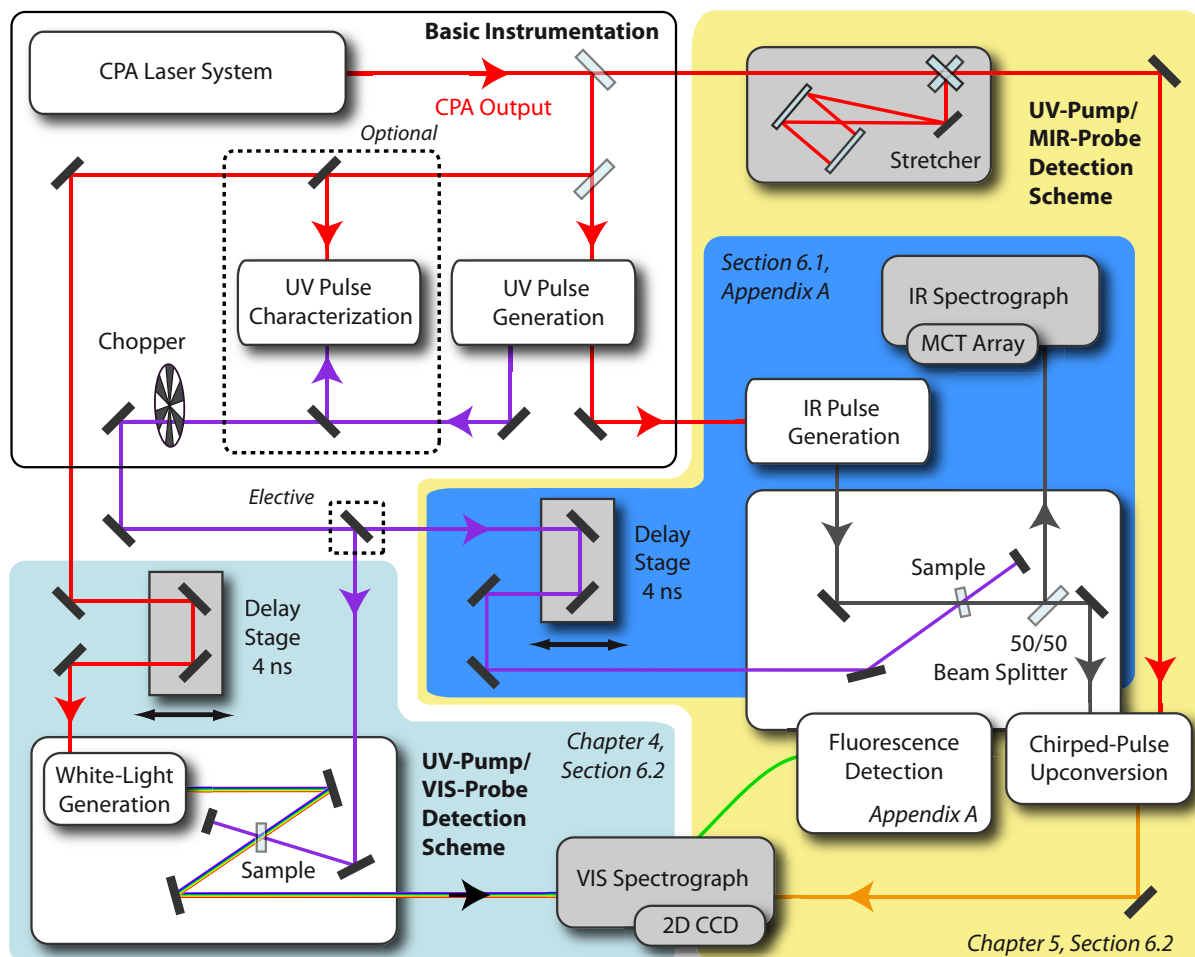
3.1 Instrumentation overview

Figure 3.1: Schematic summary of experimental techniques and methods used in femtosecond time-resolved measurements. The fundamental radiation originates from a amplified NIR laser system generating 100 fs pulses at a repetition rate of 1 kHz. The basic instrumentation (black framed area) includes tools to generate and characterize UV pulses as well as a mechanical chopper operating at half the laser's repetition rate. The subsequent instrumentation can be divided into two groups: a UV-pump/VIS-probe setup (light blue shaded area) and a UV-pump/MIR-probe setup (blue shaded area). Each setup includes instrumentation to generate the probe pulses, a delay stage to adjust the pump–probe time delay, as well as a scheme for spectrally-resolved detection. Chirped-pulse upconversion can be used to detect MIR probe pulses after upconversion to the VIS regime, extending the UV-pump/MIR-probe setup (yellow shaded area). Furthermore, a fluorescence detection scheme is implemented. Instrumentation highlighted in white is detailed in a separate figure. Note the specified usage of particular instrumentation in different parts of this thesis.

Figure 3.1 provides a schematic overview of the experimental setup used in this work. In a nutshell, the setup contains instrumentation to carry out TA measurements with UV pump pulses and probe pulses which either cover the VIS to UV, or parts of the MIR spectral region. Thus, the setup can be divided into three parts which are individually discussed in the following. The first part is the basic instrumentation (black framed area in Fig. 3.1) which is used in every experiment based on pulsed laser light throughout this thesis. As detailed in Sec. 3.2, it mainly includes the femtosecond laser system, a device to generate UV pump pulses and a unit to characterize the latter. Having the pump pulses at hand, part two contains the remaining instrumentation necessary to conduct UV-pump/VIS-probe measurements (light blue shaded area in Fig. 3.1, for explanations see Sec. 3.3). Analogous to the third part which deals with instrumentation required in UV-pump/MIR-probe measurements (blue shaded area in Fig. 3.1, for explanations see Sec. 3.4), it includes instrumentation to generate probe pulses for the respective spectral region of interest, a delay stage to regulate the pump–probe delay, as well as optics to appropriately focus the pump and probe pulses into a sample and eventually guide the transmitted probe pulses into a spectrally resolved detection unit. While the above-mentioned instrumentation was mainly constructed in the framework of previous dissertations [88, 128, 129], extensions to the UV-pump/MIR-probe setup have been added within the present work: first, the possibility to detect MIR probe pulses via chirped-pulse upconversion (CPU) in the VIS spectral regime (yellow shaded area in Fig. 3.1), and second, a fluorescence detection scheme. These extensions are likewise detailed in Sec. 3.4.2 and 3.5, respectively. The usage of different instrumentation in different parts of this thesis is denoted in Fig. 3.1. For the sake of completeness it should be mentioned that the VIS to UV and the MIR TA setups are located in adjacent rooms on different optical tables sharing the same laser system. Furthermore, each setup contains its own device to generate UV pulses and its own VIS detection unit. However, for clarity and since these devices are structurally identical, they are only depicted once in Fig. 3.1.

3.2 Basic instrumentation

In this section, basic instrumentation used both in the main part of this thesis as well as in Appendix A is introduced. The main concept of the overall setup (confer Fig. 3.1) relies on splitting the output of a chirped-pulse amplification (CPA) laser system into several parts with different relative energies for various nonlinear interaction processes. The largest share of the fundamental light is used in a noncollinear optical parametric amplifier (NOPA) to generate UV pulses. The NOPA as well as methods to characterize its output are presented in this section. Furthermore, explanations on supplementary spectrocopic methods and devices used within the scope of this thesis are discussed.

3.2.1 CPA laser system

Throughout this thesis, a commercially available 1 kHz regenerative amplifier system (Solstice, Spectra-Physics) is the source for pulsed laser light. The system, operating at a repetition rate of 1 kHz, is capable of delivering 100 fs pulses at a central wavelength of 800 nm, whereby pulse energies up to 3 mJ can be achieved. Its functionality based on the principle of *chirped pulse amplification* (CPA) [130, 131] is briefly summarized in the following.

Figure 3.2: Generation of amplified fs laser pulses. The technique of chirped pulse amplification (CPA) uses a multi-step procedure to facilitate the generation of laser pulses with energies in the order of a few mJ at a repetition rate of 1 kHz. At this, sub 100 fs NIR pulses with a repetition rate of 80 MHz are the starting point of the amplification procedure. In a first step, these so-called seed pulses, which are generated by self-mode locking in a Ti:Sapphire oscillator pumped by a continuous wave Nd:YVO$_4$ laser, are strongly stretched in time. Subsequently, every frequency component is amplified individually in a regenerative amplifier pumped by a pulsed Nd:YLF laser. Eventually, the pulses are compressed to approximately 100 fs. Specifications are taken from the user's manual (Solstice, Spectra-Physics) [132].
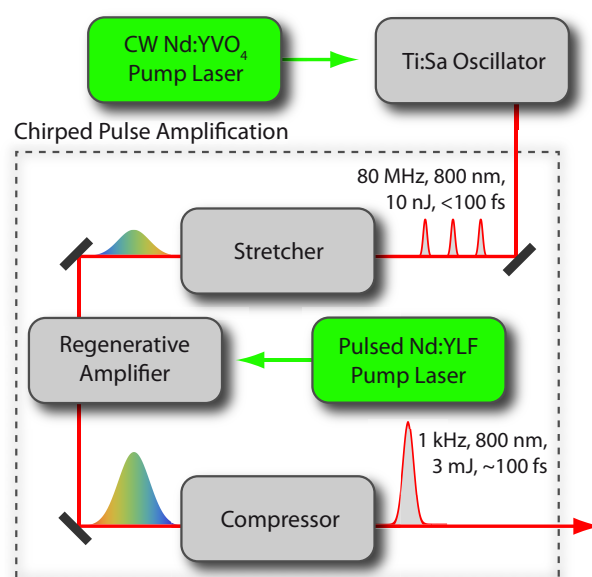
The key building block of the Solstice system is a laser oscillator, in particular, an integrated titanium doped Al$_2$O$_3$ (Ti:Sapphire) oscillator (MaiTai) pumped by a continuous wave (CW) neodymium-doped yttrium orthovanadate (Nd:YVO$_4$, 532 nm) diode laser generating sub 100 fs pulses (800 nm, 14 nm bandwidth) at a repetition rate of 80 MHz. Which longitudinal modes are amplified in an oscillator's optical resonator is determined by the amplification profile of the gain medium. The amplification of a broad spectrum is one precondition for the generation of ultrashort laser pulses [28]. Equally important, the longitudinal modes need to share a fixed phase offset in order to generate an ultrashort 'burst' of light via constructive superposition of all modes at one point in time. For the case of a Ti:Sapphire oscillator, self-mode locking is possible [133]. The oscillator principle furthermore relies on a prism pair used to compensate for the dispersion introduced by the gain medium, the Kerr lensing effect [28], meaning the stronger focusing of pulsed light owing to the higher peak intensities which enables to filter the CW mode via an aperture in the resonator, and an adjustable output slit used to fine-tune the oscillator's central wavelength [28, 32]. The weak oscillator pulses constitute the starting point of the CPA procedure, which allows for spectroscopic applications that require higher pulse

energies, e.g., frequency conversion processes or nonlinear spectroscopy.

The CPA process is sketched in Fig. 3.2. It begins with a stretcher which introduces a large positive linear chirp, therewith temporally elongating the oscillator pulses to approximately 100 ps. Before the pulses can enter a regenerative amplifier, two Pockels cells are used to select so-called *seed pulses* at a repetition rate of 1 kHz [28, 134]. In the amplifier, the stretched seed pulses are spatially and temporally overlapped with the output of a pulsed nanosecond (ns) neodymium-doped yttrium lithium fluoride (Nd:YLF) pump laser (1 kHz, 527 nm) in another Ti:Sapphire crystal. As a consequence of the positive chirp, different spectral components of the seed beam arrive at different times in the amplifier's gain medium, thereby keeping peak intensities sufficiently low to avoid damage of the amplifier material. To finally reach the desired high peak intensities, the amplified pulses are compressed in a *Treacy-type* compressor [135] to almost the bandwidth-limit by introducing negative chirp. Ti:Sapphire offers an amplification bandwidth broader than the spectrum of the seed pulses to be amplified. However, CPA output pulses are slightly temporally elongated with respect to the oscillator pulses. This is due to the phenomenon of spectral gain narrowing which leads to nonlinearities in the amplification process decreasing the pulse's spectral bandwidth, and the circumstance that third-order dispersion (TOD) is added with each amplifier round-trip which can not be removed with the compressor.

3.2.2 UV pulse generation

The generation of ultrashort UV pulses is realized using a commercially available two-stage noncollinear optical parametric amplifier (NOPA, TOPAS-White, Light Conversion Ltd) [136]. The device is capable of delivering sub 100 fs pulses between 250 and 1000 nm, whereas UV pulses are generated in an integrated SHG stage used for frequency doubling the outcome of the OPA processes. Its working principle is strongly related to the MIR collinear optical amplifier (MIR-OPA) which will be introduced in Sec. 3.4.1. In a collinear OPA design (refer Sec. 3.4.1), in which the phase matching is tuned by adjusting the crystal angle, group velocity dispersion limits the phase matching in the OPA process, thus making the generation of sub 100 fs pulses impossible. The noncollinear geometry, however, allows for overlap of the signal, idler and pump pulse over the complete crystal length, enabling the generation of tunable sub 20 fs VIS pulses in a routine manner [137, 138]. For a theoretical description of the frequency conversion processes involved in the NOPA, namely WLG, OPA, and SHG, see Secs. 2.2.2 and 2.2.3. The layout of the NOPA system, which is driven by the largest share of fundamental CPA output used in the overall experimental setup, is depicted in Fig. 3.3. A small portion of the 800 nm input beam is used to generate a white-light continuum (WLC) which is subsequently negatively chirped in a frequency domain double-pass pulse shaper in order to compensate for the WLG chirp. The shaping furthermore enables one to modify the seed bandwidth used in the OPA process, therewith modifying the bandwidth of the NOPA output. For pumping, a 400 nm pump beam is generated via frequency doubling the main part of the 800 nm input in BBO 1. The latter is split in two parts with different energy for usage in the first
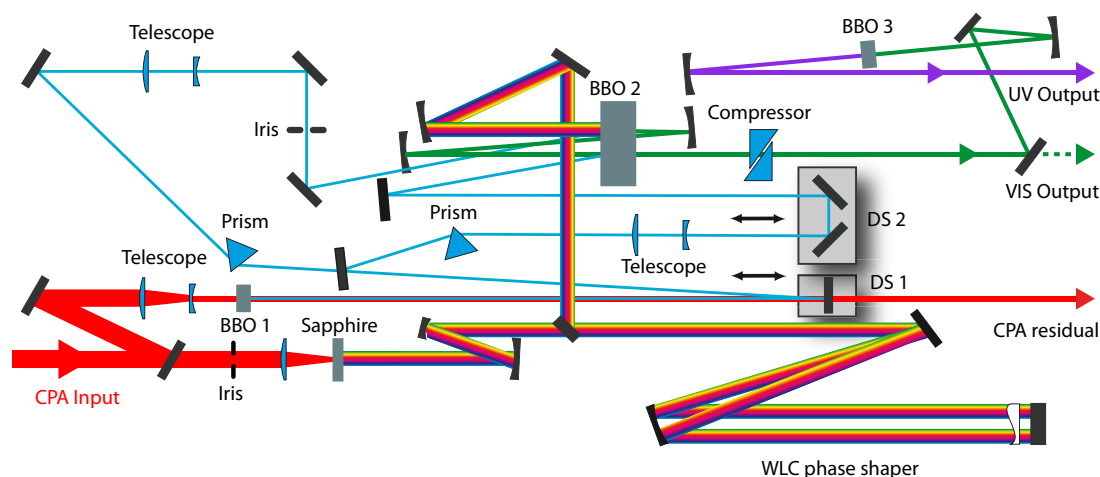
Figure 3.3: Generation of tunable UV pulses. Schematic depicts the layout of the commercial NOPA (TOPAS-White, Light Conversion Ltd). After passing a frequency domain pulse shaper, weak white light seed pulses are amplified in a two-stage NOPA process using the second harmonic of the fundamental 800 nm light for pumping. Eventually, tunable UV pulses are generated by frequency doubling the visible output of the NOPA processes after compression via two adjustable glass wedges. Specifications and further details are given in the text. Figure reprinted with minor modifications from Ref. [129].

and second NOPA stage, respectively. Under a small angle of nonlinearity β, the weak seed pulses are superposed with the weaker pump beam in BBO 2. With respect to the UV pulses employed in this thesis ($\lambda_{\text{central}} \approx 300$ nm), an angle of $\beta \approx 4°$ is used to achieve the optimal phase matching in a type I BBO [55]. This process is repeated in the second NOPA stage in the same noncollinear geometry with the stronger pump beam, thereby amplifying the signal field of the first OPA process by a factor of about 10. For each NOPA stage, the temporal overlap between the pump beam and the seed/signal beam can be regulated individually with motorized delay stages (DS 1 and DS 2). Eventually, another NC (BBO 3) is used for frequency doubling the result of the NOPA processes to generate UV pulses. Prior to this, the VIS pulses are compressed by two moveable fused silica wedges to maximize the SHG output. Typical UV output is on the order of 5 mW depending on the selected wavelength, whereas pulse durations below 50 fs can be achieved. To guide the UV output to subsequent devices and experiments, mirrors with a UV enhanced aluminum coating are used to keep loses minimal and at the same time enable the usage of different UV wavelengths without exchanging the mirrors. For TA measurements, a phase-locked mechanical chopper (Model 3501, New Focus Inc.) is used to block every other UV pump pulse. Note that the actual UV power applied in each of the following experiments is determined separately. How to align the WLC in order to achieve a stable NOPA output is explained and visualized in Ref. [129].

Compared to the generation of UV pulses via SHG or third-harmonic generation (THG) of the fundamental beam [41], the TOPAS-White system benefits from the wide spectral tunability (exemplary output spectra of the TOPAS-White system are presented in Ref. [129]). After appropriate calibration, tuning curves can be derived and stored which

afterwards can reliably be called up again. This enables the setting of a desired UV output wavelength without manual changes in the alignment.

3.2.3 UV pulse characterization

The time resolution in a pump–probe experiment is inherently limited by the convolution between the temporal intensity profiles of the pulse which triggers the photoreaction and the pulse used for probing. While methods to characterize the probe pulse in an indirect way by measuring the overall time resolution of the pump–probe scheme will be discussed in Sec. 3.3 for white-light probe pulses and in Sec. 3.4.2 for MIR probe pulses, respectively, this section deals with the characterization of the UV pump pulses. It is recalled that photodetectors do not provide a sufficiently high temporal resolution to directly characterize the temporal intensity profile of ultrashort laser pulses. Instead, the latter can only be characterized via a nonlinear interaction with itself or with another laser pulse which is already characterized.

Various methods have been demonstrated that fulfill the above-mentioned task for pulses ranging from the extreme ultraviolet (XUV) to the MIR spectral region, whereby variations of spectral-phase interferometry for direct electric field reconstruction (SPIDER) or frequency-resolved optical gating (FROG) are the most wide-spread ones [39, 139–146]. This section focuses on the technique applied within the scope of this thesis, namely a combined self- and cross-referenced FROG measurement to characterize UV pulses [147–150]. Thereby, the self-referenced FROG measurement is utilized to characterize a reference beam, which in a second step is required to characterize the UV pulses in a cross-correlation FROG (XFROG) measurement. Both measurements necessitate an interaction in a NC, involving frequency mixing processes introduced in Sec. 2.2.2. Since typical NCs such as BBOs exhibit only little transmission for wavelengths below 200 nm accompanied by drastically reduced phase-matching efficiencies towards shorter wavelengths, a direct self-referenced characterization of UV pulses is not possible.

Figure 3.4(a) schematically depicts the implements of a self-referenced FROG measurement. Since standard BBOs can be used for frequency doubling of NIR pulses, it is straightforward to use a small portion of the fundamental CPA output for a SHG-FROG measurement. The incoming beam is equally split into two beams, such that pulse copies can subsequently be overlapped in a SHG crystal with a defined temporal delay τ. Thereby, a noncollinear geometry is chosen to spatially separate the cooperative SHG signal from the two original beams and their individual SHG contributions. Roughly speaking, the pulse to be characterized is gated by its own pulse copy. By scanning τ and recording the cooperative SHG signal without frequency resolution, an intensity autocorrelation trace is recorded which provides a rough estimation of the reference beam's duration [28]. When using spectrally-resolved detection, the same measurement routine gives a FROG trace:

$$I_{\mathrm{SHG-FROG}}(\omega, \tau) = \left| \int_{-\infty}^{\infty} E(t)E(t-\tau)e^{-i\omega t}\mathrm{d}t \right|^2 . \tag{3.2.1}$$

The electric field—except the CEP—can be retrieved by an algorithm which iteratively calculates FROG traces and minimizes deviations from the measured FROG trace [39]. Note that the SHG-FROG measurement benefits from the fact that no *a priori* knowledge of pulse properties is required to conduct the characterization procedure. However, besides limitations regarding the phase matching (see above), the quadratic dependence on the electric field [confer Eq. (3.2.1)] makes the method less appropriate for weak or structured pulses.

As illustrated in Fig. 3.4(b), for the XFROG measurement the self-referenced FROG routine is basically repeated with the difference that one replica of the (already characterized) reference beam is replaced by the unknown pulse. Owing to the above-mentioned limitation regarding the usage of NCs when characterizing UV pulses, DFG in another BBO is employed to obtain XFROG traces in the VIS regime:

$$I_{\text{XFROG}}(\omega, \tau) = \left| \int_{-\infty}^{\infty} E_{\text{UV}}(t) E_{\text{ref}}^*(t - \tau) e^{-i\omega t} \mathrm{d}t \right|^2. \tag{3.2.2}$$

Having the full knowledge about the reference beam, the electric field of the unknown UV pulse can be reconstructed via another iterative algorithm [39, 151]. However, if only intensity-related information about the unknown pulse is required, one can record intensity cross-correlation traces by using a photodiode for detection instead of a spectrometer. It may, in general, be noted that cross-referenced techniques—owing to the linear dependence of the unknown field in the nonlinear process [confer Eq. (3.2.2) for the case of XFROG]—are well-suited to characterize weak laser pulses in nearly all spec-

Figure 3.4: Characterization of UV pulses via autocorrelation or FROG. (a) After passing a *Mach-Zehnder-type* interferometer, pulse-copies of an input beam (typically the 800 nm CPA beam) are overlapped in a NC for different time delays. Detecting the cooperative SHG signal with a photodiode leads to an intensity autocorrelation, whereas a SHG-FROG trace is recorded when using spectrally-resolved detection. (b) In a second step, the characterized reference beam is mixed in another NC with the unknown UV pulse for different time delays. The cooperative signal leads to an intensity cross-correlation if using a photodiode for detection or the measurement of a cross-correlation FROG (XFROG) trace when using spectrally-resolved detection. See text for further explanations.
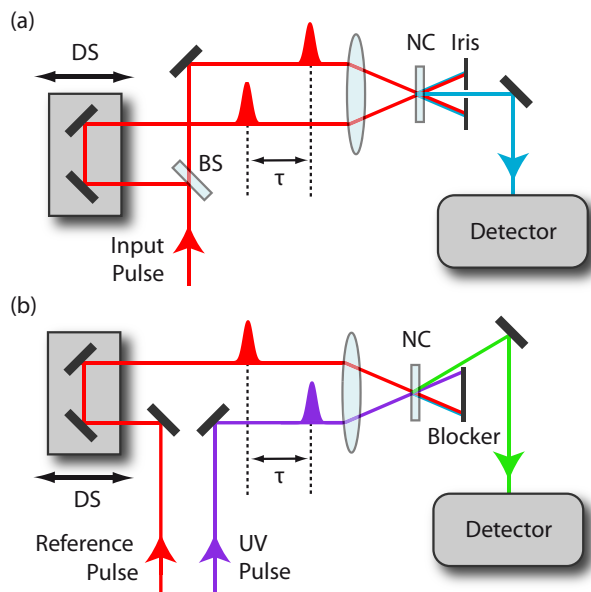
tral regimes [152, 153]. It should furthermore be mentioned, that the description of ultrashort laser pulses via their electric field in either the temporal or spectral domain (confer Sec. 2.1.1) does in most cases not provide an intuitive picture of the pulses' properties. However, so-called *joint time-frequency representations* (JTFRs) such as the Wigner, Husimi, or von Neumann distribution which connect time- and frequency-domain have proven to be valuable tools especially for the description of complicated pulses [40, 154–156]. Among many other techniques which are based on the acquisition of mixed time-frequency domain quantities, XFROG measurements can therefore be considered as an experimental way to obtain a JTFR providing a detailed and intuitive representation of the ultrashort light field.

The actual experimental setup is placed on a separate optical breadboard which can be integrated in the UV-pump/VIS-probe (confer Sec. 3.3) or UV-pump/MIR-probe detection scheme (confer Sec. 3.4), respectively, to characterize the pump pulses before carrying out TA measurements. The setup and its alignment is detailed in Ref. [129]. The UV pulses accumulate additional phase contributions when passing various optics on their way from the NOPA system to the sample [45]. Also possible changes in the spectral amplitude need to be taken into account. Accordingly, pump pulses need to be characterized at the actual sample position. Since this is not possible due to limited space around the latter, the optical path of the UV pulses towards the sample is mimicked by adding the missing optics in front of the characterization setup.

3.2.4 Supplementary spectroscopic methods

Besides the implements explained above, the basic instrumentation moreover comprises supplementary devices to investigate the basic spectroscopic properties of a sample and therewith prepare and complement a successful TA measurement. This includes spectrometers to investigate the sample's linear absorption characteristics in the UV to VIS regime (V-670 spectrophotometer, Jasco) and the IR regime (FT/IR-4100, Jasco). While the ultrafast time resolution in TA measurements enables the uncovering of photoinduced reaction pathways on a fs time scale, the overall temporal probing window is limited to several nanoseconds if only optical delay lines are employed. To extend this, both spectrometers are equipped with a 285 nm UV diode to detect changes in the respective absorption signatures upon long-term UV exposure. Other important devices are a fiber VIS spectrometer (HR2000+ combined with a QP400-2-SR fiber, Ocean Optics) which can be placed at varible positions in the experimental setup and a spectrofluorometer (FP-6300, Jasco) employed in Appendix A to record fluorescence spectra.

3.3 UV-pump/VIS-probe detection scheme

To study the photochemistry of diphenylcarbene in solvent mixtures in Chap. 4 as well as to complement measurements with MIR probe pulses when investigating the photoinduced

dynamics of a carbonyl-nitrosyl molybdenum complex in Sec. 6.2, the UV-pump/VIS-probe detection scheme is employed (confer light blue shaded area in Fig. 3.1). Its experimental implementation, including the generation of VIS to UV white-light probe pulses using a small portion of the fundamental CPA light, is discussed in the following.

Figure 3.5: Experimental setup used in UV-pump/VIS-probe measurements. The light blue shaded area includes instrumentation to spatially and temporally overlap UV-pump and VIS-probe pulses in a liquid flow cell, whereas a VIS spectrograph in combination with a thermoelectrically cooled CCD camera is used for spectrally-resolved detection of probe pulses. The latter are generated by focusing a small portion of the fundamental 800 nm light or its second harmonic into a linearly moving CaF_2 plate, producing a supercontinuum which covers the complete VIS spectral range. Even shorter wavelengths become accessible for probing when using 400 nm light for supercontinuum generation. The color assignment refers to Fig. 3.1. Note that the white box depicts the actual beam paths including all optics used. Figure adapted from Ref. [128].
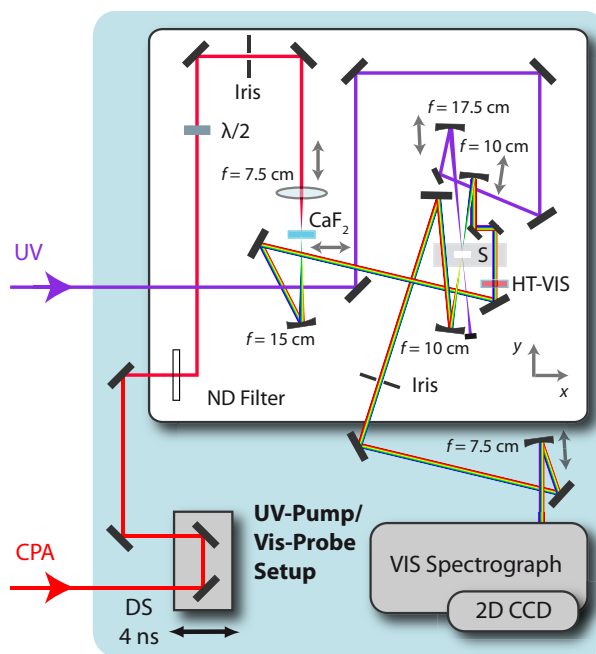
The detection scheme is depicted in Fig. 3.5. It was developed in its primal form in the dissertation of J. Buback [128] but was changed and extended several times with respect to experimental demands in various projects. To optimize the beams' overlap, the design aims at a small angle between the pump and probe beam to realize an almost collinear geometry. For clarity, Fig. 3.5 only shows optics and beam paths relevant for the present work. The setup contains optics to spatially and temporally overlap UV pump pulses stemming from the NOPA system (see Sec. 3.2.2) and supercontinuum probe pulses, which are generated in the detection scheme itself, in a sample cell. Before entering the TA setup, the UV pump pulses are shaped using an acousto-optic programmable dispersive filter (Dazzler, Fastlite [157]; device not shown in Fig. 3.1 or Fig. 3.5, respectively) in order to obtain compressed pulses at the sample position. Eventually, the transmitted probe beam is detected spectrally resolved on a shot-to-shot basis. For stability enhancement and dust protection, the inner part of the detection scheme (confer white area in Fig. 3.5) is encapsulated by housings which can be flooded with nitrogen to minimize the influence of the laboratory atmosphere.

Before and in the TA setup, the pump pulses are guided via UV enhanced aluminum mirrors in an all-reflective manner. For probe pulse generation, furthermore a small portion of the fundamental 800 nm CPA output enters the setup. Outside the detection scheme, the latter can be delayed by a motorized 60 cm linear translation stage (M-IMS600, Newport) which enables to scan a pump–probe range of 4 ns. Inside the detection

scheme, the beam can be regulated by a $\lambda/2$-plate and by an adjustable neutral density (ND) attenuator wheel. For measurements presented in Chap. 4, the beam (≈ 1 mW) is focused by a 7.5 cm lens into a linearly moving 5 mm CaF_2-plate to generate supercontinuum probe pulses with expedient spectral components down to ≈ 300 nm [20]. The movement reduces the local heat input and thereby protects the CaF_2-plate from being irreversibly damaged. Since even shorter probe wavelengths were required for experiments presented in Sec. 6.2, WLG in the same CaF_2-plate is also carried out using the second harmonic of the 800 nm fundamental beam as input. For this purpose, a BBO crystal and a shortpass filter (SPF) can be placed in front of the focusing lens (not shown in Fig. 3.5) to generate probe pulses with spectral components down to 275 nm accompanied by a strongly reduced intensity in the VIS regime. After WLG, the fundamental 400 or 800 nm beam is rejected by a HR-400 nm beam splitter or by a HT-VIS custom made filter (Laser Components), respectively. As used for the pump path, an all-reflective design is employed to guide the WLC via the sample towards the detection unit using UV enhanced aluminum mirrors. The last focusing mirrors ($f = 17.5$ cm pump, $f = 10$ cm probe) are placed on linear translation stages driven by micrometer screws to optimize the foci positions. The beams, focused to diameters of roughly 50 µm (pump) and 40 µm (probe), respectively, are spatially overlapped at the sample position, whereas the polarization directions are held at the magic angle configuration (54.7°) [158, 159]. For excitation, approximately 130 nJ pump pulses are applied (a XFROG measurement determined a pulse duration of 40 fs at the sample position), whereas the energy of the probe pulses is substantially lower. To exchange the probed sample volume between subsequent pump–probe pairs, a sample volume of typically 20 mL is perpetually pumped through a Suprasil flow cell of 200 µm pathlength using a micro annular gear pump (mzr-4605, HNP Mikrosystems). The flow cell is mounted on a 2D stage which can be translated in x-direction with a motorized linear actuator (Zaber technologies Inc.) and in y-direction with a manually adjustable micrometer screw (confer coordinate system in Fig. 3.5) allowing for fine-tuning and characterization of the beam radii at the sample position (see below). After the sample, an iris is used to clean the probe beam from scattering contributions of the pump beam.

In the measurement routine, the pump–probe delay is scanned up to 4 ns using linear step sizes within the first few picoseconds followed by exponential step sizes, whereas the average of 1000 consecutive difference spectra is recorded at each time delay. A spectrally-resolved detection of changes in optical density between the pumped and unpumped probe volume is enabled by using a visible spectrograph (Acton SP2500i, Princeton Instruments) combined with a 2D CCD camera (Pixis 2K, Princeton Instruments) with an acquisition rate of 1 kHz. Since the mechanical chopper blocks every other pump pulse, the calculation of pump-induced absorption changes is carried out between pairs of subsequent laser shots, i.e., between I_{pump} and $I_{\mathrm{no\ pump}}$:

$$\Delta OD(\lambda, \tau) = -\log_{10}\left[\frac{I_{\mathrm{pump}}(\lambda, \tau)}{I_{\mathrm{no\ pump}}(\lambda)}\right]. \tag{3.3.1}$$

The shot-to-shot processing of highly correlated laser shots significantly improves the

data quality since the influence of long-term laser fluctuations is minimized. Further information about the capabilities and specifications of the VIS spectrograph and the CCD camera are given in Sec. 3.4.2, whereby Table 3.1 summarizes settings employed in different parts of this thesis.

Before conducting a TA measurement, preparatory steps are necessary to ensure proper functionality of the experimental setup. Similar to the alignment and characterization procedure of the UV-pump/MIR-probe detection scheme which will be detailed in Sec. 3.4.2, this is based on the possibility to place additional optical devices at exactly the sample's position. A typical preparation procedure includes the following steps: first, a pinhole at the sample's position is employed to find spatial overlap between the pump and probe beam; second, by using a knife edge the beam radii at the sample position can be determined and adjusted where necessary [160, 161]; third, to fine-tune the spatial overlap and to determine time zero, meaning the setting of the pump–probe delay stage for which both beams temporally coincide in the sample, a pump–probe measurement of a test sample with well-known spectroscopic properties or a measurement in pure solvent can be conducted. The latter can furthermore be utilized to distinguish between signal contributions stemming from the sample and the solvent, respectively, and to determine the time resolution of the pump–probe detection scheme as was shown in the literature [20]. The time resolution of the present setup is on the order of 50 fs.

3.4 UV-pump/MIR-probe detection scheme

In Chap. 6, the vibrational dynamics of metal complexes containing small messenger molecules are studied using the UV-pump/MIR-probe detection scheme (confer Fig. 3.1). Regarding the signal detection, direct multichannel detection based on a mercury-cadmium telluride (MCT) array is used in Sec. 6.1, whereas chirped-pulse upconversion (CPU) is employed in Sec. 6.2. As indicated by the yellow-shaded area in Fig. 3.1, CPU can be considered as an extension for an existing setup based on MCT detection. The experimental implementation of the UV-pump/MIR-probe detection scheme with the possiblity to detect the MIR probe pulses before and after upconversion to the VIS regime is detailed in this section. At this, the fundamental CPA output is used to generate MIR probe pulses in a optical parametric amplifier (OPA) and a strongly chirped pulse (CP) in a stretcher.

3.4.1 MIR pulse generation

Within this thesis, the generation of ultrashort MIR pulses was realized with the setup schematically depicted in Fig. 3.6. Its construction was carried out within the framework of D. Wolpert's dissertation [88]. The layout, derived from Hamm *et al.* [93] and well-known for its high stability [94], includes a WLG stage, the output of which serves as seed radiation for two subsequent OPA stages pumped by the fundamental CPA output, as well as a DFG stage to eventually generate MIR radiation. Aiming at the highest stability

achievable, a detailed tutorial on how to optimally align the setup, henceforth denoted as MIR-OPA (mid-infrared optical parametric amplifier), can be found in Ref. [129]. Spectra illustrating the wide spectral tunability of the MIR-OPA's output are presented in Ref. [88]. In the following, the MIR-OPA's working principle is briefly summarized.
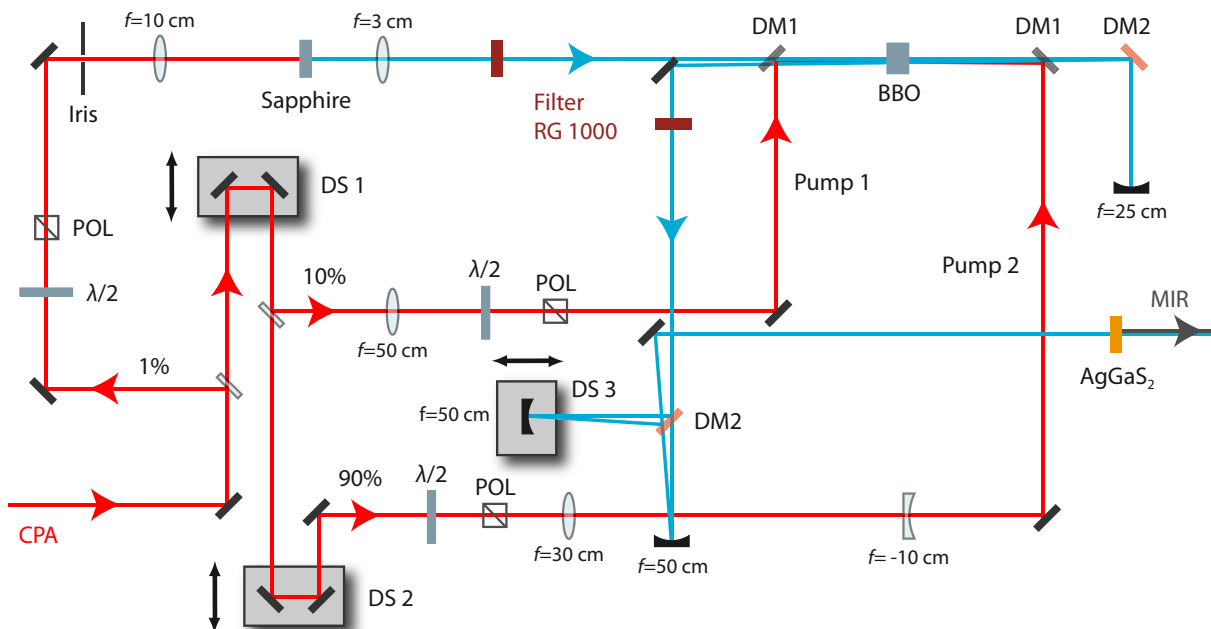

Figure 3.6: Generation of tunable MIR pulses. Schematic depicts the home-built two-stage OPA with subsequent difference-frequency generation stage following the design of [94]. Specifications and further details are given in the text. Figure reprinted with minor modifications from Ref. [88].

A portion of approximately 250 mW of the fundamental 800 nm CPA radiation is required to operate the MIR-OPA. This fundamental beam, which in this particular experimental arrangement is the residual beam of the UV-OPA's fundamental SHG process, is split into three fractions with different pulse energies. The smallest portion (approximately 1% of the total input energy) is focused by a 10 cm lens into a 4 mm sapphire disk for WLG. The resulting white-light continuum (WLC) is recollimated and focused into the 1st OPA stage with a 3 cm lens. Since a stable WLC is a crucial prerequisite for the performance of each of the subsequent nonlinear processes, the generation of multiple filaments has to be avoided. For this purpose, the power used for WLG is fine-tuned by a half-wave plate combined with a polarizer (POL). Likewise when being used to regulate the power in the MIR-OPA's pump paths, this combination furthermore sets the beam polarizations required in subsequent OPA processes.

In the first amplification step, one pump beam (approximately 10% of the total input energy), focused by a 50 cm lens, is superposed with the NIR part of the WLC seed beam in a 4 mm type II BBO crystal ($\theta = 27°$, $\phi = 30°$). Prior to this, a red glass (RG) 1000 filter blocks parts of the WLC spectrum with wavelengths shorter than 1 μm. To achieve maximum amplification and at the same time avoid WLG in the BBO, the 800 nm pump power is regulated properly. To collinearly superpose the pump and WLC

Figure 3.7: Setting the MIR-OPA's central wavelength. Spectral dependence of signal and idler versus the wavelength and wavenumber of the desired DFG signal, respectively. According to Eqs. (3.4.3) and (3.4.4), data is simulated for MIR spectra within the tuning range of the home-built two-stage OPA, whereas the wavelength of the fundamental CPA output is defined to be 800 nm.
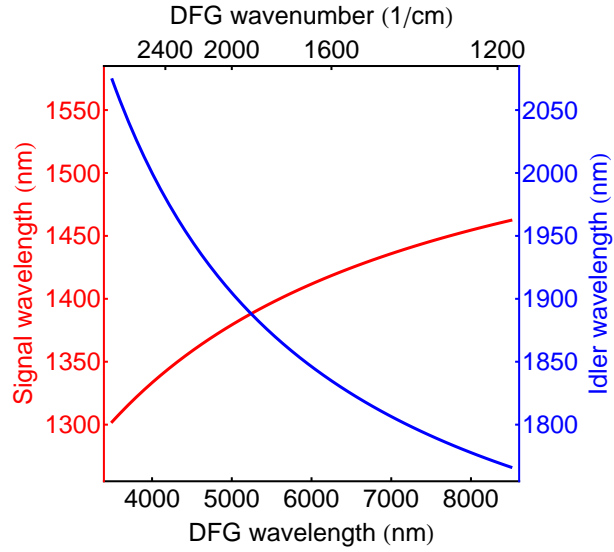
beam, a dichroic mirror (DM 1) is used, whereas the corresponding time delay is controlled by a delay stage (DS 1). As a result of the 1st OPA stage, a signal beam is generated which is further amplified in the 2nd OPA stage, whereas the nascent idler beam is filtered out by a dichroic mirror (DM 2). Which part of the WLC spectrum is amplified in the OPA process forming the signal field is determined by the phase-matching configuration of the BBO. The latter can easily be adjusted by rotating the crystal, thereby selecting a certain phase-matching angle θ. Since energy conservation needs to be fulfilled in the OPA process, a fixed relation between the wavenumber of the signal, idler, and CPA input is given:

$$\tilde{\nu}_{\text{CPA}} = \tilde{\nu}_{\text{signal}} + \tilde{\nu}_{\text{idler}} \ . \tag{3.4.1}$$

Likewise in the DFG process, energy conservation needs to be fulfilled:

$$\tilde{\nu}_{\text{DFG}} = \tilde{\nu}_{\text{signal}} - \tilde{\nu}_{\text{idler}} \ . \tag{3.4.2}$$

Thus, the final spectral position of the MIR output is already determined in the 1st OPA stage by selecting a certain signal or idler wavenumber, respectively. Two useful relations for the MIR-OPA's alignment can be derived by combining 3.4.1 and 3.4.2:

$$\tilde{\nu}_{\text{DFG}} = 2\tilde{\nu}_{\text{signal}} - \tilde{\nu}_{\text{CPA}} \ , \tag{3.4.3}$$

$$\tilde{\nu}_{\text{DFG}} = \tilde{\nu}_{\text{CPA}} - 2\tilde{\nu}_{\text{idler}} \ . \tag{3.4.4}$$

For a fixed CPA input wavelength of 800 nm, the relations 3.4.3 and 3.4.4 are visualized in Fig. 3.7.

In the 2nd OPA stage, the signal beam from the 1st OPA stage, collimated by a concave gold mirror with a focal length of 25 cm, is collinearly superposed with the second pump beam (approximately 90% of the total input energy) within the same BBO used in the

1st OPA stage. A small vertical displacement with respect to the interaction region of the 1st OPA stage is selected. To match the beam waist of the collimated signal beam and the pump beam, a 1:3 telescope is used to reduce the beam diameter of the fundamental beam. After finding temporal overlap via another delay stage (DS 2), using a dichroic mirror (DM 1) for spatial superposition, and appropriately regulating the pump power, again a signal and an idler beam emerges. Corresponding pulse energies are significantly higher with respect to the 1st OPA stage.

Since signal and idler beams are polarized perpendicular to each other, a type I AgGaS$_2$ (silverthiogalate, $\theta = 39°$, $\phi = 45°$) crystal with a thickness of 1 mm is used in the final DFG stage. Prior to the process of MIR generation, residual light from the 2nd OPA stage is removed by another RG 1000 filter and a dichroic mirror (DM 2) is used to spatially separate the signal and idler beam. With this, the temporal displacement of both components due to GVD in the BBO crystal can be compensated for using a delay stage (DS 3). Spherical gold mirrors with a focal length of 50 cm are used to focus the signal and idler beams into the DFG crystal. Having the MIR-OPA properly aligned, MIR laser pulses with an energy of up to 600 nJ tunable in a spectral range of (4-10) µm can be created.

3.4.2 Experimental implementation

Figure 3.8 illustrates the experimental implementation of the UV-pump/MIR-probe detection scheme. Main parts of this setup including the MIR-OPA are surrounded by housings which can be purged with dry air in order to minimize the influence of water vapor absorption on the MIR beam path. Before discussing the CPU extension, the standard direct multichannel MCT detection scheme (blue shaded area in Fig. 3.8) will be detailed in the following. Please note that these explanations are strongly related to Sec. 3.3 in which the implementation of the UV-pump/VIS-probe detection scheme was detailed. However, both parts can be read independently.

Two beams enter the setup's outset: the UV pump pulses stemming from the NOPA (confer to basic instrumentation discussed in Sec. 3.2.2) and the residual NOPA 800 nm CPA beam which is used to power the MIR-OPA (confer 3.4.1) generating the probe pulses. The time delay between both pulses is controlled via a motorized 60 cm linear translation stage (M-IMS600, Newport) which enables to scan a pump–probe range of 4 ns. Having the UV pump (500 Hz) and the MIR probe (1 kHz) pulses with variable time delay at hand, optics are required to adjust the spatial overlap of both beams in the sample. The lower white box in Fig. 3.8 illustrates the actual beam paths. Concerning the MIR path, only reflective optics with gold coatings are used to guide the beam from the MIR-OPA via the sample to the detection unit. Directly after the MIR-OPA, a germanium longpass filter (LPF, high transmission for $\lambda > 2.4$ µm) is used to remove the residual signal and idler beam. A 50 cm spherical concave mirror is used to recollimate the MIR-OPA output. To achieve a 60 µm beam waist at the sample position, a 1:5 telescope is used to widen the beam before focusing. The actual spot size can be adjusted by moving the sample stage along the x-direction via a micrometer screw (confer coordinate system
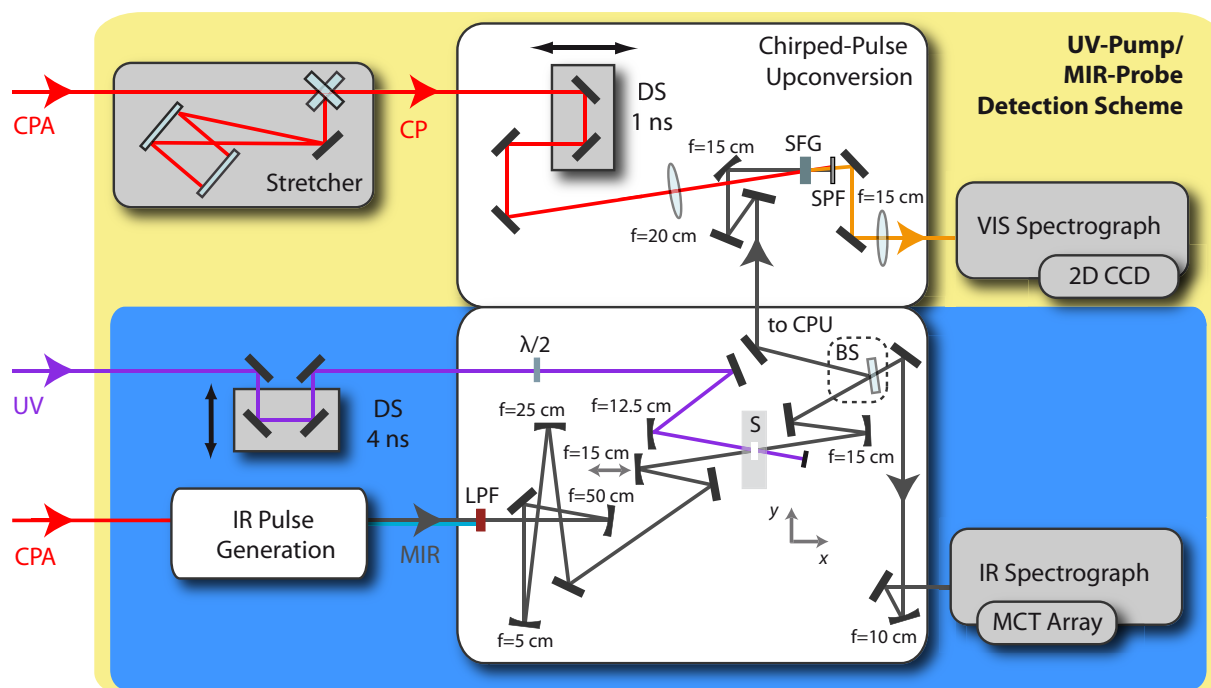
Figure 3.8: Experimental setup used in UV-pump/MIR-probe measurements. The blue shaded area includes instrumentation to spatially and temporally overlap UV-pump and MIR-probe pulses in the sample cell, whereas direct multichannel MCT detection is used for spectrally-resolved detection of probe pulses. For using chirped-pulse upconversion and direct multichannel MCT detection simultaneously (yellow shaded area), a 50/50-beam splitter (BS) is added to the MIR path guiding the probe pulses to a SFG assembly, the output of which is dispered by a VIS spectrograph and detected by a 2D CCD camera. The color assignment refers to Fig. 3.1. Note that the white boxes depict the actual beam paths including all optics used.

in Fig. 3.8). After passing the sample, the probe pulses are recollimated and, depending on the detection method, focused into the IR spectrograph or guided to the CPU scheme. Placed on a linear translation stage driven by another micrometer screw for fine-tuning, a spherical UV enhanced aluminum mirror ($f = 12.5$ cm) is used to achieve a pump beam focus of typically 85 µm at the sample position. A $\lambda/2$-plate in the pump path is further used to adjust parallel or magic angle (54.7°) polarization directions.

The sample cell consists of a pair of BaF_2 or CaF_2 windows with a thickness of 2 or 4 mm each (Omni-cell, LOT Oriel) which are highly transmissive from the UV to the MIR spectral region. The optical path length between the cuvette windows is defined by a teflon spacer with a thickness of 100 or 200 µm. To continuously exchange the sample volume in the pump–probe interaction region between successive excitations, a peristaltic pump (Masterflex L/S, Cole Parmer) pushes the dissolved sample (typically a total of 20 mL) through the tubing system and the cuvette, respectively. Apart from holding the sample cuvette in a defined distance from the last MIR focusing mirror (see above), the sample stage facilitates a manifold of preparatory steps to enable a successful TA measurement with MIR probe pulses. Any of these steps is based on the possibility to

place additional optical devices at exactly the sample's position. A typical preparation procedure includes the following steps: first, by using a knife edge and a motorized linear actuator (Zaber technologies Inc.) which can move the entire sample stage along the y-direction (confer coordinate system in Fig. 3.8), the beam radii at the sample position can be determined and adjusted where necessary [160, 161]; second, a pinhole at the sample's position is employed to find spatial overlap between the pump and probe beam; third, to fine-tune the spatial overlap and to determine time zero, meaning the setting of the pump–probe delay stage for which both beams temporally coincide in the sample, a thin silicon or germanium wafer is used to conduct a cross-correlation measurement between the UV pump and the MIR probe pulses [162]. Due to the seminconductor's quasi instantaneously rising MIR absorption upon UV excitation, this method can further be exploited to determine the time resolution of the UV-pump/MIR-probe detection scheme which ranges around 400 fs for experiments presented in this work. Further details on this preparatory steps are described elsewhere [129].

As mentioned above, the MIR pulses after passing the sample can either be guided to the IR spectrograph or the CPU scheme. For a direct juxtaposition, a KBr window is used to equally split the probe beam in order to use both detection methods simultaneously. A description of both detection methods including the implementation of the CPU scheme is given in the following, whereas denoted specifications refer to settings used in the comparative study which will be presented in Sec. 5. With minor deviations which are highlighted at the respective position, these settings are also valid for measurements presented in the Secs. 6.1 and 6.2, when using the UV-pump/MIR-probe detection scheme to investigate the ultrafast photochemistry of CO- and NO-releasing molecules. Note that with both detection methods, changes in optical density are calculated on the basis of 1 kHz single-shot readout according to Eq. (3.3.1), analogous to the data processing described in Sec. 3.3.

Direct multichannel MCT detection

One half of the probe beam is dispersed by a 150 grooves/mm grating (4.0 μm blaze wavelength) in an IR spectrograph (250 is/sm - Chromex, 4.9 μm central calibration wavelength) and detected by a 32 element MCT-array (InfraRed Associates, Inc.), resulting in a bandwidth of 10.2 nm (corresponding to $4.2 \, \mathrm{cm}^{-1}$ at the given central wavelength) per pixel. The signals of individual MCT pixel are amplified by a 32-channel preamplifier (MCT-3200, Infrared Development Corporation). Before analog to digital conversion using a National Instruments PCI-6033E card, the signals are processed in a home-built 32-channel sample and hold integrator.

Chirped-pulse upconversion (CPU)

The second half of the probe beam gets upconverted to the VIS regime: for this, the MIR signal (pulse energies of several hundred nJ), focused by a 90° off-axis parabolic mirror (152 mm effective focal length), is mixed with the 18 μJ chirped NIR pulse (CP, centered

Table 3.1: Settings of the visible spectrograph and the CCD camera employed in different parts of this thesis. In particular, the employed grating represented by its corresponding groove density and blaze wavelength, the central detection wavelength, the detection mode, and the resulting bandwidth per data point are given. For detection, either 1 kHz shot-to-shot readout is used (mode B) with a binning of 2 (8) adjacent pixels resulting in a total number of 1024 (256) data points or, for low-speed measurements when typically averaging over 300 ms of exposure time, all 2048 horizontal pixels are used separately without binning (mode A). The spectrometer is further employed to detect MIR spectra after upconversion to the VIS region (CPU).

Section	grating, λ_{blaze} (nm)	λ_{central} (nm)	mode	bandwidth per pixel (nm)
3.4.3	1200 g/mm, 750	690	A-2048-CPU	0.019
	1200 g/mm, 750	710	A-2048-CPU	0.019
4.3.2	150 g/mm, 300	429	B-256	1.4
5.2 and 5.3	1200 g/mm, 750	690	A-2048-CPU	0.019
	1200 g/mm, 750	690	B-1024-CPU	0.038
6.2	1200 g/mm, 750	690	B-1024-CPU	0.019
Appendix A	150 g/mm, 500	500	A-2048	0.18

at 12538 cm^{-1}, FWHM 143 cm^{-1}) in a noncollinear SFG arrangement ($\approx 7°$) using a MgO(5%):LiNbO$_3$ crystal (10 x 10 mm^2 x 0.45 mm, type I, 45.4° cut, Castech Inc.). To produce the CP required for upconversion, a small portion of the CPA output is split off and sent through a home-built *Treacy-type* compressor of another available CPA laser system. As a result, a downchirped CP is used, in contrast to other implementations reported in the literature [105]. As discussed in Sec. 2.5, the time delay between the CP and the MIR pulse determines the frequency of the CP which is used for upconversion. For this purpose, a motorized 10 cm linear translation stage (MT-85, Micos) is used to temporally shift the CP. Since the UV-pump/MIR-probe time delay can be controlled via a separate translation stage in the UV path (see above), no changes in CP time delay are necessary when recording TA data. For fine-tuning of the phase-matching conditions, the CPU crystal mount can be rotated in order to change the angle between the incident beams and the optical axis of the crystal in a well-defined way. The residual CP is rejected by a 750 nm shortpass filter (SPF) and a 15 cm lens is used to recollimate the CPU signal. A VIS 50 cm focal length spectrograph (Acton SP2500i, Princeton Instruments) in combination with a thermoelectrically cooled 2048 x 512 pixel front-illuminated CCD camera (Pixis 2K, Princeton Instruments) is used for the detection of VIS spectra. For low-speed measurements, 20 pixels are vertically binned and averaged over typically 300 ms (mode A). An additional binning of 2 (8) adjacent horizontal pixels enables single-shot data acquisition of single-line spectra of 1024 (256) pixels (mode B). Note that the identical combination of spectrograph and CCD camera is also used in the UV-pump/VIS-probe detection scheme described in Sec. 3.3 and the fluorescence detection scheme which will be introduced in Sec. 3.5. Table 3.1 summarizes spectrometer settings used in different parts of this thesis.

3.4.3 Calibrating the CPU detection scheme

In Sec. 2.5 it was shown that CPU spectra are affected by cross-phase modulations between the CP and MIR field if the latter contains narrow spectral features [24]. Required for the correction procedure, the second-order spectral phase parameter of the CP can be determined by recording a frequency-resolved cross correlation between the CP and the MIR pulse [126].
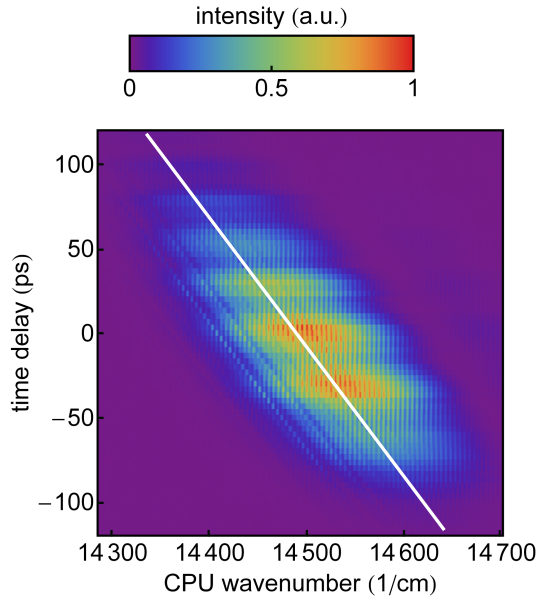
Figure 3.9: Spectrogram visualizing raw CPU spectra for varying CP time delay. In particular, MIR spectra centered around 5 μm are cross-correlated with the CP in a MgO:LiNbO$_3$ crystal, whereby the CP time delay is scanned over 250 ps. Following water vapor absorption signatures, the second-order spectral phase parameter of the CP is given by the slope of the depicted white line, which directly reflects changes in the CP momentary frequency for different time delays. See text for further explanations.

The corresponding spectrogram (Fig. 3.9), which is obtained *in situ*, i.e., without changes in the optical alignment, by recording raw CPU spectra (mode A) for CP time delays scanned over the full duration of the CP, directly reveals the instantaneous frequency and amplitude of the CP. For the case of sufficiently large chirp (confer Sec. 2.1.4), the second-order spectral phase parameter can directly be recovered from the spectrogram since the CP time delay linearly translates into a frequency shift of the complete CPU spectrum:

$$b_2 = \frac{\Delta t}{\Delta \omega_{\mathrm{CPU}}} \ . \tag{3.4.5}$$

This is particularly apparent when following the spectral shift of spectrally narrow features in CPU spectra such as water vapor absorption signatures. The slope of the white line in Fig. 3.9 reveals $b_2 = -3.97$ ps^2. Due to the fixed geometry of the stretcher used to generate the CP, this value is valid for all measurements presented in this thesis as verified several times.

Figure 3.10 illustrates the correction produre which is applied to every individual CPU spectrum (mode A and B). The raw CPU spectrum [Fig. 3.10(a)] exhibits a strong oscillatory behavior over almost its complete bandwidth. A Fourier transform reveals a distinct contribution at approximately 6.8 ps [Fig. 3.10(b), red]. Given the crystal thickness of 450 μm and a refractive index of approximately 2, this feature can be assigned
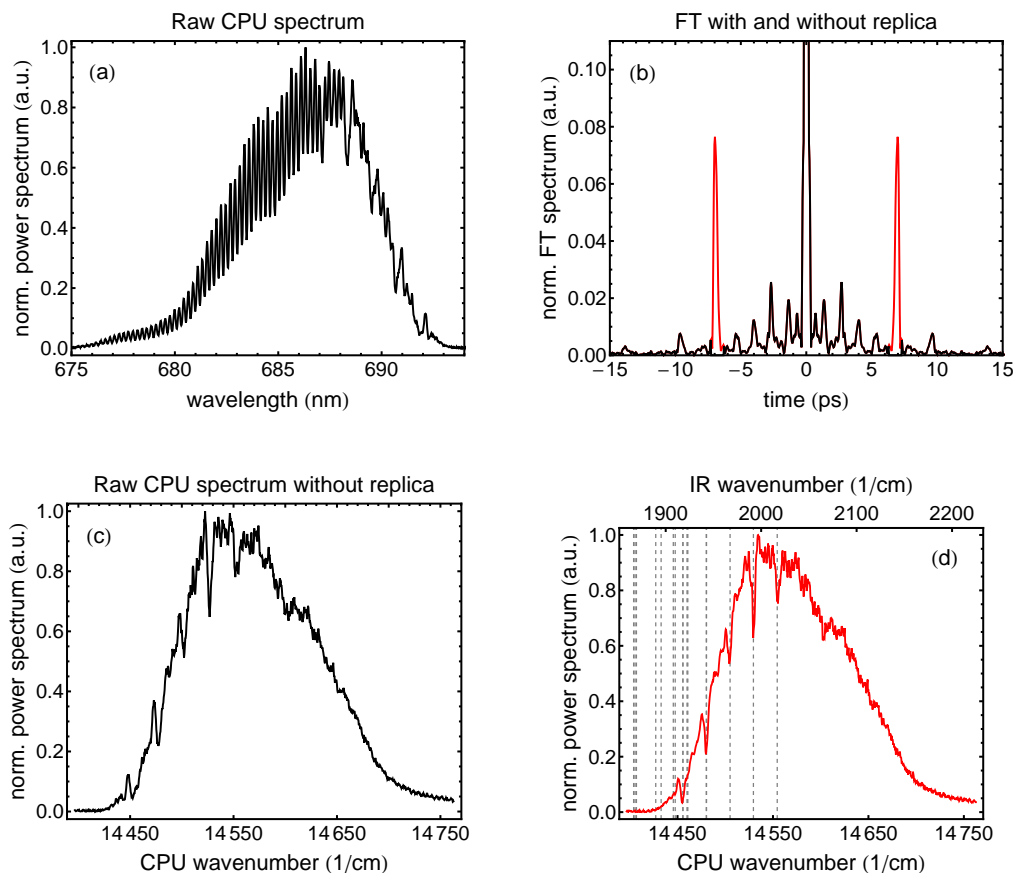
Figure 3.10: Calibrating the CPU detection scheme. (a) Raw CPU spectrum detected in mode A (confer Table 3.1). (b) Fourier transform spectra of (a) before (red) and after (black) removal of a pulse replica at 6.8 ps which originates from reflections in the upconversion crystal. (c) Raw CPU spectrum after Fourier filtering the pulse replica. (d) Corrected CPU spectrum after Fourier filtering, removal of cross-phase modulations [24], and wavenumber calibration exploiting the known spectral positions of atmospheric absorption lines [163].

to a pulse replica traveling back and forth in the upconversion crystal after twice being reflected internally. Consequently, the oscillatory structure is due to spectral interference between the main pulse and the pulse replica. After removing the feature at 6.8 ps by Fourier-filtering in an area of 1 ps [Fig. 3.10(b), black], the CPU spectrum exhibits a smooth shape interrupted by distortions around narrow spectral features which are due to cross-phase modulations [Fig. 3.10(c)]. Since $\tilde{\nu}_{\mathrm{CP}}$, the wavenumber of the CP used for upconversion, determines the relation between the CPU and the IR wavenumber axis:

$$\tilde{\nu}_{\mathrm{IR}} = \tilde{\nu}_{\mathrm{CPU}} - \tilde{\nu}_{\mathrm{CP}} \ , \tag{3.4.6}$$

it is convenient to include both axes to visualize the CPU spectrum. However, there is

an ambiguity in $\tilde{\nu}_{\mathrm{CPU}}$ since the cross-correlation measurement (see above) does not reveal the absolute time delay between the CP and the MIR pulse. To determine $\tilde{\nu}_{\mathrm{CP}}$, again the influence of water vapor in the laboratory atmosphere on MIR spectra can be exploited. Calibration can be done by shifting the CPU wavenumber axis with respect to the IR wavenumber axis defined by precisely catalogued absorption lines [163]. Though less precise due to typical spectral widths, it is also feasible to employ the absorption features of a dissolved sample in the flow cell. This can be beneficial in spectral regions in which the atmospheric absorption signatures are either too crowded or too weak, thus preventing a clear assignment. The final phase-corrected CPU spectrum is shown in Fig. 3.10(d). For the sake of completeness, it is mentioned that within this thesis a uniform frequency grid was used for processing CPU spectra, which can easily be obtained by resampling the spectrometer calibration [164]. However, since upconversion significantly reduces the relative bandwidth compared to direct MIR detection, a direct fast Fourier transform (FFT) appears to be sufficient for most applications [24].

3.5 Fluorescence detection scheme

The methods described above aim at the elucidation of photoinduced dynamical processes taking place in the excited state of a molecular system. This is done by monitoring the temporal evolution of the molecule's absorption characteristics. Another way to access the excited state of a molecular system is fluorescence spectroscopy (confer Sec. 2.3), which is often used to complement TA measurements. While fluorescence spectra *per se* do not contain direct temporal information about the spontaneous emission (fluorescence), methods such as *fluorescence upconversion* enable fs time resolution by *gating* the fluorescence in a NC with an ultrashort laser pulse [165, 166]. Besides time resolution in the detection step, it is also conceivable to have time resolution in the excitation step by involving more than just a single excitation pulse. One laser pulse could for example be employed to pre-excite the molecular ensemble, whereas a second one triggers the fluorescence after a defined time delay. This is strongly related to other quantum control experiments in the liquid phase, since changes in the fluorescence yield can be defined as a control objective [167–169]. Experimentally, it is straightforward to integrate a fluorescence detection scheme into an existing pump–probe setup, as done for the UV-pump/MIR-probe detection scheme introduced in Sec. 3.4.

Figure 3.11 shows a photography of the fluorescence detection scheme in pump–probe geometry. One the right side, the sample cuvette as well as the mirrors which are used for focusing of the pump and probe beam, respectively, are depicted. Both beams enclose only a small angle when passing through the sample. As mentioned above, the cuvette provides a thin film of dissolved sample which is perpetually exchanged. The detector consists of two microscope objectives (Plan N 4X/0.10, Olympus; 19.3 mm working distance) collinearly placed on a stage with a fixed distance of approximately 4.5 cm in opposite directions. In order to miminize contributions from scattered pump light, the fluorescence detector itself (left) is aligned in the plane spanned by the pump and probe
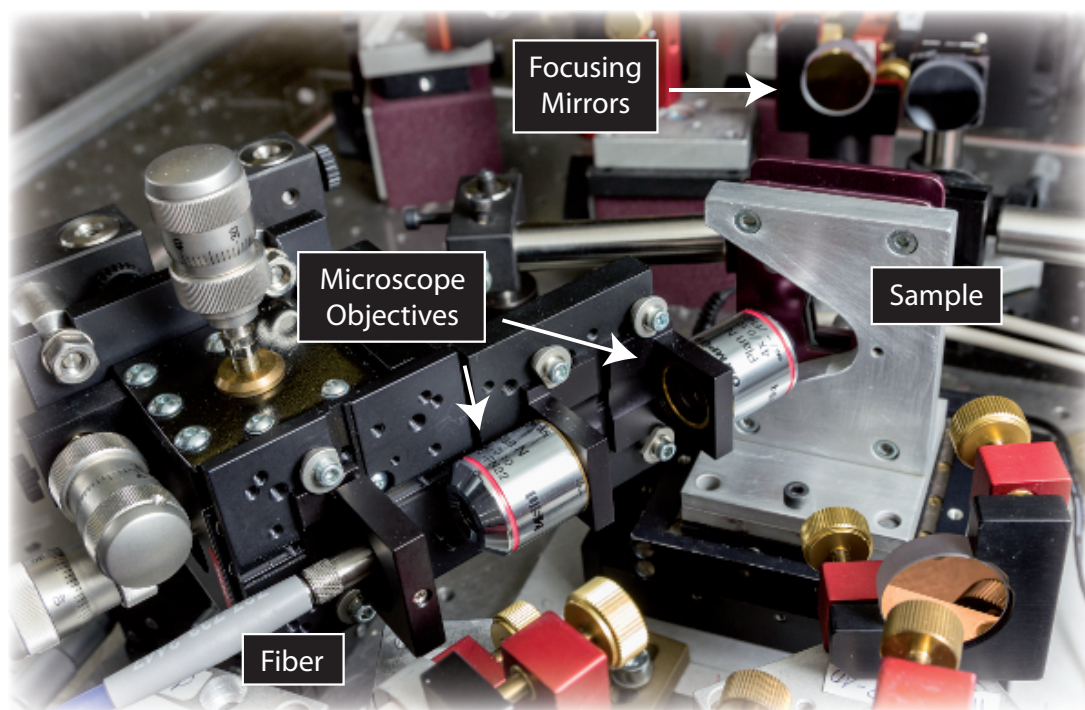
Figure 3.11: Combining transient absorption and fluorescence spectroscopy. A fluorescence detector (left) consisting of two microscope objective is placed besides the sample cuvette (right) of the UV-pump/MIR-probe detection scheme described in Sec. 3.4. After collection and collimation with one objective, a second one focuses the fluorescence into an optical fiber.

beam at an angle of approximately 45° with respect to the pump beam. A recess in the sample holder enables to place the excitation spot in the focal point of the overhanging microcope objective. Hence, one microscope objective can be used to collect and collimate a particular solid angle of the isotropic fluorescence, whereas the second microscope objective focuses the signals into an optical fiber (QP400-2-SR, Ocean Optics), which finally guides the signals to a VIS spectrometer (the same combination of VIS spectrograph and CCD camera that was detailed in Sec. 3.3 and 3.4). For fine-tuning, the entrance of the fiber is placed on a three-dimensional (3D) translation stage which is adjustable relative to the microscope objectives. For a coarse preadjustment, the complete detector is placed on a separate 3D translation stage. After proper alignment, the setup allows for 1 kHz shot-to-shot detection of fluorescence spectra, whereby both the UV as well as the MIR beam can be involved in the excitation step. A characterization of the detector's capabilities as well as a discussion on possible applications can be found in Appendix A.

Tracing primary processes of diphenylcarbene in solvent mixtures

It has been demonstated in a variety of so-called *quantum control* or *coherent control* experiments [170–178] that the usage of tailored laser pulses is one way to control chemical reactivity, e.g., to influence the outcome of a photochemical reaction by enhancing or suppressing certain reaction paths [169]. For instance, feedback-optimized laser pulses have been applied to control the reaction of bond-formation among small molecules in an adsorbate [179]. In contrast to adapting the light fields for a desired control goal, one might also think of a tailored solute environment to steer ultrafast reactions. The special importance lies on its dual role: one the hand, the solvent environment may determine a photochemical reaction's speed as well as the yield of different pathways; on the other hand, solvent molecules may also be involved in the course of the reaction. Both is true for the ultrafast photochemistry of diphenylcarbene (Ph_2C), a system which illustrates the interplay between competing reactions mediated by solute-solvent interactions in a particularly dramatic fashion. The presented results will be published in Ref. [1].
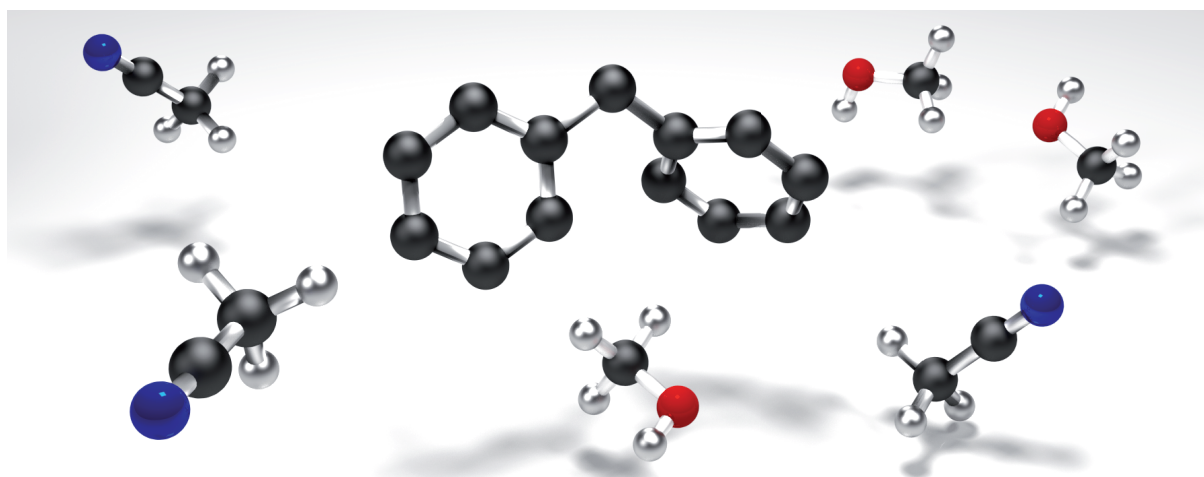
Diphenylcarbene in a mixed MeOH/MeCN solvent environment.

4.1 Introduction

Carbene chemistry is a multifaceted research area by virtue of the highly spin-dependent reactivity of carbenes [180]. Various spectrocopic investigations ranging from laser flash-photolysis [181–191], matrix-isolation studies [192] to ultrafast measurements in different environments [108, 193–200] have unveiled the role of carbenes as intermediates in (photo)chemical reactions. In particular, the reactivity of diphenylcarbene (diphenyl-methylene, Ph_2C) intrigues researchers owing to the simplicity of the system accompanied by the variety of possible reaction pathways depending on whether the spin-configuration is either a singlet or a triplet state [201–203]. Singlet carbenes are assumed to insert between O-H bonds, whereas triplet carbenes insert between C-H bonds. Studies by Eisen-thal and coworkers [181–190] have pioneered many aspects of Ph_2C reactivity in solution, e.g., effects of solvent polarity and selected cosolvents, but without the direct spectro-scopic observation of the singlet $^1Ph_2C$. This was possible in ultrafast studies, performed initially by the Chergui group [193] and further extended by Kohler and coworkers [194] in different solvents. The latter revealed that UV excitation of the diazo-compound precursor diphenyldiazomethane (Ph_2CN_2; see Fig. 4.1 for molecular structure) leads to formation of $^1Ph_2C$ on a sub-picosecond time scale, which can further react via intersystem crossing (ISC) to the triplet $^3Ph_2C$ in a few hundreds of picoseconds in aprotic solvents. However, if $^1Ph_2C$ is allowed to react with alcohols, an ultrafast intermolecular proton-transfer can occur, leading to an intermediate benzhydryl cation (Ph_2CH^+), and eventually to a diphenylalkyl ether. Kirmse and Steenken [191, 204] inferred that two alcohol molecules are needed for the protonation. Others postulated a concerted reaction pathway, possibly involving an intermediate ylide [205–207]. Recent findings in matrix-isolation experiments at low temperatures provided additional aspects of diphenylcarbene reactivity: in argon matrices doped with 0.5–1% methanol (MeOH), $^1Ph_2C$ (in contrast to $^3Ph_2C$) forms a hydrogen-bonded complex with a MeOH molecule, hence refuting the assumption of a general triplet ground state [21]. Whereas similar results have been found when replacing the MeOH dopants by water molecules, an amorphous water environment enabled the isolation of stable Ph_2CH^+ without the need for superacidic conditions [22].

Figure 4.1: Molecular structure of diphenyldiazomethane (1).
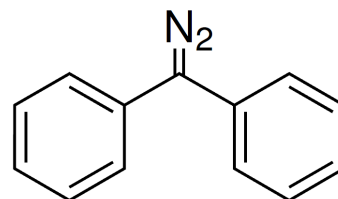
The possible reaction channels of $^1Ph_2C$ accessible under different conditions will compete with each other when the solvent environment is systematically varied. In this chapter, results from hybrid Quantum Mechanics/Molecular Mechanics (QM/MM) calculations are complemented by advanced femtosecond pump–probe spectroscopy to unravel the fate of $^1Ph_2C$ in binary mixtures of the protic solvent MeOH and the aprotic acetonitrile (MeCN) at room temperature. By going from pure MeOH to pure MeCN, a

tailored solvent environment with variable distances between the carbene and the alcohol molecules is created, also aimed at "mimicking" the MeOH doping of the matrix-isolation studies. The joint theoretical and experimental investigation directly visualizes the interplay and competition of the solvent molecules in the mixtures, discloses the amount of solvent molecules necessary for certain reaction pathways and allows to propose a concerted reaction pathway that involves an intermediate complex ^{1}Ph$_2$C··HOMe. The results emphasize that ultrafast photodynamics in solvent mixtures are more than just a linear combination of the behavior in pure solvents, and that having just few instead of abundant molecules of a certain solvent in the vicinity of the solute may be beneficial for a desired reaction outcome.

4.2 Methods and materials

Hybrid QM/MM calculations, performed by the group of Dr. Elsa Sánchez-García at the Max-Planck-Institut für Kohlenforschung in Mülheim an der Ruhr, were employed to capture the solvent effects and the specific interactions governing the stability of Ph$_2$C. Methodological details on parametrizations and optimizations are given in the Appendix B.1. The radial distribution functions of solvent molecules confirmed the structure involving hydrogen-bonds in pure MeOH and the absence of a well-structured solvent arrangement in pure MeCN. For the mixtures, the simulations indicate the absence of phase separation or aggregation, which is in line with rather weak preferential solvation, as reported in the literature [208]. In TA experiments, UV pump light is used to generate Ph$_2$C via photolysis of the diazo-compound precursor diphenyldiazomethane (**1**, CAS: 883-40-9; for details of synthesis, which has been done by Paolo Costa, see Appendix B.2). 6 mM solutions were employed resulting in an optical density of about 2 at 285 nm along the sample cells of 200 µm thickness. Even small fluctuations in the sample concentration would lead to changes in the absolute absorption change signals and therefore affect the comparison of quantitative values such as the amount of Ph$_2$CH$^+$ produced in different solvent environments. Hence, a MeOH and a MeCN parent solution was used, each containing 294 mg Ph$_2$CN$_2$ in 13 ml solvent. Despite the high concentration in the latter solutions, no problems regarding solubility have been observed. For each 20 ml sample solution, 1 ml of the corresponding parent solution was extracted using a volumetric pipette. Which parent solution is taken is determined by the desired solvent ratio. For the present study, concentrations between 0 to 90% MeCN were prepared using the MeOH parent solution, whereas the MeCN parent solution was the starting point for solutions containing 95 to 100% MeCN. To finally obtain the sample solutions under investigation, missing solvent was separately extracted using volumetric pipettes and added to the 1 ml of parent solution. Solvents (Merck Millipore, Uvasol$^®$) were used as received. All samples examined were prepared for equal molarity although the molar masses of MeOH and MeCN significantly differ. Albeit both solvents have approximately the same density, the ratio of the actual number of solvent molecules of each sort differs from the associated volume ratio. Proper sample exchange was ensured by cleaning the tubing system after

recording each data set with a pure solvent mixture which corresponded to the subsequently examined sample mixture. Details on spectrosopic methods employed in this chapter can be found in Chap. 3. The TA setup (285 nm pump pulses, VIS white-light probe pulses) in particular is detailed in Sec. 3.3. TA measurement times were kept sufficiently short to prevent major sample-degradation due to continuous photolysis of the precursor, as verified by measurements of the linear absorption spectrum. All data shown results from averaging over three subsequently recorded data sets in order to minimize long-term fluctuations (details on the measurement routine can be found in Sec. 3.3). A power-dependent series of difference spectra, confirming the linear intensity dependence of excitation, can be found in Appendix B.3. No mechanical changes in the setup-alignment were made when recording the TA data of **1** in 21 different solvent mixtures. If not otherwise specified, it is consistently referred to volume ratios of solvents in this chapter.

4.3 Results and discussion

4.3.1 QM/MM calculations

In order to elucidate whether a solvent molecule can significantly influence the balance of the Ph_2C spin states, the average QM energies of $^1Ph_2C$ and $^3Ph_2C$ are calculated. Pure MeCN stabilizes the singlet more than the triplet, but as in the gas phase the latter is energetically still favored. The situation already changes by addition of small

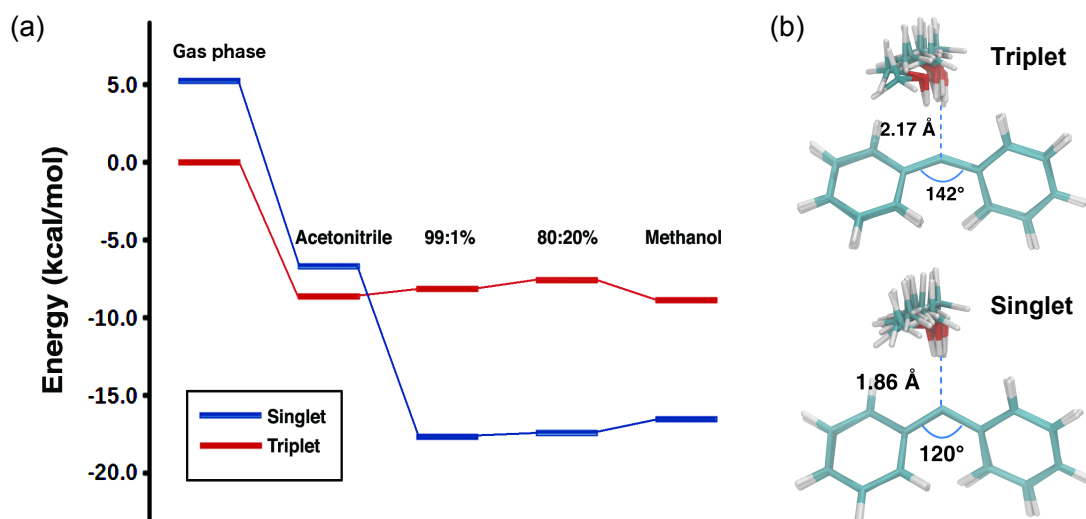**Figure 4.2: QM energies of $^1Ph_2C$ and $^3Ph_2C$.** (a) Calculated singlet-triplet energy gap of Ph_2C in different mixtures of MeOH and MeCN. (b) The H-bonded complex of MeOH with either $^1Ph_2C$ or $^3Ph_2C$. Figures used with permission from Dr. Pandian Sokkar and Dr. Elsa Sánchez-García, Max-Planck-Institut für Kohlenforschung, Mülheim an der Ruhr © (2015).

Figure 4.3: Mechanisms 1 and 2 of O-H insertion in the reaction of ^{1}Ph$_2$C with MeOH, as observed in the QM/MM MD simulation. Figure used with permission from Dr. Pandian Sokkar and Dr. Elsa Sánchez-García, Max-Planck-Institut für Kohlenforschung, Mülheim an der Ruhr © (2015).
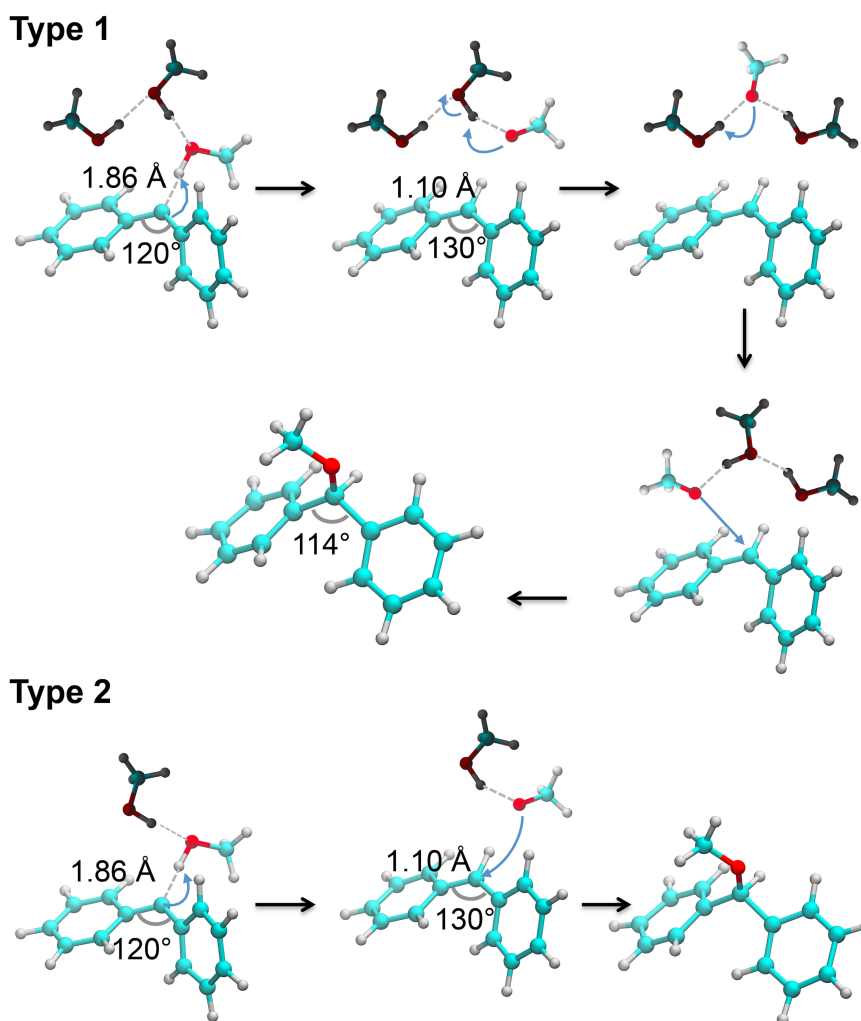
amounts of MeOH, reversing the singlet-triplet energy gap [see Fig. 4.2(a)]. The optimized structures reveal that MeOH forms a strong H-bond with the carbene center of ^{1}Ph$_2$C thereby lowering its energy, whereas in the case of the less polar ^{3}Ph$_2$C the stabilization is much less pronounced. This behavior is also directly reflected in the average distance of the H-bond in the complex ^{1}Ph$_2$C$\cdot\cdot$HOMe [see Fig. 4.2(b)]. Remarkably, the lowest energy is not found for ^{1}Ph$_2$C in pure MeOH, suggesting that if the MeOH molecule interacting with the carbene is involved in an H-bonding network with other neighboring MeOH molecules, the stabilization of ^{1}Ph$_2$C is weakened. Series of QM/MM molecular dynamics simulations also corroborated that ^{1}Ph$_2$C forms a stable complex in pure MeOH while ^{3}Ph$_2$C does not. Such complexes between ^{1}Ph$_2$C and MeOH are also conserved in solvent mixtures with lower MeOH content, but complex formation strongly depends on the diffusion of MeOH molecules to approach the carbene center.

On an ultrafast time scale, ^{1}Ph$_2$C can react with an adjacent MeOH molecule. Further simulations unveil that the reaction leading to O-H insertion always commences with the protonation of ^{1}Ph$_2$C, but two different mechanisms are active. In mechanism 1 (see Fig. 4.3), the H-bonded MeOH transfers the proton to the carbene to yield Ph$_2$CH$^+$, but the nascent methoxide ion takes up a proton from a neighboring MeOH molecule. In this way, the two charges are spatially separated and the initially H-bonded MeOH molecule is not the one completing the reaction. Instead, a third MeOH molecule donates its proton to the newly formed methoxide ion and attacks the Ph$_2$CH$^+$, forming the ether product. In mechanism 2, the H-bonded MeOH transfers the proton, and the resulting methoxide anion combines with Ph$_2$CH$^+$ to the final product. This process is facilitated by the presence of a second MeOH molecule, which does not react with the carbene (see Fig. 4.3). It should be noted that the reaction does not occur if there is not a second MeOH molecule in the vicinity. From this observation, it is clear that a reaction of ^{1}Ph$_2$C with an isolated, H-bonded MeOH molecule is disfavored.

The simulations draw a clear picture of what can happen to ^{1}Ph$_2$C when it is formed photochemically in solution. On the one hand, it can form an H-bonded complex if it encounters an isolated MeOH molecule. Subsequently, when a further MeOH molecule approaches, the ether product can be formed according to mechanism 2. Since the same MeOH transfers the proton and completes the reaction, signatures of charged intermediates will be extremely short-lived if observable at all. On the other hand, when ^{1}Ph$_2$C encounters a MeOH molecule which already interacts with a neighboring one, mechanism 1 can take place. Due to the separation of Ph$_2$CH$^+$ and the methoxide, the charged species survive for a longer time and Ph$_2$CH$^+$ is identifiable by its characteristic absorption.

4.3.2 Transient absorption measurements

For the experimental investigation, broadband TA measurements on Ph$_2$CN$_2$ in solvent mixtures of MeOH and MeCN were conducted. An extract of these measurements is presented in Fig. 4.4. In the case of pure MeOH (0% MeCN, top left panel), two distinct positive TA signals are observed, which correspond to the absorption of ^{1}Ph$_2$C centered at 355 nm and of the benzhydryl cation Ph$_2$CH$^+$ at 435 nm, respectively. The ground state bleach (GSB) of the precursor Ph$_2$CN$_2$ appears on the high-energy edge of the detection range as negative TA signal. For MeCN fractions above 90%, the GSB signal is completely overlaid by the positive TA contributions of the reaction intermediates. The spectral positions agree both with Kohler's study [194] and with the matrix experiments [21, 22], for Ph$_2$CH$^+$ furthermore with recent measurements of the Riedle group on the photoinitiated carbocation formation from benzhydryl chlorides [209–211]. Additionally, and independent of the solvent mixing ratio, one observes the spectral signature of the excited diazo compound Ph$_2$CN$_2^*$ at around 335 nm. For clarity, a detailed view on the TA of Ph$_2$CN$_2$ in MeOH within the first few picoseconds after UV excitation is given in Fig. 4.5(a). A monoexpontial fit of these early dynamics reveals a lifetime of the excited precursor of $\approx$ 150 fs [red curve in Figure 4.5(b)]. No significant deviations from this value are found in different solvent mixtures.
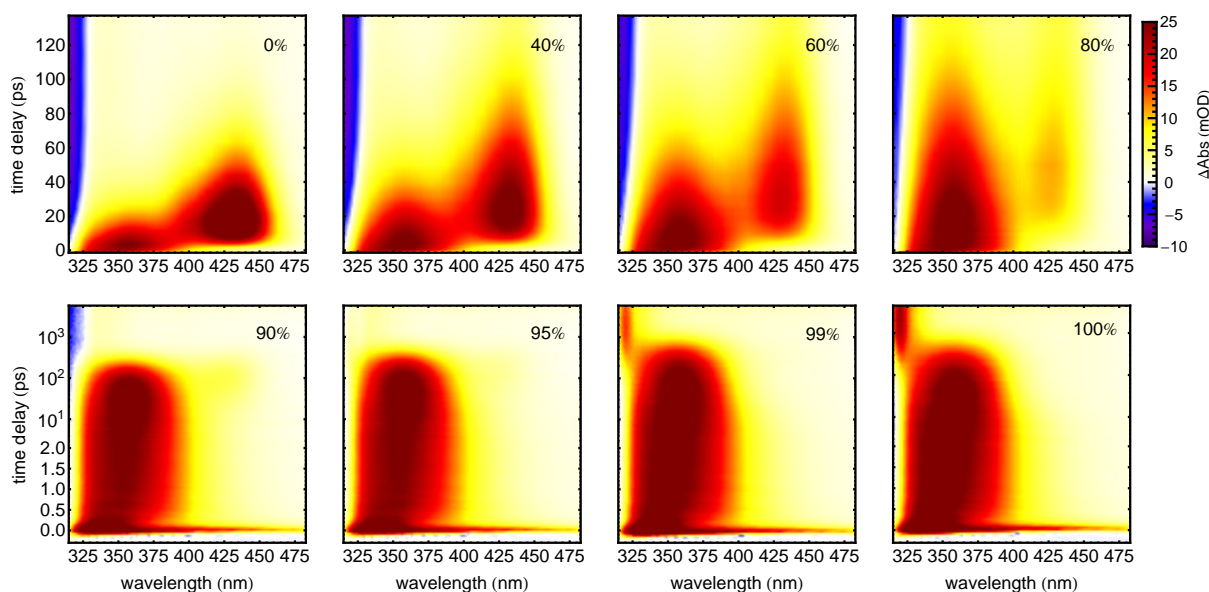
Figure 4.4: Transient absorption of Ph_2CN_2 under 285 nm excitation for different MeOH/MeCN solvent mixtures. Respective numbers depict the fraction of MeCN in the corresponding measurement. Note that for concentrations up to 80% MeCN (top row), data is shown using a linear time axis covering the first 135 ps pump–probe delay, whereas for higher MeCN concentrations (bottom row) a lin–log time axis is chosen in order to include dynamics up to 4 ns pump–probe delay.

The competition between different reaction pathways becomes evident from the TA data in solvent mixtures, where an increase in MeCN concentration leads to several changes in the dynamics: (1) the characteristic time scales increase, so $^1Ph_2C$ decays more slowly while Ph_2CH^+ is formed later and survives for a longer time (confer Fig. 4.4 and rate
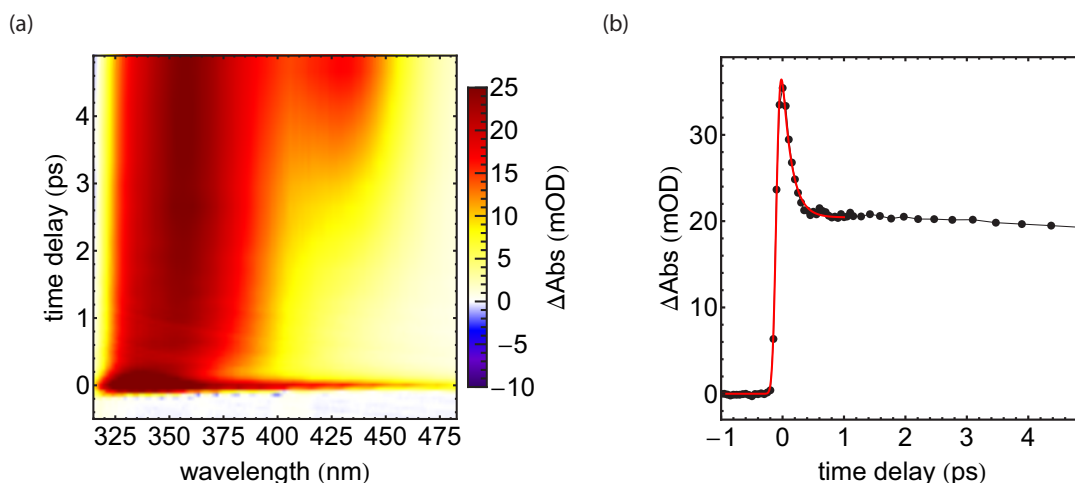

Figure 4.5: Early dynamics of the diazo-compound precursor Ph_2CN_2 in MeOH after UV excitation. (a) Broadband transient absorption in the UV to VIS spectral regime. (b) Transient absorption at a probe wavelength of 335 nm.

constants displayed in Fig. 4.6). This observation confirms that reactions of the initially formed $^1Ph_2C$ depend on the MeOH concentration, and so does the formation and the decay of Ph_2CH^+; (2) the decay rate of $^1Ph_2C$ is always lower than the rate describing the rise of Ph_2CH^+. Hence, the absorption centered at 355 nm cannot originate solely from a precursor of Ph_2CH^+, but must also be due to a species which can co-exist with Ph_2CH^+ in solution and which has a similar electronic absorption as $^1Ph_2C$. Therefore, it is concluded that the TA signal at 355 nm stems both from $^1Ph_2C$ and the complex $^1Ph_2C \cdot \cdot HOMe$; (3) the Ph_2CH^+ absorption becomes weaker compared to the initial $^1Ph_2C$ signal (see e.g., the panel for 80% MeCN in Fig. 4.4). This directly shows that for reduced MeOH concentrations, Ph_2CH^+ is formed less likely compared to $^1Ph_2C \cdot \cdot HOMe$; (4) for high MeCN fractions, the Ph_2CH^+ disappears and a new absorption around 315 nm is observed after several hundred picoseconds (lower panels in Fig. 4.4). For lack of MeOH, the ISC pathway to $^3Ph_2C$ absorbing at 315 nm becomes dominant [194, 203].

Figure 4.6: Rate constants extracted from nonlinear interpolation describing the rise of $^3Ph_2C$ (315 nm), the decay of $^1Ph_2C$ (355 nm), as well as the rise and the decay of Ph_2CH^+ (maximum wavelength) in solvent mixtures of varying MeCN mole fractions. The corresponding fit curves are shown in Appendix B.5, B.6, and B.7, respectively.
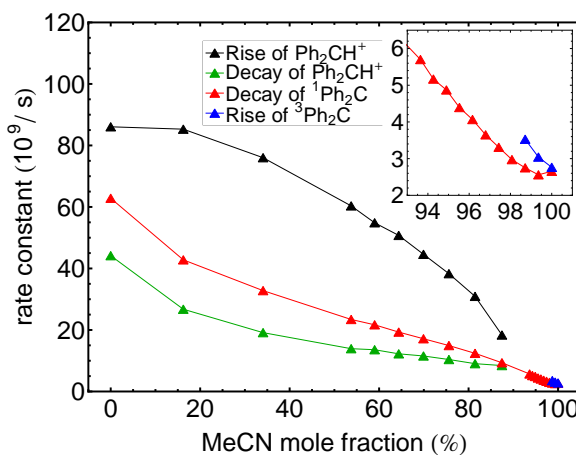
Additional information on solvent effects is deduced for the ultrafast dynamics in solvent mixtures. Extracting the peak position of the singlet carbene absorption from the TA data (see Fig. 4.7 and corresponding discussion in Appendix B.4) reveals a red-shift during the first ten ps, which is also the time scale for formation of the benzhydryl cation in pure MeOH. The solvent environment adjusted to the diazo precursor has to rearrange upon the formation of $^1Ph_2C$, and this solvent rearrangement is reflected in the spectral shift which for carbenes is bathochromic [196]. For the Ph_2CH^+ intermediate, the temporal evolution of the maximum absorption wavelength is displayed in Fig. 4.8. For all mixtures with a sufficient amount of Ph_2CH^+, the starting position is at lower wavelengths for higher MeCN fractions, as a consequence of the solvent polarity and the degree of solvation of the precursor $^1Ph_2C$ in the different mixtures. Furthermore, a red-shift of the Ph_2CH^+ signal is observed, which is due to solvation of the cation but also reflects the separation of the benzhydryl cation and the methoxide anion. This separation leads to a shrinking energy gap between the ground and excited states of the benzhydryl cation, as shown by Riedle and coworkers in studies on benzhydryl halides [211]. Hence, the simultaneously generated methoxide anion does not geminately react with Ph_2CH^+ which thereby becomes observable in the experiments. While diffusion may contribute, the involvement of a second MeOH molecule as suggested in Refs. [191, 204] and also

derived from the hybrid QM/MM calculations (mechanism 1 in Fig. 4.3) might be the basis of the separation process.
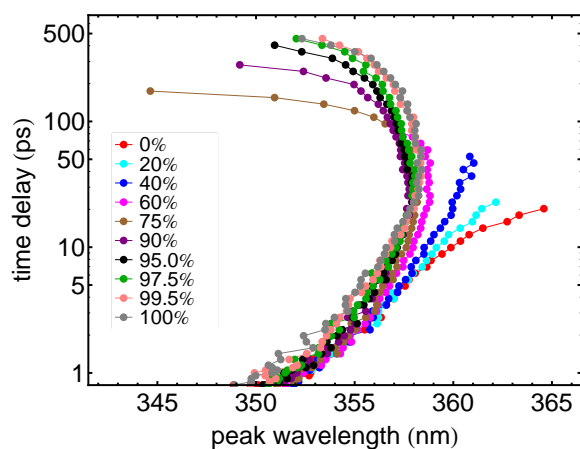

Figure 4.7: Time-dependent peak position of the ^{1}Ph$_2$C absorption band. For all solvent environments, an initial red-shift is observed, which is followed by a much slower blue-shift for those mixtures where the signal does not vanish on the time scale of Ph$_2$CH$^+$ formation. Note the logarithmic ordinate. See Appendix B.4 for details on data evaluation.
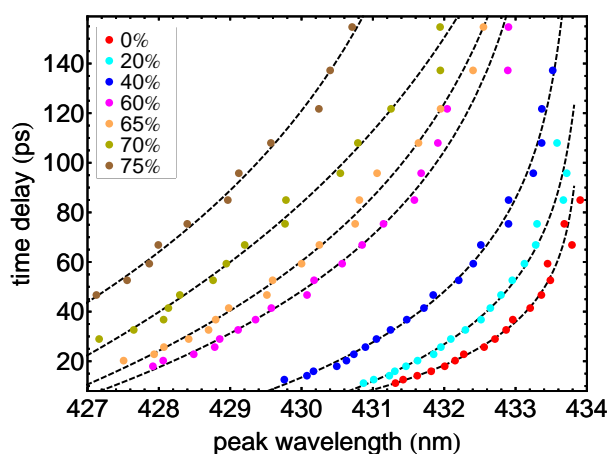

Figure 4.8: Time-dependent peak position of the Ph$_2$CH$^+$ absorption band. For all solvent mixtures, a red-shift is observed, but the initial wavelength decreases with MeCN concentration. See Appendix B.4 for details on data evaluation.

In the following, the amount of molecules which follow the different reaction pathways will be inferred. The results are summarized in Fig. 4.9. Note that the analysis relies on the assumption of an equal absorption cross section of Ph$_2$CH$^+$ and ^{3}Ph$_2$C in all solvent mixtures. Starting out with the dynamics in pure MeOH, a fraction x of the initial ^{1}Ph$_2$C molecules takes up a proton to form Ph$_2$CH$^+$, which rapidly reacts on to an ether which is dark (i.e., non-absorbing) in the accessible spectral range. Kohler and coworkers [194] showed that about 30% of the photoexcited Ph$_2$CN$_2$ molecules lead to Ph$_2$CH$^+$, but an assignment of whether the other 70% do not lead to the formation of ^{1}Ph$_2$C (i.e., $x = 1$) or follow an alternative reaction pathway to the dark product (i.e., $x = 0.3$) could not be made. However for all mixtures, the decay rate for the singlet carbene is lower than the rise of Ph$_2$CH$^+$, even in pure MeOH (Fig. 4.6), corroborating ^{1}Ph$_2$C$\cdot\cdot$HOMe formation. Hence, x cannot be one but must be smaller, and it is assumed that $x = 0.3$ in the following although also larger values cannot be ruled out. As explained in the following, a direct comparison of the TA data for different mixtures is possible by normalization to the initial ^{1}Ph$_2$C signal and the two extreme cases that in pure MeOH 30% react via Ph$_2$CH$^+$,

whereas in pure MeCN 100% form the $^3Ph_2C$ species (as evidenced by the matching decay rate of $^1Ph_2C$ and rise rate of $^3Ph_2C$ in Fig. 4.6).

Figure 4.9: Differentiating between different reaction channels. Fraction of molecules following the Ph_2CH^+ (green), the $^3Ph_2C$ (blue), and the $^1Ph_2C{\cdot}\cdot HOMe$ (red) pathway for different MeOH/MeCN solvent mixtures, as derived from the TA data. The solid curves result from the reaction scheme sketched in Fig. 4.15, where the rates exhibit different dependencies on the MeOH concentration [M].
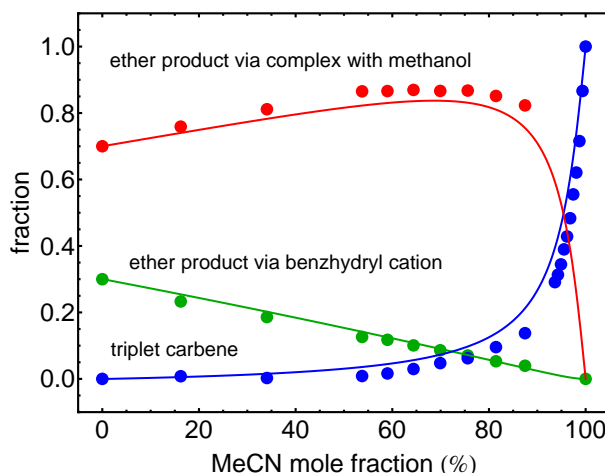
The relative amount of Ph_2CH^+ being produced in different solvent mixtures of MeOH and MeCN can be quantified by integrating the area under the fitted transients (confer Fig. B.5 in Appendix B.7) between 4 and 400 ps time delay neglecting the contribution of the constant offset, and multiplying the resulting values by the corresponding rate constants describing the decay of Ph_2CH^+ in the respective solvent mixture (confer rate models which will be described in Sec. 4.4). Since in pure MeCN no singlet carbene takes up a proton to form Ph_2CH^+, the latter values are eventually normalized between 0.3 and 0 (see blue curve in Fig. 4.9). The triplet strength for a certain solvent mixture is directly taken from the TA data: at 315 nm one finds constant absorption change signals for all solvent mixtures between 1.5 ns and 4 ns, representing the GSB of the precursor for lower MeCN fractions and the triplet absorption for higher MeCN fractions. Before normalization (see below), data points from this temporal region of interest are averaged to enhance the data quality when quantifying the amount of $^3Ph_2C$ being produced. The amount of $^3Ph_2C$ is assumed to be directly proportional to the TA signal at 315 nm because any contribution from the spectrally adjacent $^1Ph_2C$ absorption band has completely vanished after 1.5 ns pump–probe delay. For evaluating the amount of $^3Ph_2C$ being produced, it is assumed that in pure MeCN all singlet carbenes undergo ISC towards the triplet state, whereas none do so in MeOH. Hence, the result is normalized between 1 and 0 (see blue curve in Fig. 4.9).

Figure 4.9 visualizes that both fractions do not add up to one—independent of the value x—and therewith confirms the existence of a third channel (occurring more frequently in solvent mixtures) attributed to $^1Ph_2C{\cdot}\cdot HOMe$. The red data points in Fig. 4.9 correspond to the amount of molecules following this pathway, as indirectly deduced from the other fractions. The QM/MM MD simulations also indicated that the Ph_2CH^+ ions were significantly more stable in pure MeOH compared to lower MeOH concentrations. In Sec. 4.4, an analytical solution (solid lines in Fig. 4.9) describing the dynamics associated with three reaction channels will be given, together with a discussion of why simpler models cannot describe the data. To model the derived amounts of Fig. 4.9 with

this reaction scheme, the three rate constants connected to depopulation of ^{1}Ph$_2$C are required. The ISC rate constant can be calculated from the literature by combining the polarity dependence of this rate [190] with the polarity of the solvent mixtures [212], the other two are evaluated by the experimental decay rate of ^{1}Ph$_2$C in pure MeOH and the assumption $x = 0.3$. Note that no other parameter, in particular no free parameter is needed. The reaction scheme according to *model 3* can describe the experimental data very suitably and confirms that there is a solvent mixing ratio for which the amount of molecules reacting via the ^{1}Ph$_2$C$\cdot\cdot$HOMe complex reaches a maximum.

4.4 Modeling the experimental data with rate models

In order to analyze how many molecules follow a certain reaction path, three rate models for different scenarios shall be discussed. For each case, the amounts for each reaction channel will be derived.

4.4.1 Model 1: Triplet and benzhydryl cation only

Assuming that the singlet carbene ^{1}Ph$_2$C (for simplicity called "S" in the following equations) can either react to the triplet ^{3}Ph$_2$C ("T"), as in pure MeCN, or to the benzhydryl cation Ph$_2$CH$^+$ ("B"), as seen in MeOH, which further turns into the ether product ("E"), one can derive the following rate equations:

$$[\dot{\mathrm{S}}] \quad = -k_{\mathrm{SB}}[\mathrm{S}] - k_{\mathrm{ST}}[\mathrm{S}] \ , \tag{4.4.1}$$

$$[\dot{\mathrm{T}}] \quad = +k_{\mathrm{ST}}[\mathrm{S}] \ , \tag{4.4.2}$$

$$[\dot{\mathrm{B}}] \quad = +k_{\mathrm{SB}}[\mathrm{S}] - k_{\mathrm{BE}}[\mathrm{B}] \ , \tag{4.4.3}$$

$$[\dot{\mathrm{E}}] \quad = +k_{\mathrm{BE}}[\mathrm{B}] \ , \tag{4.4.4}$$

$$[\mathrm{S}]_{t=0} = S_0; \quad [\mathrm{T}]_{t=0} = 0; \quad [\mathrm{B}]_{t=0} = 0; \quad [\mathrm{E}]_{t=0} = 0 \ , \tag{4.4.5}$$

which have as solution:

$$[\mathrm{S}] = S_0 \, \mathrm{e}^{-(k_{\mathrm{SB}}+k_{\mathrm{ST}})\,t} \ , \tag{4.4.6}$$

$$[\mathrm{T}] = S_0 \, \frac{k_{\mathrm{ST}}}{k_{\mathrm{SB}} + k_{\mathrm{ST}}} \left[1 - \mathrm{e}^{-(k_{\mathrm{SB}}+k_{\mathrm{ST}})\,t} \right] \ , \tag{4.4.7}$$

$$[\mathrm{B}] = S_0 \, \frac{k_{\mathrm{SB}}}{k_{\mathrm{SB}} + k_{\mathrm{ST}} - k_{\mathrm{BE}}} \left[\mathrm{e}^{-k_{\mathrm{BE}}\,t} - \mathrm{e}^{-(k_{\mathrm{SB}}+k_{\mathrm{ST}})\,t} \right] \ , \tag{4.4.8}$$

$$[\mathrm{E}] = S_0 \left\{ \frac{k_{\mathrm{SB}}}{k_{\mathrm{SB}}+k_{\mathrm{ST}}} + \frac{k_{\mathrm{SB}}}{(k_{\mathrm{SB}}+k_{\mathrm{ST}})(k_{\mathrm{SB}}+k_{\mathrm{ST}}-k_{\mathrm{BE}})} \right.$$
$$\left. \times \left[k_{\mathrm{BE}} \mathrm{e}^{-(k_{\mathrm{SB}}+k_{\mathrm{ST}})\,t} - (k_{\mathrm{SB}}+k_{\mathrm{ST}}) \mathrm{e}^{-k_{\mathrm{BE}}\,t} \right] \right\} . \tag{4.4.9}$$

The amount of molecules following each reaction path are:

$$[\mathrm{T}]_{t=\infty} = S_0 \frac{k_{\mathrm{ST}}}{k_{\mathrm{SB}} + k_{\mathrm{ST}}} \;, \tag{4.4.10}$$

$$[\mathrm{E}]_{t=\infty} = S_0 \frac{k_{\mathrm{SB}}}{k_{\mathrm{SB}}+k_{\mathrm{ST}}} \;. \tag{4.4.11}$$

The final ether product does not show any absorption signal in the probed wavelength region. Hence, the amount of molecules following the reaction path towards the ether has to be determined from the absorption signal of the benzhydryl cation. If the experimental TA is measured, this can be done by performing the integral

$$\int_0^\infty [\mathrm{B}]\mathrm{d}t = S_0 \frac{k_{\mathrm{SB}}}{k_{\mathrm{BE}}(k_{\mathrm{SB}}+k_{\mathrm{ST}})} = \frac{1}{k_{\mathrm{BE}}} [\mathrm{E}]_{t=\infty} \tag{4.4.12}$$

and subsequent multiplication of the obtained value with the experimentally determined decay rate k_{BE} of the benzhydryl cation, thus yielding $[\mathrm{E}]_{t=\infty}$ (confer data evaluation of Fig. 4.9).

The rate constants in the general scheme described above can depend on the concentration of the solvent as well, i.e., $k_{\mathrm{SB}} = k'_{\mathrm{SB}}[\mathrm{M}]$ should depend on the concentration of MeOH ("M"). Since the amount of MeOH is much higher than the amount of carbene already for small mole fractions of MeOH in the binary solvent mixture, a pseudo-first-order behavior is assumed, i.e., $[\mathrm{M}]$ does not change during the reaction. For an exemplary calculation, k_{ST} is determined by combining the solvent polarity dependence of k_{ST} [190] with the solvent polarity parameter $\mathrm{E_T}(30)$ of binary mixtures of MeCN and MeOH [212], whereas the other two rate constants are determined from experiments in pure MeOH, i.e., in pure MeOH one has $k_{\mathrm{SB}}=(12\,\mathrm{ps})^{-1}$ and $k_{\mathrm{BE}}=(23\,\mathrm{ps})^{-1}$, while in mixtures they depend on the MeOH concentration and become $k_{\mathrm{SB}}=(12\,\mathrm{ps})^{-1}\frac{[\mathrm{M}]}{M_0}=(12\,\mathrm{ps})^{-1}v_{\mathrm{M}}$ and $k_{\mathrm{BE}}=(23\,\mathrm{ps})^{-1}\frac{[\mathrm{M}]}{M_0}=(23\,\mathrm{ps})^{-1}v_{\mathrm{M}}$, respectively, with the volume fraction v_{M} of MeOH and M_0 being the concentration of pure MeOH.

The result is shown in Figure 4.10. The curve for the triplet pathway resembles the experimentally determined one, whereas the other one does not. Clearly, in this *model 1* there are only two reaction paths, hence the two curves have to add up to one. Possible reasons for the discrepancy might be:

- the *model 1* on which the modeling is based is incomplete,

- the assumption in the modeling that the rates are constant or only depend linearly on $[\mathrm{M}]$ is too simple,
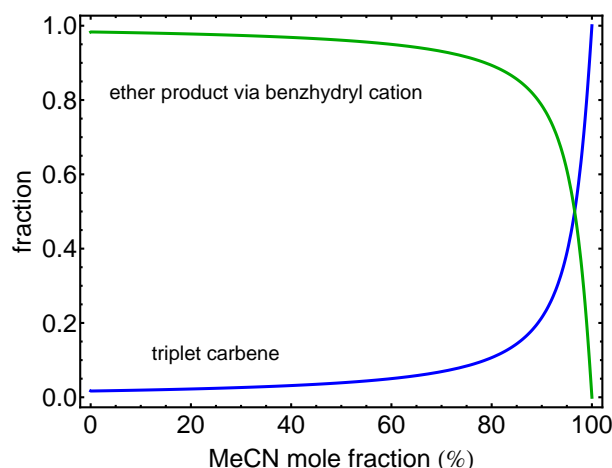
Figure 4.10: Distribution of reaction products according to model 1. Percentage of molecules taking the $^1Ph_2C \to\ ^3Ph_2C$ or the $^1Ph_2C \to Ph_2CH^+ \to$ ether reaction path.

- the absorption cross section of Ph_2CH^+ might change drastically with the mole fraction of MeCN, so that the shape of the curve derived from the experiments is obscured—this issue has been addressed for pure MeOH and MeCN by Kohler and coworkers [194] who concluded that due to similar dielectric properties, the absorption coefficient in both solvents should be roughly the same,

- since the TA bands shift spectrally with time, the integration of the experimental Ph_2CH^+ signal is too inaccurate.

While with all of these reasons one might rationalize that the experimentally determined amounts do not add up to one, the observation that the decay time of $^1Ph_2C$ and the rise time of Ph_2CH^+ differ strongly for certain solvent mixing ratios points to the first one listed (without necessarily excluding the other ones which might additionally have to be considered, see below), i.e., that *model 1* is incomplete. Therefore, one has to search for alternatives.

4.4.2 Model 2: A third decay channel

In the work by Kohler and coworkers [194], it was found that the protonation fraction of all excited molecules is about 30% in pure MeOH. One possibility is that 70% of the excited $Ph_2CN_2^*$ molecules do not dissociate but relax back to the ground state of the diazo compound (as it is for example observed when exciting diazo-Meldrum's acid [108]). However, in this scenario all the generated $^1Ph_2C$ molecules will follow the protonation pathway via Ph_2CH^+. Thus, when MeCN is added, allowing also the triplet pathway, the amount of molecules following each pathway should look similar as in Fig. 4.10. Since this is not the case, it can be concluded that another possibility mentioned in Ref. [194] is more appropriate, namely that 70% follow a reaction path from singlet carbene to the ether product which does not involve the Ph_2CH^+ intermediate. The third reaction channel comprises an intermediate complex $^1Ph_2C\cdot\cdot HOMe$ ("C") of a singlet carbene and a MeOH molecule, as e.g., suggested by Eisenthal and coworkers [187] and also observed

in the hybrid QM/MM calculations. From there, the ether product can be generated in a concerted fashion. This can be expressed in the following rate equations:

$$[\dot{S}] = -k_{SB}[S] - k_{ST}[S] - k_{SC}[S] \ , \tag{4.4.13}$$

$$[\dot{T}] = +k_{ST}[S] \ , \tag{4.4.14}$$

$$[\dot{B}] = +k_{SB}[S] - k_{BE}[B] \ , \tag{4.4.15}$$

$$[\dot{C}] = +k_{SC}[S] - k_{CE}[C] \ , \tag{4.4.16}$$

$$[\dot{E}] = +k_{BE}[B] + k_{CE}[C] \ , \tag{4.4.17}$$

$$[S]_{t=0} = S_0; \quad [T]_{t=0} = 0; \quad [B]_{t=0} = 0; \quad [C]_{t=0} = 0; \quad [E]_{t=0} = 0 \ , \tag{4.4.18}$$

with the solutions

$$[S] = S_0 \, \mathrm{e}^{-(k_{SB}+k_{ST}+k_{SC})\,t} \ , \tag{4.4.19}$$

$$[T] = S_0 \, \frac{k_{ST}}{k_{SB} + k_{ST} + k_{SC}} \left[1 - \mathrm{e}^{-(k_{SB}+k_{ST}+k_{SC})\,t} \right] \ , \tag{4.4.20}$$

$$[B] = S_0 \, \frac{k_{SB}}{k_{SB} + k_{ST} + k_{SC} - k_{BE}} \left[\mathrm{e}^{-k_{BE}\,t} - \mathrm{e}^{-(k_{SB}+k_{ST}+k_{SC})\,t} \right] \ , \tag{4.4.21}$$

$$[C] = S_0 \, \frac{k_{SC}}{k_{SB} + k_{ST} + k_{SC} - k_{CE}} \left[\mathrm{e}^{-k_{CE}\,t} - \mathrm{e}^{-(k_{SB}+k_{ST}+k_{SC})\,t} \right] \ , \tag{4.4.22}$$

$$[E] = \frac{S_0}{k_{SB}+k_{ST}+k_{SC}} \Bigg\{ k_{SB}+k_{SC}+ \Bigg[\frac{k_{SB}k_{BE}}{k_{SB}+k_{ST}+k_{SC}-k_{BE}} + \frac{k_{SC}k_{CE}}{k_{SB}+k_{ST}+k_{SC}-k_{CE}} \Bigg]$$

$$\times \mathrm{e}^{-(k_{SB}+k_{ST}+k_{SC})t} - \left(k_{SB}+k_{ST}+k_{SC} \right)$$

$$\times \Bigg[\frac{k_{SB}}{k_{SB}+k_{ST}+k_{SC}-k_{BE}} \mathrm{e}^{-k_{BE}t} + \frac{k_{SC}}{k_{SB}+k_{ST}+k_{SC}-k_{CE}} \mathrm{e}^{-k_{CE}t} \Bigg] \Bigg\} \ . \tag{4.4.23}$$

Since there are three parallel pathways starting from ^{1}Ph$_2$C, the amount of molecules following each path is given by:

$$[T]_{t=\infty} = S_0 \, \frac{k_{ST}}{k_{SB} + k_{ST} + k_{SC}} \ , \tag{4.4.24}$$

$$[E]_{t=\infty} = S_0 \, \frac{k_{SB}}{k_{SB}+k_{ST}+k_{SC}} + S_0 \, \frac{k_{SC}}{k_{SB}+k_{ST}+k_{SC}} \ , \tag{4.4.25}$$

where Eq. (4.4.25) is a sum of the paths involving either Ph$_2$CH$^+$ or the complex ^{1}Ph$_2$C$\cdot\cdot$HOMe. Both for reaching Ph$_2$CH$^+$ and ^{1}Ph$_2$C$\cdot\cdot$HOMe, the singlet carbene has to interact with a MeOH molecule. First, it is assumed that the rates are pseudo-first order with a linear dependence on [M], i.e., $k_{SB} = k'_{SB}[M]$ and $k_{SC} = k'_{SC}[M]$. In order to take into account that only $\approx 30\%$ of singlet molecules follow the Ph$_2$CH$^+$ pathway and
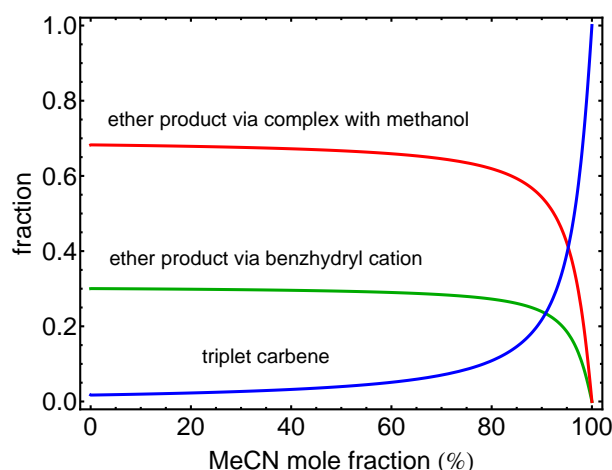
Figure 4.11: Distribution of reaction products according to model 2. Percentage of molecules taking the $^1Ph_2C\rightarrow$ $^3Ph_2C$, the $^1Ph_2C\rightarrow Ph_2CH^+\rightarrow$ether, or the $^1Ph_2C\rightarrow{}^1Ph_2C\cdot\cdot HOMe\rightarrow$ether reaction path, with rate constants linearly depending on [M] for the first step of the latter two reaction paths.

that Ph_2CH^+ in pure MeOH rises with a time constant of 12 ps, $k'_{SB}=(40\,ps)^{-1}/M_0$ and $k'_{SC}=(17.6\,ps)^{-1}/M_0$ is used in the calculation. The result is shown in Fig. 4.11. As one would expect, the shape of the curves has not changed, but now only 30% proceed via the cation towards the ether product. With the assumptions outlined above, the model gives no indication why the amount of molecules following the $^1Ph_2C\rightarrow Ph_2CH^+\rightarrow$ether pathway shows an almost linear dependence on the concentration.

4.4.3 Model 3: Non-linear dependence on methanol concentration

Instead of including further pathways or equilibria, one may concentrate on the dependence on [M], thereby particularly addressing the question what governs whether there will be protonation or a complexation in the interaction of $^1Ph_2C$ with MeOH. Kirmse and Steenken [191, 204] suggested that two MeOH molecules are needed for the protonation. As can be seen from mechanism 1 in Fig. 4.3, the hybrid QM/MM calculations reveal the involvement of at least two MeOH molecules as well. In addition, Scaiano and coworkers [213], for other carbenes in MeCN with little amounts of MeOH, have observed that MeOH oligomers are more reactive than monomers.

Hence, MeOH dimers shall be considered to be present in the solution, with the associated equilibrium $2\,MeOH\rightleftharpoons(MeOH)_2$ with equilibrium constant K. These might originate from hydrogen bonding of two adjacent MeOH molecules. For the Ph_2CH^+ formation, such a dimer would serve two processes: first, the presence of the hydrogen bond can facilitate the MeOH molecule's ability to donate a proton; second, when MeOH transfers a proton to $^1Ph_2C$ to yield Ph_2CH^+, a methoxide anion is created as well which could geminately recombine with the cation. This process might be efficiently avoided if the bonded MeOH transfers a proton to the methoxide, itself turning into a methoxide anion which however is further away from the cation. Therefore, the rate constant k_{SB}, which depends on the dimer concentration, is modified and hence $k_{SB}=k''_{SB}[(MeOH)_2]=k''_{SB}K[M]^2$. For the modeling, $k''_{SB}K=(40\,ps)^{-1}/M_0^2$ is used to match the experimental rates in pure MeOH. The result is shown in Fig. 4.12. The curve for the reaction path involving the cation is now close to a linear behavior.

Figure 4.12: Distribution of reaction products according to model 3. Percentage of molecules taking the $^1Ph_2C\rightarrow$ $^3Ph_2C$, the $^1Ph_2C\rightarrow Ph_2CH^+\rightarrow$ether, or the $^1Ph_2C\rightarrow{}^1Ph_2C\cdot\cdot HOMe\rightarrow$ether reaction path. The dependence on the MeOH concentration for the initial rate of each reaction path is zero, quadratic, and linear, respectively.
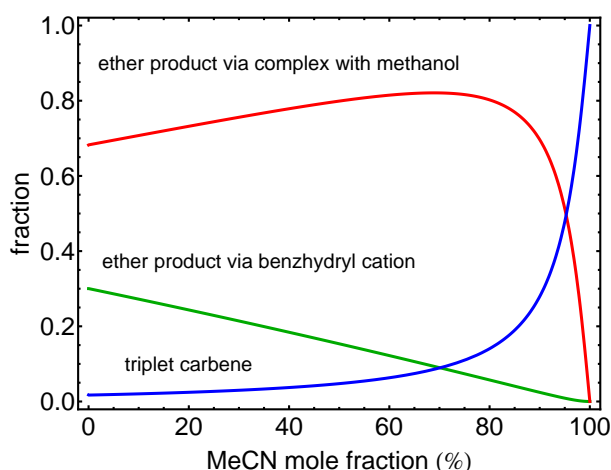
As can be seen from Fig. 4.9, it becomes evident that *model 3* (solid lines) is well suited to model the experimental observations. Thereby, in order to avoid errors from the assumption that there will be no ISC in pure MeOH, the modelled curves are calculated accordingly, thus also providing a scale between 0 and 1, i.e.,

$$T(x) = \frac{T(x) - T(x=0)}{T(x=1) - T(x=0)} \quad , \tag{4.4.26}$$

with the MeCN mole fraction x and the amount T of $^3Ph_2C$ molecules.

4.4.4 Decay of the singlet absorption

The experimental data (confer Fig. 4.6) shows that the decay rate of the singlet absorption signal is always lower than the rate associated with the rise of the benzhydryl cation. This can be explained if the complex $^1Ph_2C\cdot\cdot HOMe$ has absorption characteristics in the visible spectral domain which are very similar to those of $^1Ph_2C$. Then, the observed singlet absorption also originates from the complex. In the complex, the MeOH is bound to $^1Ph_2C$ and can eventually react with it in a concerted fashion to form the ether product. The lifetime of this complex will strongly depend on the environment, e.g., because the solvent polarity and the possibility for hydrogen bonding to another MeOH will change. To model the decay, it is assumed that the rate k_{CE} is also pseudo-first order, i.e., $k_{CE}=k'_{CE}[M]$, with a rate on the order of diffusion $k'_{CE}=(18\,\text{ps})^{-1}/M_0$. This linear dependence is also motivated by mechanism 2 found in the simulations (confer Fig. 4.3). Figure 4.13 shows exemplary transients which result from this model. Note in the right panel that the initial rise of the singlet carbene absorption signal which was observed in the experiments can be explained if the absorption coefficient for the complex $^1Ph_2C\cdot\cdot HOMe$ is larger than that of $^1Ph_2C$. Note that the rising dynamics are also observed in pure MeCN and might originate from solvation and vibrational cooling, possibly slight solvent impurities, or a slower buildup of the dipole moment in the complex, e.g., because of geometrical changes.
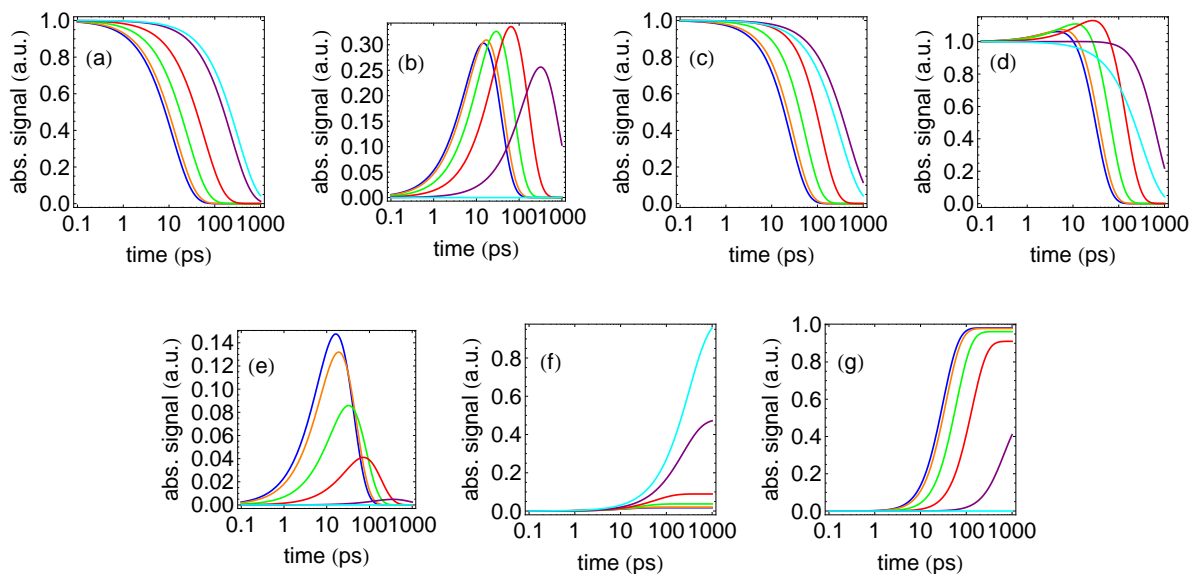
Figure 4.13: Modeled transient absorption signals for a MeCN mole fraction of 0 (blue), 0.1 (orange), 0.4 (green), 0.7 (red), 0.95 (purple), and 1 (cyan). The curves correspond to the signals of (a) $^1Ph_2C$, (b) $^1Ph_2C\cdot\cdot HOMe$, (c) $^1Ph_2C + {}^1Ph_2C\cdot\cdot HOMe$, and (d) $^1Ph_2C + {}^1Ph_2C\cdot\cdot HOMe$ with the latter contribution multiplied by a factor of 2 to mimic a higher absorption coefficient. Lower panels: (e) Ph_2CH^+, (f) $^3Ph_2C$, and (g) ether product. Simulations performed according to model 3.

The decay rate of the absorption signal of Ph_2CH^+ (see Fig. 4.6) exhibits a basically linear dependence on [M] as well. Kohler and coworkers [194] deduced by variation of the alcohol that Ph_2CH^+ reacts with a further neutral alcohol molecule rather than the alkoxide. Modeling the TA signals of Ph_2CH^+ with a decay rate of $k_{BE}=k'_{BE}[M]=(23\,\mathrm{ps})^{-1}[M]/M_0$, derived from the decay curve of the Ph_2CH^+ absorption in pure MeOH, yields curves which qualitatively reproduce the experimental ones.

4.4.5 Rate constants

It is also instructive to calculate the rates associated with the rise and decay of the Ph_2CH^+ absorption signal—as done in the following for *model 3*. The rates are shown in Fig. 4.14. Although the quadratic dependence on [M] drastically changes how many molecules take a certain path, the rate constant for Ph_2CH^+ formation (black) is still almost linear, since it is governed by the parallel singlet decay channel towards the complex $^1Ph_2C\cdot\cdot HOMe$. The complex rises with the same rate constant with which the singlet decays via three parallel channels. One further observes that the decay constant of the complex is always smaller than the one of the Ph_2CH^+ rise, explaining why in the experiment the combined absorption of $^1Ph_2C$ and $^1Ph_2C\cdot\cdot HOMe$ decays more slowly than Ph_2CH^+ appears. However, the experimental signal is the sum of several exponentials [basically of Eqs. (4.4.19) and (4.4.22)] and does not decay monoexponentially, but if $^1Ph_2C$ decays much faster

Figure 4.14: Modeled rate constants for the rise of Ph_2CH^+ (black), the decay of Ph_2CH^+ (green), and the decay of $^1Ph_2C\cdot\cdot HOMe$ (red). Simulations performed according to model 3.
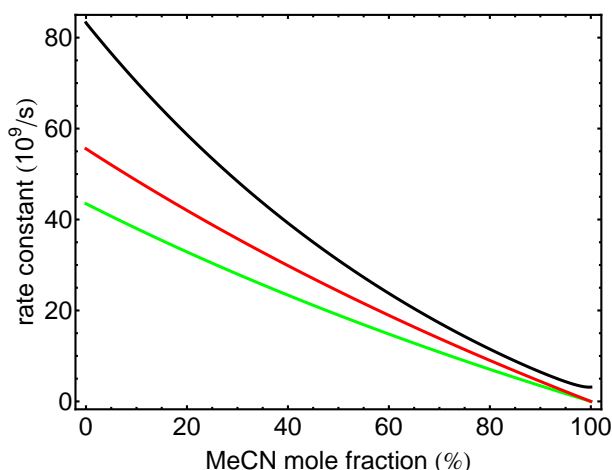
than $^1Ph_2C\cdot\cdot HOMe$, then the decay rate is approximately the one of the complex. The experimentally determined rate constants also show a behavior which is almost linear with respect to the mole fraction (confer Fig. 4.6). The most pronounced deviation is for the rise of Ph_2CH^+ in low MeCN concentrations. This might indicate that 90% or 100% MeOH does not make a big difference anymore for the rate constant, because there are always several MeOH molecules close-by.

4.5 Reaction scheme

At this point, a reaction scheme, which combines the conclusions from the theoretical and experimental studies and is in accordance with both of them, can be proposed. The simulations (mechanism 1) and the TA data—well described by *model 3*—have revealed that more than one MeOH is involved in Ph_2CH^+ formation. This will be included in the scheme as the simple case of a quadratic dependence on the MeOH concentration. Furthermore, the pathway via the complex $^1Ph_2C\cdot\cdot HOMe$ was found, which depends linearly on MeOH concentration. Both of these reactions lead to the ether product, but for the final step a further MeOH is required. As a third pathway, ISC to $^3Ph_2C$ will contribute the stronger the higher the MeCN fraction. The reaction scheme comprising all of these aspects is sketched in Fig. 4.15. Eisenthal and coworkers [187, 188] found for $^1Ph_2C$ in aprotic solvents with small amounts of MeOH cosolvent that the alcohol exerts a "two-fold effect": on the one hand stabilizing the singlet carbene and on the other hand opening a decay channel via the concerted O–H insertion. Their finding, which was deduced from comparing product ratios, is also evident from the present TA data in a straightforward way by looking at the decay rate of the singlet carbene: the lowest value is not observed for pure MeCN but around 99.5% (inset of Fig. 4.6). This again confirms mechanism 2 from the simulations, i.e., an MeOH can stabilize the singlet carbene but will not cause an insertion reaction unless other MeOH molecules are close-by. Beyond that, these room-temperature studies in solution nicely complement the argon matrix experiments at 3 K doped with 1% MeOH in which also the $^1Ph_2C\cdot\cdot HOMe$ complex is formed, eventually yielding the ether product in a tunneling process [21].
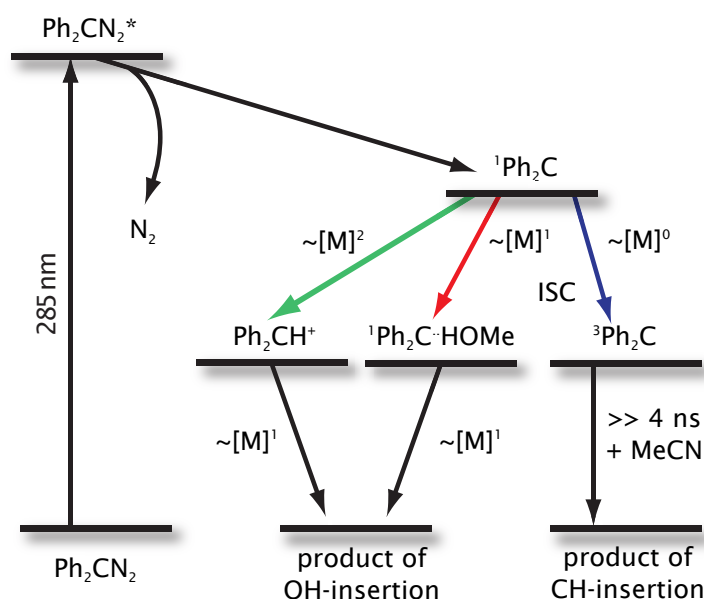
Figure 4.15: Schematic energy diagram covering reaction pathways of 1 in pure MeOH, pure MeCN, and MeOH/MeCN mixtures.

4.6 Conclusion

This joint theoretical and experimental study has unraveled the ultrafast reaction dynamics of diphenylcarbene in solvent mixtures of MeOH and MeCN at room temperature. After UV excitation of the precursor Ph_2CN_2, the singlet $^1Ph_2C$ forms on a femtosecond time scale. Three reaction mechanisms are possible depending on the number of MeOH molecules that this reactive species initially encounters: ISC to $^3Ph_2C$, an H-bonded complex $^1Ph_2C\cdot\cdot HOMe$ which reacts on to the ether product in a concerted fashion activated by a further MeOH molecule, or ether production via an intermediate Ph_2CH^+ for whose formation two MeOH molecules interact concurrently with $^1Ph_2C$. The results substantiate that a complex $^1Ph_2C\cdot\cdot HOMe$ plays a major role for all fractions of MeOH in the mixtures, and that even at room temperature the exerted stabilization is similar to the situation in cryogenic matrices. Both mechanisms leading to the ether already occur in pure MeOH, but due to the different dependencies on the MeOH concentration, there is a solvent mixing ratio for which the highest number of H-bonded complexes is formed. Hence, variation of this ratio provides a means not only to control the time scales of the reaction but also the reactivity, i.e., which reaction path is followed. For the broad field of carbene chemistry, solvent mixtures may therefore prove to be more versatile to achieve a desired outcome than currently considered.

A comparative study on CPU and direct multichannel MCT detection

In this chapter a comparative study on two spectroscopic techniques employed to detect ultrafast absorption changes in the MIR spectral range, namely direct multichannel detection via HgCdTe (MCT) photodiode arrays and the newly established technique of chirped-pulse upconversion (CPU) is presented. Whereas both methods are meanwhile individually used in a routine manner, their applicability in femtosecond pump–probe experiments based on 1 kHz shot-to-shot data acquisition is directly juxtaposed. Additionally, different phase-matching conditions in the CPU scheme for a given MIR spectrum are examined, thereby simultaneously detecting signals which are separated by more than 200 cm^{-1}. The presented results were published in Ref. [3]. Parts of the comparative study were conducted during the supervision of Jarno Riefer's Bachelor Thesis [214].
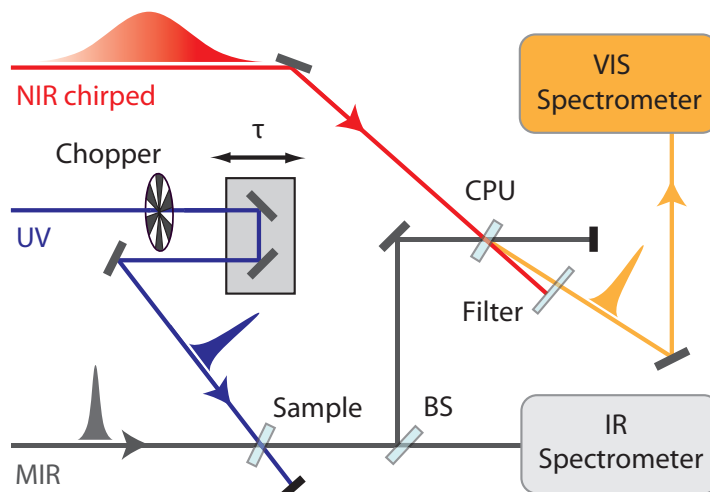
Detection of UV-induced absorption-change signals in the MIR spectral region before and after upconversion to the VIS regime. Figure adapted from Ref. [3]. © (2013) Optical Society of America.

5.1 Introduction

Very recently, Cheatum and coworkers [215] published a comparative study, examining the detection of 2D IR spectra based on a pulse-shaping apparatus, using direct singlechannel MCT detection and VIS multichannel detection via a complementary metal-oxide-semiconductor (CMOS) array, respectively. Unlike in CPU, bandwidth-narrowed 800 nm light was used for upconversion of the MIR pulses. With reference to their results, measurements presented and analyzed in Sec. 5.2 compare direct multichannel detection with an MCT array and multichannel detection with a CCD camera after upconversion with a strongly chirped NIR pulse. The goal is to determine which method is better suited to detect weak absorption-change signals on the order of a mOD or below with respect to the accessible spectral bandwidth, the spectral sampling, and the respective noise levels. Thereby, significant emphasis has been put on an experimental configuration that ensures a high degree of comparability (see Sec. 3.4). In Sec. 5.3, different phase-matching conditions in the CPU scheme are examined by varying the angle between the incident beams and the optical axis of the NC. Thereby, the possibility to optimize the shape of the CPU spectrum with respect to the detection range of the VIS detector is elucidated. Note that CPU data presented in Figs. 5.1 and 5.7 (c) has been recorded in the slow readout mode A-2048-CPU, whereas data presented in Figs. 5.2, 5.3, 5.4, 5.5, 5.6, and 5.7 (e) has been obtained with 1 kHz readout, i.e., mode B-1024-CPU (confer Table 3.1).

5.2 Accordance of spectra and noise analysis

The first part of the comparative study is carried out using the spectra shown in Fig. 5.1. In order to get a detailed picture of the MIR spectrum on the one hand, and not being restricted to 32 pixels in the direct MCT detection, the central spectrometer wavelength is scanned in steps of 1 nm and the signal is detected with the central pixel of the MCT array (blue). On the other hand, the upconverted spectrum is recorded with the VIS spectrometer. Thus, approximately the same spectral increment with both detection methods is obtained. Whereas the MCT measurement requires a few minutes of acquisition time, the corresponding CPU spectrum is obtained in less than one second of exposure (red). In contrast to measurements in the single-shot mode, spectrometer slit widths as small as possible are used and the housings are not flooded with dry air, in order to resolve distinct water vapor absorption lines convenient for calibration of the upconversion frequency (confer Sec. 3.4.3). Note that the stronger water vapor absorption in the CPU spectrum is due to a longer optical MIR path through water vapor in the laboratory atmosphere. Owing to the crystals' phase-matching capabilities, which are examined in greater detail in Sec. 5.3, the MIR spectrum (FWHM 154 cm^{-1}) gets upconverted to the VIS regime with a rather small narrowing of only 3 cm^{-1} of spectral bandwidth.
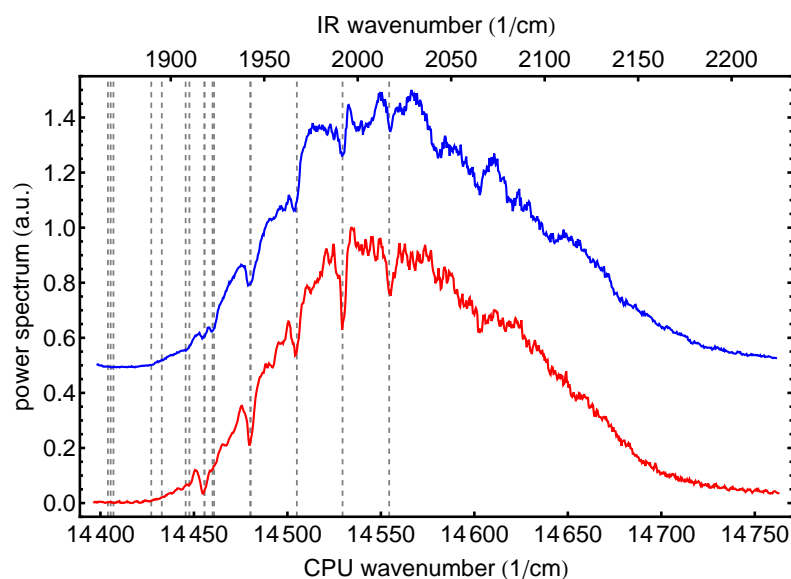
Figure 5.1: Evaluating CPU's upconversion bandwidth. MIR spectrum obtained with a single MCT pixel by scanning the central IR spectrometer wavelength in steps of 1 nm (blue, centered at 2028 cm^{-1}, FWHM 154 cm^{-1}, 100 laser shots averaged per step, 5 min total measurement time); MIR spectrum after upconversion and chirp correction detected via CCD camera (red, centered at 14554 cm^{-1}, FWHM 151 cm^{-1}, 300 ms exposure time); the frequencies of the 16 most intense water vapor lines taken from the GEISA database [163] are depicted as gridlines. Figure taken from Ref. [3]. © (2013) Optical Society of America.

To analyze the investigated detection methods when detecting ultrafast absorption changes, a 5 mM solution of $Co_4(CO)_{12}$ (**2**, CAS: 17786-31-1, Strem Chemicals, Inc.; see Fig. 5.2 for molecular structure) dissolved in CH_2Cl_2 is chosen as model system in all experiments presented in this chapter. Harris and coworkers [112] found that **2** undergoes two photochemical reaction pathways when being excited at 267 or 400 nm: besides the formation of CO-loss products arising from the dissociation of a single carbonyl ligand from the parent molecule, two rearrangement isomers are formed. These bridged intermediates, originating from cleavage of an apical-basal Co-Co bond, showed picosecond lifetimes. Compound **2** was considered to be appropriate to be employed in this comparison study owing to its rich photochemistry between 1800 and 2100 cm^{-1} and its high stability in dilute solutions. To gain an overview of the photochemical rearrangement dynamics of the molecular model system and to get a first impression of the capabilities of both detection methods, Fig. 5.2 displays the TA of **2** for pump–probe time delays up to 32 ps. Deviant from the default setting (confer Sec. 3.4), the central wavelength of the IR spectrometer was set to 4.95 μm in this particular measurement. The observed GSB signals of the parent compound as well as the positive absorption of upcoming photoproducts at lower energies are in agreement with the literature [112]. Note that each difference spectrum displays the average of only 1000 consecutively measured pump–probe pairs, already providing convincing data qualities. In order to analyze the spectral sampling and the respective noise levels of both detection methods in the following, data points of a
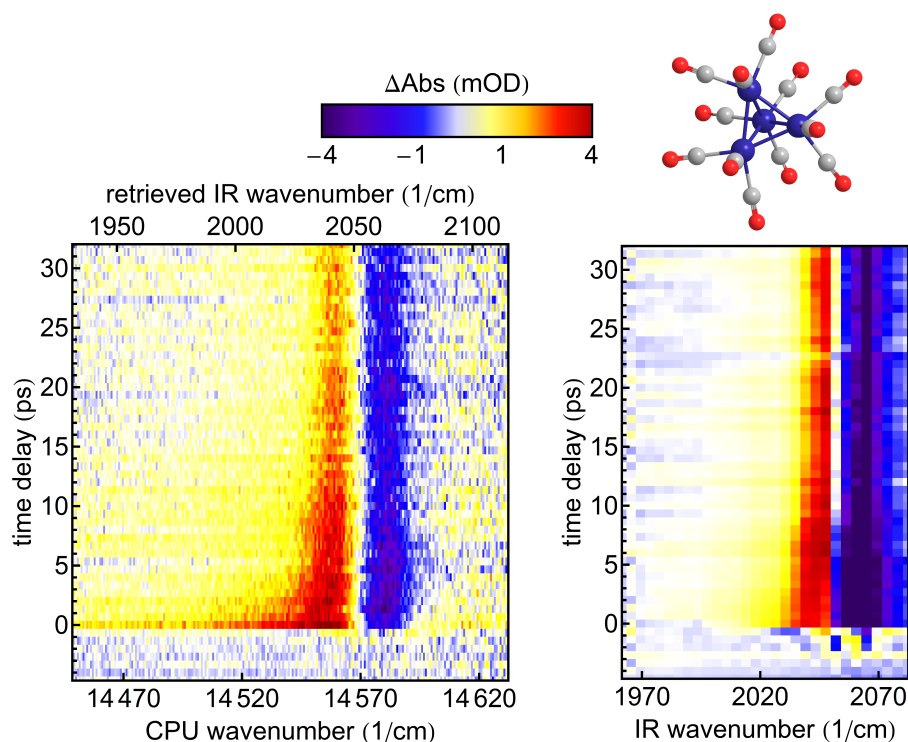
Figure 5.2: Transient absorption of compound 2 under 270 nm UV excitation. Data obtained via CPU (left) and multichannel MCT detection (right), respectively. For each time step 1000 pump–probe pairs are consecutively recorded with each detection method. No data interpolation was used in both graphics. The molecular structure of **2** is depicted in the top right corner. Figure adapted with permission from Ref. [3]. © (2013) Optical Society of America.

single difference spectrum will be scrutinized.

Using the laser settings with corresponding spectra from Fig. 5.1 at a slightly different upconversion frequency, analysis of 50000 difference spectra recorded with both spectrometers in the single-shot acquisition mode is performed. Both spectrometers cannot be read out for each laser shot simultaneously. Nevertheless, aiming at a high comparability, a measurement routine is used in which 50 loops of a sequence containing subsequent data acquisition of 2000 spectra with each spectrometer as well as data processing are recorded. Thereby, the influence of long-term laser fluctuations is minimized. Within two separate runs of the measurement routine under unaltered experimental conditions, the detection of spectra without a molecular signal, which corresponds to the baseline when calculating changes in optical density, as well as the influence of the liquid sample film between the windows in combination with a UV-pump interaction is examined. TA signals are calculated from consecutive background-corrected spectra followed by averaging. As depicted in Fig. 5.3, the resulting difference spectrum from the measurement with sample and pump-interaction after averaging over 25000 difference spectra at 6 ps pump–probe delay using CPU detection (red) illustrates the large detection range of the latter technique: for the present case, CPU detection covers more than 200 cm^{-1}, only being restricted to
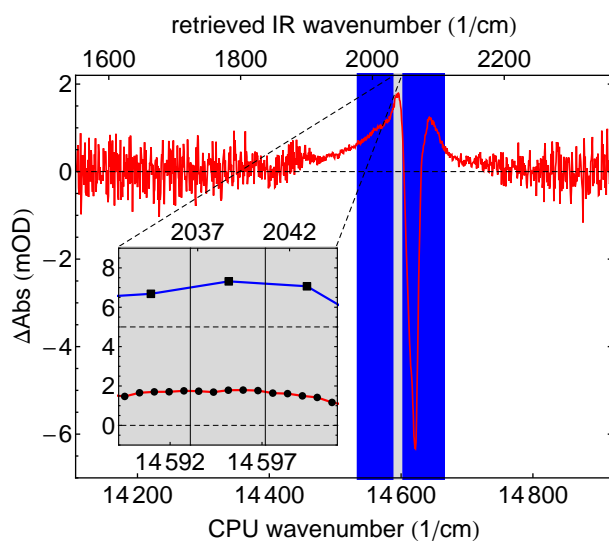
Figure 5.3: Evaluating the spectral sampling of both detection methods. Difference spectrum of compound **2** at 6 ps pump–probe delay under 270 nm UV excitation: data obtained by averaging 25000 consecutive pump–probe pairs using CPU detection (red); the blue-shaded area illustrates the full detection range of direct MIR detection; the inset depicts the spectral increment of both detection methods: data points of direct MIR detection via MCT array (blue) are shown with 5 mOD vertical offset; vertical lines confine data points which are used for analysis of individual noise levels (confer Figs. 5.4 and 5.5). Figure taken from Ref. [3]. © (2013) Optical Society of America.

the bandwidth of the upconverted spectrum, whereas the MCT detection is limited to approximately 130 cm^{-1} with the employed grating (indicated by the blue-shaded area). For MCT detection in a broader range, one has to change the grating position and repeat the measurement procedure. Especially in time-critical measurements, e.g., when samples tend to degenerate, this constitutes a significant disadvantage. Note that slightly different experimental settings result in minor deviations in the absolute values of changes in optical density with respect to Fig. 5.2. The individual data points in the inset of Fig. 5.3 illustrate the different spectral sampling. With respect to the direct MCT detection, the latter is increased by a factor five using CPU. Note that these values reflect a particular experimental situation. Using different grating settings or different array sizes, either the spectral bandwidth or the spectral sampling can be favored. Nevertheless, the higher flexibility of CPU detection is evident.

Table 5.1: Standard deviation of 50000 consecutively measured pump–probe pairs at 2039 cm^{-1} corresponding to the histograms shown in Fig. 5.4.

measurement conditions	no sample	sample and pump-interaction
MCT	2.7 mOD	3.7 mOD
CPU	8.1 mOD	8.9 mOD
CPU - 5 data points binned	7.1 mOD	7.7 mOD
CPU - spectra normalized	4.7 mOD	5.5 mOD
CPU - 5 data points binned - spectra normalized	2.5 mOD	3.1 mOD

For noise analysis, a single data point at 2039 cm^{-1}, which corresponds in the measurement with sample and pump-interaction to a positive TA signal of ≈ 2 mOD, reflecting overlapping terminal carbonyl stretches of transient photoproducts, is scrutinized. The

histograms in Fig. 5.4 illustrate the Gaussian distribution of 50000 consecutively measured pump–probe pairs. Besides the results for detection via MCT array (blue) and CPU (red), data points for an additional averaging of five adjacent CPU data points are calculated (green, confer area confined by vertical lines in the inset of Fig. 5.3), compensating for the unequal spectral coverage. The corresponding standard deviations are listed in Table 5.1. The additional binning reduces the standard deviation of CPU detection by approximately 13%. Nevertheless, with respect to MCT detection, the corresponding distributions are broadened by a factor 2.6 in the measurement with no sample and by a factor 2.1 in the measurement with sample and pump-interaction, respectively. The observed excess noise using CPU is in good agreement with the finding that the MIR OPA can run significantly more stable than the fundamental 800 nm laser output itself [94]. A rough estimate of the additional noise which is transferred to the CPU difference spectrum can be made by considering error propagation: thereby, the assumption that the CP is
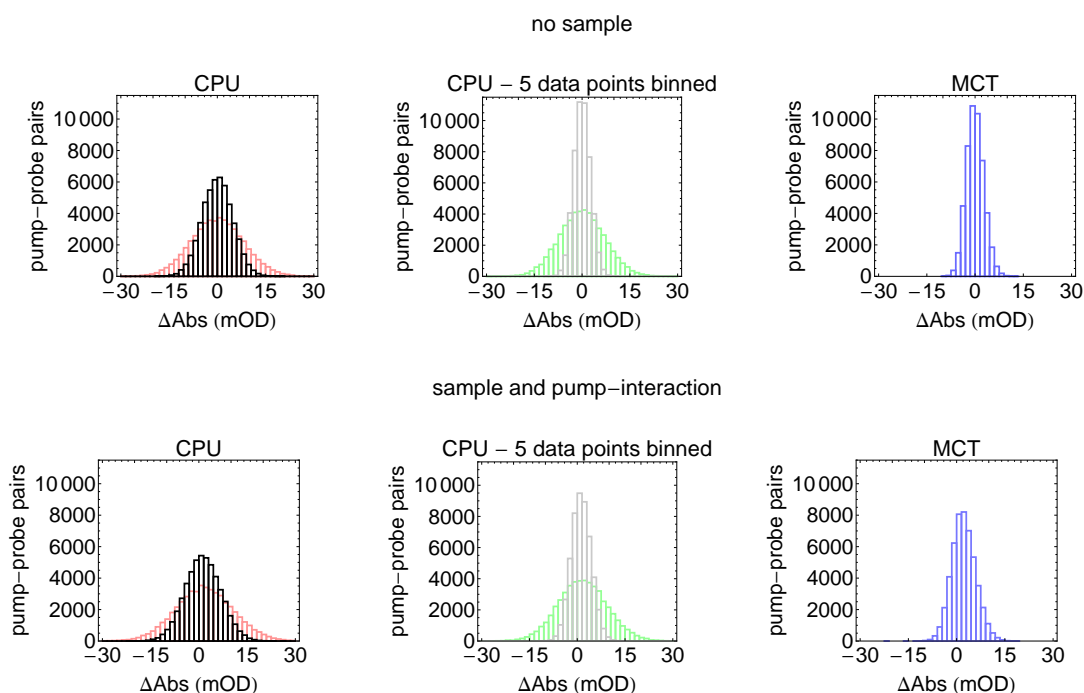
Figure 5.4: Noise analysis for possible MIR detection configurations—part one. Histograms illustrating the distribution of 50000 consecutively measured pump–probe pairs for the detection of the signal baseline (top row, no sample) and the detection of a molecular signal of ≈ 2 mOD at 2039 cm^{-1} (bottom row, sample and pump-interaction). Besides the histograms for CPU detection (left panels, red) and MCT detection (right panels, blue), representing a single data point, the results for an additional binning of five adjacent CPU data points are shown (middle panels, green). Distributions resulting after normalization of individual spectra with their integrated spectral intensity are shown for CPU detection (left panels, black) and CPU detection with an additional binning of five adjacent data points (middle panels, gray). Figure taken from Ref. [3]. © (2013) Optical Society of America.

2.4-times less stable than the MIR pulse corresponds to the factor which was observed in the measurement with no sample. Note that these results represent the detection of TA signals in the vicinity of the spectral maximum: up to 6000 counts per data point per single shot are detected in the 16 bit range of the CCD camera and the integrated photodiode signals are held below 60% of the analog-digital-conversion range using an additional ND attenuator (0.3 OD) in front of the IR spectrometer. Following the assumption that the noise in the CPU approach is dominated by fluctuations of the CP, the noise level can be reduced drastically by normalization of individual CPU spectra with the spectrally integrated signal for each laser shot. The resulting standard deviations of 50000 pump–probe pairs after normalization of individual CPU spectra can be seen from Table 5.1, corresponding distributions are shown in Fig. 5.4 (black and gray). After correction for intensity fluctuations, the standard deviation obtained using CPU with an additional binning of five adjacent data points even falls slightly below the value obtained using direct MCT detection. The CCD camera is used far from its saturation, so that increasing the CPU signal, either by employing a higher intensity of the CP or the MIR beam, should further reduce remaining noise contributions. Note that normalizing the probe spectra reduces the noise, but will affect the absolute ΔOD value because of different spectrally integrated probe signals in the presence or absence of a pump pulse. However, this scaling can be accounted for in the data evaluation.
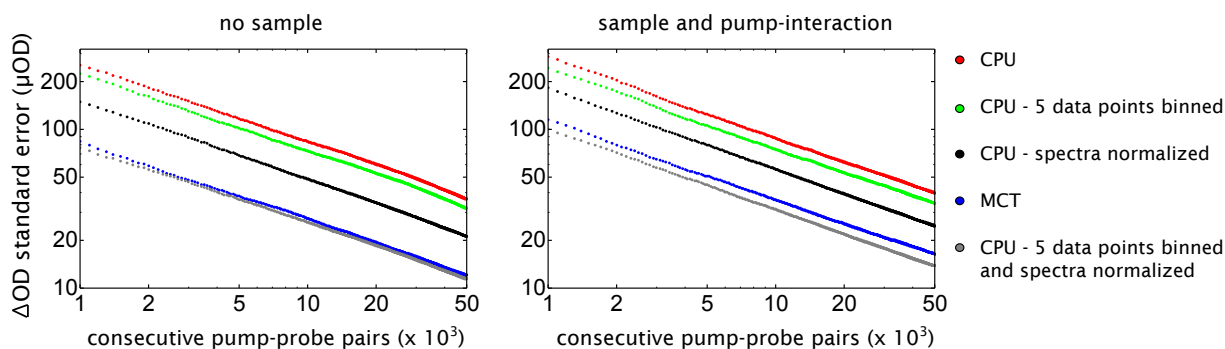
Figure 5.5: Noise analysis for possible MIR detection configurations—part two. ΔOD noise level of a single data point at 2039 cm^{-1} when detecting the signal baseline (left panel, no sample) or a molecular signal of ≈ 2 mOD (right panel, sample and pump-interaction): standard error versus the number of considered background-corrected pump–probe pairs using MCT detection (blue), CPU (red) or CPU with an additional binning of five adjacent data points (green). Noise levels resulting after normalization of individual spectra with their integrated spectral intensity are shown for CPU detection (black) and CPU detection with an additional binning of five adjacent data points (gray). Note that these graphs have a double-logarithmic scale. Figure adapted with permission from Ref. [3]. ©(2013) Optical Society of America.

Providing a measure for the time which is necessary to obtain a certain noise level in the detection of changes in optical density, Fig. 5.5 displays log-log-plots of the ΔOD standard error as a function of the considered, consecutively measured, pump–probe pairs for baseline-detection (left panel, no sample) and the detection of TA signals (right panel,

sample and pump-interaction). It shall be emphasized that each data point reflects the evaluated standard error after a particular number of pump–probe pairs, rather than just an extrapolation of the standard error based on the standard deviation of 50000 pump–probe pairs. The MCT detection exhibits considerably lower noise levels than detection via CPU. For instance, to reach a level of 50 µOD in the measurement with sample and pump-interaction using MCT detection, only 5200 pump–probe pairs are required, which is in good agreement with values reported in the literature [103]. In comparison, 31700 pump–probe pairs acquired using CPU provide the same data quality. With an additional binning of five data points, this value is reduced to 23100. Other noise levels can analogously be evaluated by looking at the intersections of the measured data with horizontal lines representing the desired data quality. Corresponding to the consequences on the standard deviation (confer Table 5.1), normalization of CPU spectra with the spectrally integrated signal leads to a reduction of the number of pump–probe pairs required for a certain noise level, so that 12600 pump–probe pairs are needed in CPU with normalized spectra to reach 50 µOD in the measurement with sample and pump-interaction. For CPU detection with an additional binning of five adjacent data points, the same noise level is reached after 4000 pump–probe pairs. As reported elsewhere [215, 216], and confirmed in a separate measurement with the setup used in this chapter, dark noise contributions of the detectors are small compared to laser shot-to-shot fluctuations and are neglected in the following analysis of individual noise contributions.

Figure 5.6: Noise analysis for possible MIR detection configurations—part three. ΔOD standard error as a function of the spectral position: data obtained via MCT (blue) and CPU detection (red) after averaging 25000 consecutive pump–probe pairs when detecting the signal baseline (solid lines, no sample) or a molecular signal (dashed lines, sample and pump-interaction, confer difference spectra in Fig. 5.3); the CPU curves with binned data points or with normalized spectra, or with both, are not shown for clarity; the corresponding CPU spectra, with sample (light red) and without sample (light gray), are shown in the background. Figure taken from Ref. [3]. © (2013) Optical Society of America.
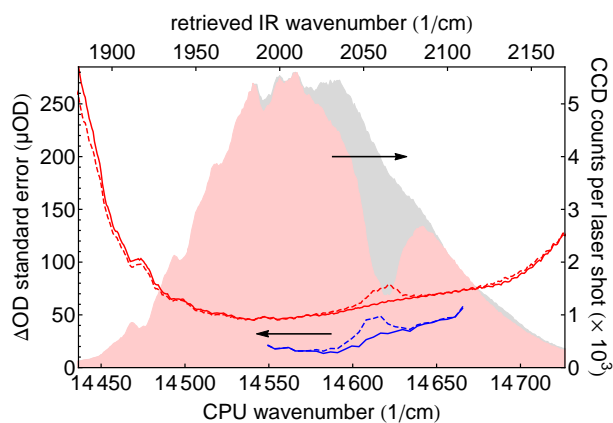
In Fig. 5.6, the ΔOD standard error is plotted versus the spectral position. With this, the influence of both the different signal strengths (confer CPU spectra in the background: respective CCD counts are depicted on the right vertical axis) and the sample under pump-interaction can be dissected. Within the FWHM of the spectrum, both detection methods exhibit almost constant baseline noise levels. Note that with MCT detection (blue), only the higher energetic part of the MIR spectrum was probed. In the measurement with sample and pump-interaction, small deviations arise around 2060 cm^{-1}. This can be

attributed to the reduced spectral intensity due to the absorption of the parent complex (≈ 0.43 OD at 2060 cm^{-1}) and the pump-induced changes in optical density. In the other regions, no deviations between both measurement runs emerge. Consequently it can be inferred that no additional noise is added by the liquid sample film.

In [215], Cheatum and coworkers found an improved signal-to-noise ratio when measuring the average of 115 2D IR spectra using CMOS array detection after upconversion instead of direct MIR detection. Their study differs from the study presented in this chapter by the facts that no chirped NIR pulse was used for upconversion, that a different VIS detector was employed, and that MIR signals were recorded with only a single MCT pixel. The measurement times to record 2D IR spectra were shortened by a factor 60 using CMOS array detection, and in this way, additional noise contributions originating from long-term laser drifts are reduced. The results presented in this chapter also confirm that noise levels comparable to direct MCT measurements can be achieved when the detection is done after upconversion. Note that all reported noise levels result from the same number of laser shots under unaltered measurement conditions representing single data points.

5.3 CPU phase-matching characteristics

The alignment of the CPU crystal is normally optimized to upconvert a given MIR spectrum as effectively as possible. However, promising possibilities also arise when the crystal's phase-matching is set differently. Imagine a situation where the features of interest are spectrally far apart and merely covered by the edges of the CPU spectrum. Whereas the central part of a bell-shaped spectrum thereby potentially saturates the detector, the spectral edges suffer from a low number of counts resulting in aggravated noise levels. In the following, the simultaneous detection of TA signals separated by more than 200 cm^{-1} using a modified CPU spectrum, of which the central part is selectively lowered by means of a changed phase-matching configuration, is demonstrated. For this purpose, a MIR spectrum which is centered at 1940 cm^{-1} is used [Fig. 5.7(a)], covering absorption bands of compound **2** at 1860 and 2060 cm^{-1} [confer MIR absorption spectrum in Fig. 5.7(b)].

The uniaxial MgO(5%):LiNbO$_3$ crystal is suited for sum-frequency mixing of 800 nm pulses with MIR pulses around 5 μm. Usually, a specific crystal cut angle θ is chosen with respect to the spectral range of interest [confer Eq. (2.2.9)]. Optimized for MIR pulses centered at 5 μm, the actual cut angle of the employed crystal is $\theta = 45.4°$ (confer Sec. 3.4.2). Nevertheless, one is able to mimic different configurations by rotating the crystal and thereby changing the angle α between the incident beams and the optical axis of the crystal. Thereby the actual change of the angle between the optical axis of the crystal and the propagation direction of the beams within the crystal ($\Delta\theta$) is determined by Snell's law. Resulting CPU spectra for different crystal settings are shown in Fig. 5.7(c). In this series, the crystal was rotated in steps of $\Delta\alpha = 0.7°$ in both directions starting at the optimal phase-matching configuration (red, $\theta = 45.5°$). Note that due to the spectral position of the given IR spectrum (central wavelength of 5.2 μm instead of 5.0 μm), the
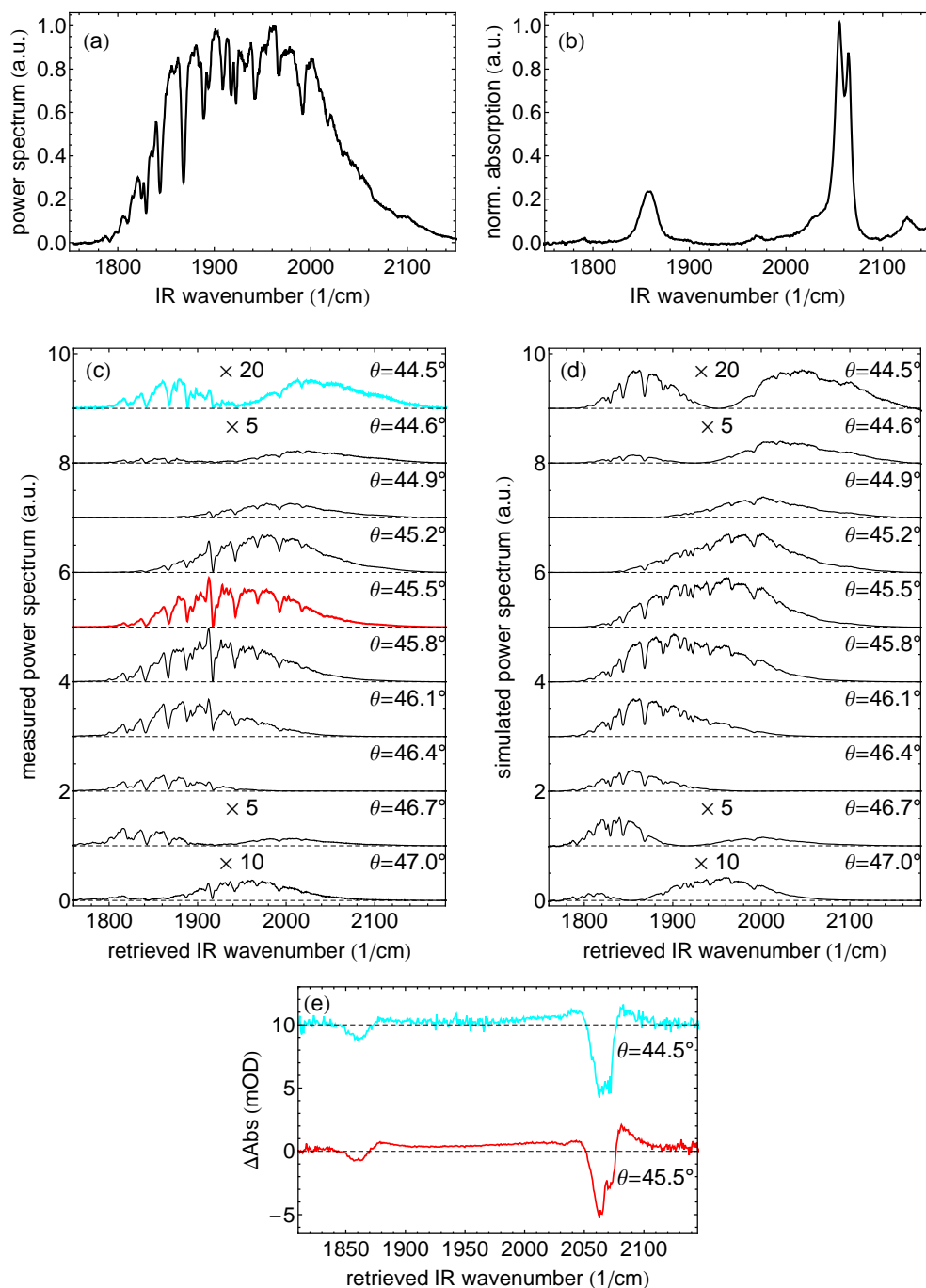
Figure 5.7: Exploiting CPU's phase-matching capabilities. (a) MIR spectrum obtained with a single MCT pixel by scanning the central IR spectrometer wavelength in steps of 1 nm (centered at 1940 cm^{-1}, FWHM 185 cm^{-1}, 100 laser shots averaged per step). (b) MIR absorption spectrum of compound **2** dissolved in CH$_2$Cl$_2$. (c) Measured CPU spectra at different phase-matching angles. (d) Simulated CPU spectra at different phase-matching angles. (e) Difference spectra of compound **2** at 6 ps pump–probe delay: data obtained by averaging 100000 consecutive pump–probe pairs at CPU phase-matching angles of $\theta = 45.5°$ (red) and $\theta = 44.5°$ (cyan, 10 mOD vertical offset). Figure taken from Ref. [3]. © (2013) Optical Society of America.

latter configuration requires an angular offset of $\Delta\theta = +0.1°$ with respect to the crystals cut angle. For increasing variations from the optimal setting, the center of the CPU spectrum shifts either to the lower or to the higher energetic regime. Aberrant from this trend, larger angles lead to the formation of double peak spectra, revealing counts primarily on the edge of the initial MIR spectrum. At $\theta = 44.5°$ an almost symmetric case is reached. Due to the reduced efficiency of upconversion, the maximum single-shot intensity is thereby reduced by approximately a factor of 20 with respect to the optimum case, whereas the intensity at the spectral edges remains almost unchanged.

To support the experimental findings, the SFG efficiencies of a 450 μm thick MgO(5%):LiNbO$_3$ crystal for different phase-matching angles when mixing MIR light with monochromatic 800 nm light in a type I SFG arrangement are calculated. Applying the Sellmeier coefficients from [217] and using the wavevector mismatch [confer Eq. (2.2.4)]

$$\Delta k = k_{\text{NIR}} + k_{\text{MIR}} - k_{\text{SFG}} \ , \tag{5.3.1}$$

the intensity of the sum-frequency signal [confer Eq. (2.2.5)] is given by

$$I_{\text{SFG}} = \frac{8d_{\text{eff}}^2 \omega_{\text{SFG}}^2 I_{\text{NIR}} I_{\text{MIR}}}{n_{\text{NIR}} n_{\text{MIR}} n_{\text{SFG}} \epsilon_0 c^2} L^2 sinc^2\left(\frac{\Delta kL}{2}\right) \ , \tag{5.3.2}$$

where d_{eff} is the nonlinear efficiency parameter, ω_{SFG} the carrier angular frequency of the upconverted field, I_{NIR} and I_{MIR} the intensities of the incident fields, and n_{NIR}, n_{MIR}, and n_{SFG} the respective refractive indices [41]. Consequently, the free parameters are λ_{MIR} and the phase-matching angle θ. CPU spectra after upconversion under different phase-matching conditions can be simulated by multiplying the MIR spectrum from Fig. 5.7(a) by the corresponding efficiency curves. Fig. 5.7(d) shows simulated CPU spectra under phase-matching angles corresponding to the series which was conducted experimentally [confer Fig. 5.7(c)]. Taking account of the different optical MIR paths resulting in different manifestations of water vapor absorption lines, the simulations are in excellent agreement with measured spectra.

The CPU intensities in the investigated setup are in general too low to saturate the CCD detector. Nevertheless, one can scrutinize different phase-matching settings when detecting TA signals. Therefore, difference spectra of 100000 pump–probe pairs using CPU spectra at $\theta = 45.5°$ (red) or $\theta = 44.5°$ (cyan), respectively, are recorded. Both difference spectra show analogue results, revealing the GSB signals of the parent complex at 1860 and 2060 cm^{-1} [Fig. 5.7(e)]. Whereas the noise level in the inner part of the detection range is significantly degraded under detection at $\theta = 44.5°$, the noise level at the spectral edges is comparable. Such a scenario could be beneficial when saturation of the detector in regions where the MIR is most intense has to be circumvented.

5.4 Conclusion

Overall, this comparative study confirms that CPU constitutes a powerful alternative to direct multichannel MCT detection. The accordance between MIR spectra before and after upconversion to the VIS regime was verified, thereby observing only negligible changes in the spectral shape and the spectral bandwidth. In an exemplarily chosen UV-pump/MIR-probe experiment in the liquid phase, the individual advantages and disadvantages of both methods when detecting TA signals on the order of a few mOD were examined. Although intensity fluctuations of the CP are transferred to MIR spectra in the additional nonlinear upconversion process, CPU spectra after normalization with the integrated spectral intensity showed noise levels similar to direct MCT detection. Moreover, CPU scores with the high pixel numbers of the easy-to-handle and more cost-effective CCD detectors. In most cases, the CPU detection bandwidth as a limiting factor can almost be excluded. Future applications of CPU might also benefit from the possibility to adapt the shape of the upconverted spectrum by using different phase-matching configurations, thereby avoiding too high signals in very intense spectral regions.

Ultrafast dynamics of CO- and NO-releasing molecules

Searching for a controllable source of gasotransmitters such as carbon monoxide (CO) or nitric oxide (NO) in biological applications, transition-metal complexes capable of releasing these small molecular messengers upon photoactivation have attracted significant attention [218]. The first part of this chapter (Sec. 6.1) is devoted to the photolytic dynamics of a water-soluble manganese tricarbonyl complex studied by UV-pump/MIR-probe TA spectroscopy. TD-DFT calculations presented in Sec. 6.1.2 were done by Prof. Dr. Ulrich Schatzschneider, DFT calculations presented in Sec. 6.1.3 by Dr. Philipp Rudolf. The study, whose extended content is moreover discussed in Refs. [129, 219], was published in Refs. [4, 220]. In the second part of this chapter (Sec. 6.2), the photolytic dynamics of a molybdenum complex containing two carbonyl and one nitrosyl ligand are investigated by employing UV-pump/VIS-probe and UV-pump/MIR-probe TA spectroscopy. Referring in particular to results presented in Sec. 6.1, the question is addressed of how the photodynamics in mixed carbonyl-nitrosyl compounds differ from systems with only carbonyl ligands. DFT calculations discussed in Sec. 6.2.2 were done by Prof. Dr. Ulrich Schatzschneider. The study will be published in Ref. [2].
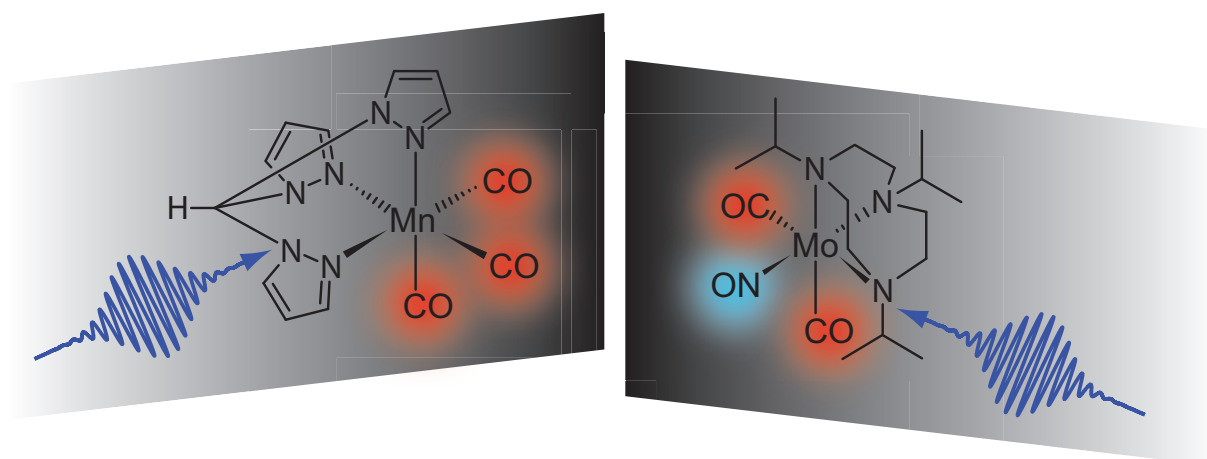
Investigated complexes containing ligands that are potentially released via UV excitation.

6.1 Photochemistry of a manganese-tricarbonyl complex

6.1.1 Introduction

Apart from its bad reputation being a silent killer, carbon monoxide (CO) exhibits a huge potential as a therapeutic agent. Recent studies demonstrated the beneficial physiological effects of CO, a gasotransmitter in higher organisms which is endogenously produced from heme by the activity of heme oxygenase (HO) enzymes [221–223], affecting important processes as inflammation, proliferation, or apoptosis. Striving for a controllable in-situ source of CO, so-called *CO-releasing molecules* (CORMs) are of growing interest with regard to biological applications [25, 26, 224–227]. CORMs are characterized by their ability to specifically accumulate in the targeted tissue where they first behave as a stable CO prodrug. The CO release itself—depending on the molecular system—is then triggered via ligand exchange reactions [228, 229], enzyme activation (so-called *ET-CORMs*) [230, 231], or via light (so-called *PhotoCORMs*) [232–234]. The latter class of molecules shows a tremendous potential for biological applications, particularly benefiting from the possibility to activate dark-stable PhotoCORMs via focused light pulses in a spatially and temporally controlled fashion. A highly promising approach in this regard are so-called *well-defined i*CORMs [235]. For this special type of PhotoCORMs, unwanted reactions of the metal complex formed after ligand dissociation can be excluded since a chelating ligand fills the free coordination site intramolecularly providing an *inactivated* CORM with well-characterized properties. Up to now, however, only little is known about the exact mechanism of ligand dissociation from the metal coordination sphere of PhotoCORMs.

A metal carbonyl whose photodissociation has been studied under various experimental conditions is iron pentacarbonyl $Fe(CO)_5$. Its CO releasing properties have been elucidated in the gas phase via transient ionization with different laser wavelengths [236–238] or by transient electron diffraction [239], and in solution with IR [240–243] or X-ray [244, 245] TA spectroscopy. In the gas phase, depending on the excitation wavelength employed, it is possible to induce the loss of several to all CO ligands, whereas in the liquid phase, depending on the solvent environment employed, $Fe(CO)_5$ releases only one or two CO ligands on an ultrafast time scale after UV excitation [241–243]. Moreover, the ultrafast photochemical dissociation of CO from metal carbonyls in the liquid phase has been studied for various other compounds that differ with respect to the number of CO ligands, the number of bonded metal atoms, and the presence of additional organic ligands [246–259]. Already 20 years ago, Anfinrud and coworkers conducted seminal work scrutinizing the CO release from heme proteins in the biologically most relevant solvent water [97, 260]. However, nothing is known about the ultrafast dynamics of CO photolysis from metal carbonyls in water, which is particularly surprising for the case of PhotoCORMs.

This section is devoted to the ultrafast photochemistry of the PhotoCORM $[Mn(CO)_3(tpm)]Cl$ with tpm = tris(2-pyrazolyl)methane [**3**, see Fig. 6.1(a)] studied by UV-pump/MIR-probe TA spectroscopy (confer Sec. 3.4 for experimental details). This

photolytically activatable CORM has proven to be selective and cytotoxic to cancer cells [261], thereby showing the ability to release two [261] or even all three CO ligands [262] when being irradiated with UV light for several minutes. Furthermore, it fulfills the requirements of being soluble in water and stable in air and water. Due to the strong absorption of water around 1800–2100 cm^{-1} [263], complex **3** (synthesis has been done by Dr. Christoph Nagel according to Ref. [261]) is studied in heavy water (D$_2$O), whereby sample concentrations of 3–5 mM were used in time-resolved measurements. Besides a strong absorption towards wavelengths below 250 nm, complex **3** exhibits two distinct absorption bands at 265 nm and 348 nm [see Fig. 6.1(b)]. In the following, both bands will be addressed in TD-DFT calculations and by studying the molecule's ultrafast CO releasing properties with pump pulses centered at 264 nm and 347 nm, respectively.

6.1.2 Results of TD-DFT calculations

The results from TD-DFT calculations, performed for the [Mn(CO)$_3$(tpm)]$^+$ cation in the gas phase, are visualized in Appendix C.1. Regarding the highest occupied molecular orbitals (HOMOs), one finds three almost degenerate states with minor contributions from metal-carbon bonding but a high electron density present at the manganese atom (three doubly occupied Mn d orbitals, as expected for a low-spin 3d^6 system). The important question of which transition can be induced by which pump wavelength [confer Fig. 6.1(b)] is addressed by calculating the molecule's first 30 singlet excited states.

Considering the lowest unoccupied molecular orbitals (LUMOs) which are accessible with both pump wavelengths, one finds electron density distributions either located on the tpm ligand (LUMO and LUMO+1) or delocalized over all three CO ligands (LUMO+2 to LUMO+5). In the first case, CO photolysis after UV excitation seems to be less likely. However, the second case implies that the excess energy introduced by a 264 nm photon is sufficient to trigger the release of several CO ligands [250]. LUMO+2 and LUMO+3, which can be reached after absorption of a 347 nm photon, exhibit a high electron density at the metal atom and one or two of the CO ligands. Hence, owing to the anti-bonding character, it is also likely that 347 nm excitation will trigger CO release.

For comparison, one may consider the photochemical properties of CpMn(CO)$_3$ compounds (Cp=cyclopentadienyl derivatives of the form C$_5$H$_4$Y, the simplest being C$_5$H$_5$). Independent of the UV excitation wavelength, a quantum yield of 1 was found for the release of one CO ligand in various organic solvents [264], whereas a quantum yield of 0.65 was found in the non-polar solvent isooctane [265]. In alkane solution, the compound exhibits two distinct UV absorption bands: one at around 250 nm, which was assigned to an intraligand $\pi \rightarrow \pi^*$ transition in the arene ring [266], and another band in the region around 325–350 nm, which was assigned to a Mn $\rightarrow$ Cp charge-transfer (CT) transition with some Mn $\rightarrow$ CO CT character. Interestingly, it was shown that irradiation of the dicarbonyl species, i.e., the compound which has already released one CO ligand, can lead to further CO release [267]. If this is also possible in the case of complex **3** studied within this section will be tested a UV-pump/UV-repump TA experiment (see below).

6.1.3 Results of DFT calculations

In the MIR spectral region, complex **3** exhibits two absorption bands originating from the symmetric CO stretching vibration (2051 cm^{-1}) and the antisymmetric CO stretching vibration (1958 cm^{-1}), which is degenerate owing to the molecule's C_{3v} symmetry resulting from the facially-ligated octahedral complex structure [confer Fig. 6.1(a) and (c)]. In order to assign the spectral positions of possible products formed after UV excitation, DFT calculations have been carried out to determine the wavenumbers of the corresponding CO vibrations (Gaussian09 [268], density functional method B3LYP 6-311+G(d,p) with the optimal scaling factor from Ref. [269]). The results in each case consider the lowest multiplicity state of an unaltered complex as well as mono- and dicarbonyl species where solvent molecules have replaced the CO ligands (see Appendix C.1). Overall, it can be deduced that spectral signatures of CO loss products should arise red-shifted with respect to the CO stretch spectrum of the intact molecule. Besides the formation of CO loss products, UV excitation might also induce the cleavage of a Mn-N bond which—if the molecule does not directly reform—in turn might lead to the formation of a carbene isomer with a Mn–C bond. Calculating a carbene isomer reveals symmetric and antisymmetric CO stretching vibrations which are significantly shifted towards lower wavenumbers compared to the N-coordinated pyrazole (1978 versus 2036 cm^{-1} and 1915/1920 versus 1943 cm^{-1}). The formation of a carbene species, however, is less likely owing to a significantly reduced spectral separation of the corresponding CO modes (61 cm^{-1} in the carbene isomer versus 90 cm^{-1} for the pyrazole binding mode).

6.1.4 Transient absorption measurements

The transient map depicted in Fig. 6.1(d) visualizes the TA of **3** upon 264 nm excitation in the MIR spectral region. As discussed in Sec. 2.4.2, around time zero, TA measurements may contain several signal contributions which do not reflect very early dynamics of the sample itself. Here, PFID contributions arise for negative pump–probe delay times at the spectral positions of the CO vibrations of the intact complex. Furthermore, the absorption of solvated electrons in D$_2$O [270] overlapping with contributions from the coherent artifact give rise to a broad signal contribution within the first few picoseconds. Hence, the latter effects mask ultrafast solvation processes in which potentially free coordination sites may be filled with solvent molecules. Only minor differences between transient maps obtained with 264 nm or 347 nm pump pulses became evident (TA data obtained using 347 nm pump pulses is presented in Refs. [129, 219]).

In the following, the ultrafast dynamics of **3** are discussed on the basis of transients at selected wavenumbers [see Fig. 6.1(e)]. Most obvious, two GSB signals appear at the spectral position of the CO vibrations of the intact complex that persist over the entire pump–probe delay range (confer transients at 1951 cm^{-1} and 2052 cm^{-1}, respectively). Hence, strong indications for ultrafast light-triggered CO loss are found. The GSB signals are accompanied by the appearence of two positive TA signals at around 1857 cm^{-1} and 1980 cm^{-1} that also persist over the entire pump–probe delay range (confer tran-
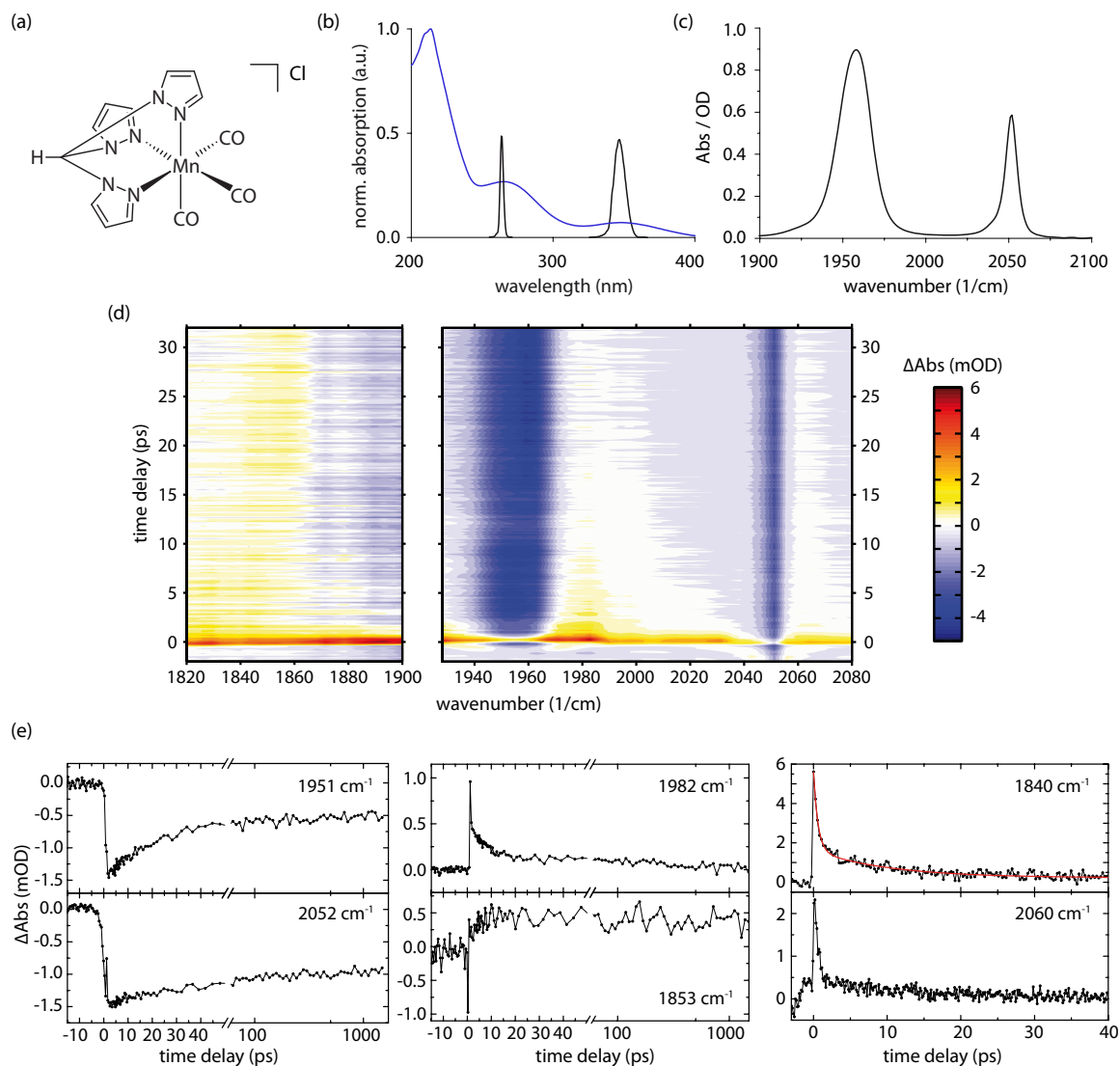
Figure 6.1: Photochemical properties of the investigated manganese-tricarbonyl CORM (3) in heavy water. (a) Molecular structure. (b) UV/VIS absorption spectrum together with spectra of the employed pump pulses. (c) MIR absorption spectrum. (d) MIR transient absorption under 264 nm excitation covering early dynamics. (e) MIR transient absorption for selected wavenumbers; except for the transient at 2060 cm^{-1} which reflects dynamics after 264 nm excitation, 347 nm pump light was used; a linear-logarithmic abscissa is used to visualize the full temporal probing window. Direct multichannel MCT detection has been used to record MIR probe spectra. Figures adapted from Ref. [4]. ©(2013) American Chemical Society.

sients at 1853 cm^{-1} and 1982 cm^{-1}, respectively). In accordance with IR absorption measurements on long-lived intermediates [262, 271] and by comparison with the results from DFT calculations (confer Appendix C.1), these newly formed absorption bands are assigned to the absorption of a stable (singlet) dicarbonyl species which is formed after ultrafast photochemical dissociation of one CO ligand whose empty site is filled by a solvent molecule.

Already half a UV photon's energy is sufficient to break the Mn–CO bond in Mn-containing CORMs [272]. As no indications for the release of two CO ligands are found, the excess energy provided by the pump photon will be distributed among vibrational modes of the product which is formed after loss of one CO ligand, i.e., the dicarbonyl species. Since hot CO bands are absent in the photolysis of dicarbonyls [249], excess energy will be transferred to low-frequency modes which afterwards will couple to the dicarbonyl's CO stretch before vibrational relaxation has occurred [251]. This behavior is reflected in dynamics observed at roughly 1980–2000 cm^{-1} and at around 1857 cm^{-1}, where cooling leads to narrowing of initially broadened product absorption bands [confer yellow colored signals in Fig. 6.1(d)]. A biexponential fit of the transient at 1840 cm^{-1} [see Fig. 6.1(e)], i.e., slightly red-shifted with respect to the relaxed spectral position of the newly formed (lower energetic) product band, reveals two time constants [(0.6±0.1) ps and (10±1) ps]. The sub ps constant is in line with solvation time scales in water [273]. However, a clear assignment is aggravated owing to unwanted effects at early pump–probe delay times as discussed above. The second time constant provides evidence for cooling of hot photoproduct molecules and highlights the unique properties of water: while the relaxation of low-frequency modes of hexacarbonyls in alkanes was reported to take place in a few tens of picoseconds [251, 252], relaxation of **3** in aqueous solution can proceed significantly faster due to effective water-assisted cooling. In general, water offers a variety of ways for reorientational dynamics and a highly dynamical solvation shell. Particularly in the case of hot CO ligands, water's ability to accept vibrational energy is manifested in significantly faster relaxation times [274, 275] compared to alkaneous solutions [251, 252].

The results presented so far revealed that **3** releases only one CO ligand on an ultrafast time scale. However, for some molecules, geminate recombination, i.e., a rebinding of the initially photolyzed CO ligand, prevents the formation of a stable CO loss product. Such a behavior was for instance found for $Cr(CO)_6$ in alkanes—being more likely the smaller the solvent molecules used [252]. In general, the process of geminate recombination is likely to be manifested in transients representing GSB signals. The transient at 1951 cm^{-1}— associated with the antisymmetric CO stretch of **3**—exhibits a GSB recovery within the first tens of picoseconds. Geminate recombination occurs within 1 ps accompanied by a spectral broadening owing to the coupling of the CO band to low-frequency modes. Hence, the recovery at this wavenumber again reflects cooling dynamics instead of recombination dynamics [252]. Furthermore, the recovery may also partially be caused by the overlapping product absorption band of the dicarbonyl species at around 1980 cm^{-1}. However, geminate recombination can be seen from the transient at 2052 cm^{-1}—associated with the symmetric CO stretch of **3**: looking at the spectral positions of putative photoproducts obtained from DFT calculations (Appendix C.1), no wavenumber above 2000 cm^{-1} is found; hence, the positive signal at 2060 cm^{-1} [confer transient in Fig. 6.1(e)] originates

from a line broadening stemming from molecules formed after geminate recombination. This signal contribution can be seen around the GSB signal—reflecting molecules which have released one CO ligand—and is evident as long as the molecule is vibrationally hot.

In general, the information provided by a single TA map does not allow one to distinguish the scenario of geminate recombination from the possibility that UV excitation does not induce CO release at all. The latter case is supported by TD-DFT calculations for certain transitions and experimentally indicated by two findings which shall be discussed in the following. The signature of an excited yet intact complex **3** at 2060 cm^{-1} appears to be more pronounced when using 264 nm instead of 347 nm pump photons (confer TA data presented in Refs. [129, 219]). For the case that recombination can be assumed to be independent of the pump wavelength, minor CO release can be expected for 264 nm pump photons as possible transitions involve LUMOs whose electron density is mostly located at the tpm ligand. The conclusion that not every UV excitation eventually leads to CO release is furthermore supported by the fact that the overall yield of photolysis for different pump wavelengths does not match the ratio of the molecule's linear absorption at the respective spectral positions [confer Fig. 6.1(b)]. To further support this conclusion, it might be revealing to assess the photolysis excitation spectrum of **3**, which, however, has not been done hitherto.

The question if further UV excitation of the dicarbonyl photoproduct can induce the loss of one or two of the remaining CO ligands is addressed in a pump–repump TA experiment. At this, an interferometer setup is used to create UV double pulse sequences with a temporal separation of 200 ps, whereby the sample's MIR absorption is probed 200 ps after the interaction with the repump pulse (for further details see Refs. [129, 219]). Both for 264 nm and for 347 nm pump–repump pulse pairs, no indications for the formation of a new photoproduct have been observed. Several reasons may be offered to explain why sequential CO release upon repeated UV excitation is not possible: first, UV excitation of the dicarbonyl photoproduct causes no bond cleavage at all; second, UV excitation of the dicarbonyl photoproduct leads to the photochemical dissociation of the D$_2$O ligand which has taken the free coordination site after CO photolysis in the first interaction step (confer Ref. [264] for the case of CpMn(CO)$_3$). As rebinding dynamics of the D$_2$O ligand would precede faster than the experiment's time resolution, dynamics caused by the repump pulse would not become evident; third, while less likely, the dicarbonyl photoproduct does not absorb in the UV spectral range (confer Ref. [265], discussing red-shifted electronic absorption bands of CpMn(CO)$_3$ after photochemical dissociation of one CO ligand). Future UV-pump/UV-probe TA experiments could elucidate the latter uncertainty.

6.1.5 Conclusion

To sum up this section, the primary processes of CO release from a manganese-tricarbonyl CORM in aqueous solution have been investigated using UV-pump/MIR-probe TA spectroscopy with different UV pump wavelengths supported by linear spectroscopy methods and quantum chemical calculations. It became evident that within the first few picoseconds after UV excitation one CO ligand is photochemically dissociated and some molecules

undergo geminate recombination. In the case of permanent CO loss, water molecules will fill the free coordination site. Pump induced excess energy is transferred to low-frequency vibrational modes leading to cooling dynamics on a 10 ps time scale in the newly formed dicarbonyl and the recombined CORM, respectively. No dependence of the initial photolysis of the CORM on the UV pump wavelength has been observed. Overall, the study allows the conclusion that further loss of CO most likely necessitates manganese oxidation as suggested in the literature [262].

6.2 Photochemistry of a carbonyl-nitrosyl molybdenum complex

6.2.1 Introduction

As diatomic molecules, CO and nitric oxide (NO) are probably the smallest natural products and signaling factors in biological systems [276, 277]. Like CO, NO is generated endogenously by enzymatic processes [223] in particular originating from nitric oxide synthase (NOS) conversion of L-arginine [278]. Both molecules have an important physiological function, in particular in response to oxidative stress, and their signaling pathways are heavily intertwined [279, 280]. Synthetic NO donors have been explored for their therapeutic potential long before the endogenous production of NO was even known, dating back about 150 years to the discovery of the beneficial activity of organic nitrates and nitrite esters in the treatment of angina pectoris [281, 282]. In contrast, it has only been in recent years that CO-releasing molecules (CORMs) have been developed as prodrugs for carbon monoxide delivery for therapeutic applications in human medicine [26, 224]. Although a large number of novel CORM lead structrues have been studied for their biological activity [235, 283–292], curiously there does not seem to be a system for dual CO and NO delivery from a single molecule. Therefore, it is of great practical importance to identify mixed-ligand carbonyl/nitrosyl complexes from which either the CO or NO ligand or both can be released in a carefully controlled manner to develop novel tools for inorganic chemical biology to study the biological activity of these two important signaling mediators. Based on the long-standing interest in transition metal-based photoactivated CO-releasing molecules (PhotoCORMs) [261], it seems reasonable to develop and investigate molecules suitable to realize light-triggered liberation of CO and NO from the coordination sphere of a metal-coligand fragment.

Quite a number of ultrafast spectroscopy studies have been carried out on the photolytic release of carbon monoxide from transition metal complexes in the liquid phase (see discussion in Sec. 6.1.1) while only very few such experimental investigations on nitrosyl [293] or mixed carbonyl-nitrosyl complexes [294] are available in the literature. However, gasphase studies could show that photoinduced NO release from transition-metal complexes is generally possible—in spite of the stronger binding of NO to the metal center compared

to CO. For instance, Wang and coworkers studied the photochemistry of $Co(CO)_3NO$ in the gas phase using time-resolved IR spectroscopy [295]. Their analysis of the branching ratio for NO vs. CO loss revealed that 355 nm excitation predominantly triggers the formation of coordinatively unsaturated species $Co(CO)_3$ and $Co(CO)_2NO$ via loss of one nitrosyl or carbonyl ligand whereas 266 nm light eventually leads to the formation of $Co(CO)_2$ and NO-retaining products. Kubota *et al.* observed NO release when studying the thermal and photolytic reactions of nitrosyl-carbonyl complexes of rhodium and iridium in the presence of triphenylphosphine [296]. NO release in form of free nitrosyl radicals was observed by Lynch when investigating sodium nitroprusside (SNP) dissolved in methanol using UV-pump/MIR-probe transient absorption spectroscopy, whereby, in addition, two metastable iron-nitrosyl linkage isomers—formed on a subpicosecond time scale—became evident [297], similar to the results found in a SNP single crystal [298]. The photochemical role of nitrosyl linkage isomerism has also been studied by low temperature photolysis experiments for similar compounds [299]. Surprisingly, no evidence of such isomerism were found for $Co(CO)_3NO$ in solution [300]. Instead, UV-pump/MIR-probe experiments revealed photoinduced bent nitrosyl excited-state complexes.

This section deals with the ultrafast photochemistry of $[Mo(CO)_2(NO)(i\text{Pr}_3\text{tacn})]\text{PF}_6$ with $i\text{Pr}_3\text{tacn} = 1,4,7$-triisopropyl-1,4,7-triazacyclononane (**4**, see Fig. 6.2), a molybdenum complex containing both carbonyl and nitrosyl ligands. The complexes' photolytic dynamics in MeCN occurring after photoexcitation are examined by employing UV-pump/VIS-probe and UV-pump/MIR-probe TA spectroscopy ($\lambda_{\text{pump}} = 285$ nm) in connection with linear absorption experiments. In particular, the question will be addressed to which extent the photodynamics of mixed carbonyl-nitrosyl compounds differ from systems with only carbonyl ligands. This is of particular importance since no ultrafast studies on mixed carbonyl-nitrosyl complexes of potential biological relevance have been reported so far. Compound **4** was prepared by Dr. Christoph Nagel in a two-step procedure from 1,4,7-triisopropyl-1,4,7-triazacyclononane and molybdenum hexacarbonyl as published by Wieghardt [301]. For further details on synthesis and X-ray crystallography, see Ref. [302]. Compound **4** was dissolved in MeCN (spectroscopic grade) at concentrations of approximately 5 mM for both the static UV/VIS and FTIR absorption experiment, as well as for all TA measurements.

6.2.2 FTIR spectroscopy and DFT calculations

The linear MIR absorption spectrum of **4** is depicted in Fig. 6.2. Three distinct bands are observed, reflecting the NO stretch of the nitrosyl ligand (1671 cm^{-1}) and the anti-symmetrical and symmetrical stretching vibrations of the *cis*-Mo(CO)$_2$ moiety (1932 and 2023 cm^{-1}). The band positions are well reproduced by the corresponding DFT calculations (see Appendix C.2). Under continuous illumination with 285 nm light for several minutes, a general decrease of the initial absorption bands becomes evident, accompanied by the rise of two new distinct signals at 1615 and 1896 cm^{-1}, one red-shifted with respect to the NO peak and the other one red-shifted with respect to the CO signal of the parent molecule. This indicates the photoinduced formation of a CO loss product, as the two
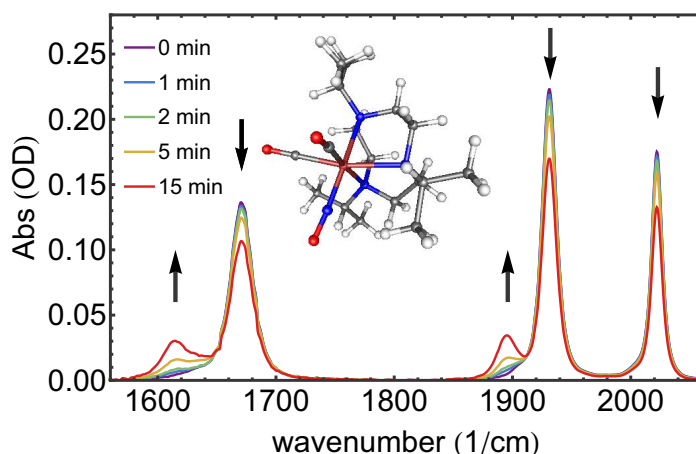
Figure 6.2: DFT-optimized structure of complex 4 and corresponding FTIR spectra in MeCN upon illumination with a 285 nm diode for different exposure times. Arrows indicate rising and decaying absorption bands.

upcoming absorption bands can be assigned to the CO and NO spectral regions, respectively. When comparing the spectral position of the nascent photoproduct with the DFT calculations, good accordance is found with the follow-up product formed upon loss of one CO ligand that is replaced by a MeCN molecule. These findings are in line with results presented in Ref. [302], where a similar illumination experiment has been performed using 254 nm light. While analogous results where found within the first minutes of exposure, employing higher energetic UV light for an illumination time of 1 h led to a shift of the newly formed absorption band at around 1615 cm^{-1} towards 1598 cm^{-1}, while the absorption feature at 1896 cm^{-1} almost vanished again. By comparing to DFT data, the band at 1598 cm^{-1} was assigned to a follow-up product of **4** that has eventually lost two CO ligands which are replaced by MeCN molecules [302]. Interestingly, even after several hours of exposure, the band at 1598 cm^{-1} has not been observed when using 285 nm light, indicating that shorter wavelengths are required to trigger a stepwise release of two CO ligands from **4**. For both excitation wavelengths, CO release becomes furthermore evident by a small feature at 2140 cm^{-1} reflecting the absorption of dissolved CO (data not shown). The formation of a NO loss product, however, can be ruled out since a spectral feature between 1600 and 1700 cm^{-1} that reflects the stretching vibration of bound NO is present at any time of exposure. The finding that NO remains bound, i.e., **4** does not act as a NO-releasing molecule, is furthermore supported by a standard myoglobin assay illumination experiment performed by the Schatzschneider group. For further reading in this regard, the interested reader is referred to Ref. [302].

6.2.3 Steady-state UV spectroscopy

Figure 6.3 depicts the steady-state UV absorption spectrum of **4** in MeCN (purple). Besides a strong absorption band at 208 nm, which is accompanied by a weak shoulder at
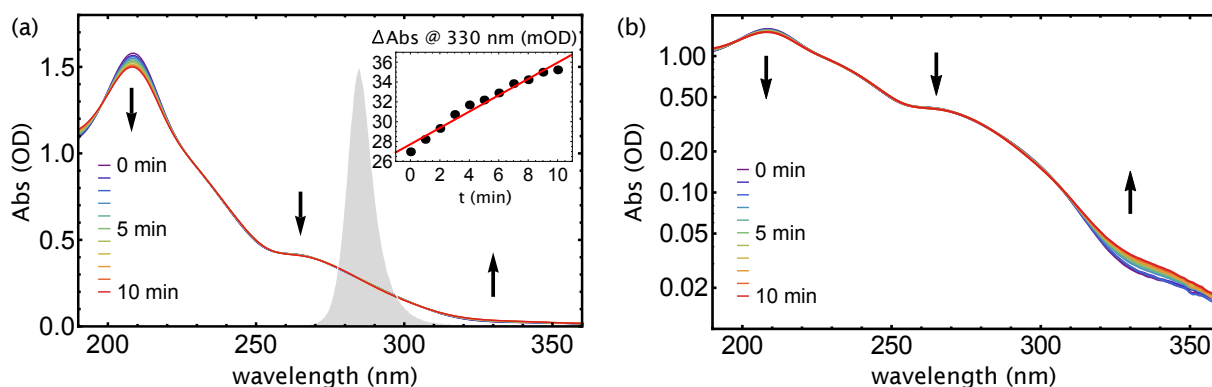
Figure 6.3: UV/VIS absorption spectra of 4 in MeCN under illumination with a 285 nm diode for different exposure times. Arrows indicate rising and decaying absorption bands. (a) Representation using a linear ordinate; the spectrum of the UV diode is shown in the background (grey shaded area). (b) Representation using a logarithmic ordinate to highlight small changes around 330 nm.

235 nm, another distinct band is found at 265 nm. The same 285 nm diode used for the MIR study shown in Fig. 6.2 is also employed to measure changes in the steady-state UV absorption spectrum of **4** upon long-term UV exposure [for a similar experiment examining **4** in dimethylsulfoxide (DMSO) under illumination with 254 nm light, see Ref. [302]]. Note that minor absorption bands appearing above 360 nm are neglected in the following discussion owing to extremely low extinction coefficients. With increasing illumination time, the two major absorption bands of **4** decrease in intensity while a new weak band grows in at 330 nm. An isosbestic point is clearly discernible at approximately 308 nm indicating that only two species that vary in concentration contribute to the absorption spectrum and that CO release does not precced via decomposition. The upcoming absorption is found to be permanent as no relaxation back to the initial absorption spectrum is evident when repeating the measurement after several hours without further sample treatment. As shown in the inset of Fig. 6.3(a), the nascent absorption band at 330 nm increases linearly with illumination time over 15 min—for clarity, see data representation using a logarithmic ordinate in Fig. 6.3(b). However, for longer exposure times (data not shown), the isosbestic point gets blurred, indicating that additional species are involved in the photoinduced conversion process. Together with the findings from the FTIR experiment, it can be concluded that the newly formed UV absorption band originates from the photoproduct formed after loss of one CO ligand. Distinct changes in the linear absorption spectrum after loss of CO ligands have been reported for several CORMs [234, 303]. For a manganese-tricarbonyl complex similar to **3**, Gonzales *et al.* [304] observed a strong shift of the lowest-lying absorption band when inducing the release of only one (or two) CO ligands via low-power illumination. Surprisingly, no comparable study on a molybenum complex can be found in the literature. Nevertheless, TD-DFT calculations performed by the Schatzschneider suggest that several electronic transitions of **4** can trigger CO release. However, these simulations will not be discussed in further detail here. Again, the interested reader is referred to Ref. [302].

6.2.4 Transient absorption measurements

In the following, the ultrafast dynamics of **4** upon UV excitation probed both in the VIS and the MIR spectral region are discussed. In the VIS regime [see Fig. 6.4(a) for dynamics up to 30 ps pump–probe delay], a broad positive absorption signal spanning from 300 to 380 nm is found. The latter absorption band decays within the first picoseconds after photoexcitation and exhibits a small remaining positive contribution which remains constant up to at least 4 ns. The spectral properties of the absorption band are in line with the result shown in Figure 6.3 and furthermore substantiate the finding of a stable photoproduct which is formed after photolysis of one CO ligand from the metal center. To verify that the observed dynamics do not originate from solvent contributions, a measurement in pure MeCN has been conducted which is presented in Appendix C.3. Fitting a biexponential model function plus a constant offset value for positive pump–probe delay times (as well as a function that accounts for the coherent artifact) to the transient at 330 nm reveals the time constants (1.0 ± 0.1) ps and (10 ± 1) ps [see Fig. 6.4(b); for clarity, data is only shown for pump–probe delay times up to 120 ps]. The offset value reveals that the positive signal decreases approximately by a factor 20 when comparing the remaining signal at longer delay times with the value found directly after UV pump excitation. Hence, it can reasonably be inferred that permanent CO loss is only observed for very few of the initially excited molecules and that most molecules undergo geminate recombination—a process that would fit the fast time constant of the 330 nm transient. The interpretation that **4** is only a weak CO releaser is furthermore supported by the observation that only minor changes in the linear absorption spectrum arise upon UV illumination (confer Fig. 6.3). The slower time constant of the 330 nm transient might reflect cooling dynamics of hot molecules, similar to the observation made for complex **3**. The dynamics discussed above should also be reflected in a recovery of the GSB of bands associated with the intact complex **4**. However, this is not observed due to the limited detection range of our TA spectrometer towards shorter wavelengths.
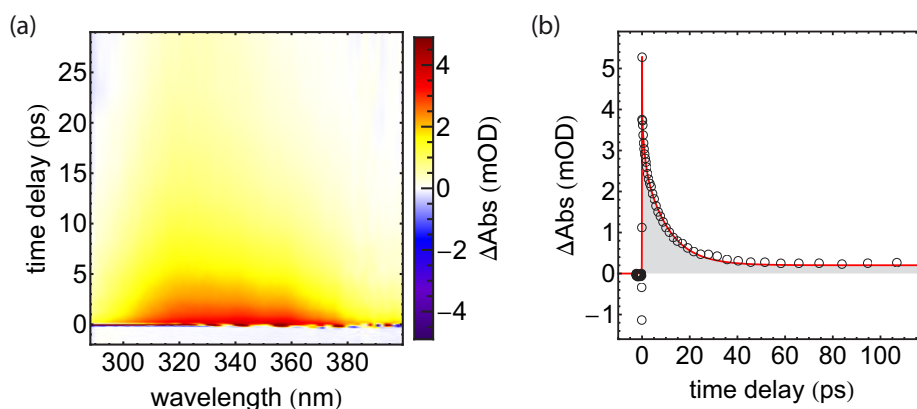
Figure 6.4: Ultrafast dynamics of 4 in MeCN under 285 nm excitation—part one. (a) Broadband transient absorption in the VIS regime showing early dynamics. (b) Transient absorption at 330 nm for time delays up to 120 ps [single-color transient referring to data shown in (a)].
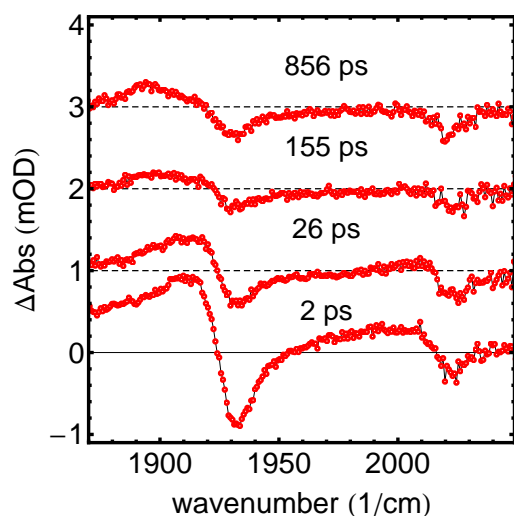
Figure 6.5: Ultrafast dynamics of 4 in MeCN under 285 nm excitation—part two. Transient absorption in the MIR spectral range for selected pump–probe delay times. Each individual difference spectrum is shown with 1 mOD vertical offset.

Selected transient absorption spectra of **4** resulting from the UV-pump/MIR-probe TA measurement are depicted in Fig. 6.5. Note that under the given experimental conditions, CPU enables simultaneous detection of MIR probe spectra with a high pixel density and a spectral bandwidth of approximately 200 cm^{-1} although absorption-change signals are ranging below 1 mOD. Directly after pump excitation (2 ps), two distinct negative TA signals are observed at 1932 and 2023 cm^{-1} which can be assigned to ground-state bleaching of the intact molecule (refer to FTIR spectra illustrating the CO stretching vibrations of **4** in Fig. 6.2). Besides a strong recovery of the feature at 1932 cm^{-1} on a time scale well comparable to the decay of the VIS absorption band at 330 nm [refer to Fig. 6.4(a)], both bleach signals remain constant for at least 4 ns after photoexcitation. The visibility of a bleach recovery of the feature at 2023 cm^{-1} is putatively overlaid by the broad short-lived absorption of hot molecules centered at about 2000 cm^{-1} which decays within the first 10 ps. On the lower energetic part of the detection range, a second positive contribution instantaneously appears with a distinct maximum at approximately 1915 cm^{-1}. The latter undergoes a spectral shift towards lower energies for increasing time delays and manifests itself at approximately 1890 cm^{-1}. These observations further support the conclusion of ultrafast CO liberation from **4** upon UV excitation drawn both from the UV-pump/VIS-probe as well as from the static absorption measurements as the remaining positive absorption at longer delay times matches the frequency of the upcoming absorption band which could be assigned to a product formed after loss of one CO ligand (refer to DFT calculations and Fig. 6.2).

6.2.5 Conclusion

With femtosecond UV-pump/VIS-probe as well as UV-pump/MIR-probe transient absorption spectroscopy, the primary photoproducts formed after 285 nm excitation of [Mo(CO)$_2$(NO)(iPr$_3$tacn)]PF$_6$ dissolved in MeCN were assigned supported by DFT calculations of the vibrational signature of potential follow-up products. The compound

releases only one of the two CO ligands under these conditions both on an ultrafast timescale as well as under exposure with 285 nm light for several minutes. No indications for a NO loss product were observed. Thus, although it carries both carbonyl and nitrosyl ligands in the metal coordination sphere, this complex exclusively acted as a photoactivatable CO-releasing molecule (PhotoCORM) in solution. Its suitability for biological applications, however, will probably be limited since tissue-damaging UV light is required to effectively trigger the CO release mechanism. Hence, the search for dual-functional CO/NO-releasers has to continue.

Summary and Outlook

The main objective of this thesis was to use time-resolved spectroscopy to shed new light on molecular systems whose ultrafast dynamics are either completely unknown or still heavily under debate. For this purpose, several pump–probe transient absorption experiments with UV pump pulses were conducted. For all molecular systems under investigation, UV excitation triggers the photolysis of certain ligands thereby initiating a subsequent reaction sequence. To gain deeper insights into experimental data, all studies were complemented by quantum chemical calculations conducted by our respective collaborators. In Chap. 4, new ground was broken when following the highly spin-dependent reactivity of diphenylcarbene (DPC, Ph$_2$C) in solution. In contrast to existing femtosecond time-resolved studies which focused on DPC's reactivity in pure solvents, the analysis of data acquired in mixed solvent environments revealed an additional reaction pathway that has remained hidden so far. While measurements on DPC were based on probing in the UV to VIS spectral range, Chap. 5 deals with technical improvements regarding the detection of MIR probe pulses. In particular, the newly-established technique of CPU was compared to standard multichannel MCT detection by means of an exemplary UV-pump/MIR-probe experiment clarifying the methods' individual pros and cons. Finally, both detection schemes were employed in Chap. 6 to follow light-triggered ligand release from a well-known PhotoCORM and from a complex that might act as a PhotoNORM, i.e., a molecules with relevance for biological applications which is capable of releasing a certain number of CO or NO ligands after photoactivation. The following paragraphs are intended to summarize the thesis' main results and to provide remarks on current scientific efforts addressing related interrogations.

Diphenylcarbene has been subject to academic studies since many decades and the successive improvement of spectroscopic methods allowed researchers to gradually gain a deeper understanding of the carbene's multifaceted photochemistry. For a long time, DPC was considered as a archetypal triplet-ground-state arylcarbene. This conclusion was recently questioned by matrix-isolation studies performed by the Sander group. Studying DPC embedded in argon matrices that were modified by small amounts of MeOH dopant molecules revealed the existence of a complex formed via H-bonding between singlet DPC and a MeOH molecule—an observation that so far has not been made under any experimental conditions. In order to find out if there is any evidence for such complexes also in the liquid phase at room temperature, UV-pump/VIS-probe transient absorption measurements on DPC were conducted, whereby the MeOH doping was mimicked by studying the carbene in mixed MeOH/MeCN solvent environments. As presented in Chap. 4, the interplay between quantum chemical calculations and experimental data allowed us to derive a general reaction scheme treating the dynamics in pure solvents as two special cases. In a first step, UV photolysis of the diazo-compound precursor Ph$_2$CN$_2$ leads to

the formation of ^{1}Ph$_2$C on a femtosecond time scale. The subsequent dynamics could be described by means of a rate model comprising three reaction channels: ISC to ^{3}Ph$_2$C, formation of an H-bonded complex ^{1}Ph$_2$C··HOMe which reacts on to an ether product in a concerted fashion activated by a further MeOH molecule, or ether production via an intermediate Ph$_2$CH$^+$ for whose formation two MeOH molecules interact concurrently with ^{1}Ph$_2$C. To which extent a certain reaction channel is influencing the carbene's overall reactivity is crucially determined by the number of MeOH molecules that this reactive species initially encounters. Similar to findings recently obtained in matrix-isolation studies at cryogenic temperatures, our liquid-phase experiments at room temperature highlight the stabilizing effect of a metastable complex ^{1}Ph$_2$C··HOMe that appears for all fractions of MeOH in the mixtures. Since both ether formation channels exhibit a different dependency on the MeOH concentration, employing solvent mixing provides a powerful means to selectively enhance or suppress certain reaction channels and therewith to decisively control the carbene's overall reactivity. This is expressed most clearly by the finding that the highest number of H-bonded complexes is not found in pure MeOH but for mixtures containing $\approx 70\%$ MeCN. It can be assumed that such a non-trivial dependence on the solvent enviroment will not only be found for the case of DPC. Hence, there is a need for future studies in order to deduce more general rules from different carbenes in various mixed solvent environments. This is further motivated by another recent study performed by the Sander group: in matrix-isolation experiments on Ph$_2$C in argon environment it became evident, that small admixtures of water evoked similar stabilizing effects as MeOH dopant molecules. To further scrutinize this, it seems appealing to extent our study by measurements in H$_2$O/MeCN solvent mixtures.

In recent years, the technique of chirped-pulse upconversion (CPU) has attracted significant attention in the field of ultrafast infrared spectroscopy. Offering an easy-to-handle alternative to commonly used direct multichannel detection via an array of mercury-cadmium telluride (MCT) photodetectors, CPU has found its way into ultrafast laboratories all over the world. However, a direct comparison scrutinizing the individual weaknesses and strenghts of both detection methods was still missing in the literature. For this purpose, an experimental setup has been established that enables the conduction of liquid phase UV-pump/MIR-probe transient absorption experiments with simultaneous 1 kHz shot-to-shot data acquisition via CPU and MCT detection. For a comparative study presented in Chap. 5, Co$_4$CO$_{12}$ dissolved in CH$_2$Cl$_2$ served as test sample. The technique of CPU shifts the characteristic MIR absorption features via a SFG process with a strongly chirped NIR pulse to the VIS regime. Hence, upconverted spectra can be detected with cost-effective CCD cameras. Therefore, the most obvious differences between both methods comprise that MCT based spectrometers used for direct MIR detection need to be refilled with liquid nitrogen every few hours, while the CPU approach requires the alignment of an additional SFG process. Besides this practical differences, the exemplary pump–probe experiment revealed that CPU detection scores with a significantly improved spectral sampling and an extended detection bandwidth. What argues against CPU ist that intensity fluctuations of the fundamental chirped NIR pulses are engraved into CPU spectra within the nonlinear upconversion process, thus lowering the signal-to-noise ratio. However, noise levels similar to those provided by standard MCT detection

can be achieved by applying a correction procedure which is based on the normalization of individual CPU spectra with their integrated spectral intensity—a procedure which has successfully been tested. A unique feature of the CPU technique is the possibility to modify the spectral profile of the upconverted spectrum by changing the phase-matching conditions in the SFG process. This additional degree of freedom was exploited in Chap. 5 to switch between a Gaussian-shaped and double-peak spectra in a stepwise manner. The application of such modified CPU spectra might improve the detection of spectrally separated features. The idea is to operate within the optimal working regime of a CCD camera without the risk of saturating the detector in areas where no signals are expected, i.e., where only minor spectral intensity is required. Since many time-resolved spectroscopic investigations aim at the elucidation of vibrational dynamics which are manifested in weak absorption change signals in the MIR spectral region—often separated by several hundreds of inverse centimeters—it can be concluded that CPU's high degree of flexibility makes the technique superior to conventional MCT detection. For future investigations, it is straightforward to combine CPU and MIR pulse characterization methods [305, 306]. For instance, this might by helpful in control experiments studying the impact of vibrational excess energy on the outcome of a photoreaction by influencing the reaction's course using shaped MIR pulses [124]. Recent developments also comprise the application of CPU to attenuated total reflectance (ATR) infrared spectroscopy—once more highlighting the technique's wide scope [307]. Since upconversion reduces the relative bandwidth of the MIR spectrum, CPU allows for the detection of MIR spectra spanning over several octaves by means of a standard grating spectrometer. Hence, CPU will probably unfold its full potential when broadband continuum IR sources will routinely be used in ultrafast MIR shot-to-shot time-resolved spectroscopy [308, 309].

There is steadily increasing interest in CO-releasing molecules (CORMs) as a promising in-situ source of carbon monoxide, which is an important endogenous gasotransmitter in higher organisms, including humans. PhotoCORM have successfully been tested for their biological applicability. So far, this class of molecules has only been studied under long-term illumination at a macroscopic level and virtually nothing is known about the primary processes happening after UV excitation. Hence, it remained unclear how many CO ligands are released on an ultrafast time scale, and for the case that several ligands are released, it is uncertain if particular CO ligands are released in a concerted or sequential manner. In Sec. 6.1, TA studies on $[Mn(CO)_3(tpm)]Cl$ with $tpm = tris(2\text{-}$ pyrazolyl)methane in aqueous solution have been carried out. This complex is of particular interest, as it showed promising properties for various biological applications, e.g., to be selective and cytotoxic against cancer cells. UV-pump/MIR-probe TA spectroscopy with different UV pump wavelengths supported by linear spectroscopy methods and quantum chemical calculations revealed that several electronic transitions in the UV will lead to CO release and that only one CO ligand is released within the first few picoseconds after UV excitation, while some molecules undergo geminate recombination. Excess energy stemming from the pump interaction is transferred to low-frequency modes, a process which is reflected in cooling dynamics on a 10 ps time scale in the follow-up product formed after loss of one CO ligand and the recombined CORM, respectively. Due to the important signaling function of nitric oxide (NO) in biological systems, it seems obvious to transfer

the concept of PhotoCORMs to PhotoNORMs, i.e., to develop photoactivatable sources NO. Hence, Sec. 6.2 highlights the CO–NO interplay and deals with the photochemistry of $[Mo(CO)_2(NO)(i Pr_3 tacn)]PF_6$ with $i Pr_3 tacn = 1,4,7$-triisopropyl-1,4,7-triazacyclononane in MeCN solvent environment. This complex, whose photochemistry was hitherto virtually unknown, was selected as it may be suited to act as a combined CO- and NO-releaser. Recording FTIR spectra while irradiating a static sample solution with 285 nm light induced the formation of a stable photoproduct. By comparing nascent spectral features to DFT calculations, the latter could be a assigned to a follow-up product formed after loss of one CO ligand, whose free coordination site has been refilled with a MeCN solvent molecule. In a corresponding UV/VIS experiment, this photoproduct appeared in form of a new absorption band at around 330 nm. Besides the static illumination experiments, femtosecond UV-pump/VIS-probe as well as UV-pump/MIR-probe transient absorption spectroscopy was used to study the molecule's primary reaction steps after UV excitation. Interestingly, the features assigned to the CO-loss product were also found just after UV pump excitation. Hence, both on an ultrafast time scale as well as under long-term irradiation, the complex acted as a photoactivatable CO-releasing molecule. The presumption that the molecule can act as a NO releaser could not be confirmed under the chosen experimental conditions. Having knowledge about the ultrafast dynamics of ligand release from this class of molecules might incentivize the development of systems with tailored CO- or NO-releasing properties for specific applications. However, the study of ligand dissociation from PhotoCORMs or PhotoNORMs on an ultrafast time scale is still at its beginning and several points may be addressed in future investigations. Due to low penetration depths and the risk of tissue damage caused by high energetic light, the in vivo applicability of molecules that require UV light to trigger the gasotransmitter release is limited. The need for UV excitation, however, might become dispensable by following one of the two following approaches. The first approach relies on triggering the ligand dissociation by two-photon absorption (TPA) [310, 311] using pump wavelengths from the so-called *therapeutic window* (600 to 1200 nm). This approach particularly benefits from higher penetration depths and the possibility to selectively excite well-defined volumes owing to the nonlinear interaction step [312–314]. Hence, future studies might aim at the elucidation of the primary reaction steps of CO- or NO-releasing molecules after absorption of two VIS photons. A corresponding experimental pump–probe setup that allows one to record molecules' two-photon excitation spectra and follow possible ligand dissociation after TPA via probing in the MIR spectral range was recently developed in the Nürnberger group [129, 315]. The second approach to realize light-triggered ligand release while omitting UV light is to use molecules that absorb in the VIS or NIR regime. A series of heterobinuclear $Mn(CO)_3/Ru(bpy)_2$ PhotoCORMs that has recently been developed in the Schatzschneider group is one promising example in this regard [302]. Hence, future VIS-pump/MIR-probe transient absorption experiments—ideally using CPU detection to cover several vibrational signatures simultaneously—are convenient to follow the process of ligand dissociation in novel CORM or NORM structure whose ultrafast dynamics are still to be deciphered. Moreover, especially for complexes containing both CO- and NO-ligands, it seems appealing to exploit the coherence properties of laser light by employing shaped pulses to selectively induce ligand release in this class of molecules.

Combining transient absorption and fluorescence spectroscopy

In this appendix, an extension for an existing UV-pump/MIR-probe TA setup is discussed. A fluorescence detection scheme is characterized which is sensitive for the observation of changes in a molecule's fluorescence steered by selective excitation of vibrational modes. Regarding this, preparatory work, which includes the setup's alignment and characterization, is carried out with respect to prospective measurements on so-called *super-photoacids*. The phenomenon of photoacidity, i.e., an increase in acidity by several orders of magnitude upon electronic excitation, is frequently met in aromatic alcohols capable of transferring a proton to a suitable acceptor [316]. The Jung group recently synthesized a promising new class of super-photoacids and their methylated counterparts based on pyrene, and demonstrated the extent of solvent induced solvatochromic effects by means of changes in the respective absorption and emission spectra [317]. Aiming at deeper insights into the underlying mechanisms contributing to excited-state proton transfer in this class of molecules, the above-mentioned fluorescence detection scheme might be utilized to explore whether vibrational excess energy has any influence on the proton-transfer process. Measurements presented in this appendix were partially conducted during the supervision of Florian Lessing's Bachelor Thesis [318].

Fluorescence of super-photoacid **5** in its protonated (left) and deprotonated form (right), respectively.

A.1 ESPT in a pyranine-derived super-photoacid

In Chap. 4, an ultrafast protonation reaction has been investigated, in which a proton is transferred from a solvent molecule to singlet DPC leading to the formation of a short-lived benzhydryl cation species [194]. Hence, the DPC precursor DPDM can be regarded as a *photobase* as the molecule shows an increased basicity after electronic excitation. Generally, also the opposite mechanism is possible: upon electronic excitation, so-called *photoacids* show a higher acidity, i.e., a higher tendency to release an acidic proton, caused by changes in the molecule's electronic distribution that in turn affect corresponding hydrogen bonds.

In 1965, Trieff and Sundheim introduced the term excited-state proton transfer (ESPT) [320]. However, more than 30 years earlier it was Weber who observed that changing the pH value in a solution containing 1,4-naphthylaminosulfonate leads to changes in the corresponding fluorescence spectrum—while leaving the absorption spectrum unaltered [321]. A few years later, Förster was able to assign this phenomenon to a different protolytic equilibrium in the molecular ground and excited state, respectively. Consequently, he introduced the so-called *Förster cycle* [see Fig. A.1(a)] which explains the basic processes occurring in photoacid systems [316, 322]. For these molecules, which are typically weak acids in their ROH form, electronic excitation decreases the pK_a value, which is defined as

$$pK_a = -\log_{10}\left[\frac{k_{\text{deprot}}}{k_{\text{prot}}}\right] \, , \tag{A.1.1}$$

with rate constants k according to Fig. A.1(a), by several orders of magnitude. The Förster cycle illustrates the existence of two different species in the excited state, namely the ROH* and the RO^{-*} species, whereby the asterik denotes the excited state. Their different energetic positions give rise to two separate emission bands back to the ground
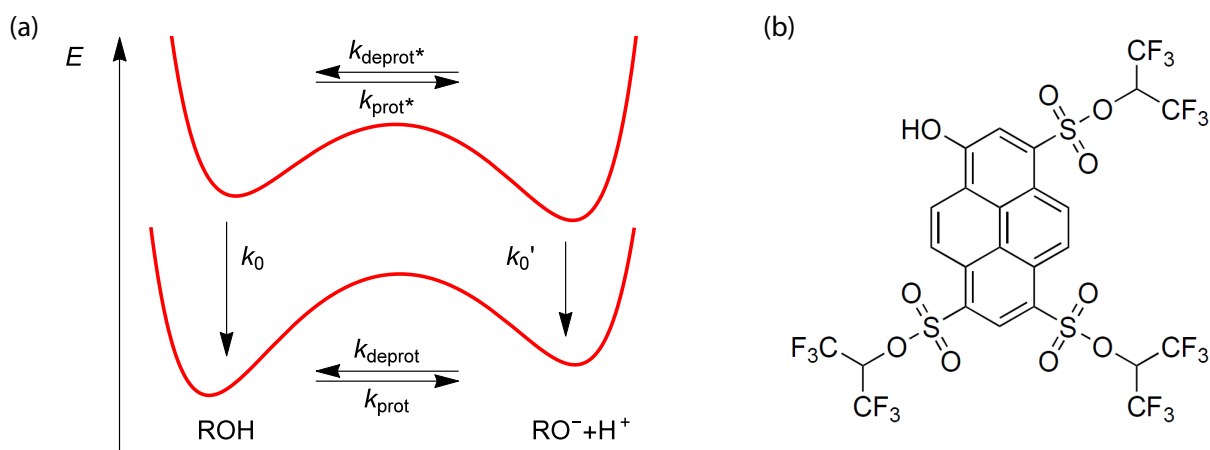

Figure A.1: (a) **Förster cycle of an exemplary photoacid system.** Arrows indicate proton transfer between the protonated and deprotonated form of the photoacid which is either in the electronic ground or excited state. Figure adapted from Ref. [319]. (b) **Molecular structure of compound 5.**

state. Given that the pK_a value is known, the Förster cycle directly reveals the pK_a^* value of the photoacid system. If the pK_a value is unknown, however, still the change in acidity upon photoexcitation can be evalutated:
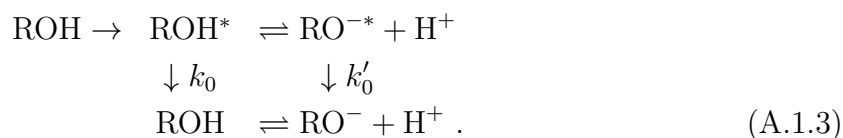
$$\Delta pK_\mathrm{a} = pK_\mathrm{a} - pK_\mathrm{a}^* = \frac{E_\mathrm{ROH} - E_\mathrm{RO^-}}{kT \ln [10]} \ , \tag{A.1.2}$$

where k is the Boltzmann constant[1] and T the temperature, and where E_ROH and $E_\mathrm{RO^-}$ are the transition energies of photoacid and anion, respectively [323, 324]. Cases in which the Förster cycle fails to describe the properties of a photoacid properly are described elsewhere [325–327]. Alternative methods to determine the pK_a^* value are discussed in Ref. [319], where one can also find an extensive overview of the variety of molecular systems which are capable of ESPT. It is also noteworthy, that besides evaluating the basic properties of photoacid systems via stationary fluorescence spectroscopy, femtosecond time-resolved experiments have made possible to follow ESPT on its actual time scale and determine k_prot—and thus also pK_a^*—directly [328]. ESPT is always linked to the presence of a suitable acceptor such as a polar solvent molecule. Most studies on ESPT were conducted in water environment which allows to study even weak photoacids due to its extraordinary good ability to stabilize a proton. One special type of photoacids are so-called *super-photoacids* which are characterized by negative pK_a^* values. This class of molecules allows one to study ESPT in various polar solvents because the photoacids are so strong, that they are able to transfer the proton to less good acceptor molecules, e.g., DMSO. It is interesting to note, here with respect to measurements presented in Chap. 4, that many studies on super-photoacids have also been carried out in solvent mixtures, for instance in water-methanol mixtures [329] or water-acetonitrile mixtures [330].

The super-photoacids synthesized and spectroscopically characterized by the Jung group are derived from pyranine (8-hydroxy-1,3,6-pyrenetrisulfonate, HPTS) and differ only in their substituents on the aromatic pyrene core [317, 331, 332]. All molecules exhibit electronic transitions in the VIS spectral region, thus being promising candidates to study proton transfer on the single-molecule level where UV excitation light typically leads to unwanted background signals. Furthermore, the compounds combine high photostability and high solubility. Steady-state measurements and solvatochromic analysis revealed that intramolecular charge transfer on the photoacid side correlates best with the observed photoacidity. The discussion in this appendix is devoted to the strongest photoacid out of this series, namely tris(1,1,1,3,3,3-hexafluoropropan-2-yl) 8-hydroxypyrene-1,3,6-trisulfonate [**5**, see Fig. A.1(b); synthesis done by Björn Finkler according to Ref. [331]]. Owing to the use of strongly electron withdrawing sulfonic ester groups, **5** exhibits an increase in acidity in the excited state of more than eight logarithmic units. This allows one to observe proton transfer even in less polar and proton accepting solvents compared, for instance, to DMSO. Absorption and and steady-state fluorescence spectra of **5** in acetone (see Fig. A.2) illustrate the occurence of ESPT which—in the context of Förster's

---

[1]$k = 1.38064852(79) \times 10^{-23}$ J/K [29]

cycle—can be described via

$$
\begin{array}{rcl}
\mathrm{ROH} \rightarrow & \mathrm{ROH}^* & \rightleftharpoons \mathrm{RO}^{-*} + \mathrm{H}^+ \\
& \downarrow k_0 & \downarrow k_0' \\
& \mathrm{ROH} & \rightleftharpoons \mathrm{RO}^- + \mathrm{H}^+ \ .
\end{array}
\tag{A.1.3}
$$

Absorption spectra shown in Fig. A.2(a) illustrate that acidification via stepwise addition of trifluoroacetic acid (TFA) shifts the photoacid's ground-state equilibrium from the RO^- form towards the ROH form. In other words, one observes a transition from the deprotonated ground state (orange curve) to the fully protonated ground state (green curve). The observation of two fluorescence bands after excitation of solely ROH [confer green curve in Fig. A.2(b)] reveals the existence of two different fluorescent species which are formed upon electronic excitation, namely the ROH^* and the RO^{-*} species, whereby the anion's fluorescence is shifted towards longer wavelengths compared to the free photoacid. In the following section, it will be discussed how ESPT in this particular super-photoacid system may be steered in a control experiment.
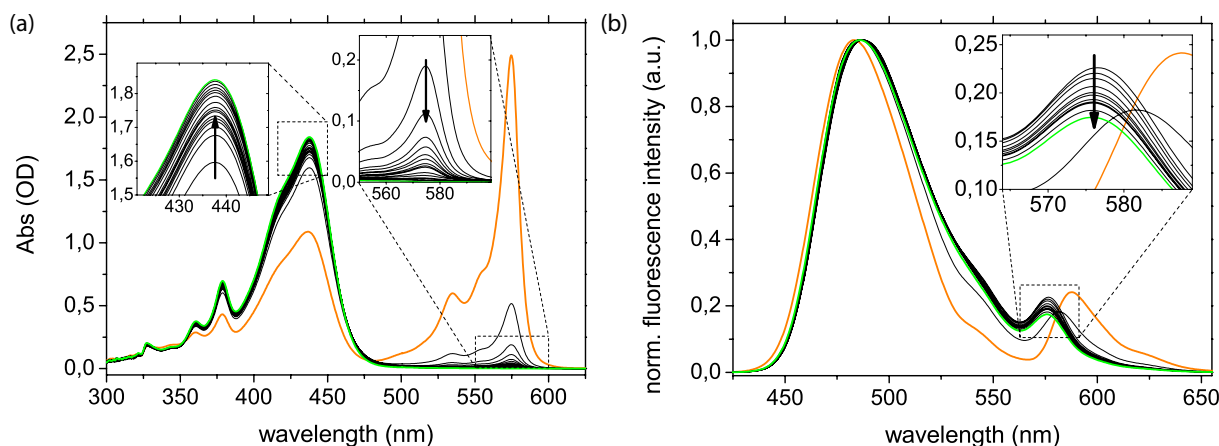
Figure A.2: Basic spectroscopic properties of 5 in acetone. Starting in the deprotonated form (orange), absorption (a) and fluorescence spectra (b) are recorded after stepwise addition of trifluoroacetic acid until the acid-base equilibrium is shifted towards the protonated form of **5** (green).

A.2 Fluorescence detection in UV-pump/MIR-pump geometry

In pump–probe TA measurements, two laser pulses of different intensity are employed to pump a molecular subensemble and after a certain time delay probe its temporal evolution. Importantly, owing to its low intensity, the probe pulse only monitors the reaction's

Figure A.3: Setup for prospective quantum control experiments. In contrast to a standard UV-pump/MIR-probe TA setup in which every second UV pump pulse is blocked in order to detect changes in absorption upon UV excitation, the mechanical chopper is placed in the MIR path enabling the detection of MIR-induced fluorescence change signals on a shot-to-shot basis. While the IR spectrometer is only needed for alignment purposes (see text for further explanations), two microscope objectives are used to collect, collimate, and focus the fluorescence into a fiber which eventually guides the signals to the VIS spectrometer for spectrally-resolved shot-to-shot detection.
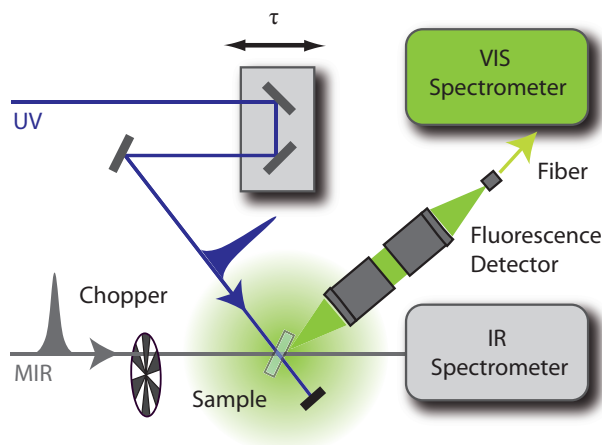
progress without influencing the actual dynamics. As shown in the literature, a deeper understanding of molecular systems can also be deduced from experiments employing two pump pulses. At this, the first pump pulse can for instance generate population in an excited state, whereby the second pump pulse interacts with the excited population after a certain time delay and either transfers molecules to an even higher lying state, i.e., the second pulse acts as *repump* pulse [333, 334], or stimulates molecules back the the ground state, i.e., the second pulse acts as *dump* pulse [334–336]. However, in both cases the second pulse alters the excited state evolution. The control concept which will be discussed in this section relies on steering a chemical reaction, which is monitored via fluorescence detection without time resolution, by selective excitation of vibrational modes. In particular, a MIR pump pulse is intended to pre- or re-excite the sample with a certain time delay with respect to the pulse which interacts with the sample to trigger fluorescence. Generally, it is common practice in gas phase experiments to achieve control over chemical reactivity by exploiting the role of vibrational excess energy [337, 338]. For a selective manipulation, the reaction thereby must be triggered and proceed faster than the randomization of the energy that is stored in particular vibrational modes. Due to additional loss channels for vibrational energy, it is challenging to transfer this control concept to liquid phase experiments (confer Sec. 2.3.3). However, the concept's feasibility has been demonstrated indirectly by the Zinth group who found the efficiency of an indolylfulgide optical switch, whose switching can be induced by an electronic excitation, significantly altered after vibrational pre-excitation [339, 340]. In their experiments, the vibrational pre-excitation is the result of a vibronic pre-excitation, i.e., the pulse which induces the switching encounters molecules which have relaxed back to the ground-state but have not yet thermalized. Hence, it is unclear in which mode the vibrational excess energy is stored. This uncertainty can be avoided when using MIR pulses to selectively excite vibrational modes before (or after) another pump pulse interacts with the sample to start the actual photoreaction.

The experimental setup developed within the scope of this thesis, which is based on the fluorescence detector that has been introduced in Sec. 3.5, is schematically depicted in Fig. A.3. Using 1 kHz readout of fluorescence spectra while blocking every other MIR pump pulse with a mechanical chopper allows one to record fluorescence spectra originating from a molecular subensemble which has either interacted with only the UV pulse or with both pump pulses. Hence, a difference signal in fluorescence, which in the following shall be defined as

$$\Delta F(\lambda, \tau) = \frac{I_{\text{MIR pump}}(\lambda, \tau)}{I_{\text{no MIR pump}}(\lambda)} - 1 \ , \tag{A.2.1}$$

can be obtained on a shot-to-shot basis. This definition allows for an easy interpretation since positive (negative) ΔF values correspond to an increased (decreased) fluorescence at a certain wavelength caused by the interaction with the MIR pump pulse. Different to a UV-pump/MIR-probe TA setup, the focus size of the UV beam at the sample in the control scheme needs to be smaller than the one of the MIR beam. This ensures that molecules whose fluorescence is detected are stemming from the interaction region of the MIR beam. In the employed setup, the UV focus is left unchanged with respect to Sec. 3.4 (85 µm beam waist) while the MIR focus is set to approximately 100 µm. While many other applications are conceivable using the setup introduced above, an exemplarily control experiment on **5** will be discussed in Sec. A.2.1. In connection with this, the alignment and the capabilities of the detection scheme are discussed in Sec. A.2.2.

A.2.1 Controlling intermolecular ESPT—an outlook

Compound **5** is capable of performing ESPT in acetone solvent environment (see Sec. A.1). The idea discussed in the following is to control the ESPT via a selective and temporally-resolved excitation of solvent vibrational modes. The IR transmission spectrum of acetone is depicted in Fig. A.4(a). To introduce vibrational excess energy, the MIR-OPA output is tuned to match the spectral position of the CO stretching vibration at 1731 cm^{-1} [confer Fig. A.4(b)]. Transmission through a 12 µm film of acetone leads to a complete absorption of the MIR spectrum at the latter spectral position [red curve in Fig. A.4(b)]. Hence, a significant amount of vibrational excess energy can selectively be stored in the solvent's CO stretching vibration until relaxation processes will eventually redistribute the energy. This excess energy may influence the solvent's proton acceptance capabilities which in turn should be manifested in ΔF signals at the spectral positions of the ROH* and RO^{-*} species, respectively.

One may ask if it is in genereal realistic to observe ΔF signals in this particular experimental situation. Therefore, a rough estimation shall be given to access the composition of molecules within the beams' interaction region. Considering a sample thickness of 15 µm and a MIR beam waist of 100 µm, then 9.7×10^{14} acetone molecules are located within the excitation volume. Assuming that about one third of the 150 nJ of total pulse energy is transferred to solvent CO stretching vibrations [confer spectra shown in Fig. A.4(b)],
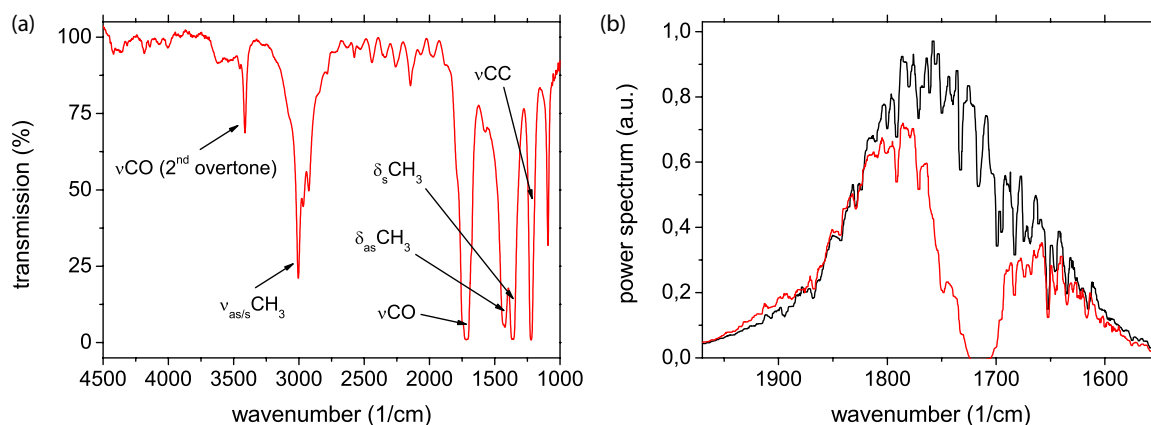
Figure A.4: Selective excitation of solvent vibrational modes. (a) Infrared transmission spectrum of acetone. (b) Exemplary MIR spectrum before (black) and after (red) propagating through a 12 μm acetone film.

then one finds 1.5×10^{12} excited acetone molecules within the excitation volume, which corresonds to approximately every 650th molecule. This number is well-comparable to the 2.1×10^{12} molecules of compound **5** that are located within the excitation volume when for instance a sample concentration of 30 mM is chosen. Note that owing to the strong MIR absorption of acetone, the region of spatial overlap between the UV and MIR beam is limited to appoximately 10 μm. To maximize putative ΔF signals, it is therefore appropriate to use thin sample cuvettes in combination with high sample concentrations.

A.2.2 Alignment procedure and detection sensitivity

It is common routine before performing pump–probe TA experiments on unknown samples to optimize the alignment of the experiental setup with respect to a well-known spectroscopic feature of a test sample, which ideally delivers a strong signal and is present over a long pump–probe delay range. After exchanging the sample, the actual measurement can subsequently be performed without changing the experimental alignment. A similar procedure has to be conducted before performing a control experiment as the one proposed in Sec. A.2.1. The alignment procedure introduced in the following contains three preparatory steps—other approaches may also be feasible:

- **1st step**: A UV-pump/MIR-probe TA experiment has to be performed, whereby the test sample's UV-VIS absorption needs to be similar to the one of the actual sample. This condition eliminates the need to change the pump wavelength—a step which may influence the alignment of the UV beam—before conducting the control experiment. Furthermore, the test molecule needs to exhibit a transient MIR feature which is covered by the same MIR spectrum which will be used for pumping in the control experiment. It may be necessary to attenuate the intensity of the MIR beam in front of the MIR spectrometer. Furthermore, due to the chosen beam radii at the sample position (confer Sec. A.2.1), one may have to deal with comparatively

small ΔOD values. This 1st step is necessary to ensure spatial and temporal overlap between the UV and MIR pulse.

- **2nd step**: Having accomplished the 1st step, the fluorescence detector itself needs to be aligned with respect to the fixed position of the sample and the laser beams. For this purpose, either the test sample is replaced by the actual sample, or one exploits the fluorescence properties of a test sample (ideally the same test sample used in the 1st step) which needs to show fluorescence upon excitation with the UV pump pulse used in the 1st step.

- **3rd step**: Finally, the UV-pump/MIR-pump measurement with fluorescence detection can be started after placing the mechanical chopper (which operates at half the laser's repetition rate) in the MIR beam path and—if this has not already been done in the 2nd step—exchanging the sample solution.

For the investigation of **5** (confer Sec. A.2.1), vitamin B$_2$ [riboflavin, **6**, CAS: 83-88-5; see Fig. A.5(a) for molecular structure] dissolved in dimethyl sulfoxide (DMSO) has been selected as test sample. The complete alignment procedure is illustrated in Fig. A.5. Besides two absorption bands in the UV region, **6** exhibits an absorption band at around 450 nm [see Fig. A.5(b)] similar to the protonated form of **5** [confer green curve in Fig. A.2(a)]. In Fig. A.5(c), the MIR absorption spectrum of **6** in DMSO furthermore reveals a distinct absorption feature at around 1710 cm^{-1} which can be covered by MIR pump/probe spectra as the one shown in Fig. A.4(b). Diller and coworkers found that 387 nm pump excitation of **6** induces the loss of a CN bond accompanied by a downshift of related vibrations. The feature at 1710 cm^{-1}, which has been assigned to a CO stretching mode, appears as a quasi instantaneously formed GSB signal which remains constant for at least 800 ps [341]. Due to overlapping absorption bands [see Fig. A.5(b)] it can be assumed that a similar behavior will also be found when using 440 nm pump pulses. Hence, the first step in the alignment procedure comprises to reproduce this feature in the standard UV-pump/MIR-probe TA configuration [see Fig. A.2(d); transient recorded with a single MCT pixel; the pump spectrum is depicted in subfigure (b)]. Optimizing the GSB signal in turn optimizes the spatial overlap between the UV and the MIR beam. Moreover, using a pump–probe TA measurement for pre-alignment allows for a precise determination of time zero between the UV and MIR pulse which is vital for the interpretation of putative ΔF signals. Note that in this case, UV and MIR pulse interact with the same molecule—DMSO does not absorb around 1710 cm^{-1}—which is not the case in the control experiment proposed in Sec. A.2.1. The fluorescence of **6** upon 440 nm excitation [see green curve in Fig. A.2(b)] appears to be only slightly red-shifted with respect to the fluorescence of **5** both in its protonated and its deprotonated form [confer Fig. A.2(b)]. While similar fluorescence characteristics of the actual sample and the test sample are in general not mandatory, in the present case it is straightforward to use **6** to align the fluorescence detector as shown in Fig. A.5(e). Apart from slight deviations at the spectral edges, which in future experiments need to be accounted for via a wavelength-dependent intensity calibration, the spectrum recorded in pump–probe geometry nicely matches the spectrum recorded with the standard spectrofluorometer.
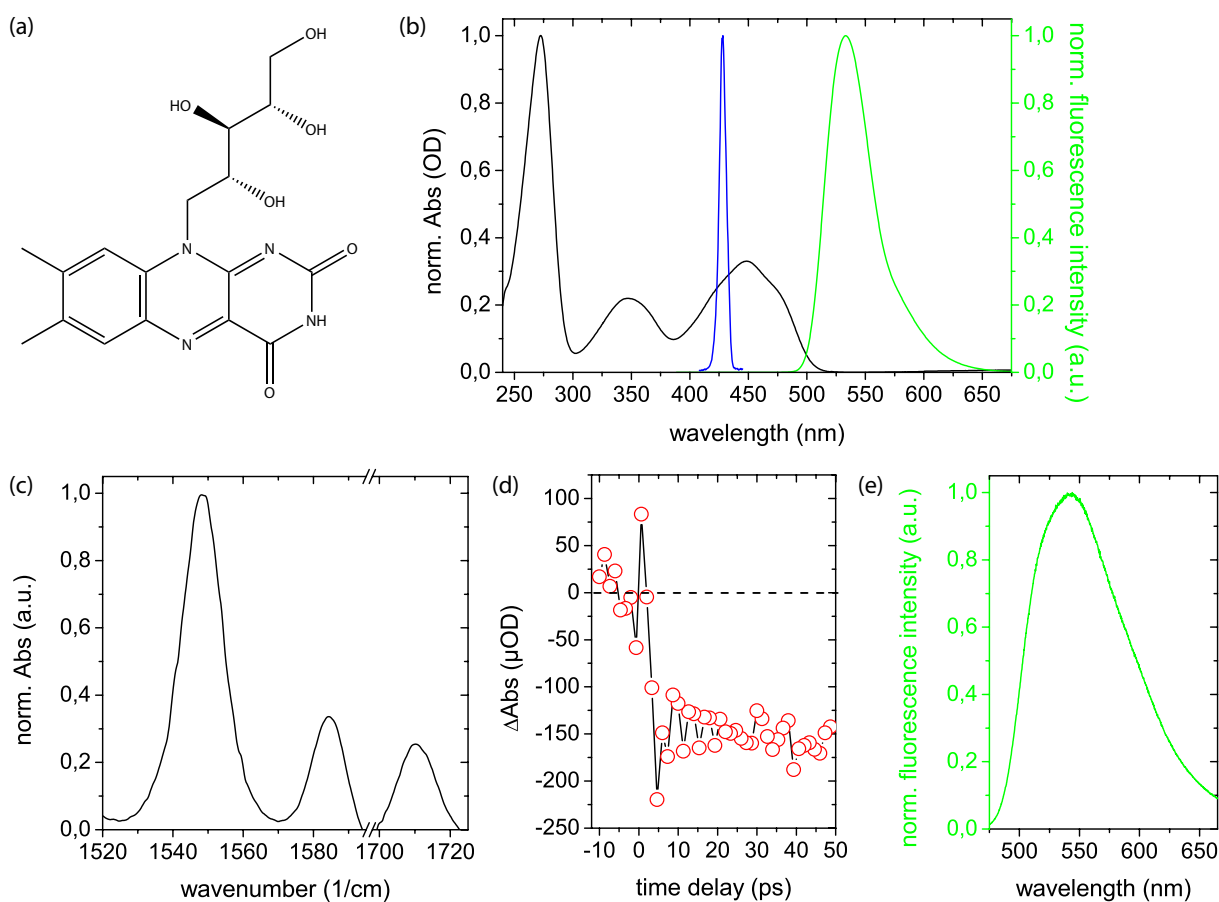
Figure A.5: Setup alignment procedure using riboflavin (6) dissolved in DMSO as test sample. (a) Molecular structure. (b) Absorption (black) and fluorescence spectrum (green) in DMSO together with the excitation spectrum used in the pump–probe experiment (blue). The fluorescence spectrum is recorded in a standard fluorescence spectrometer with an excitation wavelength of 440 nm. (c) IR absorption spectrum. (d) TA in DMSO under 440 nm excitation when probing at 1708 cm^{-1}. (e) Fluorescence spectrum recorded in pump–probe geometry using the excitation spectrum shown in (b).

When using the present setup to investigate **5**, possibly due to insufficient MIR power available, no ΔF signal has been found for any UV-pump/MIR-pump time delay even after averaging over a reasonable number of laser shots. Still, with respect to future experiments, it is beneficial to have knowledge about the detection scheme's sensitivity when searching for ΔF signals. For this purpose, 100000 subsequent fluorescence spectra of **5** have been recorded in the 1 kHz single-shot mode (confer Table 3.1). At this, the pixel with the highest intensity, held at approximately 60% of the CCD camera's 16 bit detection range, is used for noise analysis (confer procedure used in Sec. 5.2). In Fig. A.6(a), exhibiting a standard deviation of 24.3‰, the Gaussian distribution of the resulting ΔF signals is visualized. For a direct estimation of the data acquisition time which is necessary to reach a certain level of sensitivity, Fig. A.6(b) illustrates the ΔF standard error versus the number of consecutive ΔF pairs which are included in the averaging procedure. It can thus be concluded that the developed detection scheme allows

for the observation of ΔF signals on the order of 0.1‰ after reasonable data acquisition time.
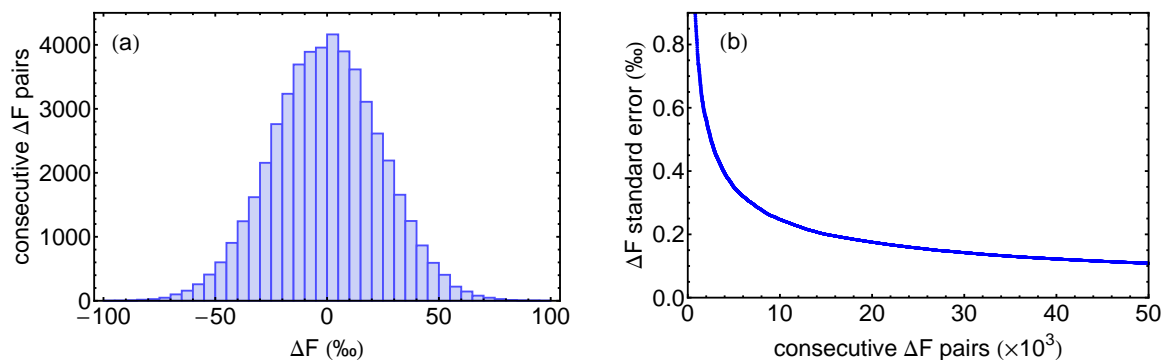
Figure A.6: Sensitivity for the detection of fluorescence-change signals ΔF. Noise analysis is carried out on the basis of 100000 fluorescence spectra subsequently recorded in the 1 kHz single-shot mode. The graphs illustrate the noise characteristics of 50000 consecutive laser-shot pairs represented by the distribution of individual ΔF signals (a) and by the ΔF standard error plotted against the number of consecutive laser-shot pairs used for averaging (b). For evaluation, the pixel with the highest count rate has been selected.

Supporting Information to Chapter 4

B.1 Quantum chemical calculations

The reactivity of diphenylcarbene (Ph_2C) and the relative stabilities of its singlet ($^1Ph_2C$) and triplet ($^3Ph_2C$) states in different solvent conditions, **I**) acetonitrile (MeCN), **II**) methanol (MeOH), **III**) acetonitrile/methanol (80:20% v/v mixture) and **IV**) acetonitrile/methanol (99:1% v/v mixture) are investigated by employing hybrid Quantum Mechanics/Molecular Mechanics (QM/MM) calculations to capture the solvent effects and specific interactions regulating the chemistry of Ph_2C. The calculations were performed by Dr. Pandian Sokkar and Dr. Elsa Sánchez-García (Max-Planck-Institut für Kohlenforschung, Mülheim an der Ruhr). This section provides information about the employed theoretical methods which led to the conclusions discussed in Chap. 4. A detailed description of the results will be published in Ref. [1].

B.1.1 Force field parameterization

Classical force field parameters for methanol and acetonitrile are available in the OPLS-all atom force field, which is able to reproduce the physical properties of these solvents in liquid simulations [342]. Since, currently, the OPLS force field is not supported by the ChemShell code [343, 344], the OPLS parameters of MeOH and MeCN were fitted in the CHARMM force field format. OPLS parameterization requires scaling-down of 1-4 non-bonded interactions (both van der Waals and Coulomb interactions) by 50 %, in contrast to full scaling in CHARMM. The non-bonded interaction, bond stretching and bond-angle bending parameters were used as such [342]. The dihedral angle parameters were modified to compensate for the full 1-4 scaling. The dihedral angle parameters were optimized to match the energy difference between eclipsed and staggered conformations (calculated at the HF/6–31G* level). The new parameters were validated by the liquid properties obtained from molecular dynamics (MD) simulations.

Ph_2C was also parameterized for preliminary classical MD simulations. The initial parameters were obtained using the SwissParam webserver (www.swissparam.ch/) [345] and the partial atomic charges were calculated by fitting the Electrostatic Potential (ESP) charges calculated at the HF/6–31G* level. The RESP ESP charge Derive (RED) webserver (*http://q4md-forcefieldtools.org/RED/*) was used for this purpose [268, 346, 347].

B.1.2 Classical MD simulation

[1]Ph$_2$C was calculated under four solvent conditions, **I**) acetonitrile, **II**) methanol, **III**) acetonitrile/methanol (80:20% v/v mixture) and **IV**) acetonitrile/methanol (99:1% v/v mixture). Setups **I**, **II** and **III** were simulated for 5 ns in a cubic periodic box at 300 K and 1 atm pressure, using 2 fs as timestep. Setup **IV** was simulated for 20 ns under the same conditions. The cutoff for short-range non-bonded interactions was 12 Å. The non-bonded potential was smoothly shifted to zero at 12 Å. Particle Mesh Ewald (PME) summation was used to account for long-range electrostatics. Ph$_2$C was kept rigid. All the classical simulations were carried out using the NAMD program. [348]

B.1.3 QM/MM MD simulation

Snapshots of Ph$_2$C in a droplet of solvent (of 30 Å radius from the carbene center) were taken from the classical MD trajectories. Then, Ph$_2$C in the solvent sphere was subjected to 10 ps QM/MM MD simulation, at 300 K with positional restraints on the carbene center. The QM region was formed by the Ph$_2$C molecule and treated at the B3LYP-D3/def2-SVP level of theory while the solvents were treated at the MM level. The ChemShell package was used for all the QM/MM calculations, with Turbomole (v6.6) for the QM region [349] and DL-POLY code [350] for the MM part. The interactions between QM and MM subsystems were calculated using an electrostatic embedding scheme, in which the MM point charges polarize the QM atoms [70].

B.1.4 QM/MM optimizations

Ten snapshots taken from the last 2 ps of the QM/MM MD simulations were used for QM/MM optimizations. During the QM/MM optimization, Ph$_2$C was treated at the B3LYP-D3/def2-TZVPP level. QM/MM MD simulations and optimizations were performed separately for singlet and triplet states.

B.2 Synthesis of compound 1

Synthesis of the diphenylcarbene precursor as performed by Paolo Costa.

Materials: Benzophenone (Sigma Aldrich 99%) and p-Toluenesulfonyl hydrazide (ABCR 98%) were used without further purification.

Diphenyldiazomethane: Benzophenone tosylhydrazone was prepared according to a literature procedure [351] by refluxing for 40 h a mixture of 1 eq. of benzophenone and 2 eq. of p-Toluenesulfonyl hydrazide in absolute ethanol (EtOH). The crude product was purified by recrystallization in EtOH. By treating the tosylhydrazone with 1.1 eq. of NaH (60% dispersion in mineral oil) in dry CH_2Cl_2 the corresponding sodium salt is formed. Sublimation of the salt on a cold substrate at 45 °C under reduced pressure yields the characteristic dark purple diphenyldiazomethane. IR (Ar, 3 K): 3070 (m), 2046 (vs), 1598 (s), 1582 (m), 1502 (s), 1497 (s), 1457 (m), 1447 (m), 1320 (m), 1268 (m), 1262 (m), 1034 (m), 936 (m), 756 (s), 750 (s), 697 (s), 692 (s), 651 (s), 482 (m) cm^{-1} H NMR (200 MHz, DMSO) $\delta =$ 7.44 (m, 4H), 7.27 (m, 6H).

B.3 Power-dependence of transient absorption spectra

Care was taken to ensure that the series of transient absorption measurements on Ph_2CN_2 in various solvent mixtures of MeOH and MeCN was carried out in the linear excitation regime. To guarantee this, transient absorption spectra for different excitation energies were recorded. Owing to the experimental setup, the latter can be controlled by the adjustable output of the Dazzler pulse shaper. The resulting pulse energy was measured before the sample position. Data for an exemplarily chosen solvent mixture at a certain
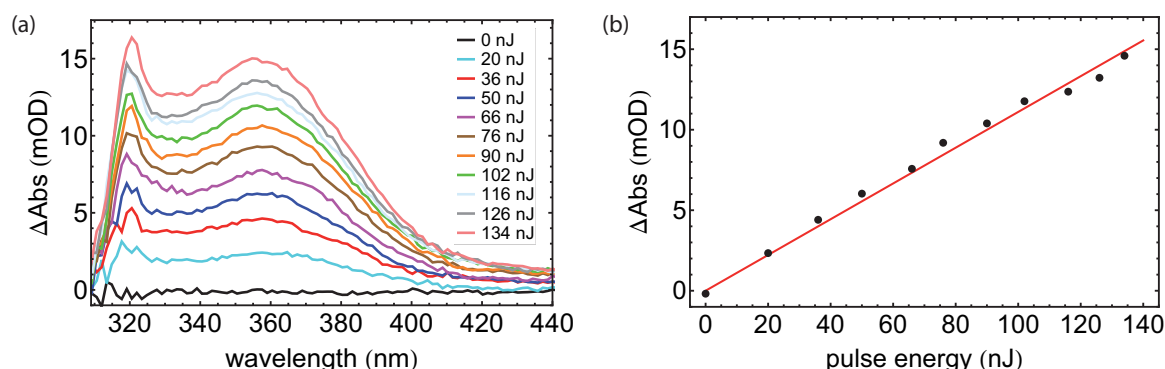
Figure B.1: Linearity of pump excitation. Transient absorption spectra of Ph_2CN_2 in MeCN at 360 ps pump–probe delay for various 285 nm pump-pulse energies (a) and linear fit of the corresponding absorption change signals at 360 nm versus the employed pulse energy (b).

time delay is depicted in Fig. B.1(a). When plotting the resulting absorption change signals for any wavelength [Fig. B.1(b), data is exemplary shown for a probe wavelength of 360 nm], one finds linear relationships, which at least hold for excitation energies up to 134 nJ, constituting the upper limit of excitation power available in the given experimental setup. In the actual measurement series, an excitation power of 130 nJ was used to achieve an excellent signal-to-noise ratio.

B.4 Peak positions of ^{1}Ph$_2$C and Ph$_2$CH$^+$

The peak wavelengths of ^{1}Ph$_2$C and Ph$_2$CH$^+$ undergo significant shifts within the first few tens of picoseconds. To quantify this behavior, a fitting procedure, which has recently been applied by Riedle et al. in a similar manner [211], was adapted. After defining a wavelength region of interest (338 to 376 nm for ^{1}Ph$_2$C and 416 to 447 nm for Ph$_2$CH$^+$), a parabola is fitted to transient absorption spectra of relevant time delays. The latter have carefully been selected by picking only spectra with a clearly discernible maximum. The maximum of the fitted parabola is then defined as the peak position of the respective feature. This procedure enables a sub-nm resolution, in contrast to being restricted to the wavelength increment of approximately 1.5 nm between adjacent data points (see graphical illustration for selected transient absorption spectra in Fig. B.2).
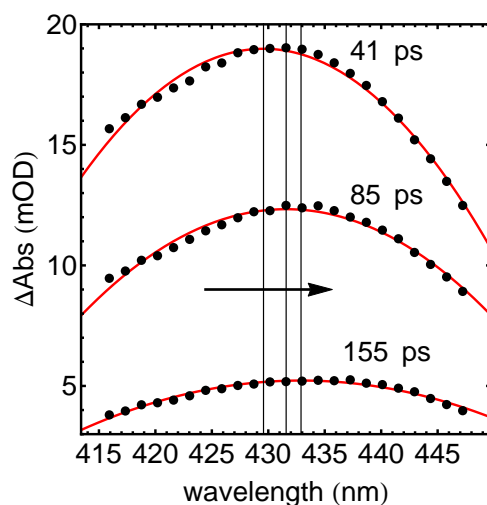
Figure B.2: Peak-shift analysis. Ph$_2$CH$^+$ absorption band after 285 nm excitation of Ph$_2$CN$_2$ in a 60:40 solvent mixture of MeCN:MeOH for different time delays. Displaced maxima of the fitted parabola curves (red) illustrate a spectral red-shift for increasing time delays.

For ^{1}Ph$_2$C, there is an initial red-shift of the peak wavelength within the first few picoseconds, characteristic for solvation of singlet carbenes [196], continued by a distinct blue-shift for longer delay times for solutions with higher MeCN fractions (see Fig. 4.7). The blue-shift on longer time scales might originate from geometrical changes of the two rings of the carbene molecule, or slow changes in the solvent environment. Since it is

also observed for the measurement in pure MeCN, it was tested if this might originate from small solvent impurities, but the same behavior was observed in dried MeCN and deliberate addition of tiny water amounts lead to clear differences, similar to addition of MeOH.

For Ph$_2$CH$^+$, one exclusively finds shifts towards longer wavelengths (plotted in Fig. 4.8). The latter dynamics can be fitted by a monoexponential decay function. By shifting each $\lambda(t)$-curve such that the data point with the highest time delay is set to $\lambda(t_{max}) = 0$, the offset value directly reveals the deviation from the final wavelength after relaxation (see Table B.1).

Table B.1: Fit of the Ph$_2$CH$^+$ peak position in MeOH/MeCN solvent mixtures using the model function $\lambda(t) = A_1 exp(-(t - t_0)/\tau) + A_2$.

MeCN (%)	A_1 (nm)	A_2 (nm)	τ (ps)	t_0 (ps)
0	-2.6	0	23.5	11.2
20	-3.0	-0.37	36.1	11.2
40	-3.9	-0.29	46.5	12.6
60	-5.6	-0.26	69.7	18.0
65	-6.1	-1.15	85.7	20.2
70	-7.6	-2.83	130.5	29.0
75	-6.6	-1.53	110.3	32.6

B.5 Transient absorption of $^3Ph_2C$

Figure B.3 depicts the transient absorption of Ph_2CN_2 under 285 nm excitation in pure MeCN and with small admixtures of MeOH at 315 nm (a)-(c). For better comparability, a normalized representation is given in the lower right panel (d). The upcoming absorption of $^3Ph_2C$ is fitted using a monoexponential model function. The corresponding time constants can be found in Table B.2.
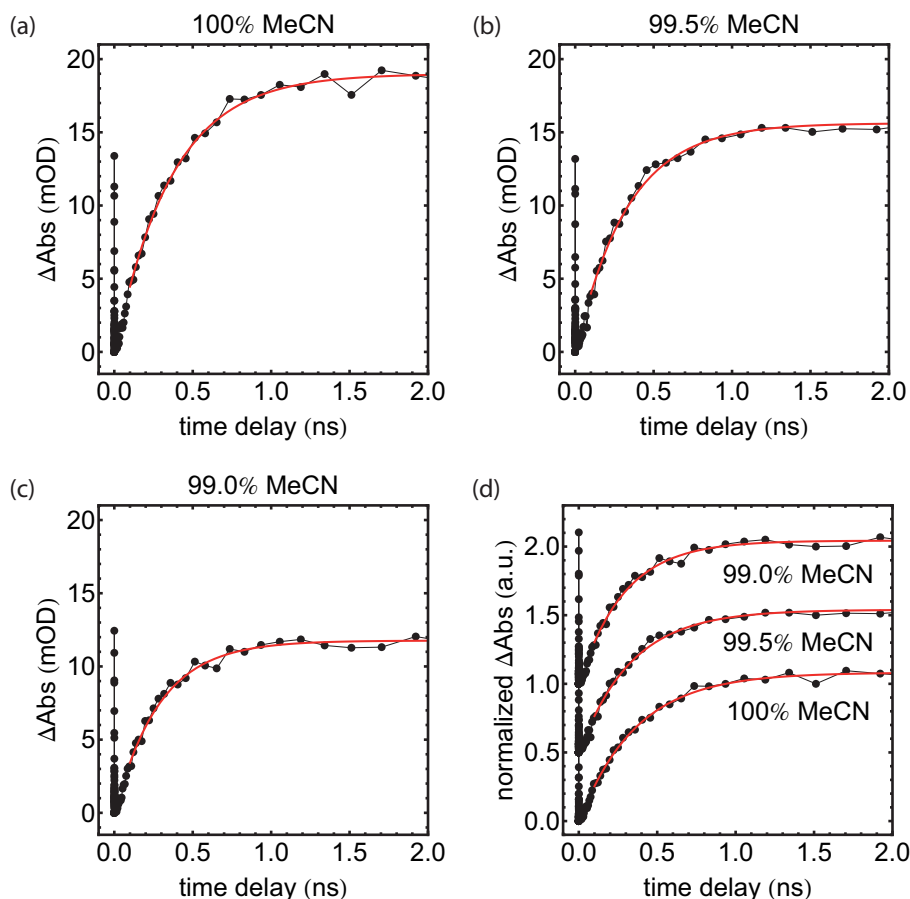
Figure B.3: Transient absorption of Ph_2CN_2 in pure MeCN and with small admixtures of MeOH at 315 nm.

Table B.2: Time constants obtained by fitting the rise of $^3Ph_2C$ in solvent mixtures of MeOH and MeCN.

MeCN (%)	100	99.5	99.0
τ (ps)	361.8	328.7	283.5

B.6 Time constants of ^{1}Ph$_2$C decay

When analyzing the transient behavior of ^{1}Ph$_2$C at its central wavelength of 355 nm, besides contributions from the coherent artifact [20, 86] and the short-lived absorption assigned to the excited precursor Ph$_2$CN$_2^*$, dynamics are observed which strongly depend on the solvent mixing ratio (see Fig. B.4). Generally, one finds slower dynamics for higher MeCN fractions. The rising dynamics at 355 nm, which e.g., comprise contributions from solvation and vibrational cooling, cannot be described by a single exponential function. However, this is possible for the decaying part of ^{1}Ph$_2$C. The resulting time constants for different MeCN fractions are listed in Table B.3. The corresponding fitting curves (red) are displayed in Fig. B.4 within the data range which has been considered in the fitting procedure.

Table B.3: Time constants obtained by fitting the decay of ^{1}Ph$_2$C in MeOH/MeCN solvent mixtures using the model function $\Delta Abs(t) = A_1 exp(-(t - t_0)/\tau) + A_2$.

MeCN (%)	0	20	40	60	65	70	75
τ (ps)	15.9	23.4	30.5	42.7	46.1	51.8	58.3

MeCN (%)	80	85	90	95.0	95.5	96.0	96.5
τ (ps)	67.0	80.6	107.1	175.4	193.5	205.3	227.6

MeCN (%)	97.0	97.5	98.0	98.5	99.0	99.5	100
τ (ps)	246.0	274.1	302.2	336.3	363.7	390.8	376.5
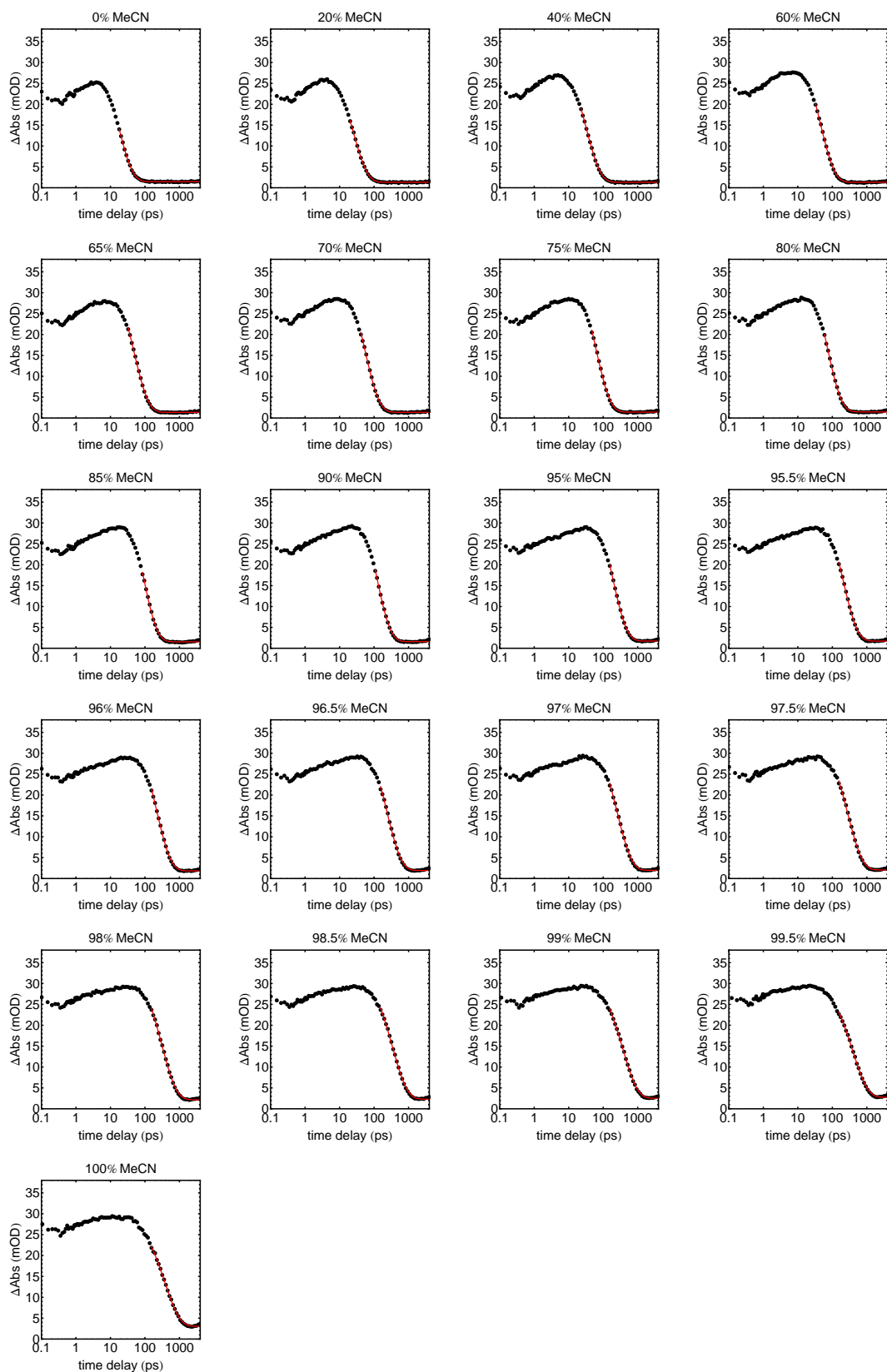
Figure B.4: Transient absorption of Ph$_2$CN$_2$ under 285 nm excitation in solvent mixtures of MeOH and MeCN at 355 nm.

B.7 Time constants of Ph_2CH^+

Early dynamics including the coherent artifact [20, 86] are neglected for fitting the rise and decay of Ph_2CH^+ in different solvent mixtures. The time constants resulting from a model function consisting of the sum of two exponential functions as well as a constant offset value are listed in Table B.4. The table also contains the wavelength of the pixel which was selected for the fitting procedure. The latter was determined by selecting the wavelength with the highest absorption change signal within the range of the Ph_2CH^+ absorption, accounting for wavelength shifts. Owing to the decreasing signal strength of Ph_2CH^+ when increasing the percentage of MeCN in the solvent mixture (see Fig. 4.4), the evaluation is limited to datasets up to 90% MeCN. The resulting fit curves together with the experimental data are depicted in Fig. B.5.

Table B.4: Time constants obtained by fitting the rise and decay of Ph_2CH^+ in MeOH/MeCN solvent mixtures using the model function $\Delta Abs(t) = A_1 exp(-(t - t_0)/\tau_1) - A_2 exp(-(t - t_0)/\tau_2) + A_3$.

MeCN (%)	0	20	40	60	65	70	75	80	85	90
λ (nm)	435.8	435.8	433.0	430.1	428.7	428.7	428.7	428.7	428.7	428.7
τ_1 (ps)	11.6	11.7	13.2	16.6	18.2	19.7	22.4	26.1	32.3	54.5
τ_2 (ps)	22.7	37.4	52.2	71.9	73.6	81.7	86.6	96.2	110.5	118.6
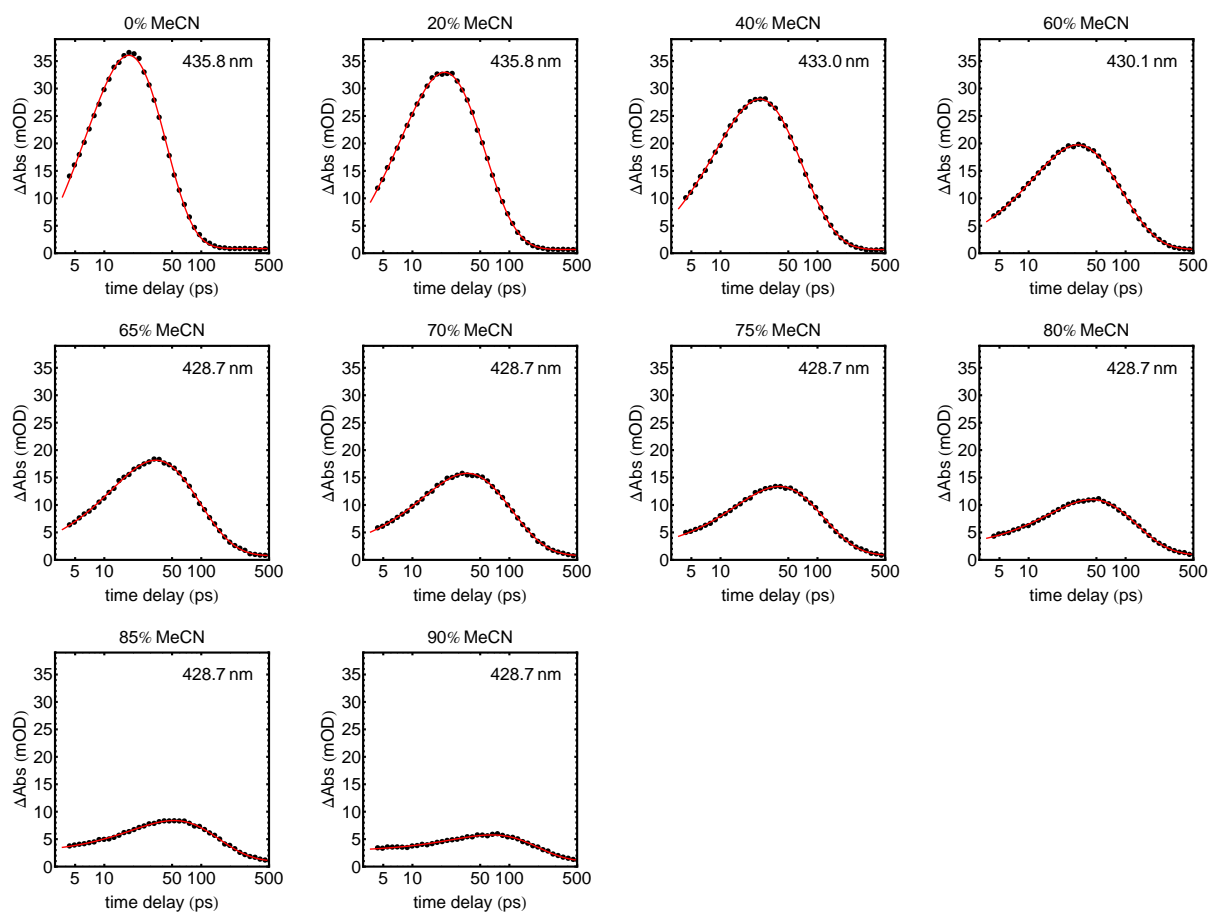
Figure B.5: Transient absorption of Ph$_2$CN$_2$ under 285 nm excitation in solvent mixtures of MeOH and MeCN at the respective center wavelengths of Ph$_2$CH$^+$.

Supporting Information to Chapter 6

C.1 Quantum chemical calculations on compound 3
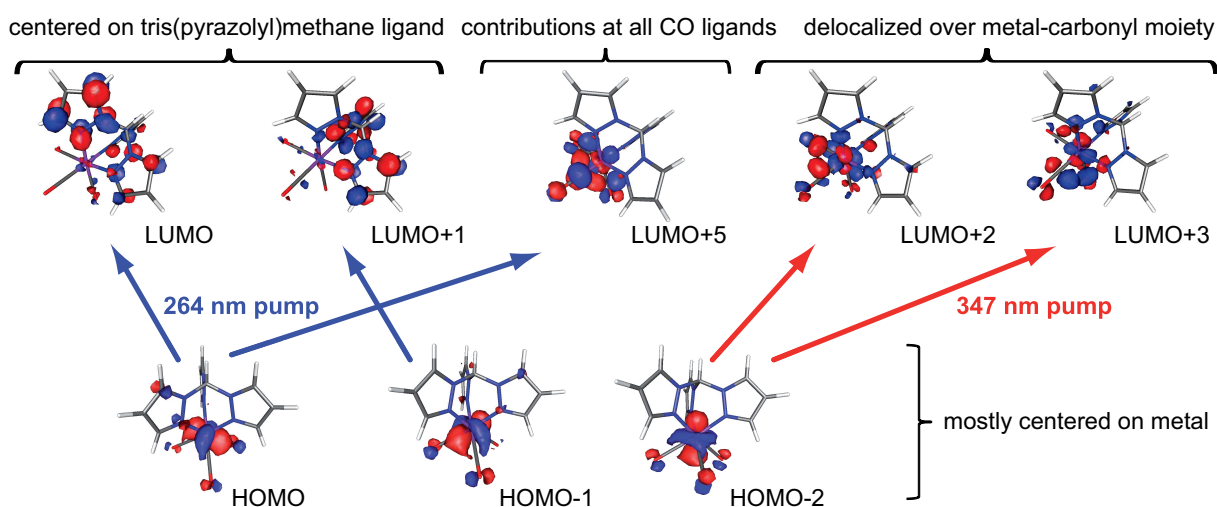
Figure C.1: TDDFT calculations performed by Prof. Dr. Ulrich Schatzschneider on compound 3 for the dominating electronic transitions induced with the employed pump pulses. Whereas the three involved HOMOs exhibit an electron density mostly located at the manganese atom, the character of the accessible LUMOs varies strongly. Calculations for exploring the electronic levels involved in the excitations were performed with ORCA 2.6 on a Linux cluster using TZV(P) or better basis sets on Mn, N, and O, and a VDZ basis set on all other atoms with the `Grid4` and `TightSCF` options [352, 353]. The first 30 singlet excited states were calculated in the gas phase. Figures reprinted from Ref. [4]. © (2013) American Chemical Society.

Table C.1: DFT calculations performed by Dr. Philipp Rudolf on the cationic unit of compound 3 and putative photoproducts formed after loss of one or two CO ligands. Calculations were performed with the software package Gaussian 09 [268], using the density functional Becke three-parameter hybrid method in combination with the Lee-Yang-Parr correlation functional (B3LYP) and the 6-311+G(d,p) basis set. The aqueous surrounding was included by a polarizable continuum model (PCM) in the self-consistent reaction field (SCRF). Wavenumbers were rescaled with the optimal scaling parameter from Ref. [269]. Table taken from Ref. [4]. © (2013) American Chemical Society.

molecule	DFT (1/cm)	assignment
$[\mathrm{Mn(CO)_3(tpm)}]^+$	1943 (FTIR 1958)	$\tilde{\nu}_{\mathrm{asym}}$ (CO)
	1943 (FTIR 1958)	$\tilde{\nu}_{\mathrm{asym}}$ (CO)
	2036 (FTIR 2051)	$\tilde{\nu}_{\mathrm{sym}}$ (CO)
$[\mathrm{Mn(CO)_3(\kappa\text{-}C\text{-}tpm)}]^+$	1915	$\tilde{\nu}_{\mathrm{asym}}$ (CO)
	1920	$\tilde{\nu}_{\mathrm{asym}}$ (CO)
	1978	$\tilde{\nu}_{\mathrm{sym}}$ (CO)
$[\mathrm{Mn(CO)_2(tpm)}]^+$	1885	$\tilde{\nu}_{\mathrm{asym}}$ (CO)
	1975	$\tilde{\nu}_{\mathrm{sym}}$ (CO)
$[\mathrm{Mn(CO)_2(tpm)(D_2O)}]^+$	1864	$\tilde{\nu}_{\mathrm{asym}}$ (CO)
	1955	$\tilde{\nu}_{\mathrm{sym}}$ (CO)
$[\mathrm{Mn(CO)(tpm)}]^+$	1875	$\tilde{\nu}$ (CO)
$[\mathrm{Mn(CO)(tpm)(D_2O)}]^+$	1833	$\tilde{\nu}$ (CO)
$[\mathrm{Mn(CO)(tpm)(D_2O)_2}]^+$	1821	$\tilde{\nu}$ (CO)

C.2 Quantum chemical calculations on compound 4

Table C.2: DFT calculations performed by Prof. Dr. Ulrich Schatzschneider on the cationic unit of compound 4 and putative photoproducts formed after loss of CO or NO ligands. Calculations were carried out on the Linux cluster of the Leibniz-Rechenzentrum (LRZ) in Munich with ORCA version 2.8, using the BP86 functional with the resolution-of-the-identity (RI) approximation, a def2-TZVP/def2-TZVP/J basis set, the `tightscf` and `grid4` options, and the COSMO solvation model with acetonitrile as the solvent for geometry optimizations and subsequent calculation of vibrational frequencies to characterize the structures obtained as minima by inspection for absence of imaginary modes. A scaling factor of 1.018 was used to match calculated wavenumbers with experimental values presented in Ref. [302] (the experimental wavenumbers presented in Ref. [302] are in good agreement with the ones presented in this dissertation). Calculated wavenumbers and the FTIR wavenumber marked with an asterik* are taken from Ref. [302].

molecule	DFT (1/cm)	assignment
$[\mathrm{Mo(CO)_2(NO)}(i\mathrm{Pr_3tacn})]^+$	1704 (FTIR 1671)	$\tilde{\nu}$ (NO)
	1906 (FTIR 1932)	$\tilde{\nu}_{\mathrm{asym}}$ (CO)
	2006 (FTIR 2023)	$\tilde{\nu}_{\mathrm{sym}}$ (CO)
$[\mathrm{Mo(CO)_2(CH_3CN)}(i\mathrm{Pr_3tacn})]^+$	1654	$\tilde{\nu}_{\mathrm{asym}}$ (CO)
	1754	$\tilde{\nu}_{\mathrm{sym}}$ (CO)
$[\mathrm{Mo(CO)(NO)(CH_3CN)}(i\mathrm{Pr_3tacn})]^+$	1647 (FTIR 1615)	$\tilde{\nu}$ (NO)
	1886 (FTIR 1896)	$\tilde{\nu}$ (CO)
$[\mathrm{Mo(NO)(CH_3CN)_2}(i\mathrm{Pr_3tacn})]^+$	1584 (FTIR 1598*)	$\tilde{\nu}$ (NO)
$[\mathrm{Mo(CO)(CH_3CN)_2}(i\mathrm{Pr_3tacn})]^+$	1637	$\tilde{\nu}$ (CO)

C.3 Transient absorption on pure MeCN
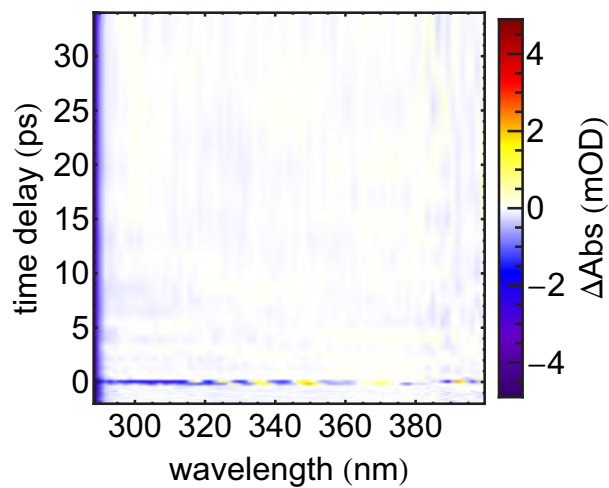
Figure C.2: Transient absorption of MeCN in the VIS to UV regime after 285 nm excitation. The negative signal at short probe wavelengths is due to scattering of the pump beam.

List of Abbreviations

2D two-dimensional

3D three-dimensional

ATR attenuated total reflectance

a.u. arbitrary unit

BBO β-barium borate

BS beam splitter

CCD charge-coupled device

CEP carrier envelope phase

cm centimeter

CMOS complementary metal-oxide-semiconductor

CO carbon monoxide

CORM CO-releasing molecule

CP chirped pulse

CPA chirped-pulse amplification

CPU chirped-pulse upconversion

CT charge transfer

CW continuous wave

D$_2$O heavy water

DFG difference-frequency generation

DFT density functional theory

DM dichroic mirror

DMSO dimethyl sulfoxide

DS delay stage

e.g. exempli gratia

eq. equivalent

ESA excited-state absorption

EtOH ethanol

FFT fast Fourier transform

FID free induction decay

FROG frequency-resolved optical gating

fs femtosecond

FT Fourier transform

FWHM full width at half maximum

FWM four-wave mixing

GDD group-delay dispersion

GSA ground-state absorption

GSB ground-state bleaching

GVD group-velocity dispersion

h hours

H$_2$O water

HOMO highest occupied molecular orbital

HR high reflection

HT high transmission

IC internal conversion

i.e. id est

IR infrared

ISC intersystem crossing

IVR intramolecular vibrational relaxation

JTFR joint time-frequency representation

LBO lithium triborate (LiB_3O_5)

LNB lithium niobate ($LiNbO_3$)

LPF longpass filter

LUMO lowest unoccupied molecular orbital

MCT mercury cadmium telluride (HgCdTe)

MD molecular dynamics

MeCN acetonitrile

MeOH methanol

MgO magnesium oxide

MIR mid-infrared

MM molecular mechanics

mm millimeter

NC nonlinear crystal

ND neutral density

NIR near-infrared

nm nanometer

NMR nuclear magnetic resonance

NO nitric oxide

NOPA noncollinear optical parametric amplifier

nr non-radiative

ns nanosecond

OD optical density

OPA optical parametric amplifier *or* optical parametric amplification

PA product absorption

PES potential energy surface

PFID perturbed free induction decay

Ph$_2$C diphenylcarbene

Ph$_2$CH$^+$ benzhydryl cation

Ph$_2$CN$_2$ diphenyldiazomethane

POL polarizer

PR probe pulse

ps picosecond

QM quantum mechanics

r radiative

RG red glass

S sample *or* singlet—depending on the context

SE stimulated emission

SFG sum-frequency generation

SHG second-harmonic generation

SPF shortpass filter

SPIDER spectral phase interferometry for direct electric field reconstruction

SPM self-phase modulation

SVEA slowly varying envelope approximation

T triplet

TA transient absorption

TD-DFT time-dependent density functional theory

TEA time-encoded arrangement

TEM transversal electromagnetic

TFA trifluoroacetic acid

Ti:Sapphire titanium-doped aluminium oxide (Al$_2$O$_3$)

TOD third-order dispersion

TPA two-photon absorption

UV ultraviolet

VC vibrational cooling

VET vibrational energy transfer

VIS visible

WLC white-light continuum

WLG white-light generation

XPM cross-phase modulation

XUV extreme ultraviolet

Bibliography

[1] J. Knorr, P. Sokkar, S. Schott, P. Costa, W. Thiel, W. Sander, E. Sánchez-García, and P. Nuernberger,
Tracing Primary Processes of Diphenylcarbene in Solvent Mixtures: A Solvent Rivalry.
manuscript in preparation (2015).

[2] J. Knorr, S. Schott, J. Riefer, C. Nagel, U. Schatzschneider, and P. Nuernberger,
Ultrafast photochemistry of a carbonyl-nitrosyl molybdenum complex.
manuscript in preparation (2015).

[3] J. Knorr, P. Rudolf, and P. Nuernberger,
A comparative study on chirped-pulse upconversion and direct multichannel MCT detection.
Opt. Express **21**, 30693–30706 (2013).

[4] P. Rudolf, F. Kanal, J. Knorr, C. Nagel, J. Niesel, T. Brixner, U. Schatzschneider, and P. Nuernberger,
Ultrafast Photochemistry of a Manganese-Tricarbonyl CO-Releasing Molecule (CORM) in Aqueous Solution.
J. Phys. Chem. Lett. **4**, 596–602 (2013).

[5] H. Thierschmann, M. Henke, J. Knorr, L. Maier, C. Heyn, W. Hansen, H. Buhmann, and L. W. Molenkamp,
Diffusion thermopower of a serial double quantum dot.
New J. Phys. **15**, 123010 (2013).

[6] T. S. Rose, M. J. Rosker, and A. H. Zewail,
Femtosecond real-time observation of wave packet oscillations (resonance) in dissociation reactions.
J. Chem. Phys. **88**, 6672–6673 (1988).

[7] A. H. Zewail,
Femtochemistry: Atomic-Scale Dynamics of the Chemical Bond.
J. Phys. Chem. A **104**, 5660–5694 (2000).

[8] J. Spencer Baskin and A. H. Zewail,
Freezing Atoms in Motion: Principles of Femtochemistry and Demonstration by Laser Stroboscopy.
J. Chem. Educ. **78**, 737–751 (2001).

[9] G. A. Voth and R. M. Hochstrasser,
Transition State Dynamics and Relaxation Processes in Solutions: A Frontier of Physical Chemistry.
J. Phys. Chem. **100**, 13034–13049 (1996).

[10] J. Buback, M. Kullmann, F. Langhojer, P. Nuernberger, R. Schmidt, F. Würthner, and T. Brixner,
Ultrafast Bidirectional Photoswitching of a Spiropyran.
J. Am. Chem. Soc. **132**, 16510–16519 (2010).

[11] J. Buback, P. Nuernberger, M. Kullmann, F. Langhojer, R. Schmidt, F. Würthner, and T. Brixner,
Ring-Closure and Isomerization Capabilities of Spiropyran-Derived Merocyanine Isomers.
J. Phys. Chem. A **115**, 3924–3935 (2011).

[12] T. Brixner, J. Stenger, H. M. Vaswani, M. Cho, R. E. Blankenship, and G. R. Fleming,
Two-dimensional spectroscopy of electronic couplings in photosynthesis.
Nature **434**, 625–628 (2005).

[13] G. S. Engel, T. R. Calhoun, E. L. Read, T.-K. Ahn, T. Mančal, Y.-C. Cheng, R. E. Blankenship,
and G. R. Fleming,
Evidence for wavelike energy transfer through quantum coherence in photosynthetic systems.
Nature **446**, 782–786 (2007).

[14] D. B. Turner, K. W. Stone, K. Gundogdu, and K. A. Nelson,
Three-dimensional electronic spectroscopy of excitons in GaAs quantum wells.
J. Chem. Phys. **131**, 144510 (2009).

[15] Z. Zhang, K. L. Wells, M. T. Seidel, and H.-S. Tan,
Fifth-Order Three-Dimensional Electronic Spectroscopy Using a Pump–Probe Configuration.
J. Phys. Chem. B **117**, 15369–15385 (2013).

[16] S. Ruetzel, M. Diekmann, P. Nuernberger, C. Walter, B. Engels, and T. Brixner,
Multidimensional spectroscopy of photoreactivity.
Proc. Natl. Acad. Sci. USA **111**, 4764–4769 (2014).

[17] P. Nuernberger, S. Ruetzel, and T. Brixner,
Multidimensional Electronic Spectroscopy of Photochemical Reactions.
Angew. Chem. Int. Ed. **54**, 11368–11386 (2015).

[18] P. O. Stoutland, R. B. Dyer, and W. H. Woodruff,
Ultrafast infrared spectroscopy.
Science **257**, 1913–1917 (1992).

[19] M. D. Fayer,
Ultrafast Infrared Vibrational Spectroscopy.
CRC Press, Boca Raton (USA) (2013).

[20] U. Megerle, I. Pugliesi, C. Schriever, C. F. Sailer, and E. Riedle,
*Sub-50 fs broadband absorption spectroscopy with tunable excitation: putting the analysis of ultrafast
molecular dynamics on solid ground.*
Appl. Phys. B **96**, 215–231 (2009).

[21] P. Costa and W. Sander,
Hydrogen Bonding Switches the Spin State of Diphenylcarbene from Triplet to Singlet.
Angew. Chem. Int. Ed. **53**, 5122–5125 (2014).

[22] P. Costa, M. Fernandez-Oliva, E. Sánchez-García, and W. Sander,
The Highly Reactive Benzhydryl Cation Isolated and Stabilized in Water Ice.
J. Am. Chem. Soc. **136**, 15625–15630 (2014).

[23] K. J. Kubarych, M. Joffre, A. Moore, N. Belabas, and D. M. Jonas,
Mid-infrared electric field characterization using a visible charge-coupled-device-based spectrometer.
Opt. Lett. **30**, 1228–1230 (2005).

[24] K. F. Lee, P. Nuernberger, A. Bonvalet, and M. Joffre,
Removing cross-phase modulation from midinfrared chirped-pulse upconversion spectra.
Opt. Express **17**, 18738–18744 (2009).

[25] R. Alberto and R. Motterlini,
Chemistry and biological activities of CO-releasing molecules (CORMs) and transition metal complexes.
Dalton Trans. pp. 1651–1660 (2007).

[26] C. C. Romão, W. A. Blättler, J. D. Seixas, and G. J. L. Bernardes,
Developing drug molecules for therapy with carbon monoxide.
Chem. Soc. Rev. **41**, 3571–3583 (2012).

[27] J. D. Jackson,
Classical Electrodynamics.
Third edition. Wiley & Sons, New York, NY (USA) (1999).

[28] J.-C. Diels and W. Rudolph,
Ultrashort Laser Pulse Phenomena: Fundamentals, Techniques, and Applications on a Femtosecond Time Scale (Optics and Photonics Series).
Second edition. Academic Press, Burlington (2006).

[29] P. J. Mohr, B. N. Taylor, and D. B. Newell.
The 2014 CODATA recommended values of the fundamental physical constants.
URL http://physics.nist.gov/cuu/Constants/index.html (2014).

[30] R. Bracewell,
The Fourier Transform and Its Applications.
Third edition. McGraw-Hill, Boston (USA) (1999).

[31] D. T. Reid,
Few cycle EM pulses.
Contemp. Phys. **40**, 193–204 (1999).

[32] M. Wollenhaupt, A. Assion, and T. Baumert. *Femtosecond Laser Pulses: Linear Properties, Manipulation, Generation and Measurement.* In F. Träger (Ed.), *Springer Handbook of Lasers and Optics*, pp. 937–983. Springer, New York, NY (USA) (2007).

[33] D. J. Jones, S. A. Diddams, J. K. Ranka, A. Stentz, R. S. Windeler, J. L. Hall, and S. T. Cundiff,
Carrier-Envelope Phase Control of Femtosecond Mode-Locked Lasers and Direct Optical Frequency Synthesis.
Science **288**, 635–639 (2000).

[34] A. Apolonski, A. Poppe, G. Tempea, C. Spielmann, T. Udem, R. Holzwarth, T. W. Hänsch, and F. Krausz,
Controlling the Phase Evolution of Few-Cycle Light Pulses.
Phys. Rev. Lett. **85**, 740–743 (2000).

[35] T. Udem, R. Holzwarth, and T. W. Hänsch,
Optical frequency metrology.
Nature **416**, 233–237 (2002).

[36] H. P. Hsu,
Fourier Analysis.
Simon & Schuster, New York, NY (USA) (1970).

[37] J.-C. M. Diels, J. J. Fontaine, I. C. McMichael, and F. Simoni,
Control and measurement of ultrashort pulse shapes (in amplitude and phase) with femtosecond accuracy.
Appl. Opt. **24**, 1270–1282 (1985).

[38] E. Sorokin, G. Tempea, and T. Brabec,
Measurement of the root-mean-square width and the root-mean-square chirp in ultrafast optics.
J. Opt. Soc. Am. B **17**, 146–150 (2000).

[39] R. Trebino,
Frequency-Resolved Optical Gating: The Measurement of Ultrashort Laser Pulses.
Har/Cdr edition. Springer Netherlands (2002).

[40] L. Cohen,
Time-frequency distributions – a review.
Proc. IEEE **77**, 941–981 (1989).

[41] R. W. Boyd,
Nonlinear Optics.
Third edition. Academic Press, Burlington (2008).

[42] G. B. Arfken,
Mathematical Methods for Physicists.
Third edition. Academic Press, San Diego, Ca (USA) (1985).

[43] D. J. Tannor,
Introduction to Quantum Mechanics: A Time-Dependent Perspective.
University Science Books, Sausalito, CA (USA) (2007).

[44] P. Nürnberger.
Adaptive Control of Quantum Systems with Femtosecond Laser Pulses.
Dissertation. Universität Würzburg (2007).

[45] I. Walmsley, L. Waxer, and C. Dorrer,
The role of dispersion in ultrafast optics.
Rev. Sci. Instrum. **72**, 1–29 (2001).

[46] T. Brixner.
Adaptive Femtosecond Quantum Control.
Dissertation. Universität Würzburg (2001).

[47] S. Rützel.
Pulse-Sequence Approaches for Multidimensional Electronic Spectroscopy of Ultrafast Photochemistry.
Dissertation. Universität Würzburg (2014).

[48] Y. R. Shen,
The Principles of Nonlinear Optics.
Wiley classics edition. Wiley & Sons, New York, NY (USA) (2002).

[49] V. G. Dmitriev, G. G. Gurzadyan, and D. N. Nikogosyan,
Handbook of Nonlinear Optical Crystals.
Third edition. Springer, Berlin (Germany) (1999).

[50] P. Lokai, B. Burghardt, D. Basting, and W. Mückenheim,
Type-I second harmonic and sum frequency generation in β-BaB_2O_4.
Laser und Optoelektronik **19**, 296–300 (1987).

[51] P. A. Franken and J. F. Ward,
Optical Harmonics and Nonlinear Phenomena.
Rev. Mod. Phys. **35**, 23–39 (1963).

[52] R. R. Alfano and S. L. Shapiro,
Emission in the Region 4000 to 7000 Å Via Four-Photon Coupling in Glass.
Phys. Rev. Lett. **24**, 584–587 (1970).

[53] R. R. Alfano and S. L. Shapiro,
Observation of Self-Phase Modulation and Small-Scale Filaments in Crystals and Glasses.
Phys. Rev. Lett. **24**, 592–594 (1970).

[54] S. A. Kovalenko, A. L. Dobryakov, J. Ruthmann, and N. P. Ernsting,
Femtosecond spectroscopy of condensed phases with chirped supercontinuum probing.
Phys. Rev. A **59**, 2369–2384 (1999).

[55] G. Cerullo and S. De Silvestri,
Ultrafast optical parametric amplifiers.
Rev. Sci. Instrum. **74**, 1–18 (2003).

[56] G. Yang and Y. R. Shen,
Spectral broadening of ultrashort pulses in a nonlinear medium.
Opt. Lett. **9**, 510–512 (1984).

[57] I. Buchvarov, A. Trifonov, and T. Fiebig,
Toward an understanding of white-light generation in cubic media—polarization properties across the entire spectral range.
Opt. Lett. **32**, 1539–1541 (2007).

[58] C. Rullière (Ed.),
Femtosecond Laser Pulses: Principles and Experiments.
Springer, Berlin (Germany) (1998).

[59] G. Steinmeyer and G. Stibenz,
Generation of sub-4-fs pulses via compression of a white-light continuum using only chirped mirrors.
Appl. Phys. B **82**, 175–181 (2006).

[60] E. Matsubara, K. Yamane, T. Sekikawa, and M. Yamashita,
Generation of 2.6 fs optical pulses using induced-phase modulation in a gas-filled hollow fiber.
J. Opt. Soc. Am. B **24**, 985–989 (2007).

[61] D. A. McQuarrie and J. D. Simon,
Physical Chemistry: A Molecular Approach.
University Science Books, Sausalito, CA (USA) (1997).

[62] B. H. Bransden and C. J. Joachain,
Physics of Atoms and Molecules.
Second edition. Pearson Education, Harlow (England) (2003).

[63] J. J. Sakurai and J. Napolitano,
Modern Quantum Mechanics.
Second edition. Addison-Wesley, Boston, MA (USA) (2011).

[64] L. E. Reichl,
A Modern Course in Statistical Physics.
Third edition. Wiley-VCH, Weinheim (Germany) (2009).

[65] W. Domcke, D. R. Yarkony, and H. Köppel (Eds.),
Conical Intersections: Theory, Computation and Experiment.
World Scientific, Singapore (2011).

[66] G. Herzberg,
Molecular Spectra and Molecular Structure: II. Infrared and Raman Spectra of Polyatomic Molecules.
Van Nostrand Reinhold Company, New York, NY (USA) (1945).

[67] A. Steinbacher.
Circular dichroism and accumulative polarimetry of chiral femtochemistry.
Dissertation. Universität Würzburg (2015).

[68] E. T. J. Nibbering, H. Fidder, and E. Pines,
Ultrafast Chemistry: Using Time-Resolved Vibrational Spectroscopy for Interrogation of Structural Dynamics.
Annu. Rev. Phys. Chem. **56**, 337–367 (2005).

[69] H. Lin and D. G. Truhlar,
QM/MM: what have we learned, where are we, and where do we go from here?
Theor. Chem. Acc. **117**, 185–199 (2007).

[70] H. M. Senn and W. Thiel,
QM/MM Methods for Biomolecular Systems.
Angew. Chem. Int. Ed. **48**, 1198–1229 (2009).

[71] G. Groenhof. *Introduction to QM/MM Simulations.* In L. Monticelli and E. Salonen (Eds.), *Biomolecular Simulations: Methods and Protocols*, volume 924 of *Methods in Molecular Biology*, pp. 43–66. Springer (2013).

[72] R. G. Parr and W. Yang,
Density-Functional Theory of Atoms and Molecules.
Oxford University Press, New York, NY (USA) (1989).

[73] W. Koch and M. C. Holthausen,
A Chemist's Guide to Density Functional Theory.
Second edition. Wiley-VCH, Weinheim (Germany) (2001).

[74] L. Serrano-Andrés and M. Merchán,
Quantum chemistry of the excited state: 2005 overview.
J. Mol. Struct. (Theochem) **729**, 99–108 (2005).

[75] D. Jacquemin, V. Wathelet, E. A. Perpete, and C. Adamo,
Extensive TD-DFT Benchmark: Singlet-Excited States of Organic Molecules.
J. Chem. Theory Comput. **5**, 2420–2435 (2009).

[76] C. A. Guido, D. Jacquemin, C. Adamo, and B. Mennucci,
On the TD-DFT Accuracy in Determining Single and Double Bonds in Excited-State Structures of Organic Molecules.
J. Phys. Chem. A **114**, 13402–13410 (2010).

[77] A. D. Laurent and D. Jacquemin,
TD-DFT Benchmarks: A Review.
Int. J. Quantum Chem. **113**, 2019–2039 (2013).

[78] R. G. W. Norrish and G. Porter,
Chemical Reactions Produced by Very High Light Intensities.
Nature **164**, 658 (1949).

[79] G. Porter,
Flash Photolysis and Spectroscopy. A New Method for the Study of Free Radical Reactions.
Proc. R. Soc. London Ser. A **200**, 284–300 (1950).

[80] N. J. Turro, V. Ramamurthy, and J. C. Scaiano,
Modern Molecular Photochemistry of Organic Molecules.
University Science Books, Sausalito, CA (USA) (2010).

[81] K. Wynne and R. M. Hochstrasser,
The theory of ultrafast vibrational spectroscopy.
Chem. Phys. **193**, 211–236 (1995).

[82] M. Kasha,
Characterization of electronic transitions in complex molecules.
Discuss. Faraday Soc. **9**, 14–19 (1950).

[83] I. H. M. van Stokkum, D. S. Larsen, and R. van Grondelle,
Global and target analysis of time-resolved spectra.
Biochim. Biophys. Acta **1657**, 82–104 (2004).

[84] M. V. Lebedev, O. V. Misochko, T. Dekorsy, and N. Georgiev,
On the nature of "coherent artifact".
J. Exp. Theor. Phys. **100**, 272–282 (2005).

[85] B. Dietzek, T. Pascher, V. Sundström, and A. Yartsev,
*Appearance of coherent artifact signals in femtosecond transient absorption spectroscopy in depen-
dence on detector design.*
Laser Phys. Lett. **4**, 38–43 (2007).

[86] K. Ekvall, P. van der Meulen, C. Dhollande, L.-E. Berg, S. Pommeret, R. Naskrecki, and J.-C.
Mialocq,
Cross phase modulation artifact in liquid phase transient absorption spectroscopy.
J. Appl. Phys. **87**, 2340–2352 (2000).

[87] M. Lorenc, M. Ziolek, R. Naskrecki, J. Karolczak, J. Kubicki, and A. Maciejewski,
Artifacts in femtosecond transient absorption spectroscopy.
Appl. Phys. B **74**, 19–27 (2002).

[88] D. Wolpert.
Quantum Control of Photoinduced Chemical Reactions.
Dissertation. Universität Würzburg (2008).

[89] M. Rasmusson, A. N. Tarnovsky, E. Åkesson, and V. Sundström,
*On the use of two-photon absorption for determination of femtosecond pump–probe cross-correlation
functions.*
Chem. Phys. Lett. **335**, 201–208 (2001).

[90] P. Hamm,
Coherent effects in femtosecond infrared spectroscopy.
Chem. Phys. **200**, 415–429 (1995).

[91] S. Yan, M. T. Seidel, and H.-S. Tan,
Perturbed free induction decay in ultrafast mid-IR pump–probe spectroscopy.
Chem. Phys. Lett. **517**, 36–40 (2011).

[92] P. Nuernberger, K. F. Lee, A. Bonvalet, T. Polack, M. H. Vos, A. Alexandrou, and M. Joffre,
Suppression of perturbed free-induction decay and noise in experimental ultrafast pump–probe data.
Opt. Lett. **34**, 3226–3228 (2009).

[93] P. Hamm, S. Wiemann, M. Zurek, and W. Zinth,
Highly sensitive multichannel spectrometer for subpicosecond spectroscopy in the midinfrared.
Opt. Lett. **19**, 1642–1644 (1994).

[94] P. Hamm, R. A. Kaindl, and J. Stenger,
Noise suppression in femtosecond mid-infrared light sources.
Opt. Lett. **25**, 1798–1800 (2000).

[95] J. N. Moore, P. A. Hansen, and R. M. Hochstrasser,
A new method for picosecond time-resolved infrared spectroscopy: applications to CO photodissociation from iron porphyrins.
Chem. Phys. Lett. **138**, 110–114 (1987).

[96] T. P. Dougherty and E. J. Heilweil,
Dual-beam subpicosecond broadband infrared spectrometer.
Opt. Lett. **19**, 129–131 (1994).

[97] M. Lim, T. A. Jackson, and P. A. Anfinrud,
Binding of CO to myoglobin from a heme pocket docking site to form nearly linear Fe-C-O.
Science **269**, 962–966 (1995).

[98] I. V. Rubtsov, T. Zhang, H. Nakajima, S. Aono, G. I. Rubtsov, S. Kumazaki, and K. Yoshihara,
Conformational Dynamics of the Transcriptional Regulator CooA Protein Studied by Subpicosecond Mid-Infrared Vibrational Spectroscopy.
J. Am. Chem. Soc. **123**, 10056–10062 (2001).

[99] J. Herbst, K. Heyne, and R. Diller,
Femtosecond Infrared Spectroscopy of Bacteriorhodopsin Chromophore Isomerization.
Science **297**, 822–825 (2002).

[100] H. J. Bakker, H.-K. Nienhuys, G. Gallot, N. Lascoux, G. M. Gale, J.-C. Leicknam, and S. Bratos,
Transient absorption of vibrationally excited water.
J. Chem. Phys. **116**, 2592–2598 (2002).

[101] E. T. J. Nibbering and T. Elsaesser,
Ultrafast Vibrational Dynamics of Hydrogen Bonds in the Condensed Phase.
Chem. Rev. **104**, 1887–1914 (2004).

[102] J. Bredenbeck, J. Helbing, J. R. Kumita, G. A. Woolley, and P. Hamm,
α-Helix formation in a photoswitchable peptide tracked from picoseconds to microseconds by time-resolved IR spectroscopy.
Proc. Natl. Acad. Sci. USA **102**, 2379–2384 (2005).

[103] M. L. Groot, L. J. G. W. van Wilderen, and M. Di Donato,
Time-resolved methods in biophysics. 5. Femtosecond time-resolved and dispersed infrared spectroscopy on proteins.
Photochem. Photobiol. Sci. **6**, 501–507 (2007).

[104] W. J. Schreier, T. E. Schrader, F. O. Koller, P. Gilch, C. E. Crespo-Hernández, V. N. Swaminathan, T. Carell, W. Zinth, and B. Kohler,
Thymine Dimerization in DNA Is an Ultrafast Photoreaction.
Science **315**, 625–629 (2007).

[105] J. Treuffet, K. J. Kubarych, J.-C. Lambry, E. Pilet, J.-B. Masson, J.-L. Martin, M. H. Vos, M. Joffre, and A. Alexandrou,
Direct observation of ligand transfer and bond formation in cytochrome c oxidase by using mid-infrared chirped-pulse upconversion.
Proc. Natl. Acad. Sci. USA **104**, 15705–15710 (2007).

[106] D. Cringus, A. Bakulin, J. Lindner, P. Vöhringer, M. S. Pshenichnikov, and D. A. Wiersma,
Ultrafast Energy Transfer in Water-AOT Reverse Micelles.
J. Phys. Chem. B **111**, 14193–14207 (2007).

[107] Y. Zhang, G. Burdzinski, J. Kubicki, and M. S. Platz,
Direct Observation of Carbene and Diazo Formation from Aryldiazirines by Ultrafast Infrared Spectroscopy.
J. Am. Chem. Soc. **130**, 16134–16135 (2008).

[108] P. Rudolf, J. Buback, J. Aulbach, P. Nuernberger, and T. Brixner,
Ultrafast Multisequential Photochemistry of 5-Diazo Meldrum's Acid.
J. Am. Chem. Soc. **132**, 15213–15222 (2010).

[109] S. Yan, M. T. Seidel, Z. Zhang, W. K. Leong, and H.-S. Tan,
Ultrafast vibrational relaxation dynamics of carbonyl stretching modes in $Os_3(CO)_{12}$.
J. Chem. Phys. **135**, 024501 (2011).

[110] P. Nuernberger, K. F. Lee, A. Bonvalet, L. Bouzhir-Sima, J.-C. Lambry, U. Liebl, M. Joffre, and M. H. Vos,
Strong Ligand–Protein Interactions Revealed by Ultrafast Infrared Spectroscopy of CO in the Heme Pocket of the Oxygen Sensor FixL.
J. Am. Chem. Soc. **133**, 17110–17113 (2011).

[111] Y. Yang, M. Linke, T. von Haimberger, J. Hahn, R. Matute, L. González, P. Schmieder, and K. Heyne,
Real-Time Tracking of Phytochrome's Orientational Changes During Pr Photoisomerization.
J. Am. Chem. Soc. **134**, 1408–1411 (2012).

[112] J. P. Lomont, S. C. Nguyen, and C. B. Harris,
Ultrafast TRIR and DFT Studies of the Photochemical Dynamics of $Co_4(CO)_{12}$ in Solution.
Organometallics **31**, 4031–4038 (2012).

[113] A. Lukacs, R.-K. Zhao, A. Haigney, R. Brust, G. M. Greetham, M. Towrie, P. J. Tonge, and S. R. Meech,
Excited State Structure and Dynamics of the Neutral and Anionic Flavin Radical Revealed by Ultrafast Transient Mid-IR to Visible Spectroscopy.
J. Phys. Chem. B **116**, 5810–5818 (2012).

[114] N. T. Hunt,
2D-IR spectroscopy: ultrafast insights into biomolecule structure and function.
Chem. Soc. Rev. **38**, 1837–1848 (2009).

[115] E. J. Heilweil,
Ultrashort-pulse multichannel infrared spectroscopy using broadband frequency conversion in $LiIO_3$.
Opt. Lett. **14**, 551–553 (1989).

[116] M. F. DeCamp and A. Tokmakoff,
Upconversion multichannel infrared spectrometer.
Opt. Lett. **30**, 1818–1820 (2005).

[117] G. W. Jones, D. L. Marks, C. Vinegoni, and S. A. Boppart,
       High-spectral-resolution coherent anti-Stokes Raman scattering with interferometrically detected broadband chirped pulses.
       Opt. Lett. **31**, 1543–1545 (2006).

[118] P. Nuernberger, G. Vogt, R. Selle, S. Fechner, T. Brixner, and G. Gerber,
       Generation of shaped ultraviolet pulses at the third harmonic of titanium-sapphire femtosecond laser radiation.
       Appl. Phys. B **88**, 519–526 (2007).

[119] M. J. Nee, R. McCanne, K. J. Kubarych, and M. Joffre,
       Two-dimensional infrared spectroscopy detected by chirped pulse upconversion.
       Opt. Lett. **32**, 713–715 (2007).

[120] M. J. Nee, C. R. Baiz, J. M. Anna, R. McCanne, and K. J. Kubarych,
       Multilevel vibrational coherence transfer and wavepacket dynamics probed with multidimensional IR spectroscopy.
       J. Chem. Phys. **129**, 084503 (2008).

[121] P. Nuernberger, K. F. Lee, A. Bonvalet, M. H. Vos, and M. Joffre,
       Multiply Excited Vibration of Carbon Monoxide in the Primary Docking Site of Hemoglobin Following Photolysis from the Heme.
       J. Phys. Chem. Lett. **1**, 2077–2081 (2010).

[122] J. M. Anna, M. J. Nee, C. R. Baiz, R. McCanne, and K. J. Kubarych,
       Measuring absorptive two-dimensional infrared spectra using chirped-pulse upconversion detection.
       J. Opt. Soc. Am. B **27**, 382–393 (2010).

[123] M. Di Donato and M. L. Groot,
       Ultrafast infrared spectroscopy in photosynthesis.
       Biochim. Biophys. Acta **1847**, 2–11 (2015).

[124] R. Maksimenka, P. Nuernberger, K. F. Lee, A. Bonvalet, J. Milkiewicz, C. Barta, M. Klima, T. Oksenhendler, P. Tournois, D. Kaplan, and M. Joffre,
       Direct mid-infrared femtosecond pulse shaping with a calomel acousto-optic programmable dispersive filter.
       Opt. Lett. **35**, 3565–3567 (2010).

[125] J. Zhu, T. Mathes, A. D. Stahl, J. T. M. Kennis, and M. L. Groot,
       Ultrafast mid-infrared spectroscopy by chirped pulse upconversion in 1800-1000cm^{-1} region.
       Opt. Express **20**, 10562–10571 (2012).

[126] C. R. Baiz and K. J. Kubarych,
       Ultrabroadband detection of a mid-IR continuum by chirped-pulse upconversion.
       Opt. Lett. **36**, 187–189 (2011).

[127] Y. Nomura, Y.-T. Wang, T. Kozai, H. Shirai, A. Yabushita, C.-W. Luo, S. Nakanishi, and T. Fuji,
       Single-shot detection of mid-infrared spectra by chirped-pulse upconversion with four-wave difference frequency generation in gases.
       Opt. Express **21**, 18249–18254 (2013).

[128] J. Buback.
       Femtochemistry of Pericyclic Reactions and Advances towards Chiral Control.
       Dissertation. Universität Würzburg (2011).

[129] P. Rudolf.
Uncovering photoinduced chemical reaction pathways in the liquid phase with ultrafast vibrational spectroscopy.
Dissertation. Universität Würzburg (2014).

[130] D. Strickland and G. Mourou,
Compression of amplified chirped optical pulses.
Opt. Commun. **55**, 447–449 (1985).

[131] P. Maine, D. Strickland, P. Bado, M. Pessot, and G. Mourou,
Generation of ultrahigh peak power pulses by chirped pulse amplification.
IEEE J. Quantum Electron. **24**, 398–403 (1988).

[132] *Solstice – One-box ultrafast amplifier system.*
Spectra-Physics (User's Manual).

[133] D. E. Spence, P. N. Kean, and W. Sibbett,
60-fsec pulse generation from a self-mode-locked Ti:sapphire laser.
Opt. Lett. **16**, 42–44 (1991).

[134] A. E. Siegman,
Lasers.
University Science Books, Sausalito, CA (USA) (1986).

[135] E. B. Treacy,
Optical pulse compression with diffraction gratings.
IEEE J. Quantum Electron. **5**, 454–458 (1969).

[136] *TOPAS Series Traveling-wave Optical Parametric Amplifiers.*
Light Conversion Ltd (User's Manual).

[137] T. Wilhelm, J. Piel, and E. Riedle,
Sub-20-fs pulses tunable across the visible from a blue-pumped single-pass noncollinear parametric converter.
Opt. Lett. **22**, 1494–1496 (1997).

[138] G. Cerullo, M. Nisoli, and S. De Silvestri,
Generation of 11 fs pulses tunable across the visible by optical parametric amplification.
Appl. Phys. Lett. **71**, 3616–3618 (1997).

[139] J.-K. Rhee, T. S. Sosnowski, A.-C. Tien, and T. B. Norris,
Real-time dispersion analyzer of femtosecond laser pulses with use of a spectrally and temporally resolved upconversion technique.
J. Opt. Soc. Am. B **13**, 1780–1785 (1996).

[140] B. A. Richman, M. A. Krumbügel, and R. Trebino,
Temporal characterization of mid-IR free-electron-laser pulses by frequency-resolved optical gating.
Opt. Lett. **22**, 721–723 (1997).

[141] C. Iaconis and I. A. Walmsley,
Spectral phase interferometry for direct electric-field reconstruction of ultrashort optical pulses.
Opt. Lett. **23**, 792–794 (1998).

[142] C. Iaconis and I. A. Walmsley,
Self-referencing spectral interferometry for measuring ultrashort optical pulses.
IEEE J. Quantum Electron. **35**, 501–509 (1999).

[143] J. W. Nicholson, J. Jasapara, W. Rudolph, F. G. Omenetto, and A. J. Taylor,
Full-field characterization of femtosecond pulses by spectrum and cross-correlation measurements.
Opt. Lett. **24**, 1774–1776 (1999).

[144] P. O'Shea, M. Kimmel, X. Gu, and R. Trebino,
Highly simplified device for ultrashort-pulse measurement.
Opt. Lett. **26**, 932–934 (2001).

[145] V. V. Lozovoy, I. Pastirk, and M. Dantus,
Multiphoton intrapulse interference. IV. Ultrashort laser pulse spectral phase characterization and compensation.
Opt. Lett. **29**, 775–777 (2004).

[146] A. Kosuge, T. Sekikawa, X. Zhou, T. Kanai, S. Adachi, and S. Watanabe,
Frequency-Resolved Optical Gating of Isolated Attosecond Pulses in the Extreme Ultraviolet.
Phys. Rev. Lett. **97**, 263901 (2006).

[147] D. J. Kane and R. Trebino,
Characterization of arbitrary femtosecond pulses using frequency-resolved optical gating.
IEEE J. Quantum Electron. **29**, 571–579 (1993).

[148] R. Trebino, K. W. DeLong, D. N. Fittinghoff, J. N. Sweetser, M. A. Krumbügel, B. A. Richman, and D. J. Kane,
Measuring ultrashort laser pulses in the time-frequency domain using frequency-resolved optical gating.
Rev. Sci. Instrum. **68**, 3277–3295 (1997).

[149] S. Linden, H. Giessen, and J. Kuhl,
XFROG – A New Method for Amplitude and Phase Characterization of Weak Ultrashort Pulses.
Phys. Stat. Sol. B **206**, 119–124 (1998).

[150] S. Linden, J. Kuhl, and H. Giessen,
Amplitude and phase characterization of weak blue ultrashort pulses by downconversion.
Opt. Lett. **24**, 569–571 (1999).

[151] K. W. DeLong, D. N. Fittinghoff, R. Trebino, B. Kohler, and K. Wilson,
Pulse retrieval in frequency-resolved optical gating based on the method of generalized projections.
Opt. Lett. **19**, 2152–2154 (1994).

[152] D. T. Reid, P. Loza-Alvarez, C. T. A. Brown, T. Beddard, and W. Sibbett,
Amplitude and phase measurement of mid-infrared femtosecond pulses by using cross-correlation frequency-resolved optical gating.
Opt. Lett. **25**, 1478–1480 (2000).

[153] T. Sekikawa, T. Kanai, and S. Watanabe,
Frequency-Resolved Optical Gating of Femtosecond Pulses in the Extreme Ultraviolet.
Phys. Rev. Lett. **91**, 103902 (2003).

[154] E. Wigner,
On the Quantum Correction For Thermodynamic Equilibrium.
Phys. Rev. **40**, 749–759 (1932).

[155] K. Husimi,
Some formal properties of the density matrix.
Proc. Phys. Math. Soc. Jpn. **22**, 264–314 (1940).

[156] S. Fechner, F. Dimler, T. Brixner, G. Gerber, and D. J. Tannor,
The von Neumann picture: a new representation for ultrashort laser pulses.
Opt. Express **15**, 15387–15401 (2007).

[157] S. Coudreau, D. Kaplan, and P. Tournois,
Ultraviolet acousto-optic programmable dispersive filter laser pulse shaping in KDP.
Opt. Lett. **31**, 1899–1901 (2006).

[158] H. E. Lessing and A. Von Jena,
Separation of rotational diffusion and level kinetics in transient absorption spectroscopy.
Chem. Phys. Lett. **42**, 213–217 (1976).

[159] S. Schott, A. Steinbacher, J. Buback, P. Nuernberger, and T. Brixner,
Generalized magic angle for time-resolved spectroscopy with laser pulses of arbitrary ellipticity.
J. Phys. B: At. Mol. Opt. Phys. **47**, 124014 (2014).

[160] J. M. Khosrofian and B. A. Garetz,
Measurement of a Gaussian laser beam diameter through the direct inversion of knife-edge data.
Appl. Opt. **22**, 3406–3410 (1983).

[161] M. A. C. de Araújo, R. Silva, E. de Lima, D. P. Pereira, and P. C. de Oliveira,
Measurement of Gaussian laser beam radius using the knife-edge technique: improvement on data analysis.
Appl. Opt. **48**, 393–396 (2009).

[162] T. M. Jedju and L. Rothberg,
Tunable femtosecond radiation in the mid-infrared for time-resolved absorption in semiconductors.
Appl. Opt. **27**, 615–618 (1988).

[163] N. Jacquinet-Husson, N. A. Scott, A. Chédin, L. Crépeau, R. Armante, V. Capelle, J. Orphal, A. Coustenis, C. Boonne, N. Poulet-Crovisier, A. Barbe, M. Birk, L. R. Brown, C. Camy-Peyret, C. Claveau, K. Chance, N. Christidis, C. Clerbaux, P. F. Coheur, V. Dana, L. Daumont, M. R. De Backer-Barilly, G. Di Lonardo, J. M. Flaud, A. Goldman, A. Hamdouni, M. Hess, M. D. Hurley, D. Jacquemart, I. Kleiner, P. Köpke, J. Y. Mandin, S. Massie, S. Mikhailenko, V. Nemtchinov, A. Nikitin, D. Newnham, A. Perrin, V. I. Perevalov, S. Pinnock, L. Régalia-Jarlot, C. P. Rinsland, A. Rublev, F. Schreier, L. Schult, K. M. Smith, S. A. Tashkun, J. L. Teffo, R. A. Toth, V. G. Tyuterev, J. Vander Auwera, P. Varanasi, and G. Wagner,
The GEISA spectroscopic database: Current and future archive for Earth and planetary atmosphere studies.
J. Quant. Spectrosc. Radiat. Transfer **109**, 1043–1059 (2008).

[164] C. Dorrer, N. Belabas, J.-P. Likforman, and M. Joffre,
Spectral resolution and sampling issues in Fourier-transform spectral interferometry.
J. Opt. Soc. Am. B **17**, 1795–1802 (2000).

[165] D. C. Todd, J. M. Jean, S. J. Rosenthal, A. J. Ruggiero, D. Yang, and G. R. Fleming,
Fluorescence upconversion study of cis-stilbene isomerization.
J. Chem. Phys. **93**, 8658–8668 (1990).

[166] A. J. Ruggiero, D. C. Todd, and G. R. Fleming,
Subpicosecond fluorescence anisotropy studies of tryptophan in water.
J. Am. Chem. Soc. **112**, 1003–1014 (1990).

[167] C. J. Bardeen, V. V. Yakovlev, K. R. Wilson, S. D. Carpenter, P. M. Weber, and W. S. Warren,
Feedback quantum control of molecular electronic population transfer.
Chem. Phys. Lett. **280**, 151–158 (1997).

[168] V. I. Prokhorenko, A. M. Nagy, and R. J. D. Miller,
Coherent control of the population transfer in complex solvated molecules at weak excitation. An experimental study.
J. Chem. Phys. **122**, 184502 (2005).

[169] P. Nuernberger, G. Vogt, T. Brixner, and G. Gerber,
Femtosecond quantum control of molecular dynamics in the condensed phase.
Phys. Chem. Chem. Phys. **9**, 2470–2497 (2007).

[170] D. J. Tannor and S. A. Rice,
Control of selectivity of chemical reaction via control of wave packet evolution.
J. Chem. Phys. **83**, 5013–5018 (1985).

[171] P. Brumer and M. Shapiro,
Control of unimolecular reactions using coherent light.
Chem. Phys. Lett. **126**, 541–546 (1986).

[172] T. Baumert, M. Grosser, R. Thalweiser, and G. Gerber,
Femtosecond Time-Resolved Molecular Multiphoton Ionization: The Na_2 System.
Phys. Rev. Lett. **67**, 3753–3756 (1991).

[173] E. D. Potter, J. L. Herek, S. Pedersen, Q. Liu, and A. H. Zewail,
Femtosecond laser control of a chemical reaction.
Nature **355**, 66–68 (1992).

[174] R. S. Judson and H. Rabitz,
Teaching Lasers to Control Molecules.
Phys. Rev. Lett. **68**, 1500–1503 (1992).

[175] K. Bergmann, H. Theuer, and B. W. Shore,
Coherent population transfer among quantum states of atoms and molecules.
Rev. Mod. Phys. **70**, 1003–1025 (1998).

[176] H. Rabitz, R. de Vivie-Riedle, M. Motzkus, and K. Kompa,
Whither the Future of Controlling Quantum Phenomena?
Science **288**, 824–828 (2000).

[177] T. Brixner, N. H. Damrauer, P. Niklaus, and G. Gerber,
Photoselective adaptive femtosecond quantum control in the liquid phase.
Nature **414**, 57–60 (2001).

[178] N. V. Vitanov, T. Halfmann, B. W. Shore, and K. Bergmann,
Laser-induced population transfer by adiabatic passage techniques.
Annu. Rev. Phys. Chem. **52**, 763–809 (2001).

[179] P. Nuernberger, D. Wolpert, H. Weiss, and G. Gerber,
Femtosecond quantum control of molecular bond formation.
Proc. Natl. Acad. Sci. USA **107**, 10366–10370 (2010).

[180] W. Kirmse,
Carbene Chemistry.
Second edition. Academic Press (1971).

[181] Y. Wang, E. V. Sitzmann, F. Novak, C. Dupuy, and K. B. Eisenthal,
Reactions of excited triplet diphenylcarbene studied with picosecond lasers.
J. Am. Chem. Soc. **104**, 3238–3239 (1982).

[182] E. V. Sitzmann, Y. Wang, and K. B. Eisenthal,
Picosecond laser studies on the reaction of excited triplet diphenylcarbene with alcohols.
J. Phys. Chem. **87**, 2283–2285 (1983).

[183] E. V. Sitzmann, J. Langan, and K. B. Eisenthal,
Picosecond laser studies of the charge-transfer reaction of excited triplet diphenylcarbene with electron donors.
Chem. Phys. Lett. **102**, 446–450 (1983).

[184] K. B. Eisenthal, R. A. Moss, and N. J. Turro,
Divalent Carbon Intermediates: Laser Photolysis and Spectroscopy.
Science **225**, 1439–1445 (1984).

[185] E. V. Sitzmann, J. Langan, and K. B. Eisenthal,
Intermolecular Effects on Intersystem Crossing Studied on the Picosecond Time Scale: The Solvent Polarity Effect on the Rate of Singlet to Triplet Intersystem Crossing of Diphenylcarbene.
J. Am. Chem. Soc. **106**, 1868–1869 (1984).

[186] J. G. Langan, E. V. Sitzmann, and K. B. Eisenthal,
Picosecond laser studies on the effect of structure and environment on intersystem crossing in aromatic carbenes.
Chem. Phys. Lett. **110**, 521–527 (1984).

[187] E. V. Sitzmann, J. G. Langan, and K. B. Eisenthal,
Picosecond laser studies of the effects of reactants on intramolecular energy relaxation of diphenylcarbene: Reaction of diphenylcarbene with alcohols.
Chem. Phys. Lett. **112**, 111–116 (1984).

[188] K. B. Eisenthal, N. J. Turro, E. V. Sitzmann, I. R. Gould, G. Hefferon, J. Langan, and Y. Cha,
Singlet-triplet interconversion of diphenylmethylene. Energetics, dynamics and reactivities of different spin states.
Tetrahedron **41**, 1543–1554 (1985).

[189] J. G. Langan, E. V. Sitzmann, and K. B. Eisenthal,
Inverse deuterium isotope effect in the intersystem crossing of diphenylcarbene.
Chem. Phys. Lett. **124**, 59–62 (1986).

[190] E. V. Sitzmann, J. G. Langan, D. Griller, and K. B. Eisenthal,
Effects of solvent polarity and structure on intersystem crossing in diphenylcarbenes. A picosecond laser study on dimesitylcarbene.
Chem. Phys. Lett. **161**, 353–360 (1989).

[191] W. Kirmse, M. Guth, and S. Steenken,
Production of α-Siloxycarbenium Ions by Protonation of Photochemically Generated α-Siloxycarbenes. Formation Mechanism and Reactivities with Nucleophiles.
J. Am. Chem. Soc. **118**, 10838–10849 (1996).

[192] W. Sander, G. Bucher, and S. Wierlacher,
Carbenes in Matrices—Spectroscopy, Structure, and Reactivity.
Chem. Rev. **93**, 1583–1621 (1993).

[193] M. T. Portella-Oberli, C. Jeannin, B. Soep, G. Zerza, and M. Chergui,
Femtosecond study of the rise and decay of carbenes in solution.
Chem. Phys. Lett. **296**, 323–328 (1998).

[194] J. Peon, D. Polshakov, and B. Kohler,
Solvent Reorganization Controls the Rate of Proton Transfer from Neat Alcohol Solvents to Singlet Diphenylcarbene.
J. Am. Chem. Soc. **124**, 6428–6438 (2002).

[195] B. M. Showalter and J. P. Toscano,
Time-resolved IR studies of α-lactones.
J. Phys. Org. Chem. **17**, 743–748 (2004).

[196] J. Wang, J. Kubicki, T. L. Gustafson, and M. S. Platz,
The Dynamics of Carbene Solvation: An Ultrafast Study of p-Biphenylyltrifluoromethylcarbene.
J. Am. Chem. Soc. **130**, 2304–2313 (2008).

[197] J. Wang, Y. Zhang, J. Kubicki, and M. S. Platz,
Ultrafast studies of some diarylcarbenes.
Photochem. Photobiol. Sci. **7**, 552–557 (2008).

[198] G. Burdzinski and M. S. Platz,
Ultrafast time-resolved studies of the photochemistry of diazo carbonyl compounds.
J. Phys. Org. Chem. **23**, 308–314 (2010).

[199] A. Steinbacher, S. Roeding, T. Brixner, and P. Nuernberger,
Ultrafast photofragment ion spectroscopy of the Wolff rearrangement in 5-diazo Meldrum's acid.
Phys. Chem. Chem. Phys. **16**, 7290–7298 (2014).

[200] G. Burdzinski and M. S. Platz. *Ultrafast Kinetics of Carbene Reactions.* In R. A. Moss and M. P. Doyle (Eds.), *Contemporary Carbene Chemistry*, pp. 166–192. John Wiley & Sons, Inc. (2013).

[201] W. Kirmse, L. Horner, and H. Hoffmann,
Über Lichtreaktionen IX. Umsetzungen photochemisch erzeugter Carbene.
Liebigs Ann. Chem. **614**, 19–30 (1958).

[202] D. Griller, A. S. Nazran, and J. C. Scaiano,
Reaction of diphenylcarbene with methanol.
J. Am. Chem. Soc. **106**, 198–202 (1984).

[203] L. M. Hadel, M. S. Platz, and J. C. Scaiano,
Study of hydrogen atom abstraction reactions of triplet diphenylcarbene in solution.
J. Am. Chem. Soc. **106**, 283–287 (1984).

[204] S. Steenken,
Production of carbenium ions from carbenes by protonation.
Pure Appl. Chem. **70**, 2031–2038 (1998).

[205] D. Bethell, A. R. Newall, G. Stevens, and D. Whittaker,
Intermediates in the decomposition of aliphatic diazo-compounds. Part VII. Mechanisms for formation of benzophenone azine and diphenylmethanol in the thermal decomposition of diphenyldiazomethane.
J. Chem. Soc. B pp. 749–754 (1969).

[206] N. J. Turro, Y. Cha, and I. R. Gould,
Temperature dependence of the reactions of singlet and triplet diphenylcarbene.: Evidence for reversible ylide formation in the reaction with alcohols.
Tetrahedron Lett. **26**, 5951–5954 (1985).

[207] J. Xue, H. L. Luk, and M. S. Platz,
Direct Observation of a Carbene-Alcohol Ylide.
J. Am. Chem. Soc. **133**, 1763–1765 (2011).

[208] Y. Marcus,
Preferential solvation in mixed solvents. Part 6.—Binary mixtures containing methanol, ethanol, acetone or triethylamine and another organic solvent.
J. Chem. Soc., Faraday Trans. **87**, 1843–1849 (1991).

[209] J. Ammer, C. F. Sailer, E. Riedle, and H. Mayr,
Photolytic Generation of Benzhydryl Cations and Radicals from Quaternary Phosphonium Salts: How Highly Reactive Carbocations Survive Their First Nanoseconds.
J. Am. Chem. Soc. **134**, 11481–11494 (2012).

[210] B. P. Fingerhut, C. F. Sailer, J. Ammer, E. Riedle, and R. de Vivie-Riedle,
Buildup and Decay of the Optical Absorption in the Ultrafast Photo-Generation and Reaction of Benzhydryl Cations in Solution.
J. Phys. Chem. A **116**, 11064–11074 (2012).

[211] C. F. Sailer, S. Thallmair, B. P. Fingerhut, C. Nolte, J. Ammer, H. Mayr, I. Pugliesi, R. de Vivie-Riedle, and E. Riedle,
A Comprehensive Microscopic Picture of the Benzhydryl Radical and Cation Photogeneration and Interconversion through Electron Transfer.
Chem. Phys. Chem. **14**, 1423–1437 (2013).

[212] J. Ortega, C. Ràfols, E. Bosch, and M. Rosés,
Solute–solvent and solvent–solvent interactions in binary solvent mixtures. Part 3. The $E_T(30)$ polarity of binary mixtures of hydroxylic solvents.
J. Chem. Soc., Perkin Trans. 2 pp. 1497–1503 (1996).

[213] D. Griller, M. T. H. Liu, and J. C. Scaiano,
Hydrogen bonding in alcohols: its effect on the carbene insertion reaction.
J. Am. Chem. Soc. **104**, 5549–5551 (1982).

[214] J. Riefer.
Sensitiver Nachweis von Molekülschwingungen mit Femtosekundenlaserpulsen im Infraroten.
Bachelor thesis. Universität Würzburg (2013).

[215] W. Rock, Y.-L. Li, P. Pagano, and C. M. Cheatum,
2D IR Spectroscopy using Four-Wave Mixing, Pulse Shaping, and IR Upconversion: A Quantitative Comparison.
J. Phys. Chem. A **117**, 6073–6083 (2013).

[216] M. Kaucikas, J. Barber, and J. J. Van Thor,
Polarization sensitive ultrafast mid-IR pump probe micro-spectrometer with diffraction limited spatial resolution.
Opt. Express **21**, 8357–8370 (2013).

[217] D. E. Zelmon, D. L. Small, and D. Jundt,
Infrared corrected Sellmeier coefficients for congruently grown lithium niobate and 5 mol. % magnesium oxide–doped lithium niobate.
J. Opt. Soc. Am. B **14**, 3319–3322 (1997).

[218] U. Schatzschneider,
Photoactivated Biological Activity of Transition-Metal Complexes.
Eur. J. Inorg. Chem. pp. 1451–1467 (2010).

[219] F. Kanal.
Femtosecond Transient Absorption Spectroscopy – Technical Improvements and Applications to Ultrafast Molecular Phenomena.
Dissertation. Universität Würzburg (2015).

[220] P. Rudolf, F. Kanal, D. Gehrig, J. Niesel, T. Brixner, U. Schatzschneider, and P. Nuernberger,
Femtosecond Mid-Infrared Study of the Aqueous Solution Photochemistry of a CO-Releasing Molecule (CORM).
EPJ Web of Conferences **41**, 05004 (2013).

[221] M. D. Maines,
The Heme Oxygenase System: A Regulator of Second Messenger Gases.
Annu. Rev. Pharmacol. Toxicol. **37**, 517–554 (1997).

[222] T. Matsui, M. Unno, and M. Ikeda-Saito,
Heme Oxygenase Reveals Its Strategy for Catalyzing Three Successive Oxygenation Reactions.
Acc. Chem. Res. **43**, 240–247 (2010).

[223] T. L. Poulos,
Heme Enzyme Structure and Function.
Chem. Rev. **114**, 3919–3962 (2014).

[224] R. Motterlini and L. E. Otterbein,
The therapeutic potential of carbon monoxide.
Nat. Rev. Drug Discov. **9**, 728–743 (2010).

[225] B. E. Mann. *Carbon Monoxide: An Essential Signalling Molecule.* In G. Jaouen and N. Metzler-Nolte (Eds.), *Medicinal Organometallic Chemistry*, volume 32 of *Topics in Organometallic Chemistry*, pp. 247–285. Springer Berlin Heidelberg (2010).

[226] U. Schatzschneider,
PhotoCORMs: Light-triggered release of carbon monoxide from the coordination sphere of transition metal complexes for biological applications.
Inorg. Chim. Acta **374**, 19–23 (2011).

[227] R. Dale Rimmer, A. E. Pierri, and P. C. Ford,
Photochemically activated carbon monoxide release for biological targets. Toward developing air-stable photoCORMs labilized by visible light.
Coord. Chem. Rev. **256**, 1509–1519 (2012).

[228] W.-Q. Zhang, A. J. Atkin, I. J. S. Fairlamb, A. C. Whitwood, and J. M. Lynam,
Synthesis and Reactivity of Molybdenum Complexes Containing Functionalized Alkynyl Ligands: A Photochemically Activated CO-Releasing Molecule (PhotoCO-RM).
Organometallics **30**, 4643–4654 (2011).

[229] A. J. Atkin, I. J. S. Fairlamb, J. S. Ward, and J. M. Lynam,
CO Release from Norbornadiene Iron(0) Tricarbonyl Complexes: Importance of Ligand Dissociation.
Organometallics **31**, 5894–5902 (2012).

[230] S. Romanski, B. Kraus, U. Schatzschneider, J.-M. Neudörfl, S. Amslinger, and H.-G. Schmalz,
Acyloxybutadiene Iron Tricarbonyl Complexes as Enzyme-Triggered CO-Releasing Molecules (ET-CORMs).
Angew. Chem. Int. Ed. **50**, 2392–2396 (2011).

[231] N. S. Sitnikov, Y. Li, D. Zhang, B. Yard, and H.-G. Schmalz,
Design, Synthesis, and Functional Evaluation of CO-Releasing Molecules Triggered by Penicillin G Amidase as a Model Protease.
Angew. Chem. Int. Ed. **54**, 12314–12318 (2015).

[232] C. S. Jackson, S. Schmitt, Q. P. Dou, and J. J. Kodanko,
Synthesis, Characterization, and Reactivity of the Stable Iron Carbonyl Complex [Fe(CO)(N4Py)](ClO$_4$)$_2$: Photoactivated Carbon Monoxide Release, Growth Inhibitory Activity, and Peptide Ligation.
Inorg. Chem. **50**, 5336–5338 (2011).

[233] J. S. Ward, J. M. Lynam, J. W. B. Moir, D. E. Sanin, A. P. Mountford, and I. J. S. Fairlamb,
A therapeutically viable photo-activated manganese-based CO-releasing molecule (photo-CO-RM).
Dalton Trans. **41**, 10514–10517 (2012).

[234] A. E. Pierri, A. Pallaoro, G. Wu, and P. C. Ford,
A Luminescent and Biocompatible PhotoCORM.
J. Am. Chem. Soc. **134**, 18197–18200 (2012).

[235] C. Nagel, S. McLean, R. K. Poole, H. Braunschweig, T. Kramer, and U. Schatzschneider,
Introducing [Mn(CO)$_3$(tpa-$\kappa^3 N$)]$^+$ as a novel photoactivatable CO-releasing molecule with well-defined iCORM intermediates – synthesis, spectroscopy, and antibacterial activity.
Dalton Trans. **43**, 9986–9997 (2014).

[236] L. Bañares, T. Baumert, M. Bergt, B. Kiefer, and G. Gerber,
Femtosecond photodissociation dynamics of Fe(CO)$_5$ in the gas phase.
Chem. Phys. Lett. **267**, 141–148 (1997).

[237] L. Bañares, T. Baumert, M. Bergt, B. Kiefer, and G. Gerber,
The ultrafast photodissociation of Fe(CO)$_5$ in the gas phase.
J. Chem. Phys. **108**, 5799–5811 (1998).

[238] S. A. Trushin, W. Fuss, K. L. Kompa, and W. E. Schmid,
Femtosecond Dynamics of Fe(CO)$_5$ Photodissociation at 267 nm Studied by Transient Ionization.
J. Phys. Chem. A **104**, 1997–2006 (2000).

[239] H. Ihee, J. Cao, and A. H. Zewail,
Ultrafast Electron Diffraction of Transient [Fe(CO)$_4$]: Determination of Molecular Structure and Reaction Pathway.
Angew. Chem. Int. Ed. **40**, 1532–1536 (2001).

[240] P. T. Snee, C. K. Payne, S. D. Mebane, K. T. Kotz, and C. B. Harris,
Dynamics of Photosubstitution Reactions of Fe(CO)$_5$: An Ultrafast Infrared Study of High Spin Reactivity.
J. Am. Chem. Soc. **123**, 6909–6915 (2001).

[241] P. Portius, J. Yang, X.-Z. Sun, D. C. Grills, P. Matousek, A. W. Parker, M. Towrie, and M. W. George,
Unraveling the Photochemistry of Fe(CO)$_5$ in Solution: Observation of Fe(CO)$_3$ and the Conversion between ^{3}Fe(CO)$_4$ and ^{1}Fe(CO)$_4$(Solvent).
J. Am. Chem. Soc. **126**, 10713–10720 (2004).

[242] M. Besora, J.-L. Carreón-Macedo, A. J. Cowan, M. W. George, J. N. Harvey, P. Portius, K. L. Ronayne, X.-Z. Sun, and M. Towrie,

A Combined Theoretical and Experimental Study on the Role of Spin States in the Chemistry of Fe(CO)₅ Photoproducts.
J. Am. Chem. Soc. **131**, 3583–3592 (2009).

[243] S. C. Nguyen, J. P. Lomont, M. C. Zoerb, A. D. Hill, J. P. Schlegel, and C. B. Harris,
Chemistry of the Triplet 14-Electron Complex Fe(CO)₃ in Solution Studied by Ultrafast Time-Resolved IR Spectroscopy.
Organometallics **31**, 3980–3984 (2012).

[244] B. Ahr, M. Chollet, B. Adams, E. M. Lunny, C. M. Laperle, and C. Rose-Petruck,
Picosecond X-ray absorption measurements of the ligand substitution dynamics of Fe(CO)₅ in ethanol.
Phys. Chem. Chem. Phys. **13**, 5590–5599 (2011).

[245] P. Wernet, M. Beye, F. de Groot, S. Düsterer, K. Gaffney, S. Grübel, R. Hartsock, F. Hennies, I. Josefsson, B. Kennedy, K. Kunnus, T. Leitner, T. Mazza, M. Meyer, D. Nordlund, M. Odelius, W. Quevedo, P. Radcliffe, I. Rajkovic, B. Schlotter, M. Scholz, S. Schreck, E. Suljoti, S. Techert, J. Turner, C. Weniger, W. Zhang, and A. Föhlisch,
Mapping chemical bonding of reaction intermediates with femtosecond X-ray laser spectroscopy.
EPJ Web of Conferences **41**, 05025 (2013).

[246] J. D. Simon and X. Xie,
Photodissociation of chromium hexacarbonyl in solution: direct observation of the formation of pentacarbonyl(methanol)chromium.
J. Phys. Chem. **90**, 6751–6753 (1986).

[247] J. Z. Zhang and C. B. Harris,
Photodissociation dynamics of Mn₂(CO)₁₀ in solution on ultrafast time scales.
J. Chem. Phys. **95**, 4024–4032 (1991).

[248] J. C. King, J. Z. Zhang, B. J. Schwartz, and C. B. Harris,
Vibrational relaxation of M(CO)₆ (M=Cr, Mo, W): Effect of metal mass on vibrational cooling dynamics and non-Boltzmann internal energy distributions.
J. Chem. Phys. **99**, 7595–7601 (1993).

[249] T. P. Dougherty and E. J. Heilweil,
Transient infrared spectroscopy of (η⁵-C₅ H₅)Co(CO)₂ photoproduct reactions in hydrocarbon solutions.
J. Chem. Phys. **100**, 4006–4009 (1994).

[250] T. P. Dougherty, W. Tandy Grubbs, and E. J. Heilweil,
Photochemistry of Rh(CO)₂(acetylacetonate) and Related Metal Dicarbonyls Studied by Ultrafast Infrared Spectroscopy.
J. Phys. Chem. **98**, 9396–9399 (1994).

[251] T. P. Dougherty and E. J. Heilweil,
Ultrafast transient infrared absorption studies of M(CO)₆ (M = Cr, Mo or W) photoproducts in n-hexane solution.
Chem. Phys. Lett. **227**, 19–25 (1994).

[252] T. Lian, S. E. Bromberg, M. C. Asplund, H. Yang, and C. B. Harris,
Femtosecond Infrared Studies of the Dissociation and Dynamics of Transition Metal Carbonyls in Solution.
J. Phys. Chem. **100**, 11994–12001 (1996).

[253] J. C. Owrutsky and A. P. Baronavski,
Ultrafast infrared study of the ultraviolet photodissociation of Mn$_2$(CO)$_{10}$.
J. Chem. Phys. **105**, 9864–9873 (1996).

[254] T. Jiao, Z. Pang, T. J. Burkey, R. F. Johnston, T. A. Heimer, V. D. Kleiman, and E. J. Heilweil,
Ultrafast Ring Closure Energetics and Dynamics of Cyclopentadienyl Manganese Tricarbonyl Derivatives.
J. Am. Chem. Soc. **121**, 4618–4624 (1999).

[255] D. A. Steinhurst, A. P. Baronavski, and J. C. Owrutsky,
Transient infrared spectroscopy of Mn$_2$(CO)$_{10}$ with 400 nm excitation.
Chem. Phys. Lett. **361**, 513–519 (2002).

[256] F. W. Vergeer, F. Hartl, P. Matousek, D. J. Stufkens, and M. Towrie,
First direct observation of a CO-bridged primary photoproduct of [Ru$_3$(CO)$_{12}$] by picosecond time-resolved IR spectroscopy.
Chem. Commun. pp. 1220–1221 (2002).

[257] E. A. Glascoe, M. F. Kling, J. E. Shanoski, R. A. DiStasio, Jr., C. K. Payne, B. V. Mork, T. Don Tilley, and C. B. Harris,
Photoinduced β-Hydrogen Elimination and Radical Formation with CpW(CO)$_3$(CH$_2$CH$_3$): Ultrafast IR and DFT Studies.
Organometallics **26**, 1424–1432 (2007).

[258] A. R. Ridley, A. I. Stewart, K. Adamczyk, H. N. Ghosh, B. Kerkeni, Z. X. Guo, E. T. J. Nibbering, C. J. Pickett, and N. T. Hunt,
Multiple-Timescale Photoreactivity of a Model Compound Related to the Active Site of [FeFe]-Hydrogenase.
Inorg. Chem. **47**, 7453–7455 (2008).

[259] T. T. To, E. J. Heilweil, C. B. Duke, K. R. Ruddick, C. E. Webster, and T. J. Burkey,
Development of Ultrafast Photochromic Organometallics and Photoinduced Linkage Isomerization of Arene Chromium Carbonyl Derivatives.
J. Phys. Chem. A **113**, 2666–2676 (2009).

[260] M. Lim, T. A. Jackson, and P. A. Anfinrud,
Ultrafast rotation and trapping of carbon monoxide dissociated from myoglobin.
Nat. Struct. Biol. **4**, 209–214 (1997).

[261] J. Niesel, A. Pinto, H. W. Peindy N'Dongo, K. Merz, I. Ott, R. Gust, and U. Schatzschneider,
Photoinduced CO release, cellular uptake and cytotoxicity of a tris(pyrazolyl)methane (tpm) manganese tricarbonyl complex.
Chem. Commun. pp. 1798–1800 (2008).

[262] H.-M. Berends and P. Kurz,
Investigation of light-triggered carbon monoxide release from two manganese photoCORMs by IR, UV–Vis and EPR spectroscopy.
Inorg. Chim. Acta **380**, 141–147 (2012).

[263] M. Falk and T. A. Ford,
Infrared spectrum and structure of liquid water.
Can. J. Chem. **44**, 1699–1707 (1966).

[264] W. Strohmeier and D. von Hobe,
Quantenausbeute als Funktion der Wellenlänge bei der photochemischen Bildung von Metallcarbonylderivaten.
Z. Phys. Chem. **34**, 393–400 (1962).

[265] P. J. Giordano and M. S. Wrighton,
Photosubstitution Behavior of Dicarbonyl(η^5-cyclopentadienyl)pyridinomanganese and -rhenium and Related Complexes.
Inorg. Chem. **16**, 160–166 (1977).

[266] G. L. Geoffroy and M. S. Wrighton,
Organometallic Photochemistry.
Academic Press, New York, NY (USA) (1979).

[267] W. Strohmeier, D. von Hobe, G. Schönauer, and H. Laporte,
Einfluß des Zentralatoms und der Donatoren auf die photochemische Bildung von Metallcarbonyl-Derivaten.
Z. Naturforsch. B **17**, 502–504 (1962).

[268] M. J. Frisch, G. W. Trucks, H. B. Schlegel, G. E. Scuseria, M. A. Robb, J. R. Cheeseman, G. Scalmani, V. Barone, B. Mennucci, G. A. Petersson, H. Nakatsuji, M. Caricato, X. Li, H. P. Hratchian, A. F. Izmaylov, J. Bloino, G. Zheng, J. L. Sonnenberg, M. Hada, M. Ehara, K. Toyota, R. Fukuda, J. Hasegawa, M. Ishida, T. Nakajima, Y. Honda, O. Kitao, H. Nakai, T. Vreven, J. A. Montgomery, Jr., J. E. Peralta, F. Ogliaro, M. Bearpark, J. J. Heyd, E. Brothers, K. N. Kudin, V. N. Staroverov, R. Kobayashi, J. Normand, K. Raghavachari, A. Rendell, J. C. Burant, S. S. Iyengar, J. Tomasi, M. Cossi, N. Rega, J. M. Millam, M. Klene, J. E. Knox, J. B. Cross, V. Bakken, C. Adamo, J. Jaramillo, R. Gomperts, R. E. Stratmann, O. Yazyev, A. J. Austin, R. Cammi, C. Pomelli, J. W. Ochterski, R. L. Martin, K. Morokuma, V. G. Zakrzewski, G. A. Voth, P. Salvador, J. J. Dannenberg, S. Dapprich, A. D. Daniels, Ö. Farkas, J. B. Foresman, J. V. Ortiz, J. Cioslowski, and D. J. Fox,
Gaussian 09 Revision A.1.
Gaussian Inc. Wallingford CT (2009).

[269] M. P. Andersson and P. Uvdal,
New Scale Factors for Harmonic Vibrational Frequencies Using the B3LYP Density Functional Method with the Triple-ζ Basis Set 6-311+G(d,p).
J. Phys. Chem. A **109**, 2937–2941 (2005).

[270] R. Laenen, T. Roth, and A. Laubereau,
Novel Precursors of Solvated Electrons in Water: Evidence for a Charge Transfer Process.
Phys. Rev. Lett. **85**, 50–53 (2000).

[271] W. Huber, R. Linder, J. Niesel, U. Schatzschneider, B. Spingler, and P. C. Kunz,
A Comparative Study of Tricarbonylmanganese Photoactivatable CO Releasing Molecules (Photo-CORMs) by Using the Myoglobin Assay and Time-Resolved IR Spectroscopy.
Eur. J. Inorg. Chem. pp. 3140–3146 (2012).

[272] S. V. C. Vummaleti, D. Branduardi, M. Masetti, M. De Vivo, R. Motterlini, and A. Cavalli,
Theoretical Insights into the Mechanism of Carbon Monoxide (CO) Release from CO-Releasing Molecules.
Chem. Eur. J. **18**, 9267–9275 (2012).

[273] S. K. Pal, J. Peon, B. Bagchi, and A. H. Zewail,
Biological Water: Femtosecond Dynamics of Macromolecular Hydration.
J. Phys. Chem. B **106**, 12376–12395 (2002).

[274] J. T. King, M. R. Ross, and K. J. Kubarych,
Water-Assisted Vibrational Relaxation of a Metal Carbonyl Complex Studied with Ultrafast 2D-IR.
J. Phys. Chem. B **116**, 3754–3759 (2012).

[275] J. T. King, E. J. Arthur, C. L. Brooks, and K. J. Kubarych,
Site-Specific Hydration Dynamics of Globular Proteins and the Role of Constrained Water in Solvent Exchange with Amphiphilic Cosolvents.
J. Phys. Chem. B **116**, 5604–5611 (2012).

[276] A. K. Mustafa, M. M. Gadalla, and S. H. Snyder,
Signaling by Gasotransmitters.
Sci. Signal. **2**, re2 (1–8) (2009).

[277] M. Kajimura, R. Fukuda, R. M. Bateman, T. Yamamoto, and M. Suematsu,
Interactions of Multiple Gas-Transducing Systems: Hallmarks and Uncertainties of CO, NO, and H_2S Gas Biology.
Antioxid. Redox Signal. **13**, 157–192 (2010).

[278] B. R. Crane, J. Sudhamsu, and B. A. Patel,
Bacterial Nitric Oxide Synthases.
Annu. Rev. Biochem. **79**, 445–470 (2010).

[279] C. Szabo,
Gaseotransmitters: New Frontiers for Translational Science.
Sci. Transl. Med. **2**, 59ps54 (2010).

[280] B. Wegiel, D. W. Hanto, and L. E. Otterbein,
The social network of carbon monoxide in medicine.
Trends Mol. Med. **19**, 3–11 (2013).

[281] P. G. Wang, M. Xian, X. Tang, X. Wu, Z. Wen, T. Cai, and A. J. Janczuk,
Nitric Oxide Donors: Chemical Activities and Biological Applications.
Chem. Rev. **102**, 1091–1134 (2002).

[282] C. Napoli and L. J. Ignarro,
Nitric Oxide–Releasing Drugs.
Annu. Rev. Pharmacol. Toxicol. **43**, 97–123 (2003).

[283] A. R. Marques, L. Kromer, D. J. Gallo, N. Penacho, S. S. Rodrigues, J. D. Seixas, G. J. L. Bernardes, P. M. Reis, S. L. Otterbein, R. A. Ruggieri, A. S. G. Gonçalves, A. M. L. Gonçalves, M. N. De Matos, I. Bento, L. E. Otterbein, W. A. Blättler, and C. C. Romão,
Generation of Carbon Monoxide Releasing Molecules (CO-RMs) as Drug Candidates for the Treatment of Acute Liver Injury: Targeting of CO-RMs to the Liver.
Organometallics **31**, 5810–5822 (2012).

[284] P. Govender, S. Pai, U. Schatzschneider, and G. S. Smith,
Next Generation PhotoCORMs: Polynuclear Tricarbonylmanganese(I)-Functionalized Polypyridyl Metallodendrimers.
Inorg. Chem. **52**, 5470–5478 (2013).

[285] H. Pfeiffer, T. Sowik, and U. Schatzschneider,
Bioorthogonal oxime ligation of a $Mo(CO)_4(N–N)$ CO-releasing molecule (CORM) to a TGF β-binding peptide.
J. Organomet. Chem. **734**, 17–24 (2013).

[286] S. Pai, K. Radacki, and U. Schatzschneider,
Sonogashira, CuAAC, and Oxime Ligations for the Synthesis of Mn^I Tricarbonyl PhotoCORM Peptide Conjugates.
Eur. J. Inorg. Chem. pp. 2886–2895 (2014).

[287] S. Pai, M. Hafftlang, G. Atongo, C. Nagel, J. Niesel, S. Botov, H.-G. Schmalz, B. Yard, and U. Schatzschneider,
New modular manganese(I) tricarbonyl complexes as PhotoCORMs: in vitro detection of photoinduced carbon monoxide release using COP-1 as a fluorogenic switch-on probe.
Dalton Trans. **43**, 8664–8678 (2014).

[288] I. Chakraborty, S. J. Carrington, and P. K. Mascharak,
Photodelivery of CO by Designed PhotoCORMs: Correlation between Absorption in the Visible Region and Metal–CO Bond Labilization in Carbonyl Complexes.
ChemMedChem **9**, 1266–1274 (2014).

[289] X. Jiang, L. Long, H. Wang, L. Chen, and X. Liu,
Diiron hexacarbonyl complexes as potential CO-RMs: CO-releasing initiated by a substitution reaction with cysteamine and structural correlation to the bridging linkage.
Dalton Trans. **43**, 9968–9975 (2014).

[290] J. S. Ward, J. M. Lynam, J. Moir, and I. J. S. Fairlamb,
Visible-Light-Induced CO Release from a Therapeutically Viable Tryptophan-Derived Manganese(I) Carbonyl (TryptoCORM) Exhibiting Potent Inhibition against E. coli.
Chem. Eur. J. **20**, 15061–15068 (2014).

[291] J. L. Wilson, S. Fayad Kobeissi, S. Oudir, B. Haas, B. Michel, J.-L. Dubois Randé, A. Ollivier, T. Martens, M. Rivard, R. Motterlini, and R. Foresti,
Design and Synthesis of New Hybrid Molecules That Activate the Transcription Factor Nrf2 and Simultaneously Release Carbon Monoxide.
Chem. Eur. J. **20**, 14698–14704 (2014).

[292] S. J. Carrington, I. Chakraborty, and P. K. Mascharak,
Exceptionally rapid CO release from a manganese(I) tricarbonyl complex derived from bis(4-chlorophenylimino)acenaphthene upon exposure to visible light.
Dalton Trans. **44**, 13828–13834 (2015).

[293] C. De La Cruz and N. Sheppard,
A structure-based analysis of the vibrational spectra of nitrosyl ligands in transition-metal coordination complexes and clusters.
Spectrochim. Acta Mol. Biomol. Spectrosc. **78**, 7–28 (2011).

[294] X. Wang, M. Zhou, and L. Andrews,
Manganese Carbonyl Nitrosyl Complexes in Solid Argon: Infrared Spectra and Density Functional Calculations.
J. Phys. Chem. A **104**, 7964–7973 (2000).

[295] W. Wang, F. Chen, J. Lin, and Y. She,
Time-resolved IR Studies of Gas-phase Photochemistry of Co(CO)$_3$NO.
J. Chem. Soc., Faraday Trans. **91**, 847–853 (1995).

[296] M. Kubota, M. K. Chan, D. C. Boyd, and K. R. Mann,
Thermal and Photolytic Reactions of Nitrosyl–Carbonyl Complexes of Rhodium and Iridium with Triphenylphosphine.
Inorg. Chem. **26**, 3261–3264 (1987).

[297] M. S. Lynch, M. Cheng, B. E. Van Kuiken, and M. Khalil,
Probing the Photoinduced Metal–Nitrosyl Linkage Isomerism of Sodium Nitroprusside in Solution Using Transient Infrared Spectroscopy.
J. Am. Chem. Soc. **133**, 5255–5262 (2011).

[298] G. Gallé, M. Nicoul, T. Woike, D. Schaniel, and E. Freysz,
Unraveling the mechanism of NO ligand photoisomerism by time-resolved infrared spectroscopy.
Chem. Phys. Lett. **552**, 64–68 (2012).

[299] T. E. Bitterwolf,
Photochemical nitrosyl linkage isomerism/metastable states.
Coord. Chem. Rev. **250**, 1196–1207 (2006).

[300] K. R. Sawyer, R. P. Steele, E. A. Glascoe, J. F. Cahoon, J. P. Schlegel, M. Head-Gordon, and C. B. Harris,
Direct Observation of Photoinduced Bent Nitrosyl Excited-State Complexes.
J. Phys. Chem. A **112**, 8505–8514 (2008).

[301] J. Böhmer, G. Haselhorst, K. Wieghardt, and B. Nuber,
The First Mononuclear Nitrosyl(oxo)molybdenum Complex: Side-On Bonded and μ_3-Bridging NO Ligands in [{MoL(NO)(O)(OH)}$_2$]NaPF$_6 \cdot H_2O$.
Angew. Chem. Int. Ed. **33**, 1473–1476 (1994).

[302] C. Nagel.
Novel manganese- and molybdenum-based photoactivatable CO-releasing molecules: Synthesis and biological activity.
Dissertation. Universität Würzburg (2015).

[303] M. A. Gonzalez, S. J. Carrington, N. L. Fry, J. L. Martinez, and P. K. Mascharak,
Syntheses, Structures, and Properties of New Manganese Carbonyls as Photoactive CO-Releasing Molecules: Design Strategies That Lead to CO Photolability in the Visible Region.
Inorg. Chem. **51**, 11930–11940 (2012).

[304] M. A. Gonzalez, M. A. Yim, S. Cheng, A. Moyes, A. J. Hobbs, and P. K. Mascharak,
Manganese Carbonyls Bearing Tripodal Polypyridine Ligands as Photoactive Carbon Monoxide-Releasing Molecules.
Inorg. Chem. **51**, 601–608 (2012).

[305] K. F. Lee, K. J. Kubarych, A. Bonvalet, and M. Joffre,
Characterization of mid-infrared femtosecond pulses [Invited].
J. Opt. Soc. Am. B **25**, A54–A62 (2008).

[306] A. A. Lanin, A. B. Fedotov, and A. M. Zheltikov,
Ultrabroadband XFROG of few-cycle mid-infrared pulses by four-wave mixing in a gas.
J. Opt. Soc. Am. B **31**, 1901–1905 (2014).

[307] H. Shirai, C. Duchesne, Y. Furutani, and T. Fuji,
Attenuated total reflectance spectroscopy with chirped-pulse upconversion.
Opt. Express **22**, 29611–29616 (2014).

[308] P. B. Petersen and A. Tokmakoff,
Source for ultrafast continuum infrared and terahertz radiation.
Opt. Lett. **35**, 1962–1964 (2010).

[309] H. Shirai, T.-T. Yeh, Y. Nomura, C.-W. Luo, and T. Fuji,
Ultrabroadband Midinfrared Pump-Probe Spectroscopy Using Chirped-Pulse Up-conversion in Gases.
Phys. Rev. Appl. **3**, 051002 (2015).

[310] M. Göppert-Mayer,
Über Elementarakte mit zwei Quantensprüngen.
Ann. Phys. **401**, 273–294 (1931).

[311] W. G. Fisher, W. P. Partridge, Jr., C. Dees, and E. A. Wachter,
Simultaneous Two-Photon Activation of Type-I Photodynamic Therapy Agents.
Photochem. Photobiol. **66**, 141–155 (1997).

[312] W. R. Zipfel, R. M. Williams, and W. W. Webb,
Nonlinear magic: multiphoton microscopy in the biosciences.
Nat. Biotechnol. **21**, 1369–1377 (2003).

[313] F. Helmchen and W. Denk,
Deep tissue two-photon microscopy.
Nat. Methods **2**, 932–940 (2005).

[314] A. M. Smith, M. C. Mancini, and S. Nie,
Bioimaging: Second window for in vivo imaging.
Nat. Nanotechnol. **4**, 710–711 (2009).

[315] H. Hildenbrand.
Zwei-Photonen-Anregung mit Nachweis im Infraroten.
Bachelor thesis. Universität Würzburg (2012).

[316] T. Förster,
Fluoreszenzspektrum und Wasserstoffionenkonzentration.
Naturwissenschaften **36**, 186–187 (1949).

[317] C. Spies, B. Finkler, N. Acar, and G. Jung,
Solvatochromism of pyranine-derived photoacids.
Phys. Chem. Chem. Phys. **15**, 19893–19905 (2013).

[318] F. Lessing.
Erweiterung eines Aufbaus zur transienten Absorption mit einem Fluoreszenznachweis.
Bachelor thesis. Universität Würzburg (2013).

[319] C. Spies.
Solvent- and Time-dependent Fluorescence of Photoacids based on Pyranine.
Dissertation. Universität des Saarlandes (2014).

[320] N. M. Trieff and B. R. Sundheim,
The Effect of Solvent on the Acid–Base Kinetics of the Excited State of β-Naphthol.
J. Phys. Chem. **69**, 2044–2059 (1965).

[321] K. Weber,
Über die enge Beziehung der Fluoreszenzauslöschung zur Hemmung photochemischer Reaktionen.
Z. Phys. Chem. B **15**, 18 (1931).

[322] T. Förster,
Elektrolytische Dissoziation angeregter Moleküle.
Z. Elektrochem. **54**, 42–46 (1950).

[323] T. Förster,
Diabatic and adiabatic processes in photochemistry.
Pure Appl. Chem. **24**, 443–450 (1970).

[324] L. M. Tolbert and K. M. Solntsev,
Excited-State Proton Transfer: From Constrained Systems to "Super" Photoacids to Superfast Proton Transfer.
Acc. Chem. Res. **35**, 19–27 (2002).

[325] L. G. Arnaut and S. J. Formosinho,
Excited-state proton transfer reactions I. Fundamentals and intermolecular reactions.
J. Photochem. Photobiol. A **75**, 1–20 (1993).

[326] J. T. Hynes, J. P. Klinman, H.-H. Limbach, and R. L. Schowen (Eds.),
Hydrogen-Transfer Reactions.
Wiley-VCH, Weinheim (Germany) (2006).

[327] J. M. Paredes, L. Crovetto, A. Orte, J. M. Alvarez-Pez, and E. M. Talavera,
Influence of the solvent on the ground- and excited-state buffer-mediated proton-transfer reactions of a xanthenic dye.
Phys. Chem. Chem. Phys. **13**, 1685–1694 (2011).

[328] R. Simkovitch, E. Kisin-Finfer, S. Shomer, R. Gepshtein, D. Shabat, and D. Huppert,
Ultrafast excited-state proton transfer from hydroxycoumarin-dipicolinium cyanine dyes.
J. Photochem. Photobiol. A **254**, 45–53 (2013).

[329] K. M. Solntsev, D. Huppert, N. Agmon, and L. M. Tolbert,
Photochemistry of "Super" Photoacids. 2. Excited-State Proton Transfer in Methanol/Water Mixtures.
J. Phys. Chem. A **104**, 4658–4669 (2000).

[330] J. L. Pérez-Lustres, F. Rodriguez-Prieto, M. Mosquera, T. A. Senyushkina, N. P. Ernsting, and S. A. Kovalenko,
Ultrafast Proton Transfer to Solvent: Molecularity and Intermediates from Solvation- and Diffusion-Controlled Regimes.
J. Am. Chem. Soc. **129**, 5408–5418 (2007).

[331] B. Finkler, C. Spies, M. Vester, F. Walte, K. Omlor, I. Riemann, M. Zimmer, F. Stracke, M. Gerhards, and G. Jung,
Highly photostable "super"-photoacids for ultrasensitive fluorescence spectroscopy.
Photochem. Photobiol. Sci. **13**, 548–562 (2014).

[332] C. Spies, S. Shomer, B. Finkler, D. Pines, E. Pines, G. Jung, and D. Huppert,
Solvent dependence of excited-state proton transfer from pyranine-derived photoacids.
Phys. Chem. Chem. Phys. **16**, 9104–9114 (2014).

[333] S. L. Logunov, V. V. Volkov, M. Braun, and M. A. El-Sayed,
The relaxation dynamics of the excited electronic states of retinal in bacteriorhodopsin by two-pump-probe femtosecond studies.
Proc. Natl. Acad. Sci. USA **98**, 8475–8479 (2001).

[334] D. S. Larsen, E. Papagiannakis, I. H. M. van Stokkum, M. Vengris, J. T. M. Kennis, and R. van Grondelle,
Excited state dynamics of β-carotene explored with dispersed multi-pulse transient absorption.
Chem. Phys. Lett. **381**, 733–742 (2003).

[335] Q. Zhong, Z. Wang, Y. Sun, Q. Zhu, and F. Kong,
Vibrational relaxation of dye molecules in solution studied by femtosecond time-resolved stimulated emission pumping fluorescence depletion.
Chem. Phys. Lett. **248**, 277–282 (1996).

[336] S. A. Kovalenko, J. Ruthmann, and N. P. Ernsting,
Femtosecond hole-burning spectroscopy with stimulated emission pumping and supercontinuum probing.
J. Chem. Phys. **109**, 1894–1900 (1998).

[337] K. V. Reddy and M. J. Berry,
A nonstatistical unimolecular chemical reaction: isomerization of state-selected allyl isocyanide.
Chem. Phys. Lett. **66**, 223–229 (1979).

[338] F. F. Crim,
Vibrationally Mediated Photodissociation: Exploring Excited-State Surfaces and Controlling Decomposition Pathways.
Annu. Rev. Phys. Chem. **44**, 397–428 (1993).

[339] S. Draxler, T. Brust, S. Malkmus, J. A. DiGirolamo, W. J. Lees, W. Zinth, and M. Braun,
Ring-opening reaction of a trifluorinated indolylfulgide: mode-specific photochemistry after pre-excitation.
Phys. Chem. Chem. Phys. **11**, 5019–5027 (2009).

[340] T. Brust, S. Draxler, J. Eicher, W. J. Lees, K. Rück-Braun, W. Zinth, and M. Braun,
Increasing the efficiency of the ring-opening reaction of photochromic indolylfulgides by optical pre-excitation.
Chem. Phys. Lett. **489**, 175–180 (2010).

[341] M. M. N. Wolf, C. Schumann, R. Gross, T. Domratcheva, and R. Diller,
Ultrafast Infrared Spectroscopy of Riboflavin: Dynamics, Electronic Structure, and Vibrational Mode Analysis.
J. Phys. Chem. B **112**, 13424–13432 (2008).

[342] W. L. Jorgensen, D. S. Maxwell, and J. Tirado-Rives,
Development and Testing of the OPLS All-Atom Force Field on Conformational Energetics and Properties of Organic Liquids.
J. Am. Chem. Soc. **118**, 11225–11236 (1996).

[343] P. Sherwood, A. H. de Vries, M. F. Guest, G. Schreckenbach, C. Richard, A. Catlow, S. A. French, A. A. Sokol, S. T. Bromley, W. Thiel, A. J. Turner, S. Billeter, F. Terstegen, S. Thiel, J. Kendrick, S. C. Rogers, J. Casci, M. Watson, F. King, E. Karlsen, M. Sjøvoll, A. Fahmi, A. Schäfer, and C. Lennartz,
QUASI: A general purpose implementation of the QM/MM approach and its application to problems in catalysis.
J. Mol. Struct. (Theochem) **632**, 1–28 (2003).

[344] S. Metz, J. Kästner, A. A. Sokol, T. W. Keal, and P. Sherwood,
ChemShell—a modular software package for QM/MM simulations.
WIREs Comput. Mol. Sci. **4**, 101–110 (2014).

[345] V. Zoete, M. A. Cuendet, A. Grosdidier, and O. Michielin,
SwissParam: A Fast Force Field Generation Tool for Small Organic Molecules.
J. Comput. Chem. **32**, 2359–2368 (2011).

[346] E. Vanquelef, S. Simon, G. Marquant, E. Garcia, G. Klimerak, J. C. Delepine, P. Cieplak, and F.-Y. Dupradeau,
R.E.D. Server: a web service for deriving RESP and ESP charges and building force field libraries for new molecules and molecular fragments.
Nucl. Acids Res. **39**, W511–W517 (2011).

[347] F.-Y. Dupradeau, A. Pigache, T. Zaffran, C. Savineau, R. Lelong, N. Grivel, D. Lelong, W. Rosanski, and P. Cieplak,
The R.E.D. tools: advances in RESP and ESP charge derivation and force field library building.
Phys. Chem. Chem. Phys. **12**, 7821–7839 (2010).

[348] J. C. Phillips, R. Braun, W. Wang, J. Gumbart, E. Tajkhorshid, E. Villa, C. Chipot, R. D. Skeel, L. Kalé, and K. Schulten,
Scalable Molecular Dynamics with NAMD.
J. Comput. Chem. **26**, 1781–1802 (2005).

[349] R. Ahlrichs, M. Bär, M. Häser, H. Horn, and C. Kölmel,
Electronic structure calculations on workstation computers: The program system turbomole.
Chem. Phys. Lett. **162**, 165–169 (1989).

[350] I. T. Todorov and W. Smith,
DL_POLY_3: the CCP5 national UK code for molecular-dynamics simulations.
Phil. Trans. R. Soc. Lond. A **362**, 1835–1852 (2004).

[351] K. Inamoto, T. Saito, M. Katsuno, T. Sakamoto, and K. Hiroya,
Palladium-Catalyzed C–H Activation/Intramolecular Amination Reaction: A New Route to 3-Aryl/Alkylindazoles.
Org. Lett. **9**, 2931–2934 (2007).

[352] A. Schäfer, H. Horn, and R. Ahlrichs,
Fully optimized contracted Gaussian basis sets for atoms Li to Kr.
J. Chem. Phys. **97**, 2571–2577 (1992).

[353] F. Neese,
The ORCA program system.
WIREs Comput. Mol. Sci. **2**, 73–78 (2012).

Permissions

Reuse of Reference [3]

- **www.osapublishing.org** − *For OSA to consider a copyright permission request we require in writing by e-mail, fax, or mail:*
    - *a complete citation of the item to be reproduced, including figure numbers, etc.,*
    - *a clear explanation of the intended use of the item, and*
    - *the requestor's complete contact information.*

- The e-mail correspondence is provided below.

Dear Johannes Knorr,

Thank you for contacting The Optical Society.

Because you are the author of the source paper from which you wish to reproduce material, OSA considers your requested use of its copyrighted materials to be permissible within the author rights granted in the Copyright Transfer Agreement submitted by the requester on acceptance for publication of his/her manuscript. It is requested that a complete citation of the original material be included in any publication. This permission assumes that the material was not reproduced from another source when published in the original publication.

Please let me know if you have any questions.

Kind Regards,

Susannah Lehman

Susannah Lehman
March 30, 2015
Authorized Agent, The Optical Society

——Original Message——
From: Johannes Knorr [mailto:Johannes.Knorr@ruhr-uni-bochum.de]
Sent: Sunday, March 29, 2015 5:48 AM
To: pubscopyright
Subject: Reuse/republication of an entire work in dissertation

To whom it may concern,

I would like to request permission to reuse the full following article, of which I am the
first author, in my dissertation:

Johannes Knorr, Philipp Rudolf, and Patrick Nuernberger, *A comparative study on
chirped-pulse upconversion and direct multichannel MCT detection*, Optics Express, Vol.
21, Issue 25, pp. 30693–30706 (2013), http://dx.doi.org/10.1364/OE.21.030693

Best regards,

Johannes Knorr

Reuse of Reference [4]

- **From www.acs.org** – *Reuse/Republication of the Entire Work in Theses or Collections: Authors may reuse all or part of the Submitted, Accepted or Published Work in a thesis or dissertation that the author writes and is required to submit to satisfy the criteria of degree-granting institutions.*

- The RightsLink permission is provided below.

Copyright Clearance Center

RightsLink®

Home | Create Account | Help

ACS Publications
Most Trusted. Most Cited. Most Read.

Title: Ultrafast Photochemistry of a Manganese-Tricarbonyl CO-Releasing Molecule (CORM) in Aqueous Solution

Author: Philipp Rudolf, Florian Kanal, Johannes Knorr, et al

Publication: Journal of Physical Chemistry Letters

Publisher: American Chemical Society

Date: Feb 1, 2013

Copyright © 2013, American Chemical Society

LOGIN

If you're a copyright.com user, you can login to RightsLink using your copyright.com credentials. Already **a RightsLink user** or want to learn more?

Quick Price Estimate

Permission for this particular request is granted for print and electronic formats, and translations, at no charge. Figures and tables may be modified. Appropriate credit should be given. Please print this page for your records and provide a copy to your publisher. Requests for up to 4 figures require only this record. Five or more figures will generate a printout of additional terms and conditions. Appropriate credit should read: "Reprinted with permission from {COMPLETE REFERENCE CITATION}. Copyright {YEAR} American Chemical Society." Insert appropriate information in place of the capitalized words.

I would like to...	reuse in a Thesis/Dissertation
Requestor Type	Author (original work)
Portion	Full article
Format	Print and Electronic
Will you be translating?	No
Select your currency	EUR - €
Quick Price	Click Quick Price

This service provides permission for reuse only. If you do not have a copy of the article you are using, you may copy and paste the content and reuse according to the terms of your agreement. Please be advised that obtaining the content you license is a separate transaction not involving Rightslink.

QUICK PRICE | CONTINUE

To request permission for a type of use not listed, please contact the publisher directly.

Copyright
Clearance
Center

RightsLink®

Home | Create Account | Help

ACS Publications
Most Trusted. Most Cited. Most Read.

Title: Ultrafast Photochemistry of a Manganese-Tricarbonyl CO-Releasing Molecule (CORM) in Aqueous Solution

Author: Philipp Rudolf, Florian Kanal, Johannes Knorr, et al

Publication: Journal of Physical Chemistry Letters

Publisher: American Chemical Society

Date: Feb 1, 2013

Copyright © 2013, American Chemical Society

LOGIN

If you're a copyright.com user, you can login to RightsLink using your copyright.com credentials. Already **a RightsLink user** or want to learn more?

PERMISSION/LICENSE IS GRANTED FOR YOUR ORDER AT NO CHARGE

This type of permission/license, instead of the standard Terms & Conditions, is sent to you because no fee is being charged for your order. Please note the following:

- Permission is granted for your request in both print and electronic formats, and translations.
- If figures and/or tables were requested, they may be adapted or used in part.
- Please print this page for your records and send a copy of it to your publisher/graduate school.
- Appropriate credit for the requested material should be given as follows: "Reprinted (adapted) with permission from (COMPLETE REFERENCE CITATION). Copyright (YEAR) American Chemical Society." Insert appropriate information in place of the capitalized words.
- One-time permission is granted only for the use specified in your request. No additional uses are granted (such as derivative works or other editions). For any other uses, please submit a new request.

BACK | CLOSE WINDOW

Acknowledgements

This dissertation was conducted at the Institute for Physical and Theoretical Chemistry at the University of Würzburg. Many people were involved in the process of making this thesis possible. At this point, I would like to express my sincere gratitude to:

- **Prof. Dr. Patrick Nürnberger** for supervising my PhD project. From the first day when starting as a laser-rookie in his young research group, work was characterized by intriguing projects and continuous support. His open-minded attitude created an inspiring working atmosphere with enough room to pursue own research ideas. This thesis benefited a lot from his enthusiams about science and his willingness to extensively discuss the latest results or possible new experiments. Furthermore, I am thankful for providing any possible support to visit several national and international conferences and present own research results. Thank you very much!

- **Prof. Dr. Tobias Brixner**, second member of my GSST supervisory board, for his extraordinary support and advices regarding every project I worked on during my PhD project. Moreover, I am thankful for the possibility to work with state-of-the-art equipment.

- **Prof. Dr. Volker Engel** for the willingness to support me during my PhD project as third member of the GSST supervisory board.

- **Prof. Dr. Wolfram Sander** for initiating the carbene project.

- **Prof. Dr. Ulrich Schatzschneider** for continuous support and fruitful discussions regarding the gasotransmitter project.

- **Prof. Dr. Gregor Jung** for the excellent collaboration in the super-photoacid project.

- **Prof. Dr. Manuel Joffre** for stimulating input on the topic of chirped-pulse up-conversion.

- **Dr. Elsa Sánchez-García** and **Dr. Pandian Sokkar** for simulating the dynamics of diphenylcarbene in solvent mixtures.

- **Dr. Christoph Nagel** for the synthesis of CO-releasing molecules.

- **Björn Finkler** for the synthesis of super-photoacids.

- **Paolo Costa** for the synthesis of the diphenylcarbene precursor.

- **Dr. Philipp Rudolf** for teaching me a lot about how to handle invisible beams, his patience, and the successful teamwork regarding the comparative study.

- **Dr. Christian Spies** for helpful discussions about the chemistry of super-photoacids and for carefully proofreading the associated parts of this thesis.

- **Sebastian Schott** for thoroughly proofreading parts of this thesis, for countless enjoyable discussions about physics and beyond, for his conscientious way of working, for managing the reference data base, and for the superb teamwork in the carbene project when learning that the first solution is not always THE solution.

- **Sebastian Götz** for testing my physical limits in innumerable joint training sessions, for uncountable discussions about important topics such as the optimal nutrition strategy while running a marathon or how to optimally prepare cross-country skies for specific snow conditions, and for sharing his expertise in photography and the creation of 3D computer graphics.

- **Dr. Andreas Steinbacher**, **Bernhard Huber**, **Christoph Schwarz**, **Sebastian Röding**, and **Simon Draeger** for smoothly managing all the computer-related challenges in our group.

- **Florian Lessing**, **Heiko Hildenbrand**, and **Jarno Riefer** for their support in the laboratory and their valuable contributions from a chemist's point of view.

- **Christian Kramer** for always spreading a good mood, although supporting the wrong soccer team.

- **Simon Draeger** and **Dr. Stefan Rützel** for securing permanent coffee supply.

- All the other colleagues both from Würzburg and Bochum who have enriched my time as a doctoral student: **Dr. Albert King**, **Anja Hasenkopf**, **Christian Dreher**, **Dr. Christian Rewitz**, **Dr. Cristina Consani**, **Domenik Schleier**, **Federico Koch**, **Dr. Florian Kanal**, **Dr. Jakub Dostál**, **Julia Heitmüller**, **Lea Reß**, **Lena Grimmelsmann**, **Dr. Martin Kullmann**, **Marco Flock**, **Marco Schmid**, **Mark Babin**, **Matthias Wurdack**, **Meike Diekmann**, **Michel Keller**, **Dr. Monika Pawłowska**, **Dr. Pramod Kumar Verma**, **Sebastian Pres**, **Tom Bolze**, and **Dr. Xiaonan Ma**.

- **Andrea Gehring**, **Anna Rosenfeldt**, and **Christel Tönnissen** for managing any kind of organizational problem.

- **Belinda Böhm** and **Sabine Fuchs** for taking care of the chemistry lab and the laser maintenance, and for always having a friendly word.

- **Gerhard Bömmel**, **Jürgen Zimmermann**, **Katharina Schreckling**, **Peter Lang**, **Ralf Kohrmann**, **Reiner Eck**, and **Wolfgang Liebler** for mastering any challenge regarding electronics and mechanics, thus laying the foundations for me to build up new experiments.

- **Dr. Ole Riemann** and **Dr. Stephan Schröder-Köhne** for organizing inspiring workshops within the GSST study program.

- The **Deutsche Forschungsgemeinschaft** for support within the research unit "FOR 1809 (Lichtinduzierte Dynamik in molekularen Aggregaten)", the Emmy-Noether program, and the Cluster of Excellence RESOLV (EXC1069).

- The **Wilhelm und Else Heraeus-Stiftung** for financially supporting annual visits of the DPG spring meetings.

Finally, I would like to thank my family. I could not have done this without your love and support!

Affidavit

I hereby confirm that my thesis entitled

Femtosecond spectroscopy of photolysis reactions in the liquid phase

is the result of my own work. I did not receive any help or support from commercial consultants. All sources and / or materials applied are listed and specified in the thesis. Furthermore, I confirm that this thesis has not yet been submitted as part of another examination process neither in identical nor in similar form.

Würzburg, December 2, 2015

Johannes Walter Knorr

Eidesstattliche Erklärung

Hiermit erkläre ich an Eides statt, die Dissertation mit dem Titel

Femtosekundenspektroskopie von Photolysereaktionen in der flüssigen Phase

eigenständig, d.h. insbesondere selbständig und ohne Hilfe eines kommerziellen Promotionsberaters, angefertigt und keine anderen als die von mir angegebenen Quellen und Hilfsmittel verwendet zu haben.
Ich erkläre außerdem, dass die Dissertation weder in gleicher noch in ähnlicher Form bereits in einem anderen Prüfungsverfahren vorgelegen hat.

Würzburg, 02. Dezember 2015

Johannes Walter Knorr